ELECTROMAGNETIC MOMENTS IN NUCLEI: SENSITIVE PROBES OF ELECTROMAGNETIC FIELD ENVIRONMENT IN SOLIDS

By

SOURAV KUMAR DEY

PHYS05201504001

Saha Institute of Nuclear Physics, Kolkata

A thesis submitted to the

Board of Studies in Physical Sciences

In partial fulfillment of requirements

for the Degree of

DOCTOR OF PHILOSOPHY

of

HOMI BHABHA NATIONAL INSTITUTE

December, 2018

Homi Bhabha National Institute

Recommendations of the Viva Voce Committee

As members of the Viva Voce Committee, we certify that we have read the dissertation prepared by **Sourav Kumar Dey** entitled **"Electromagnetic moments in nuclei: Sensitive probes of electromagnetic field environment in solids"** and recommend that it may be accepted as fulfilling the thesis requirement for the award of Degree of Doctor of Philosophy.

Chairman - Prof. Satyaranjan Bhattacharyya SBhattacharyya	Date: 28/02/2019
Guide/Convener - Prof. Chandi Charan Dey Chandi Charan Dey	Date: 27.2.19
Co-guide - Prof. Satyajit Saha Sahe	Date: 27/2/2019
Examiner - Prof. S. N. Mishra, TIFR Surendra Nath Mishra	Date: 27/2/19
Member 1 - Prof. Asimananda Goswami	Date:
Member 2 - Dr. Sarmistha Bhattacharyya S. Bhattacharyya	Date: 27/2/19

Final approval and acceptance of this thesis is contingent upon the candidate's submission of the final copies of the thesis to HBNI.

We hereby certify that we have read this thesis prepared under our direction and recommend that it may be accepted as fulfilling the thesis requirement.

Date: 27.2.19

Place:

Co-guide: Sahe. Prof. Satyajit Saha

Guide: Chandi Charan Dey Prof. Chandi Charan Dey

STATEMENT BY AUTHOR

This dissertation has been submitted in partial fulfillment of requirements for an advanced degree at Homi Bhabha National Institute (HBNI) and is deposited in the Library to be made available to borrowers under rules of the HBNI.

Brief quotations from this dissertation are allowable without special permission, provided that accurate acknowledgement of source is made. Requests for permission for extended quotation from or reproduction of this manuscript in whole or in part may be granted by the Competent Authority of HBNI when in his or her judgment the proposed use of the material is in the interests of scholarship. In all other instances, however, permission must be obtained from the author.

Sourav Kumar Dey

Sourav Kumar Dey

DECLARATION

I, hereby declare that the investigation presented in the thesis has been carried out by me. The work is original and has not been submitted earlier as a whole or in part for a degree / diploma at this or any other Institution / University.

Sourav Kumar Dey

Sourav Kumar Dey

List of Publications arising from the thesis

Journal

1. "Crystalline phases in Zr_9Ni_{11} and Hf_9Ni_{11} intermetallics; Investigations by perturbed angular correlation spectroscopy and ab initio calculations",
   S.K. Dey, C.C. Dey, S. Saha, G. Bhattacharjee, J. Belošević-Čavor, D. Toprek, *Journal of Solid State Chemistry*, **2019**, 269, 476-485.

2. "Identification of phase components in Zr-Ni and Hf-Ni intermetallic compounds; investigations by perturbed angular correlation spectroscopy and first principles calculations",
   S.K. Dey, C.C. Dey, S. Saha, J. Belošević-Čavor, D. Toprek, *Journal of Alloys and Compounds*, **2017**, 723, 425-433.

3. "Electric field gradients in Zr_8Ni_{21} and Hf_8Ni_{21} intermetallic compounds; results from perturbed angular correlation measurements and first-principles density functional theory",
   S.K. Dey, C.C. Dey, S. Saha, J. Belošević-Čavor, *Intermetallics*, **2017**, 84, 112-120.

4. "Effects of Zr impurity on microscopic behavior of Hf metal",
   S.K. Dey, C.C. Dey, S. Saha, *Journal of Physics and Chemistry of Solids*, **2016**, 95, 98-105.

5. "Low temperature structural modification in Rb_2ZrF_6 : Investigations by perturbed angular correlation spectroscopy",
   S.K. Dey, C.C. Dey, S. Saha, *Journal of Physics and Chemistry of Solids*, **2016**, 93, 145-156.

6. "Low temperature structural phase transition in hafnium and zirconium tetrafluoride trihydrates",
   S.K. Dey, C.C. Dey, S. Saha, *Journal of Physics and Chemistry of Solids*, **2016**, 91, 18-24.

Chapters in books and lecture notes

NIL

Conferences

1. **Poster Presentation** at the 60th DAE-BRNS Symposium on Nuclear Physics, Sri Sathya Sai Institute of Higher Learning, Prasanthi Nilayam, Andhra Pradesh, December 7-11, 2015, "Comparative performances of $LaBr_3$(Ce) and BaF_2 scintillators", S.K. Dey, C.C. Dey, S. Saha, *Proceedings of the DAE-BRNS Symposium on Nuclear Physics*, **2015**, 60, 992-993.

2. **Poster Presentation** at the 61th DAE-BRNS Symposium on Nuclear Physics, Saha Institute of Nuclear Physics, Kolkata, December 5-9, 2016, "Observation of band structure and new isomeric levels in ^{204}At", S.K. Dey, D. Kanjilal, A. Bisoi, M. Das, C.C. Dey, S. Ray, R. Palit, S. Saha, J. Sethi, S. Nag, S. Saha, *Proceedings of the DAE-BRNS Symposium on Nuclear Physics*, **2016**, 61, 256-257.

3. **Poster Presentation** at the 13th DAE-BRNS Symposium on Nuclear Physics, DAE-BRNS Nuclear and Radiochemistry Symposium, KIIT University, Bhubaneswar, February 6-10, 2017, "Studies in Zr_7Ni_{10} and Hf_7Ni_{10} intermetallic compounds by Perturbed Angular Correlation Spectroscopy", S.K. Dey, C.C. Dey, S. Saha.

4. **Oral Presentation** at the Advanced Detectors for Nuclear, High Energy and Astroparticle Physics Conference, Bose Institute, Kolkata, February 15-17, 2017, "$LaBr_3$(Ce): a new generation detector for timing spectroscopy", S.K. Dey, C.C. Dey, S. Saha.

5. **Poster Presentation** at the 62nd DAE-BRNS Symposium on Nuclear Physics, Thapar University, Patiala, Punjab, December 20-24, 2017, "Development of a time-differential perturbed angular correlation spectrometer using $LaBr_3$(Ce) and

BaF_2 detectors", S.K. Dey, R. Sewak, C.C. Dey, S. Saha, *Proceedings of the DAE-BRNS Symposium on Nuclear Physics*, **2017**, 62, 1072-1073.

6. **Poster Presentation** at the 24th WIEN2k workshop, TU Wien, Vienna, Austria, September 18-22, 2017, "Electric field gradients at ^{181}Ta probe in Zr_7Ni_{10} and Hf_7Ni_{10} intermetallic binary alloys; investigations by time-differential perturbed angular correlation spectroscopy", S.K. Dey, C.C. Dey, S. Saha.

7. **Oral Presentation** at the Hyperfine 2019 international conference, International Center Goa, Goa, India, (organized by TIFR in association with Goa University) February 10-15, 2019, "Component phases and local electric field gradient in Zr_7Ni_{10}", S.K. Dey, C.C. Dey, S. Saha, G. Bhattacharjee, D. Banerjee, D. Toprek. (Presentation)

Others

1. "Phase components in Zr_7Ni_{10} and Hf_7Ni_{10} binary alloys; Investigations by perturbed angular correlation spectroscopy and first principles calculations", S.K. Dey, C.C. Dey, S. Saha, G. Bhattacharjee, D. Banerjee, D. Toprek (arXiv:1809.08114)

Sourav Kumar Dey

Sourav Kumar Dey

DEDICATIONS

Dedicated to my parents

ACKNOWLEDGEMENTS

This thesis is a result of four years of work and during this time I have received support and encouragement from many people. It is my great pleasure to thank them all now. First and foremost, I would like to express my sincere gratitude to my supervisors Prof. Chandi Charan Dey and Prof. Satyajit Saha who have supported throughout my thesis with their enthusiasm, patience, knowledge and suggestions. I am very grateful and indebted to them for the their insightful discussions. Without their inspiration and dedicated supervision, it would have never been possible to complete my thesis work. I express my sincere gratitude to the doctoral committee members Prof. Satyaranjan Bhattacharyya, Prof. Asimananda Goswami and Dr. Sarmistha Bhattacharyya (VECC) for providing invaluable suggestions. I am greatly indebted to Prof. Jelena Belošević-Čavor and Dr. Drogan Toprek (Institute of Nuclear Sciences Vinca, University of Belgrade, Serbia) for the fruitful collaboration and for providing us the results of theoretical calculations of hyperfine parameters. I am grateful to Debasmita di for her continuous co-operation and suggestions in the study of nuclear structure. I extend my heartiest thanks to Dr. Biswarup Satpati and Gourab for carrying out the TEM measurements and analysis. I wish to thank Mr. Anish Karmahapatra for carrying out the XRD measurements, and Santanu da and Mily di for their help in XRD analysis. I am thankful to Dr. Debasish Banerjee (VECC) for the procurement of probe for PAC measurements. I also like to acknowledge Marik da, Mr. C. Palanivel, Pradipta da, Prabir da, Dilip da for their technical support during my thesis experiments. I would like to thank Rajni da, Hitesh da, Abhik da, Deb Sankar da, Meghna di, Bankim, Jaydeep, Arpita, Sayan, Sridhar, Prasant, Anil, Promita, Shubham, Ram, Vishal for their encouragement and stimulating discussions. I am thankful to Aminul da, Arindam da, Anisur da, Arijit da, Asim da, Tapas da, Kuntal da, Anshu da, Palash da, Abhijit da, Rome, Shamik, Sukannya, Mugdha, Sudeshna, Shramana, Maireyee, Biswarup, Biswajit, Abhishek, Amit, Mithun for motivating me and making research life more enjoyable. I find no word to express my gratitude to my parents and family members who stood by me and encouraged me in every steps of my life. I am thankful to Tania for her love, encouragement and constant support which helped me overcome various difficult phases.

Contents

Synopsis

In the present thesis, the roles of nuclear multipole moments in the characterization of solid materials through the nuclear technique of perturbed angular correlation (PAC) spectroscopy and in the study of nuclear structure properties at high spin states in the proton-rich trans-lead region by gamma ray spectroscopy have been described.

Nuclear moments are intrinsic properties of a nucleus. The nuclear magnetic moment is related to the angular momentum of the nucleus. The angular momentum, in turn, is related to the orbital configuration of protons and neutrons which generates the nuclear spin I. All nuclear levels with non-zero spin possess nuclear magnetic moments. The nuclear electric dipole moment is zero due to the definite parity of nuclear states. The next significant term, nuclear electric quadrupole moment is related to the spin of nucleus and its projection along the "z"-axis. This parameter describes asphericity of the nuclear charge distribution. Any nuclear state with spin angular momentum $I > \frac{1}{2}\hbar$ has a finite quadrupole moment. These nuclear moments can be useful to probe charge density inside a non-cubic material or the internal magnetic field in a magnetic material through study of hyperfine interactions. Gamma ray transitions, occurring between nuclear states, carry information about the corresponding transition probabilities, which in turn, may be directly correlated to the corresponding nuclear multipole moments of the decaying nuclear levels. The transition rate for magnetic dipole transition is sensitive to nuclear magnetic dipole moment and the transition rate for electric quadrupole transition is associated with nuclear electric quadrupole moment.

In the first part of the thesis, studies of structural properties of some solid materials through the hyperfine interaction of electric quadrupole moment with the electric field gradient generated at the probe nuclear site due to surrounding charge distribution with a non-cubic symmetry have been carried out. This nuclear technique of studying solid materials through the hyperfine interaction is known as perturbed angular correlation (PAC). In this technique, using the known values of electromagnetic moments of the probe nucleus, the EFG and/or the magnetic field (MF) strength in a magnetic material are determined. The measured value of EFG is then compared with that calculated by density functional theory (DFT) considering the known crystal structure of the material. The EFG and MF are the local structure effects of the probe nucleus.

Second part of the thesis deals with gamma-ray spectroscopic studies which were carried out to determine the structural properties of proton-rich astatine nucleus at high spin states. It is well known that the gamma transition rates depend on, apart from other factors, the transition probabilities. The life time of the high spin states and their systematics carry the footprint of the interplay between some of the valance nucleon spins, which is directly correlated with either the magnetic moments or the electric moments related to the internal charge distribution of the nuclei. The targeted nucleus is produced by bombarding a high energy projectile beam on a target material by fusion-evaporation reaction. The excited compound nucleus then de-excites by emitting γ-rays. By observing the γ-rays at different detector angles with respect to the beam direction, the spin and parity of excited nuclear levels are determined. Multipolarity and linear polarization of emitted γ-rays are measured by the spin differences of the nuclear levels and angles at which these γ-rays are Compton-scattered in the detector crystals with respect to beam direction, respectively. By studying the systematics of the transition probabilities of dipole and quadrupole transitions, single particle and/or collective nature of the nucleus are determined.

In PAC technique, a suitable probe nucleus which emits two coincident γ-rays is intro-

duced into the investigated material. The important requirements for PAC measurement are the existence of an isomeric intermediate level whose lifetime (τ_N) falls in the range from few ns to microsecond and a large anisotropic angular correlation of coincident γ-rays and having large values of electromagnetic moments (electric quadrupole moment $Q \geq 0.1$ b and magnetic dipole moment $\mu \geq \mu_N$). The observation of first gamma ray of the γ_1-γ_2 cascade in a fixed direction selects an aligned ensemble of nuclear spin of the intermediate state, thus creating an anisotropic angular distribution for the γ_2 with respect to the direction of γ_1. The probe substitutes some of the lattice atoms of the host matrix which have similar atomic radius or electronegativity as the probe atom. Doping of the probe into the material is done in high dilution so that the crystal structure of the host matrix remains unaltered. For a non-cubic crystal symmetry of the material, the electric field gradient is created by the surrounding charge distribution of the probe nucleus which interacts with the nuclear quadrupole moment, and the internal magnetic field of any magnetic host material interacts with the nuclear dipole moment of the probe nucleus. The technique has got some advantage over the other complementary material characterization techniques due to its atomic scale resolution and its sensitivity with temperature. Thus, phase stability of any material can be determined by temperature dependent PAC studies. For the studies of different materials in the present thesis, ^{181}Hf probe which undergoes β^- decay to ^{181}Ta ($T_{1/2}$=42.4 d) has been used. This daughter isotope then emits 133-482 keV coincident γ-rays passing through the intermediate 482 keV level with $T_{1/2}$= 10.8 ns, μ=3.24(5) μ_N, Q= 2.36(5) b [1].

For present PAC measurements, we have used two PAC spectrometers developed in our laboratory, a four detector BaF_2-BaF_2 and a four detector $LaBr_3$(Ce)-BaF_2. From four slow-fast coincidence combinations (two at 90° and two at 180°), the perturbation function $G_2(t)$ [1,2] is obtained. The $G_2(t)$ contains three transition frequencies between the sublevels that arise due to hyperfine splitting of the intermediate 482 keV level of ^{181}Ta and the EFG is derived from these three transition frequencies. From the three transition frequencies, generated by the hyperfine splitting of the intermediate level,

contained in $G_2(t)$, the quadrupole frequency and EFG are determined. For temperature dependent PAC measurements (up to 1073 K), a locally made resistive furnace was used. The investigated materials by PAC technique have been categorized in two parts due to the different procedures involved in the preparation of samples. a) Chemical samples: $ZrF_4{\cdot}3H_2O/HfF_4{\cdot}3H_2O$, Rb_2ZrF_6/Cs_2HfF_6; b) Intermetallic samples: Zr_8Ni_{21}/Hf_8Ni_{21}, $ZrNi_3/HfNi_3$, Zr_9Ni_{11}/Hf_9Ni_{11} and Zr_7Ni_{10}/Hf_7Ni_{10}.

The two trihydrate tetrafluoride compounds, viz., $ZrF_4{\cdot}3H_2O$ and $HfF_4{\cdot}3H_2O$ have been studied by PAC to resolve the structural anomalies of these compounds reported earlier. From XRD measurements [3], both the monoclinic and triclinic modifications of $ZrF_4{\cdot}3H_2O$ were found but for $HfF_4{\cdot}3H_2O$, only the monoclinic modification was reported. The triclinic structure of $ZrF_4{\cdot}3H_2O$ is formed by the discrete dimeric groups $Zr_2F_8(H_2O)_6$ where the Zr atoms share $F\cdots F$ common edge. On the other hand, the monoclinic structures of $ZrF_4{\cdot}3H_2O$ and $HfF_4{\cdot}3H_2O$ are polymeric. In the co-ordination sphere of Zr/Hf atom, four fluorine atoms and two H_2O molecules are attached with the central Zr/Hf atom and one of the water molecule resides between the chains. Furthermore, the anhydrous ZrF_4 and HfF_4 have applications in developing optical coating materials due to their excellent transmission properties [4]. Therefore, it is important also to study the phase transitions from hydration to dehydration and their structural stabilities with temperature and these have been studied by the PAC technique. From our measurements, both monoclinic and triclinic structural modifications were found in $HfF_4{\cdot}3H_2O$ and $ZrF_4{\cdot}3H_2O$. In $HfF_4{\cdot}3H_2O$, a predominant component was found due to triclinic structural modification and the monoclinic fraction was produced as a minor component. In $ZrF_4{\cdot}3H_2O$, a major component was found due to its triclinic structure. Interestingly, a minor fraction due to monoclinic modification of zirconium tetrafluoride trihydrate was found in this sample. From temperature dependent PAC studies, a structural transition at 318 K was found in $ZrF_4{\cdot}3H_2O$ due to the production of HF adducted $ZrF_4{\cdot}HF{\cdot}2H_2O$. In $HfF_4{\cdot}3H_2O$, both monoclinic and triclinic components disappeared completely at 333 K and three new phases, viz., Hf adducted hafnium tetrafluride di-

hydrate ($HfF_4 \cdot HF \cdot 2H_2O$), hafnium tetrafluoride monohydrate ($HfF_4 \cdot H_2O$), Hf_2OF_6 and anhydrous HfF_4 were found.

The compounds Rb_2ZrF_6 and Cs_2HfF_6 have been studied to resolve ambiguities in earlier measurements, particularly, to study the nuclear relaxation effects due to fluorine activation in the materials and also to find any structural phase transition in Rb_2ZrF_6 with temperature. From our PAC measurements in Rb_2ZrF_6, four structural modifications were found. A new fraction due to the rotated ZrF_6^{2-} octahedron was observed similar to the results found in analogous Rb_2HfF_6 [5]. Time dependent spin-relaxation effect was observed at 773 K in one of the samples of Rb_2ZrF_6 due to the fluctuation of fluorine atom in the ZrF_6^{2-} octahedral cage. In Cs_2HfF_6, on the other hand, two structural modifications were found.

A major portion of the present thesis is the studies of Zr-Ni and Hf-Ni intermetallic systems of different stoichiometric compositions. The alloys based on Zr-Ni system have numerous technological applications due to their high thermo-chemical stability. These are used as an integral part to form high temperature eutectics, bulk glassy alloys, corrosion resistance materials etc. Some of the Zr-Ni binary alloys, viz., Zr_8Ni_{21}, Zr_9Ni_{11}, Zr_7Ni_{10}, $ZrNi_3$, Zr_2Ni_7 and ZrNi have received considerable attention due to their excellent high rate capacity of gasious hydrogen storage in interstitial sites and reversibility of hydrogen dissociation at room temperature. These alloys are potential candidate to form metal hydride (MH) which have application as a negative electrode in Ni-MH rechargeable batteries. These batteries are used in fuel cells and hybrid electric vehicles for their high energy density and environmentally friendly characteristics. In Zr_8Ni_{21} base alloy, other secondary phases, Zr_7Ni_{10} and Zr_2Ni_7 were found to be present after annealing treatment [6]. Therefore, it is very important to study multiple phase components that are produced at high temperatures in these alloys which will help in the future development of MH with better electrochemical properties.

In the present thesis, Zr_8Ni_{21}, $ZrNi_3$, Zr_9Ni_{11} and Zr_7Ni_{10} alloys have been studied to

i) determine the component phases in the samples from PAC, X-ray diffraction (XRD) and transmission electron microscopy/selected area electron diffraction (TEM/SAED) measurements ii) to determine the EFG for different phase components and compare the results with those obtained from theoretical calculations by density functional theory (DFT) considering the known crystal structure of the crystalline compound and iii) to determine the structural stability of the compounds with temperature from temperature dependent PAC studies. The EFGs at the ^{181}Ta impurity atom have been calculated by density functional theory. In most cases, more than one EFG is found due to different non-equivalent Zr/Hf sites for a particular compound or for different phases present in the sample. The compounds Hf_8Ni_{21}, Hf_7Ni_{10}, Hf_9Ni_{11} and $HfNi_3$ have also been studied by PAC technique to determine the isostructurality of isoformulae Zr-Ni and Hf-Ni compounds and to compare their temperature dependent properties. The Hf-Ni alloys have tecnhological applications also. The Hf-Ti-Ni alloys are used to form shape memory alloys.

The intermetallic Zr-Ni and Hf-Ni samples were prepared in argon arc furnace by melting the constituent elements taken in stoichiometric ratios. The radioactive ^{181}Hf wire which was prepared by neutron activation in the Dhruva reactor, Mumbai was then inserted within the sample by further melting. In most cases, the loss of sample during preparation in arc furnace was less than 1% and a shiny globule sample was found. For high temperature measurements, the sample was sealed in an evacuated quartz tube.

For XRD and TEM/SAED measurements, separate inactive samples were prepared in a similar manner and these were then powdered using a mortar and pestle. The XRD measurements were carried out using the Rigaku X-ray diffractometer TTRAX-III and Cu K_α radiation. Transmission electron microscopy measurements were carried out using FEI, Tecnai G2 F30, S-Twin microscope equipped with a high angle annular dark-field (HAADF) detector, a scanning unit and a energy dispersive X-ray spectroscopy (EDX) unit to perform the scanning transmission electron microscopy (STEM-HAADF-EDX).

In the Zr-Ni phase diagram, eight stable Zr-Ni crystalline phases have been found. The compounds Zr_2Ni_7, Zr_2Ni and ZrNi are congruently melting phases, and the alloys Zr_8Ni_{21}, Zr_9Ni_{11} and Zr_7Ni_{10} and $ZrNi_5$ are formed peritectically. The phase $ZrNi_3$ is formed in a peritectoid reaction between Zr_2Ni_7 and Zr_8Ni_{21}. The phase Zr_9Ni_{11} decomposes to ZrNi and Zr_7Ni_{10} phases eutectoidally at $\sim$975°C. In the Hf-Ni binary system, nine stable intermediate crystalline phases, viz., Hf_2Ni_7, HfNi, Hf_2Ni, Hf_3Ni_7, $HfNi_3$, $HfNi_5$, Hf_8Ni_{21}, Hf_9Ni_{11} and Hf_7Ni_{10} were found. The phases Hf_2Ni_7 and HfNi were reported to be congruently melting phases. All other phases are formed by peritectic reactions.

The isostructural compounds Zr_8Ni_{21} and Hf_8Ni_{21} have triclinic crystal structure with space group $P\bar{1}$. From our PAC measurement, two non-equivalent Zr/Hf crystallographic sites in Zr_8Ni_{21}/Hf_8Ni_{21} were found. Quadrupole frequencies for these sites decrease with temperature following $T^{3/2}$-temperature dependent relationship. In Zr_8Ni_{21}, a secondary phase due to Zr_7Ni_{10} was observed and in stoichiometric Hf_8Ni_{21}, weak signal due to $HfNi_3$ phase was detected. At 1073 K, the Hf_8Ni_{21} phase was found to decompose to $HfNi_3$ phase eutectoidally. The phase $HfNi_3$ appeared as a dominating phase when re-measured at room-temperature after measurement at 1073 K.

The $ZrNi_3$ compound has hexagonal close-packed structure with space group $P6_3/mmc$. The phase $HfNi_3$ has two polymorphs, one is α-$HfNi_3$ which is stable above 1200°C and another phase is β-$HfNi_3$ which is stable below 1200°C. The α-$HfNi_3$ phase has trigonal crystal structure with space group $R\bar{3}m$ and the β-$HfNi_3$ has hexagonal crystal structure with space group $P6_3/mmc$. The β-$HfNi_3$ phase is isostructural with $ZrNi_3$. In $ZrNi_3$, single Zr site whereas in $HfNi_3$, two non-equivalent Hf sites were found from our PAC measurements. In stoichiometric $ZrNi_3$, the phase $ZrNi_3$ itself is produced as a weak fraction but in $HfNi_3$ sample, the phase $HfNi_3$ is largely produced. Presence of multiple phases, viz., Zr_2Ni_7, Zr_7Ni_{10} and Zr_8Ni_{21} were found in the $ZrNi_3$ sample. In $HfNi_3$, secondary phases due to Hf_2Ni_7 and Hf_8Ni_{21} were found in the sample. Temperature

dependent PAC measurements show that the phase $HfNi_3$ is a stable phase.

The Zr_9Ni_{11} and Hf_9Ni_{11} compounds have tetragonal crystal structure with space group $I4/m$. In the stoichiometric sample of Zr_9Ni_{11}, the phase Zr_9Ni_{11} is found to be predominant up to 673 K from our PAC measurements. The phase Zr_8Ni_{21} is produced as a minor fraction in the sample. At 773 K, the phase Zr_9Ni_{11} partially decomposed to Zr_7Ni_{10} and at 973 K, it completely decomposed to ZrNi and Zr_7Ni_{10} phases eutectoidally. In Hf_9Ni_{11}, the phase HfNi is produced as a dominating phase and a weak signal due to phase Hf_9Ni_{11} was detected. The phase Hf_9Ni_{11} was found to be stable up to 873 K.

The stoichiometric Zr_7Ni_{10} and Hf_7Ni_{10} alloys crystallize in orthorhombic $Cmca$ space group. Three Zr-Ni phases have been observed from our PAC studies in the stoichiometric Zr_7Ni_{10} sample. Apart from the Zr_7Ni_{10} phase, the phases Zr_2Ni_7 and Zr_8Ni_{21} were found in the sample. The phase Zr_2Ni_7 is found to be a predominant up to 1073 K in the sample. In Hf_7Ni_{10}, the phase $HfNi_3$ was appeared as a dominating phase and Hf_7Ni_{10} phase was produced as a minor fraction. However, the phase fraction of Hf_7Ni_{10} was found to enhance with temperature at the expense of $HfNi_3$ phase.

The DFT calculations were done using WIEN2k simulation package [7]. The basis set used is (linearized) augmented plane wave + local orbitals [(L)APW+lo]. The exchange correlation potential was calculated using generalized gradient approximation (GGA). In the APW basis function, electrons which are far away from the nucleus are treated as free electrons and are described by plane waves. The electrons which are near to the nuclei behave more-like they are in free atom and thus these electrons are described by atomic like wave-functions. Therefore, the entire reciprocal space is divided into two regions. A sphere is drawn around each atom which is called muffin-tin sphere and the remaining space outside the sphere is interstitial region. In the linearized APW method, the eigenenergy of the searched eigenfunction is linearized by Taylor expanding the atomic-like wavefunction about a chosen energy value. But, it becomes difficult to guess the energy value for low-lying valance states where the electrons are not contained

in the core or valance states entirely. These are called semi-core states. To resolve this ambiguity, concept of local orbital is introduced. A local orbital is defined for every orbital and magnetic quantum number of spherical harmonics of the atomic-like wavefunction and for every atom including the equivalent atoms in the unit cell. A local orbital is zero in the interstitial region and in the muffin-tin spheres of other atoms. For the calculation of EFG, a supercell approach is used in WIEN2k software. Each of the non-equivalent Zr/Hf atoms in the unit cell was replaced by Ta (probe) subsequently preserving the point group symmetry around original atom. The probe atom resides at the center of the supercell whose volume is large enough to allow significant relaxation. The calculated electric field gradients and asymmetry parameter at the Ta positions were then compared with the measured values from PAC spectroscopy.

Nuclear structure in the trans-lead region are not very well understood due to the difficulty of the production of targeted nuclei by fusion evaporation technique. In addition, the fission channel dominates here creating unwanted background of gamma rays, which limits the observation and study of the systematics of very weak transitions. Isotopes of neutron deficient ^{204}At nucleus in the trans-lead region have not been explored in detail. Observation of possible shears band in ^{204}At nucleus was reported by Hartley et al. [8] through their Gammasphere experiment, but the level scheme was incomplete due to the absence of linking transitions between the main yrast sequence and the possible magnetic rotational band. In fact, M1 band was first reported from this observation at Gammasphere, but no crossover E2 transition in the M1 band was found in the earlier study [8]. To re-investigate the high spin states and to give more insight into the shears band in ^{204}At nucleus, we have carried out gamma ray spectroscopic measurements in ^{204}At. The excited proton rich astatine nuclei are produced by bombarding ^{197}Au target with ^{12}C beam. At 65 MeV and 75 MeV beam energies, it predominantly produces ^{205}At and ^{204}At nuclei as evaporation residues. Exhaustive work on ^{205}At nucleus has been made earlier [9]. From our measurement in ^{204}At, a significant number of new γ-transitions were found by gating on the previously known 601, 491 keV γ-rays and on

astatine X-rays. The directional correlation of oriented nuclei (DCO) and polarization directional correlation of oriented nuclei (PDCO) measurements of γ-transitions have been carried out to estimate the multipolarity and electric/magnetic nature of transitions, respectively. The main yrast sequence and the $\Delta I = 1$ band were linked by newly observed γ-transitions. Crossover E2 transitions in the $\Delta I = 1$ band were also observed. The value of B(M1)/B(E2) for several transitions in the $\Delta I = 1$ band were determined from the measured intensities. The falling trend of B(M1)/B(E2) with increasing spin further confirms the presence of shears band in this nucleus. Matrices generated by gating on the time window indicate the possible presence of isomers along the pathway linking $\Delta I = 1$ sequence and main yrast sequence.

List of Figures

List of Tables

CHAPTER 1

Introduction

1.1 Motivation

The nucleus inside an atom is a many body system consisting of neutrons and protons bound by the strong force. The nuclei are built up to form nuclear structure that is governed by the interaction of these nucleons (viz. neutrons and protons) with the many particle system. It can be stated that the individual neutrons and protons form bound states where they themselves, as an ensemble, govern the nuclear structure of the nuclei. Being a quantum mechanical many particle system, the governing interaction is basically the mean field generated by the nuclei themselves. Measuring the nuclear properties reveal the nature of these interactions and their subtleties in governing the nature of the bound states. With a nucleus of mass $A = Z + N$ (where Z and N are the number of protons and the neutrons in the bound nucleus), which is stable or long lived, there exists more than ten nuclei on the average, which are unstable. Thus, for approximately a few hundreds of stable or long lived nuclei, we have several thousands of nuclei which are unstable or metastable, but are known or predicted to be bound nuclei. These unstable nuclei are artificially produced by several techniques involving nuclear reactions between stable or metastable (or 'radioactive') beams from an accelerator and also stable or metastable targets. More than 2000 of such nuclei are produced till date,

and for several hundreds of them, basic properties such as mass, lifetime, decay and excitation scheme, spins and multipole electric/magnetic moments have been studied and the results are published or archived in various data bases.

Knowledge of these basic properties allows us to obtain information on the nuclear structure, and also the nature of the strong force at play in the nuclear many body systems. Comparison of the experimentally measured properties of unstable (or 'exotic' in the common parlance) nuclei to calculated results based on different nuclear models and their variants and also to that of the stable nuclei, provide a testing ground for the predictive power and acceptability of these models. These comparative studies also hint at the suggested modifications of the theoretical models and their parameters. Some of these properties are either sensitive to the neutron-proton interaction, while others reveal more information about the collective properties, such as deformation and pairing interaction.

Static nuclear moments are extremely important parameters to understand the single particle or collective nature of the nuclear states. The magnetic moments are sensitive to the single particle nature of the valence nucleons, while the electric quadrupole moments are sensitive to the nuclear collective properties viz. deformation. A non-spherical nucleus has rotational motion due to its angular momentum. The quantum energy levels of the excited nuclear states are designated by total angular momentum or spin I and parity π quantum number. The nuclear magnetic dipole moment (μ) is related with the angular momentum of the nucleus. Any nuclear level with spin $I \neq 0$ has a magnetic dipole moment (μ). The nucleus is not always spherical, i.e. the mass and charge distribution inside the nucleus may deviate from spherical symmetry. Deformation of a nucleus is primarily designated by the electric quadrupole moment (Q) of the nucleus. For a spherical nucleus, the quadrupole moment is zero. The nuclear electric dipole moment for a nucleus is zero due to definite parity of nuclear states. Quadrupole moment of a nucleus is also related with the spin (I) of the nucleus and its projection along the z-axis. For

any nucleus with spin $I > \frac{1}{2}\hbar$, the nucleus has a non-zero value of quadrupole moment. For more than half a century, the nuclear moments of stable, long lived and unstable nuclei are studied, both in the ground states, and in the isomeric states, i.e. metastable states, by producing these nuclei using mostly the fusion evaporation reactions or in a few rare cases, using fusion-fission reactions. As a result, most of these nuclei were either near the valley of stability, or in the neutron deficient side, except in a few rare cases, in the neutron rich side. With the advent of the radioactive ion beams from the nineties, the neutron rich side of the valley of stability has been explored using various efficient methods of isolating these rare and short lived nuclei. The most striking discovery made by these studies is the halo structure of these exotic nuclei. Another important aspect that has been brought out is the vanishing of magic numbers, and also manifestation of new magic numbers.

Interesting co-operative phenomena take place in an ensemble of nucleons forming the nuclei. Starting from the simplest model, namely the liquid drop model, where the protons can be assumed to have a uniform distribution over a spherical liquid drop, a refinement of the model can be considered where the protons and the neutrons move independently inside the so-called liquid drop giving rise to multipole moments. Deviation from spherical shape of the liquid drop in its simplest form gives rise to higher magnetic and electric multipole moments due to obvious reason. The protons and the neutrons contribute to the single particle magnetic dipole moments, which result from the vector sum of the magnetic dipole moments of the individual nucleons in the mean field of the nucleus. The nuclear magnetic moment of each of the constituent nucleons is the weighted vector sum of the orbital contribution and the spin contribution to the magnetic moments, where the weight factors are the respective gyromagnetic factors. While it is easy to envisage the orbital contribution to the magnetic dipole moment of the protons having charge content, that for the neutrons are a bit difficult to envisage since they do not have charge. However, inside a nucleus, the neutrons interact with the nucleons belonging to the core, resulting in core polarization that generates the orbital

magnetic field and in turn, an effective charge is attributed to the neutrons inside the nucleus.

In the same spirit, the nuclear shell model of nuclear structure is established where the individual on-shell or valence nucleons interact with the mean field of the nucleus through the residual interactions. Therefore, the valence nucleons are effectively considered to interact with the core nucleus, usually belonging to magic number in protons and/or neutrons. Same is true when we consider the corresponding proton holes and the neutron holes. For the proton deficient high Z nuclei near the doubly magic Lead, the large angular momentum shell model orbitals (considered as high j orbitals) arising from the proton particles (or holes) and the neutron particles (or holes) give rise to many interesting phenomena at high angular momenta. One such phenomenon is the magnetic rotation (MR) band, which arises from rotation of the large magnetic dipole moments of the proton and the neutron particles (or holes) around the angular momentum quantization axis. These effects, arising out of the experimental investigation of high spin states, backed by theoretical support have attracted lot of attention in recent years. The nuclear magnetic dipole moments, thus, have played an important role in the build up of a class of collective nuclear structure.

The nuclear moments play an important role in exploring the atomic environment of a material through hyperfine interaction. The interaction of nuclear moments of a probe nucleus with the electromagnetic field created by the electron environment surrounding the nucleus is called hyperfine interaction. When a probe nucleus with non-spherical charge distribution ($Q \neq 0$) interacts with electric field gradient generated by the surrounding charge distribution, the nuclear energy level with spin $I > 1/2\ \hbar$ splits into non-degenerate sub-levels and the interaction is called electric quadrupole interaction/electric hyperfine interaction. Electric field gradient (EFG) strongly depends upon the lattice parameters and the crystal structure of the lattice. In the magnetic hyperfine interaction, the magnetic dipole moment of the probe nucleus ($I \neq 0$) interacts with

the magnetic field at the nuclear site. In the magnetic hyperfine interaction, the magnetic dipole moment of the probe nucleus ($I \neq 0$) interacts with the magnetic field at the nuclear site which is known as magnetic hyperfine field (B_{hf}). The B_{hf} is created in a material mainly due to orbital motion of electrons, distribution of electron spin around the probe nucleus and Fermi contact field produced by the differences of spin-up and spin-down electron populations of s electrons at the probe nuclear position. In a non-magnetic material i.e in a material without magnetic ordering, the effective magnetic field (B_{eff}) in the presence of externally applied magnetic field (B_{ext}) at the probe nuclear site can be written as $B_{eff} = (1 + K)(1 - \sigma)\beta B_{ext}$, where K is the Knight shift, σ is the diamagnetic shielding and β is the paramagnetic enhancement factor. The $\beta - 1 = \frac{B_{hf}}{B_{ext}}$ is equal to the local susceptibility χ_{loc} of the probe impurity atom. The magnetic dipole moment (μ) of the probe nucleus precesses about the effective magnetic field with Larmor precession frequency (ω_L). Due to this magnetic dipole interaction, degeneracy of the nuclear energy level of the probe nucleus is lifted. As a result, the angular emission characteristics of the associated gamma rays change with time in correlation with precession motion of the nucleus with respect to the quantization axis. The time scale of such a change should be small compared to the life time of the nuclear excited states involved. This phenomenon, known as the time-differential perturbed angular correlation (TDPAC), also called PAC, is an important nuclear technique based on the interaction of electromagnetic moments (electric quadrupole or magnetic dipole) of a specific nuclear level with the electric field gradient or the magnetic field generated at the nuclear site by the surrounding environment of the probe nucleus. Effects of a γ-γ angular correlation in a crystalline environment are measured by this technique. This technique is, therefore, sensitive to the change of local field environment of the probe nucleus.

The first part of the thesis contains the results of structural properties of some solid materials including intermetallic compounds through the study of electric hyperfine interaction between the electric field gradient at the probe nuclear position in a non-cubic

lattice with the electric quadrupole moment of the probe nucleus. The PAC technique has been employed for this study of hyperfine interaction. In this technique, known values of nuclear moments of the probe nucleus are used to determine the EFG of non-cubic material or magnetic hyperfine field (MHF) inside a ferromagnetic material. The measured values of EFG or MHF are compared with those calculated by density functional theory (DFT) considering the known crystal structure of the materials.

The second part of the thesis describes the gamma-ray spectroscopic measurements to determine the nuclear structure of proton-rich astatine nucleus at high spin states. The nuclear moments of the nucleons here play the role of the cuts of jigsaw puzzle called the nuclear structure. The nucleus, when excited by some external agency, undergoes transition between different energy levels by emitting gamma rays and / or other nucleons or clusters. The gamma transition rates of excited nuclear levels are related to the transition probabilities. The study of lifetime of high spin states and their systematics bring out the information of the interactions between some of the valance nucleon spins. The transition probability of nuclear states is correlated with the lifetime of the decaying nuclear level and multipole mixing ratio of transition. The nuclear moments of the decaying nuclear energy level are required to obtain the multipole mixing ratio. By observing the gamma-rays through detectors placed at different angles with respect to the beam direction, spin and parity of excited nuclear levels can be determined. The multipolarity and linear polarization of gamma rays are obtained from the spin differences of the nuclear levels involved in the decay and by observing the parallel or perpendicular Compton scattering of gamma rays using segmented crystal in detectors, respectively. The study of transition probabilities and its systematics tell us about the single particle or collective nature of a nucleus.

1.2 Experimental technique: PAC

In the PAC technique, a suitable radioactive probe nucleus which emits two coincident γ-rays is introduced into the investigated material. The important requirements of the probe nucleus are the presence of an isomeric intermediate energy level (few ns to μs), large angular anisotropy ($|A_{22}| \geq 0.05$ [13]) of the sequential γ-rays and high values of electric quadrupole moment ($Q \geq 0.1$ b) and magnetic dipole moment ($\mu \geq \mu_N$) [1] of the intermediate nuclear energy level. In general, any radioactive source emits γ rays isotropically in all directions. The probability of emission of any particle or γ-rays from excited nuclear states of a radioactive source depends on the angle between the nuclear spin axis and the direction of emission. The angular correlation of the coincident γ-rays is observed when the emission of γ-rays occur from an oriented nucleus. In the PAC measurement, detection of the first gamma ray (γ_1) of the γ-γ cascade in a particular direction selects an ensemble of nuclei whose spin axis are oriented along the detection direction of γ_1 and if the second gamma ray (γ_2) is detected in coincidence with γ_1, an anisotropic angular distribution of γ_2 is observed with respect to the emission direction of γ_1 due to specific spatial orientation of nuclei. The probe atoms substitute some of the atoms in the host lattice which have similar charge and atomic radius. Doping of probe atoms is done in high dilution ($\sim 10^{18}$ atoms [14]) so that the probe atoms do not change the lattice structure of the investigated material. When these probe atoms are introduced into a non-cubic material, the electric field gradient or the gradient of electrostatic field created by the surrounding charge distribution at the probe nuclear site interacts with the nuclear electric quadrupole moment and/or magnetic field inside a magnetic material interacts with the magnetic dipole moment of the intermediate nuclear energy state of the probe nucleus. This interaction of nuclear electric/magnetic moments with extranuclear electric/magnetic fields is called electric/magnetic hyperfine interaction. Due to this hyperfine interaction, the degeneracy of the magnetic substates of the intermediate nuclear energy level is lifted and the level splits into different non-degenerate magnetic

Table 1.1: $T_{1/2}^{\text{parent}}$: Half-life of the parent nucleus; $T_{1/2}$: Half-life of the intermediate state of the daughter nucleus [1]

Parent→Daughter	Decay mode	$T_{1/2}^{\text{parent}}$ (days)	γ_1 (keV)	γ_2 (keV)	I^π	$T_{1/2}$ (ns)	μ (μ_N)	Q (barn)
^{111}In → ^{111}Cd	EC	2.83	171	245	$\frac{5}{2}^+$	85	-0.7656(25)	0.83(13)
^{181}Hf → ^{181}Ta	β^-	42.4	133	482	$\frac{5}{2}^+$	10.8	3.24(5)	2.36(5)

sublevels. On the other hand, due to this interaction during the time the probe nuclei reside in the intermediate state, the nuclei are reoriented from the initial state after the emission of γ_1 to a different state from which the γ_2 is emitted. Thus, angular correlation of the coincident γ-rays is perturbed due to this hyperfine interaction. Measuring this perturbation in angular correlation of γ-rays, internal lattice configuration of a non-cubic material or magnetic field inside a ferromagnetic material can be determined. This nuclear technique of obtaining hyperfine fields in a material is called perturbed angular correlation (PAC). Combined effects of magnetic hyperfine interaction and electric hyperfine interaction in a non-cubic magnetically ordered system have been also studied by PAC spectroscopy [15]. The electric field gradient is inversely proportional to the cubic power of distance from the probe nuclear site. So, the measurement of EFG by PAC technique gives local structure which is sensitive to the change of lattice configuration near the probe atom. Thus, short range order in materials can be studied by this PAC technique which offers atomic scale resolution. Apart from this γ-γ perturbed angular correlation technique, two other similar techniques are used also to determine the local structure which are β-γ and e^--γ perturbed angular correlations [16]. The perturbed angular correlation technique is also used to determine the magnetic dipole moment of excited nuclear states by applying known external magnetic field or internal hyperfine magnetic field (transient [17] or static field) on the probe nucleus. In fact, this is the only method to determine the magnetic dipole moment of highly excited nuclear state having lifetime $\tau_N \leq$ few ps [17, 18]. The most commonly used probe isotopes for PAC measurements are ^{181}Hf and ^{111}In. Several other isotopes that are used for PAC spectroscopic measurement can be found in the references [19, 20]. The characteristics of ^{181}Hf and ^{111}In probe nuclei are summarized in the Table 1.1. For our PAC measurements, we

have used ^{181}Hf probe. Natural hafnium (∼30% ^{180}Hf) is irradiated by thermal neutron capture to produce the probe ^{181}Hf. Several techniques are employed to insert the probe atoms into the investigated material. 1) Mechanical alloying of the activated probe metal along with the investigated sample in large dilution (probe atom <0.01 at%); 2) if any of the constituent element of the investigated material can be activated to a PAC probe, then the sample after preparation is allowed to undergo nuclear reaction (e.g. neutron irradiation) which converts some atoms of that constituent element to probe; 3) ion-implantation of the probe atom inside the investigated material by an ion-implanter 4) thermal diffusion of probe into the investigated material by taking the probe solution and sample in an evacuated quartz tube and annealing at high temperature.

1.3 Applications of PAC spectroscopy

The PAC method has been successfully applied to study different types of materials viz. metal [21], intermetallic alloy [22, 23], ceramics [24], thin flim [25–28], nano material [28–32], single crystal [33], amorphous material, oxide material [28, 34–36], chemical samples [37, 38]. Several novel phenomena viz. oxygen ordering in superconducting material [39], structural and magnetic properties of heavy fermion system [40, 41] and pressure induced valency change [42, 43], structural property of ferroelectric materials [44], defect dynamics in semiconductor [45], structural [36] and magnetic [46] phase transitions have been investigated by PAC spectroscopy. The physics of interaction of dilute magnetic impurity in a ferromagnetic and anti-ferromagnetic host material has been extensively studied by PAC spectroscopy [47–53]. Point defects (vacancy or interstitial) [54, 55] and diffusion of atom/molecule [56] inside a material can also be studied by the perturbed angular correlation (PAC) technique. When any atom/molecule jumps near the probe site, the probe atom experiences a fluctuating EFG which causes a dynamic nuclear spin relaxation. Activation enthalpy can be deduced from the study of jump diffusion frequency of vacancies [54, 55]. To study the effect of defect-probe

interaction in a material, defects in a matrix is purposefully created by irradiating the material with high energy particles viz. neutron, α, proton. The sample is then annealed by isochronous annealing consecutively at higher temperatures and finally the sample is cooled down to the measuring temperature. The defects (mainly interstitial impurity and vacancies) are trapped by the probe atoms in the process of annealing and subsequently cooling down the sample. Biological samples have also been studied by PAC spectroscopy. Coordination chemistry and bio-chemistry have been a subject of investigation by PAC spectroscopy [57, 58]. Dynamics of biomolecular metal sites have been explored by PAC technique [19, 57, 59–62].

1.4 Comparison with other techniques

There are several other nuclear probing techniques apart from PAC to determine the lattice environment by observing the spin motion of nucleus viz. Mössbauer Spectroscopy (MS), Nuclear Quadrupole Resonance (NQR)/ Nuclear Mganetic Resonance (NMR). There are some advantages of PAC technique over these other hyperfine techniques. Very small amount of sample (typically 1-100 mg) is sufficient to carry out PAC measurement. There is no restriction on reaction vessel material as high energy γ rays are used for PAC spectroscopy as compared with MS where favorable conditions arise when low energy γ-ray sources are used. The sensitivity of MS (through Debye-Waller factor [1]), NMR/NQR techniques depend on temperature whereas PAC sensitivity is independent of temperature, which makes it useful to study the structural/displacive [5] or magnetic phase transition [46] of materials. Electric field gradient or magnetic hyperfine field can be determined with same accuracy at high and as well as low temperatures as the resolution and efficiency of PAC technique do not depend on temperature. Solid state reactions can be determined by PAC spectroscopy [22]. PAC technique can be very useful to study the polymorphic phase transition as it can observe formation of compound at very early stage [57]. Various other applications of PAC technique can be found in the

references [14, 57, 58, 63, 64]. Measurements by MS technique are often only feasible on materials which have Fe or Sn as a major constituent element. In PAC, the number of probe atoms required are very less $\sim 10^{11}$-10^{12} whereas MS and NQR measurements require $\sim 10^{14}$ and $\sim 10^{18}$ probe atoms, respectively [14]. Also, the sample for PAC study does not have any solid state restrictions i.e. the sample can be solid, liquid or gaseous.

1.5 Objectives of the present PAC studies

The investigated materials by PAC technique in the present thesis have been categorized in two parts due to the different procedures involved in the preparation of samples. a) Chemical samples: $ZrF_4{\cdot}3H_2O$/$HfF_4{\cdot}3H_2O$, Rb_2ZrF_6/Cs_2HfF_6; b) Intermetallic samples: Zr_8Ni_{21}/Hf_8Ni_{21}, $ZrNi_3$/$HfNi_3$, Zr_9Ni_{11}/Hf_9Ni_{11} and Zr_7Ni_{10}/Hf_7Ni_{10}. For present PAC measurements, we have used two PAC spectrometers developed in our laboratory, a four detector BaF_2-BaF_2 and a four detector $LaBr_3$(Ce)-BaF_2. From four slow-fast coincidence combinations (two at 90° and two at 180°), the perturbation function $G_2(t)$ (defined in chapter 2) [1, 2] is obtained. The $G_2(t)$ contains three transition frequencies between the sublevels that arise due to hyperfine splitting of the intermediate 482 keV level of ^{181}Ta and the EFG is derived from these three transition frequencies. From the three transition frequencies, generated by the hyperfine splitting of the intermediate level, contained in $G_2(t)$, the quadrupole frequency and EFG are determined. For temperature dependent PAC measurements (up to 1073 K), a locally made resistive furnace was used.

Isoformulae compounds of Zr and Hf are found to have similar crystal structure. However, two trihydrate tetrafluoride compounds, viz. $ZrF_4{\cdot}3H_2O$ and $HfF_4{\cdot}3H_2O$ were reported to have different crystal structures. From XRD measurements [3], both the monoclinic and triclinic modifications of $ZrF_4{\cdot}3H_2O$ were found but for $HfF_4{\cdot}3H_2O$, only the monoclinic modification was reported. We have studied these materials by PAC to resolve the structural anomalies of these compounds reported earlier. The anhydrous

ZrF_4 and HfF_4 have applications in developing optical coating materials due to their excellent transmission properties over the infrared region [4]. Therefore, it is important also to study the phase transitions from hydration to dehydration and their structural stabilities with temperature and these have been studied by the PAC technique.

The compounds Rb_2ZrF_6 and Cs_2HfF_6 have been studied to resolve ambiguities in earlier measurements, particularly, to study the nuclear relaxation effects due to fluorine activation in the materials and also to find any structural phase transition in Rb_2ZrF_6 with temperature. In Rb_2HfF_6, a displacive phase transition was found by C.C. Dey [5] and a fluctuating electric field gradient at temperatures ≥ 413 K in Rb_2HfF_6 and Cs_2HfF_6 was found by Vasquez et al. [65, 66]. In the isomorphous compounds Rb_2ZrF_6 and Rb_2HfF_6, a phase transition denoted by abrupt change of site fractions of different phase components was found ∼740 K by Martínez et al. [67].

A major portion of the present thesis is the studies of Zr-Ni and Hf-Ni intermetallic systems of different stoichiometric compositions. The alloys based on Zr-Ni system have numerous technological applications due to their high thermo-chemical stability. These are used as an integral part to form high temperature eutectics, bulk glassy alloys, corrosion resistance materials etc. Some of the Zr-Ni binary alloys, viz. Zr_8Ni_{21}, Zr_9Ni_{11}, Zr_7Ni_{10}, $ZrNi_3$, Zr_2Ni_7 and ZrNi have received considerable attention [68–75] due to their excellent high rate capacity of gasious hydrogen storage in interstitial sites and reversibility of hydrogen dissociation at room temperature. These alloys are potential candidate to form metal hydride (MH) which have application as a negative electrode in Ni-MH rechargeable batteries. These batteries are used in fuel cells and hybrid electric vehicles for their high energy density and environmentally friendly characteristics. These alloys generally produce multiple phases along with their stoichiometric compounds [6, 69,70,75,76]. Therefore, it is very important to study multiple phase components that are produced at high temperatures in these alloys which will help in the future development of MH with better electrochemical properties.

In the present thesis, phase components and their stability, structural/compositional phase transformation in Zr_8Ni_{21}/Hf_8Ni_{21}, $ZrNi_3/HfNi_3$, Zr_9Ni_{11}/Hf_9Ni_{11} and Zr_7Ni_{10}/Hf_7Ni_{10} alloys have been studied by observing the temperature dependence of PAC parameters. Additionally, we have carried out X-ray diffraction (XRD) and transmission electron microscopy (TEM)/selected area electron diffraction (SAED) measurements to determine the phase components in these samples. Calculations of EFG and asymmetry parameter (η) at ^{181}Ta impurity site have also been carried out within the framework of density functional theory (DFT) in these compounds to compare with the experimental results from PAC measurements and therefrom to assign these phases. The DFT calculations were performed using WIEN2k simulation package [7] by considering full potential-(linearized) augmented plane wave + local orbitals [FP-(L)APW+lo] basis sets. The compounds Hf_8Ni_{21}, Hf_7Ni_{10}, Hf_9Ni_{11} and $HfNi_3$ have also been studied by PAC technique to determine the isostructurality of isoformulae Zr-Ni and Hf-Ni compounds and to compare their temperature dependent properties. The Hf-Ni alloys have tecnhological applications also. The Hf-Ti-Ni alloys are used to form shape memory alloys.

1.6 Objectives of exploring nuclear structure

Nuclear structure in the trans-lead region are not very well understood due to the difficulty of the production of targeted nuclei by fusion evaporation technique. In addition, the fission channel dominates here creating unwanted gamma ray background, which limits the observation and study of the systematics of very weak transitions. Isotopes of neutron deficient astatine nucleus in the trans-lead region have not been explored in detail. Observation of possible shears band in ^{204}At nucleus was reported by Hartley et al. [8] through their Gammasphere experiment, but the level scheme was incomplete due to the absence of linking transitions between the main yrast sequence and the possible magnetic rotational band. In fact, M1 band was first reported from this observation

at Gammasphere, but no crossover E2 transition in the M1 band was found earlier [8]. To re-investigate the high spin states and to give more insight into the shears band in ^{204}At nucleus, we have carried out gamma ray spectroscopic measurements. The major difficulty in extracting the nuclear structure information of ^{204}At is the predominant production of ^{205}At as evaporation residue along with ^{204}At nucleus. Exhaustive work on ^{205}At nucleus was done earlier [9]. In the present thesis, the directional correlation of oriented nuclei (DCO) and polarization directional correlation of oriented nuclei (PDCO) measurements of γ-transitions have been carried out to estimate the multipolarity and electric/magnetic nature of transitions, respectively.

CHAPTER 2

Perturbed angular correlation

2.1 Hyperfine interaction

Hyperfine interaction is described as the interaction of nuclear moments (electric or magnetic) with the electromagnetic fields. The perturbed γ-γ angular correlation is a hyperfine spectroscopic technique where the internal electromagnetic field in a material is determined by observing the hyperfine interaction between the nuclear moments of probe atom and surrounding electromagnetic field. The local electromagnetic fields are created by the electrons and nuclei in the vicinity of the probe nucleus. External magnetic field can also be applied to observe the hyperfine interaction. The hyperfine interaction was first observed in atomic spectroscopy and later, it was found in nuclear spectroscopy. The perturbed angular correlation was first started as a tool to determine the dipole moments of excited nuclear states of the probe nucleus by applying external magnetic field. With the advent of highly sensitive detectors and fast pulse processing units, the perturbed angular correlation technique was found to have great potential in microscopic investigation of materials. In the following sections, electric/magnetic nuclear moments and electric/magnetic hyperfine interactions have been introduced, and method of observing the electric/magnetic hyperfine interactions by studying the perturbation of γ-γ angular correlation has been presented.

2.1.1 Nuclear magnetic dipole moment

Nuclear magnetic dipole moment is produced mainly by the orbital motion of charged protons whose motion create electric current density and the intrinsic magnetic moment of the nucleons (proton and neutron) due to their intrinsic spin. Nuclear magnetic dipole moment ($\vec{\mu}$) is proportional to the total angular momentum ($\vec{I}$) of the nucleus in the classical picture:

$$\vec{\mu} = \gamma \vec{I}, \tag{2.1}$$

where γ is called the nuclear gyromagnetic ratio and is defined as $\gamma = g\frac{\mu_N}{\hbar}$. Here, g is called the g-factor and μ_N is the nuclear magneton, defined by $\mu_N = \frac{e\hbar}{2m_p}$. In quantum mechanics, the magnetic dipole moment is defined as expectation value of the z-component of the magnetic dipole moment (i.e. μ_z) in the state $|I, M\rangle$ with $M = I$:

$$\begin{aligned} \mu = & \langle I, I| \mu_z |I, I\rangle \\ =& \gamma \langle I, I| I_z |I, I\rangle \\ =& \gamma I \hbar. \end{aligned} \tag{2.2}$$

The spin or total angular momentum of the nucleus has two parts, one is the the orbital angular momentum $\vec{L}$ and another is the spin angular momentum $\vec{S}$. For the orbital angular momentum $\vec{L}$ of the nuclei, the g-factors for the nucleons are classically given by

$$\begin{aligned} g_L = & 1 \qquad \text{(for proton)} \\ =& 0 \qquad \text{(for neutron).} \end{aligned} \tag{2.3}$$

The g-factors related to the spin angular momentum ($\vec{S}$) for the free nucleons are given by

$$\begin{aligned} g_S = & +5.59 \qquad \text{(for proton)} \\ =& -3.83 \qquad \text{(for neutron).} \end{aligned} \tag{2.4}$$

If the magnetic moment is created by the outermost nucleon outside a closed nuclear shell, then the spin or total angular momentum $\vec{I}$ ($=\vec{L}+\vec{S}$) of the outer nucleon is related

to the magnetic moment ($\vec{\mu}$) by [1, 77]

$$\vec{\mu} = g_L \vec{L} + g_S \vec{S}, \tag{2.5}$$

where μ is expressed in the units of μ_N, and L and S are expressed in the units of $\hbar$. From the generalized Landé formula [1], the g-factor for single particle can be written as

$$g = g_L \pm \frac{g_S - g_L}{2L+1} \quad \text{with} \quad I = L \pm 1/2. \tag{2.6}$$

A detailed description about nuclear magnetic dipole moment can be found in the reference [78].

2.1.2 Nuclear electric quadrupole moment

Electric quadrupole moment of the nucleus is the measure of deformation of nuclear charge density from a spherical shape where still there exists a symmetry axis. A nucleus with charge density $\rho(\vec{r})$ creates an electrostatic potential $\phi(\vec{r})$ given by

$$\phi(\vec{r}) = \frac{1}{4\pi\epsilon_0} \int \frac{\rho(\vec{r}')dV'}{|\vec{r} - \vec{r}'|}. \tag{2.7}$$

This electrostatic potential in multipole expansion can be expressed in terms of Legendre polynomial as

$$\phi(\vec{r}) = \frac{1}{4\pi\epsilon_0 r} \int \rho(\vec{r}') \sum_{l=0}^{\infty} P_l(\cos\theta)(\frac{r}{r'})^l dV'. \tag{2.8}$$

where, θ is the angle between $\vec{r}$ and $\vec{r}'$. In the summation, the term for l=2 gives the quadrupolar contribution which is given by [1, 77]

$$\phi(\vec{r})|_{l=2} = \phi_2(\vec{r}) = \frac{1}{4\pi\epsilon_0} \int \rho(\vec{r}') \frac{\sum_{i,j} x_i(3x_i'x_j' - r'^2\delta_{ij})x_j}{2r^5} d^3r'. \tag{2.9}$$

Quadrupole moment of the nucleus is defined by a symmetric, traceless, 2nd rank tensor. In the equation 2.9, the quadrupole tensor of the nuclear charge distribution is written as

$$Q_{ij} = \frac{1}{e}\int \rho(\vec{r}')(3x'_i x'_j - r'^2\delta_{ij})d^3r'. \tag{2.10}$$

Quadrupole moment of the nucleus is classically expressed by Q_{zz}:

$$Q = Q_{zz} = \frac{1}{e}\int \rho(\vec{r})(3z^2 - r^2)d^3r. \tag{2.11}$$

Now, using $z = rcos\theta$, the above equation 2.11 can be written in terms of spherical harmonic Y_2^0 as

$$Q = \frac{1}{e}\sqrt{\frac{16\pi}{5}}\int r^2 Y_2^0 \rho(\vec{r})d^3r. \tag{2.12}$$

In Quantum mechanics, the quadrupole moment operator is expressed as the expectation value of $\sqrt{\frac{16\pi}{5}}Zr^2Y_2^0$ in the state $|I, M = I\rangle$:

$$Q = \sqrt{\frac{16\pi}{5}}\langle I, M = I|\, Zr^2Y_2^0\,|I, M = I\rangle = \langle Q_{20}\rangle\,. \tag{2.13}$$

where Z is the atomic number. Using Wigner-Eckart theorem, the above equation 2.13 can be written as [1]

$$\langle I, M|\, Q_{20}\,|I, M\rangle = (-1)^{I-M}\begin{pmatrix} I & 2 & I \\ -M & 0 & M \end{pmatrix}\langle I|\,|Q_2|\,|I\rangle\,. \tag{2.14}$$

The term in the bracket is called Wigner's $3j$ symbol. For $I < 1$, the Wigner's $3j$ symbol is zero which gives the value of quadrupole moment Q=0 and $\langle I|\,|Q_2|\,|I\rangle$ is the reduced matrix element whose value does not depend on the z-projection (M) of the spin (I). Quadrupole moment is expressed in units of barn where, 1 barn = 10^{-28} m^2. The value of Q can both be positive and negative. The positive (prolate) and negative (oblate) values of quadrupole moment indicates cigar-like and disc like nuclear charge

distribution. As the quadrupole moment operator acts on the state vectors $|I, M\rangle$, the quadrupole moment should be expressed in terms of angular momentum operators I_i. The operator formulation of quadrupole moment is given by the following relation [1]

$$\hat{Q}_{ij} = \frac{Q}{I(2I-1)}\Big[\frac{3}{2}(\hat{I}_i\hat{I}_j + \hat{I}_j\hat{I}_i) - \delta_{ij}\hat{I}^2\Big]. \tag{2.15}$$

Here, i, j represents cartesian coordinates.

2.1.3 Electric hyperfine interaction

The interaction energy of the nuclear charge density $\rho(\vec{r})$ in the extra-nuclear electrostatic potential $\Phi(\vec{r})$ created by the surrounding charge distribution in a material is given by

$$E = \int \rho(\vec{r})\Phi(\vec{r})d^3r, \tag{2.16}$$

where

$$\int \rho(\vec{r})d^3r = Ze \tag{2.17}$$

is the nuclear charge. If we expand the electrostatic potential created by the external electric field, we get the following equation

$$\Phi(\vec{r}) = \Phi(0) + \sum_{i=1}^{3}\Big(\frac{\partial\Phi}{\partial x_i}\Big)_0 x_i + \frac{1}{2}\sum_{i,j}\Big(\frac{\partial^2\Phi}{\partial x_i\partial x_j}\Big)_0 x_i x_j + ... \quad . \tag{2.18}$$

Here, x_i, x_j are Cartesian coordinates. After substituting $\Phi(\vec{r})$ in the equation 2.16, we get the following expression of the interaction energy

$$\begin{aligned} E &= \Phi(0)\int \rho(\vec{r})d^3r + \sum_{i=1}^{3}\Big(\frac{\partial\Phi}{\partial x_i}\Big)_0 \int \rho(\vec{r})x_i d^3r + \frac{1}{2}\sum_{i,j}\Big(\frac{\partial^2\Phi}{\partial x_i\partial x_j}\Big)_0 \int \rho(\vec{r})x_i x_j d^3r + .. \\ &= E_0 + E_1 + E_2 + ... \quad . \end{aligned} \tag{2.19}$$

Now,

$$\begin{aligned} E_0 &= \Phi(0) \int \rho(\vec{r}) d^3r \\ &= \Phi(0) Ze. \end{aligned} \tag{2.20}$$

This term gives the potential energy of a point charge in an external potential and does not change for different isotopes of the same element. This term does not split the nuclear energy levels and thus is not of our interest. The second term is

$$\begin{aligned} E_1 &= \sum_{i=1}^{3} \Big(\frac{\partial \Phi}{\partial x_i}\Big)_0 \int \rho(\vec{r}) x_i d^3r \\ &= -\Big(\boldsymbol{\nabla}\Phi(\vec{r}) \cdot \vec{p}\Big)_{r=0}. \end{aligned} \tag{2.21}$$

Here, $\boldsymbol{\nabla}\Phi(\vec{r}) = -\frac{\partial \Phi}{\partial x_i}$ is the electrostatic field and $\int \rho(\vec{r}) x_i d^3r$ is the nuclear electric dipole moment ($\vec{p_i}$). Due to the fact that nuclear states have definite parity, the nuclear electric dipole moment is zero [78]. The next significant term is

$$\begin{aligned} E_2 =& \frac{1}{2} \sum_{i,j} \Big(\frac{\partial^2 \Phi}{\partial x_i \partial x_j}\Big)_0 \int \rho(\vec{r}) x_i x_j d^3r \\ =& \frac{1}{2} \sum_{i,j} \Phi_{ij} \int \rho(\vec{r}) x_i x_j d^3r \\ =& \frac{1}{6} \sum_{i} \Phi_{ii} \int \rho(\vec{r}) r^2 d^3r + \frac{1}{2} \sum_{ij} \Phi_{ij} \int \rho(\vec{r}) \Big(x_i x_j - \frac{r^2}{3}\delta_{ij}\Big) d^3r. \end{aligned} \tag{2.22}$$

We have defined $\Phi_{ij} = \Big(\frac{\partial \Phi}{\partial x_i \partial x_j}\Big)_0$ which is the electric field gradient due to external electric field at the nuclear site. The electrostatic potential obeys the Poisson's equation and thus

$$\boldsymbol{\nabla}^2 \Phi(\vec{r})|_{r=0} = \sum_i \Phi_{ii} = e\frac{|\psi(0)|^2}{\epsilon_0}, \tag{2.23}$$

where $|\psi(0)|^2$ is the probability density of electron wave function and -$e|\psi(0)|^2$ is the electronic charge density at the nuclear site. The density has a significant contribution from the s-electron surrounding the probe nuclear site. The term E_2 can now be written

as

$$\begin{aligned} E_2 = &\frac{e}{6\epsilon_0}|\psi(0)|^2 \int \rho(\vec{r}) r^2 d^3r + \frac{1}{2}\sum_{ij}\Phi_{ij}\int \rho(\vec{r})\Big(x_i x_j - \frac{r^2}{3}\delta_{ij}\Big)d^3r \\ =&E_C + E_Q, \end{aligned} \tag{2.24}$$

where E_C is the monopolar interaction energy and E_Q is the quadrupolar hyperfine interaction energy. Mean-square radius of the nucleus can be expressed as

$$\left\langle r^2 \right\rangle = \frac{1}{Ze}\int \rho(\vec{r}) r^2 d^3r. \tag{2.25}$$

Thus, the monopole term becomes

$$E_C = \frac{Ze^2}{6\epsilon_0}|\psi(0)|^2 \left\langle r^2 \right\rangle. \tag{2.26}$$

This monopolar term gives a shift in the interaction energy but does not split the energy levels into non-degenerate magnetic sub-levels. Due to slightly different nuclear radii of isotopes of the same nucleus, the mean square nuclear radius gives different monopolar contribution.

2.1.4 Electric quadrupole interaction

The quadrupole hyperfine interaction energy is defined by

$$\begin{aligned} E_Q = &\frac{1}{2}\sum_{ij}\Phi_{ij}\int \rho(\vec{r})\Big(x_i x_j - \frac{r^2}{3}\delta_{ij}\Big)d^3r \\ =&\frac{e}{6}\sum_{ij}\Phi_{ij}Q_{ij} \quad \text{(substituting equation 2.10)}. \end{aligned} \tag{2.27}$$

Now, as both ϕ_{ij} is a symmetric matrix, it is possible to diagonalize the matrix in a particular eigenvector basis. So, the quadrupole interaction energy takes the form

$$E_Q = \frac{e}{6}\sum_{i}\Phi_{ii}Q_{ii}. \tag{2.28}$$

Multipole expansion of the electrostatic potential which gives rise to the term E_Q is only valid if the source of charges that produce the electric field gradient does not coincide with the nuclear charge distribution. As the electric field gradient tensor is a traceless tensor, the Laplace's equation ($\boldsymbol{\nabla}^2\Phi(\vec{r})$=0) is valid here. Thus, we can more generally describe the electric field gradient by

$$\Phi_{ij} = V_{ij} + \frac{1}{3}Tr(\Phi). \tag{2.29}$$

$Tr(\Phi) = \sum_i \Phi_{ii}$ is the trace of Φ. Here, V_{ij} is a traceless matrix (i.e. $\sum_i V_{ii}$=0). The second term $\frac{1}{3}Tr(\Phi)$ does not contribute to the quadrupole interaction energy term (equation 2.28) as the quadrupole moment is a traceless tensor. So, V_{ij} gives the value of electric field gradient which contributes to electric hyperfine interaction energy. The electric field gradient (V_{ij}) created by the surrounding charge distribution of electrons, ion core electrons that contain the nucleus of interest and the positive charges of other nuclei in a material at the site of the probe nucleus, can be written as [2]

$$V_{ij} = \frac{\partial E_j}{\partial x_i} = \frac{\partial^2\Phi(\vec{r})}{\partial x_i \partial x_j} = \int \frac{1}{r^5}(3x_i x_j - r^2\delta_{ij})\rho(\vec{r})^{\mathrm{EN}} d^3r. \tag{2.30}$$

Here, the charges external to the nuclear site only contributes to V_{ij} and $\rho(\vec{r})^{\mathrm{EN}}$ is extra-nuclear (EN) charge density. Dependence of EFG on $\frac{1}{r^3}$ restricts the determination of electric field gradient for only non-cubic or non-spherical crystal systems. Because of the $\frac{1}{r^3}$ dependence of EFG, the determination of EFG extracts the local structure near the probe atom and it is very sensitive to small changes in the lattice configuration. However, if surrounding defects distort the symmetry of the cubic lattice near the probe atom, a non-zero electric field gradient is found. The s-electrons (l=0) are spherically symmetric and does not contribute to the electric field gradient. Thus, the electronic charges with $l \geq 1$ contributes to the electric field gradient and in E_Q. As the electric field gradient is symmetric, it can be diagonalized. The principal components of the EFG are denoted by V_{xx}, V_{yy} and V_{zz}. Due to the traceless property of the EFG, only

two independent parameters are required to express V_{ij}. With the choice of a suitable principle axis system, we can have $|V_{zz}| \geq |V_{yy}| \geq |V_{xx}|$. We can define the symmetry of the electric field gradient which is a measure of how much the electric field gradient deviates from axial symmetry of the lattice, by the following relation

$$\eta = \frac{V_{xx} - V_{yy}}{V_{zz}} \qquad (0 \leq \eta \leq 1). \tag{2.31}$$

For a cubic or spherically symmetric charge distribution (e.g. s electrons) surrounding the nucleus, the electric field gradient (V_{zz}) at the probe nuclear site is zero as $V_{xx} = V_{yy} = V_{zz}$ and $V_{xx} + V_{yy} + V_{zz} = 0$. For tetragonal, hexagonal and rhombohedral crystal systems, the asymmetry parameter is zero [2, 63]. In this case, the principal axis is in the same direction as that of the symmetry axis of the crystal. For lower symmetry crystals, viz. monoclinic, triclinic and orthorhombic crystal systems, the $V_{zz} \neq 0$ and $0 \leq \eta \leq 1$ [2, 63]. Using the traceless properties of the electric field gradient as well as quadrupole moment tensor and the expression of η, we can write the quadrupole interaction energy as

$$E_Q = \frac{eV_{zz}}{12}\Big[3Q_{zz} + \eta(Q_{xx} - Q_{yy})\Big]. \tag{2.32}$$

Using the quantum formulation of the quadrupole tensor from the equation 2.15, the interaction Hamiltonian of the nuclear state with spin I $\hbar$ can be written as

$$\hat{H_Q} = \frac{eQV_{zz}}{4I(2I-1)}\Big[3\hat{I_z^2} - \hat{I^2} + \eta(\hat{I_x^2} - \hat{I_y^2})\Big]. \tag{2.33}$$

Now, using the raising and lowering operator, $\hat{I_+} = \hat{I_x} + i\hat{I_y}$ and $\hat{I_-} = \hat{I_x} + i\hat{I_y}$, respectively, we get the following expression of the interaction Hamiltonian

$$\hat{H_Q} = \frac{eQV_{zz}}{4I(2I-1)}\Big[3\hat{I_z^2} - \hat{I^2} + \frac{\eta}{2}(\hat{I_+^2} + \hat{I_-^2})\Big]. \tag{2.34}$$

The non-zero matrix element of the interaction Hamiltonian $\langle I, M| \hat{H} |I, M'\rangle$ are the following:

$$H_{M,M} = \hbar\omega_Q \Big[3M^2 - I(I+1)\Big] \tag{2.35}$$

$$H_{M,M\pm2} = \frac{\hbar\omega_Q\eta}{2}\sqrt{(I \mp M - 1)(I \mp M)(I \pm M + 1)(I \pm M + 2)}, \tag{2.36}$$

where ω_Q is the quadrupole frequency

$$\omega_Q = \frac{eQV_{zz}}{4I(2I-1)\hbar}. \tag{2.37}$$

If we consider axially symmetric electric field gradient i.e. $\eta = 0$, the energy difference between two sublevels is

$$E_Q = E(M) - E(M') = 3\hbar\omega_Q|M^2 - M'^2|. \tag{2.38}$$

The absolute value $|M^2 - M'^2|$ is always integer and we see transition frequencies are the multiples of ω_Q and the fundamental observable frequency ω_Q^0 is related to ω_Q as

$$\begin{aligned} \omega_Q^0 &= 6\omega_Q \qquad \text{for } I \text{ half-integer} \\ \omega_Q^0 &= 3\omega_Q \qquad \text{for } I \text{ integer.} \end{aligned} \tag{2.39}$$

2.1.5 Magnetic hyperfine interaction

When a nucleus is exposed in a magnetic field (it can be external or the internal magnetic field in a ferromagnetic material), it exerts a torque to the magnetic dipole moment of the nucleus, and as a result, the nuclear magnetic dipole moment start precessing about the magnetic field in the classical picture. The interaction energy can be written as

$$E_m = \vec{\mu} \cdot \vec{B}. \tag{2.40}$$

This interaction energy lifts the degeneracy of the nuclear state and splits the nuclear state in non-degenerate m-sublevels. The quantization of the nuclear spin allows only certain directions of the nuclear moment. Thus, by choosing the magnetic field parallel to the z axis, the interaction in the state $|I, M\rangle$ is

$$\begin{aligned} E_M =& \langle I, M| - \mu_z B_z |I, M\rangle \\ =& - g\frac{\mu_N}{\hbar} B_z \langle I, M| I_z |I, M\rangle \\ =& - g\mu_N B_z M \\ =& M\hbar\omega_L, \end{aligned} \tag{2.41}$$

where $\mu_z = \frac{g\mu_N}{\hbar} I_z = \gamma I_z$ (γ: gyromagnetic ratio) and $\omega_L = -\frac{g\mu_N B_z}{\hbar}$ is the Larmor precession frequency. The difference in energy between two adjacent level is

$$E_{magn}(M+1) - E_{magn}(M) = -g\mu_N B_z = \hbar\omega_L. \tag{2.42}$$

This means that the sublevels are equidistant. The energy difference of successive energy sub-levels is $\hbar\omega_L$ and the transitions between different M-sublevels occur with frequencies that are integer multiple of ω_L [1, 2, 47]. Quantum-mechanically, it means that the population of m-substates modulates periodically with Larmor precession frequency ω_L.

There are different sources of magnetic field at the nucleus inside a magnetically ordered system. Without any external magnetic field and disregarding any demagnetization and Lorentz field we see three main contribution [47]. The first one is generated due to the orbital motion of the electron (B_{orb}) and B_{dip} is produced due to orientation of the nuclear spin around the nucleus. The term B_{dip} can be sub-divided into two parts. The first one is due to the the spin density of the electrons of the atom where the nucleus resides. The other part comes due to all other atoms or ions except the ion or atom of interest. One of the major contribution in the magnetic hyperfine field comes due to Fermi contact field (B_{Fermi}). This is measured by the difference of densities of spin-up

and spin-down electronic states at the nuclear site.

2.2 Directional angular correlation of γ-rays

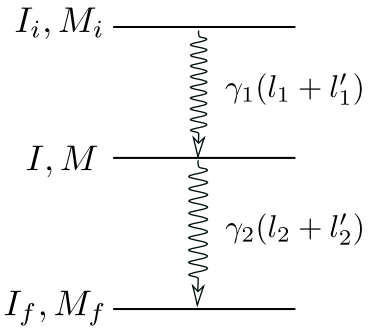

Figure 2.1: γ-γ cascade emitting from nuclear energy levels. M_i, M and M_f are the projection of the nuclear spins I_i, I and I_f, respectively. The l_1, l_1' and l_2, l_2' are the multipolarities for mixed γ_1 and γ_2 transitions, respectively [1].

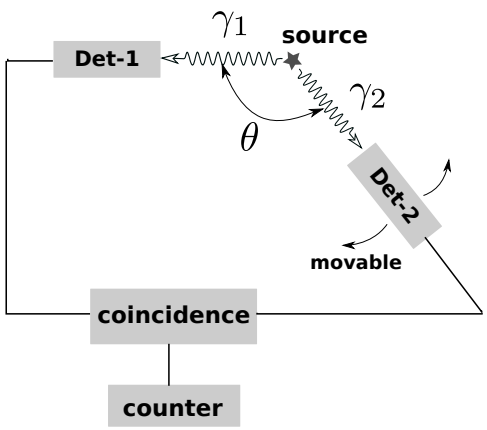

Figure 2.2: Measurement of angular correlation of γ-rays [1].

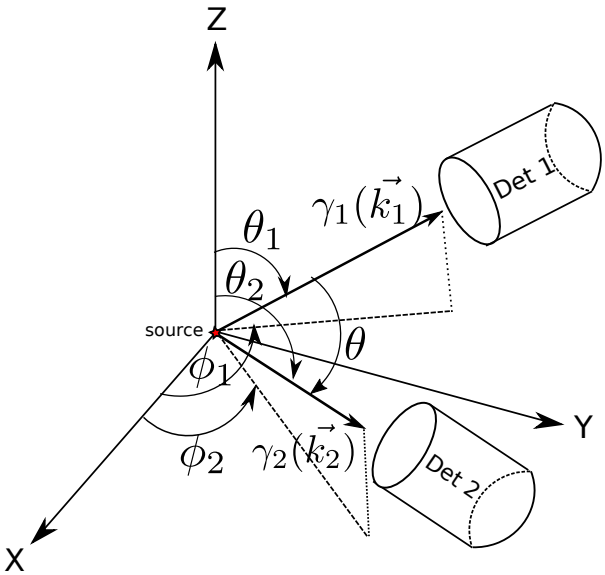

Figure 2.3: General co-ordinate system for measuring γ-γ angular correlation. k_1 and k_2 are the wavevectors corresponding to γ_1 and γ_2, respectively [1].

Quantum energy levels of radioactive nuclei are characterized by spin I and parity (π) quantum number. Unstable nuclei decays by emitting γ-rays whose probability depend

on the nuclear spin axis and the direction of emission. In general, spin axis of nuclei are oriented random in space co-ordinate and thus γ-rays are emitted isotropically from the nucleus. If a nucleus decays by emitting two sequential γ-rays (Figure 2.1), by detecting the first γ-ray (γ_1) of the γ-γ cascade cascade in a particular direction, a subset of nuclei are chosen whose spin axis points towards the detection direction of γ_1. Now, if the second γ-ray (γ_2) of the γ-γ cascade is observed in coincidence with the γ_1 (Figure 2.2), the emission of the γ_2 becomes anisotropic because of the un-equal population of M-substates of the intermediate energy level. Anisotropic observation of γ-rays can also be obtained by a similar method called perturbed angular distribution [13] where, the excited nuclear state of the probe nucleus is produced by a nuclear reaction of projectile beam with target nucleus. In this case, the direction of beam acts as a reference similar to that of γ_1 in perturbed γ-γ angular correlation spectroscopy. For the measurement of angular correlation, the anisotropy coefficient (A_{kk}) should be large and the intensities of γ rays should be high.

Directional angular correlation of the coincident γ-rays can be described by the angular correlation function ($W(\vec{k}_1, \vec{k}_2)$) which is the probability of observing the γ_2 at an angle θ with respect to the detection of γ_1 (Figure 2.3) [1, 77, 79–82]:

$$W(\vec{k}_1, \vec{k}_2) = W(\theta) = \sum_{\substack{k=0 \\ even}}^{k_{max}} A_{kk} P_k(cos\theta), \tag{2.43}$$

where A_{kk} is the anisotropy coefficient and $P_k(cos\theta)$ is the k^{th} Legendre polynomial. The summation in the expression of $W(\theta)$ is finite because of the conservation of angular momentum. The value of k_{max} is obtained from the relation, k_{max}=min($2I$, l_1+l'_1, l_2+l'_2), where, l_1+l'_1 and l_2+l'_2 are the multipolarities of γ_1 and γ_2 transitions, respectively, and I is the spin of the intermediate nuclear state. For pure multipole transition, l'_1=l_1 and l'_2=l_2. Conservation of parity in γ-transitions and the fact that the γ-ray polarization is not measured here rule out k=odd terms in the summation and the terms involving k=even are allowed only in the equation of angular correlation. The anisotropy

coefficients are defined as

$$A_{kk} = A_k(\gamma_1)A_k(\gamma_2). \tag{2.44}$$

The anisotropy coefficients $A_k(\gamma_1)$ and $A_k(\gamma_2)$ depend on the multipolarity of the respective γ-ray transitions and the spin differences of the nuclear levels involved in the respective γ-decay. These coefficients can be written as

$$\begin{aligned} &A_k(\gamma_1) = A_k(l_1, l_1', I_i, I) = \\ &\frac{F_{k_1}(l_1, l_1; I_i, I) + (-1)^{l_1 - l_1'} 2\delta(\gamma_1) F_{k_1}(l_1, l_1'; I_i, I) + \delta^2(\gamma_1) F_{k_1}(l_1', l_1'; I_i, I)}{1 + \delta^2(\gamma_1)} \end{aligned} \tag{2.45}$$

and

$$\begin{aligned} &A_k(\gamma_2) = A_k(l_2, l_2'; I_f, I) = \\ &\frac{F_{k_2}(l_2, l_2; I_f, I) + 2\delta(\gamma_2) F_{k_2}(l_2, l_2'; I_f, I) + \delta^2(\gamma_2) F_{k_2}(l_1', l_1', I_i, I)}{1 + \delta^2(\gamma_2)}, \end{aligned} \tag{2.46}$$

where the F-coefficients are defined by Wigner 3-j and 6-j symbols

$$\begin{aligned} F_k(l, l'; I', I) =& (-1)^{I'+I-1} \sqrt{(2l+1)(2l'+1)(2I+1)(2k+1)} \\ &\times \begin{pmatrix} l & l' & k \\ 1 & -1 & 0 \end{pmatrix} \begin{Bmatrix} I & I & k \\ l' & l & I' \end{Bmatrix}. \end{aligned} \tag{2.47}$$

The $\delta(\gamma_1)$ and $\delta(\gamma_2)$ are the multipole mixing ratios for γ_1 and γ_2 transitions, respectively. It gives the mixing of angular momentum during emission of γ-rays.

2.3 Perturbed γ-γ angular correlation

When a nucleus which decays by emitting γ-γ cascade is placed in an extranuclear electromagnetic field, the hyperfine interaction occurs between the nuclear moments and the electromagnetic fields. Due to this hyperfine interaction, the degeneracy of the intermediate nuclear energy level is lifted and induces transitions between different M-

sublevels of the intermediate energy level of the γ-γ cascade. As a result, time dependent redistribution of the population of M-substates occurs during the time the nucleus resides in the intermediate level which causes perturbation in angular correlation [1, 77, 80].

The effect of extranuclear field on the re-distribution of M-substates depends on how much time the nucleus gets to interact with the nuclear moments in the intermediate state. As the intermediate state decays exponentially, we can visualize the time development of the angular correlation as a function of time using a set of fixed detectors. As the emission probability of γ_2 oscillates with time, modulations in the angular correlation can be determined by observing the time differences of the coincident detection of γ_2 with γ_1 by a fixed set of detectors at a particular angle.

Now, if $\Lambda(t)$ is considered the time development operator which changes the initially populated M_a sublevel to the final M_b substates from which the γ_2 is emitted. So,

$$|M_b\rangle = \Lambda(t)\,|M_a\rangle\,. \tag{2.48}$$

The perturbed angular correlation is defined as [1, 77]

$$\begin{aligned} W(\gamma_1,\gamma_2,t) = \sum_{k_1,k_2,N_1,N_2} & A_{k_1}(\gamma_1)A_{k_2}(\gamma_2)[(2k_1+1)(2k_2+1)]^{-1/2} \\ & \times G^{N_1N_2}_{k_1k_2}(t)Y^{N_1*}_{k_1}(\theta_1,\phi_1)Y^{N_2}_{k_2}(\theta_2,\phi_2). \end{aligned} \tag{2.49}$$

The perturbation function is given by [1, 2, 80]

$$\begin{aligned} G^{N_1N_2}_{k_1k_2}(t) = \sum_{M_a,M_b} & (-1)^{2I+M_a+M_b}\sqrt{(2k_1+1)(2k_2+1)} \\ & \times \begin{pmatrix} I & I & k_1 \\ M'_a & -M_a & N_1 \end{pmatrix} \begin{pmatrix} I & I & k_2 \\ M'_b & -M_b & N_2 \end{pmatrix} \langle M_b|\,\Lambda(t)\,|M_a\rangle\,\langle M'_b|\,\Lambda(t)\,|M'_a\rangle^*\,. \end{aligned} \tag{2.50}$$

Here, $N_1 = M_a - M'_a$ and $N_2 = M_b - M'_b$. The M_a, M'_a, M_b, M'_b are the magnetic substates of the intermediate energy level designated by the spin I. The values of k_i are restricted to k_i=0, 2, $\cdots \min\{2I, l_i + l'_i\}$ (i=1,2) and the values of N_i are restricted by the relation $|N_i| \leq k_i$. The angular correlation probability changes periodically towards a given detector due to the interaction of nuclear moments with extranuclear field. In the actual time-differential PAC experiment, the second radiation is accepted at time t after the emission of γ_1 with probability $f(t-T)$ which is the response time of the experimental set-up. The second radiation is delayed by time T to ensure that the first γ ray reaches the coincidence analyzer system first than the second γ-ray. The expression of periodically modulating correlation function in a time-interval τ_R centered at T can be expressed as

$$W(\theta_1, \theta_2, \phi_1, \phi_2, T) = \frac{\int_0^\infty f(t-T)\exp(-t/\tau_N)W(\theta_1, \theta_2, \phi_1, \phi_2, t)dt}{\int_0^\infty f(t-T)\exp(-t/\tau_N)dt}. \tag{2.51}$$

Here, $\exp(-t/\tau_N)$ shows the exponential decay of the intermediate energy level where τ_N is the mean lifetime of the intermediate energy level of the γ-γ cascade. This response function is often approximated by a step function

$$\begin{aligned} f(t-T) &= 1 \quad \text{when} \quad T - \tau_R/2 \leq t \leq T + \tau_R/2 \\ &= 0 \quad \text{when} \quad t < T - \tau_R/2 \quad \text{and} \quad t > T + \tau_R/2, \end{aligned} \tag{2.52}$$

where τ_R is the prompt time resolution of the experimental set up. Thus,

$$W(\theta_1, \theta_2, \phi_1, \phi_2, T) = \frac{\int_{T-\tau_R/2}^{T+\tau_R/2}\exp(-t/\tau_N)W(\theta_1, \theta_2, \phi_1, \phi_2, t)dt}{\int_{T-\tau_R/2}^{T+\tau_R/2}\exp(-t/\tau_N)dt}. \tag{2.53}$$

Now, if the time resolution of the experimental set-up is greater than the mean lifetime of the intermediate state ($\tau_R \gg \tau$), then, time-integral perturbed angular correlation

measurement is done. The time integrated angular correlation function is given by [1]

$$W(\theta_1, \theta_2, \phi_1, \phi_2, \infty) = \frac{1}{\tau_N} \int_0^\infty \exp(-t/\tau_N) W(\theta_1, \theta_2, \phi_1, \phi_2, t) dt, \tag{2.54}$$

and the time integrated perturbation function is defined by a similar manner as

$$\overline{G_{k_1 k_2}^{N_1 N_2}(\infty)} = \frac{1}{\tau} \int_0^\infty \exp\{-t/\tau\} G_{k_1 k_2}^{N_1 N_2}(t) dt. \tag{2.55}$$

2.4 Perturbation function: Axially symmetric hyperfine interactions

From the equation 2.50, it is not difficult to obtain numerical solution for the perturbation function. But, it is useful to derive analytical expression of perturbation function for some special cases. A special case of hyperfine interaction is axially symmetric hyperfine interaction, where the nuclear electric quadrupole moment interacts with axially symmetric EFG , i.e. η=0 or $V_{xx} = V_{yy}$. For symmetric magnetic hyperfine interaction, the magnetic field that interacts with nuclear magnetic dipole moment, should have a particular direction. For a homogeneous external magnetic field, the condition of axial magnetic field is readily satisfied. But for internal magnetic field, it is not always the case as the direction of internal magnetic field vectors can vary spatially. Here, we are excluding non-axially symmetric hyperfine fields. If z-axis is chosen as the direction of the axial field, the matrix element $\langle M_b | \Lambda(t) | M_a \rangle$ can be written as [1, 77, 80]

$$\begin{aligned} \langle M_b | \Lambda(t) | M_a \rangle &= \langle M_b | \exp\left\{ -\frac{i}{\hbar} H t \right\} | M_a \rangle \\ &= \exp\left\{ -\frac{i}{\hbar} E(M) t \right\} \delta_{M,M_a} \delta_{M,M_b} \\ &= \exp\left\{ -\frac{i}{\hbar} E(M) t \right\}, \end{aligned} \tag{2.56}$$

where $M_a = M_b = M$ and a similar expression holds for$\langle M'_b| \Lambda(t) |M'_a\rangle$. So, for axially symmetric hyperfine interactions, the time development operator causes only a phase change and no repopulation of M-substates occurs. Now by substituting the above equation into equation 2.50, we get a simplified form of perturbation function for the axially symmetric hyperfine interaction which is given by

$$G^{NN}_{k_1k_2}(t) = \sum_M \sqrt{(2k_1+1)(2k_2+1)} \times \begin{pmatrix} I & I & k_1 \\ M' & -M & N \end{pmatrix} \begin{pmatrix} I & I & k_2 \\ M' & -M & N \end{pmatrix} \exp\Big\{-\frac{i}{\hbar}\Big[E(M) - E(M')\Big]t\Big\}, \tag{2.57}$$

where $N = M - M'$.

2.4.1 Axially symmetric electric hyperfine interaction

For axially symmetric electric hyperfine interaction, the energy difference between the magnetic M-sublevels can be obtained from the equation 2.38. Substituting the values of $E(M) - E(M')$=$3|M^2 - M'^2|\hbar\omega_Q$ into equation 2.57, we can get the final form of perturbation function as

$$G^{NN}_{k_1k_2}(t) = \sqrt{(2k_1+1)(2k_2+1)} \sum_M \begin{pmatrix} I & I & k_1 \\ M' & -M & N \end{pmatrix} \begin{pmatrix} I & I & k_2 \\ M' & -M & N \end{pmatrix} \exp\Big[-3i|M - M'^2|\omega_Q t\Big]. \tag{2.58}$$

Perturbation function can be re-written as

$$G^{NN}_{k_1K_2}(t) = \sum_n S^{k_1k_2}_{nN} \cos(n\omega^0_Q t). \tag{2.59}$$

Here,

$$\omega_Q^0 = 3\omega_Q \quad \text{and} \quad n = |M^2 - M'^2| \quad \text{for} \quad I \quad \text{integral} \tag{2.60}$$

$$\omega_Q^0 = 6\omega_Q \quad \text{and} \quad n = \frac{1}{2}|M^2 - M'^2| \quad \text{for} \quad I \quad \text{half integral,} \tag{2.61}$$

and

$$S_{nN}^{k_1 k_2} = \sqrt{(2k_1+1)(2k_2+1)} \sum_{M,M'} \begin{pmatrix} I & I & k_1 \\ M' & -M & N \end{pmatrix} \begin{pmatrix} I & I & k_2 \\ M' & -M & N \end{pmatrix}. \tag{2.62}$$

The summation indices M and M' takes only the values for which the equations 2.60 and 2.61 are satisfied. The results obtained in equation 2.59 says the angular correlation pattern modulates with ω_Q^0, $2\omega_Q^0$, $3\omega_Q^0$, $\cdots$, $n_{max}\omega_Q^0$ frequencies where the corresponding weighting factor is given by $S_{nN}^{k_1 k_2}$ coefficients. The angular correlation function and perturbation function get even more simplified for a polycrystalline sample where the crystallites are oriented randomly and the direction of axially symmetric EFGs also becomes randomly oriented. For axially symmetric hyperfine interaction in a polycrystalline sample, the angular correlation function can be written as

$$W(\theta, t) = \sum_{\substack{k=0 \\ even}}^{k_{max}} A_{kk} G_{kk}(t) P_k(cos\theta), \tag{2.63}$$

and the perturbation function is written as

$$G_{kk}(t) = \sum_{n=0}^{n_{max}} S_{kn} \cos(n\omega_Q^0 t), \tag{2.64}$$

and the S_{kn} coefficients are written as

$$S_{kn} = \sum_{M,M'} \begin{pmatrix} I & I & k \\ M' & -M & M - M' \end{pmatrix}^2. \tag{2.65}$$

For the randomly oriented powder sample, the dependence of perturbation function on N is lifted and interference terms in the anisotropic coefficient $A_{k_1k_2}$ do not appear and we obtain $A_{k_1k_2} = A_{kk}$.

2.4.2 Oriented magnetic hyperfine interaction

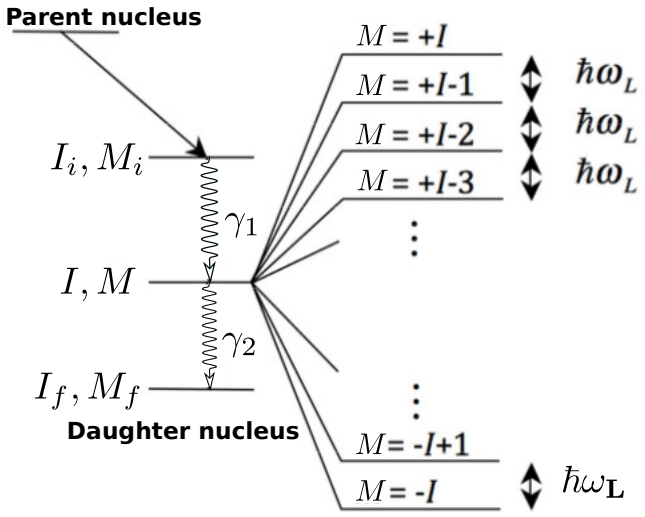

Figure 2.4: Quantum mechanical picture of magnetic hyperfine interaction. The ω_L is Larmor precession frequency [2].

The energy difference between M-sublevels for magnetic hyperfine interaction (Figure 2.4) can be obtained from the equation 2.41. So the $E(M) - E(M') = (M - M')\hbar\omega_L = N\hbar\omega_L$. The perturbation function (equation 2.57) takes the following form for an external or internal magnetic field oriented along z-axis

$$G^{NN}_{k_1k_2}(t) = \sqrt{(2k_1+1)(2k_2+1)}\exp(-iN\omega_L t)\sum_M \begin{pmatrix} I & I & k_1 \\ M' & -M & N \end{pmatrix}\begin{pmatrix} I & I & k_2 \\ M' & -M & N \end{pmatrix}, \tag{2.66}$$

which can be further simplified using orthogonality rule for Wigner $3j$-symbols as [1]

$$\begin{aligned} G^{NN}_{k_1k_2}(t) =& \sqrt{(2k_1+1)(2k_2+1)}\exp(-iN\omega_L t)\frac{1}{\sqrt{(2k_1+1)(2k_2+1)}}\delta_{k_1k_2} \\ =& \exp(-iN\omega_L t). \end{aligned} \tag{2.67}$$

From the above equation 2.67, we can say that no interference terms appear in the angular correlation function

$$W(\vec{k}_1,\vec{k}_2,t) = \sum_{k,N} A_{kk}\frac{1}{2k+1}\exp\{-iN\omega_L t\}Y_k^{N*}(\theta_1,\phi_1)Y_k^N(\theta_2,\phi_2). \tag{2.68}$$

Thus, due to the interaction of nuclear dipole moment with axial magnetic field, the angular correlation of γ-rays or population of the M substates of the intermediate level oscillates with fundamental frequency ω_L and its higher harmonics $N\omega_L$.

Now if the external magnetic field is applied perpendicular to the plane of detectors, then, the angular correlation depends only on the difference of azimuthal angles of $\vec{k_1}$ and $\vec{k_2}$, i.e. $\theta = \phi_1 - \phi_2$ and $\theta_1 = \theta_2$=90°. The form of angular correlation becomes

$$\begin{aligned} W(\theta,t) &= \sum_{\substack{k=0 \\ even}}^{k_{max}} A_{kk}P_k[\cos(\theta-\omega_L t)] \\ &= \sum_{\substack{k=0 \\ even}}^{k_{max}} A_{kk}G^{NN}_{kk}(t)P_k(cos\theta). \end{aligned} \tag{2.69}$$

For a polycrystalline sample, the perturbation function becomes even more simplified and it does no more depend on N

$$G_{kk}(t) = \frac{1}{2k+1}\Big(1+2\sum_{n=1}^{k}\cos(n\omega_L t)\Big). \tag{2.70}$$

Now, if only dipole transition is considered i.e. k=2, the perturbation function becomes

$$G_{22}(t) = \frac{1}{5}\Big[1+2\cos(\omega_L t)+2\cos(2\omega_L t)\Big]. \tag{2.71}$$

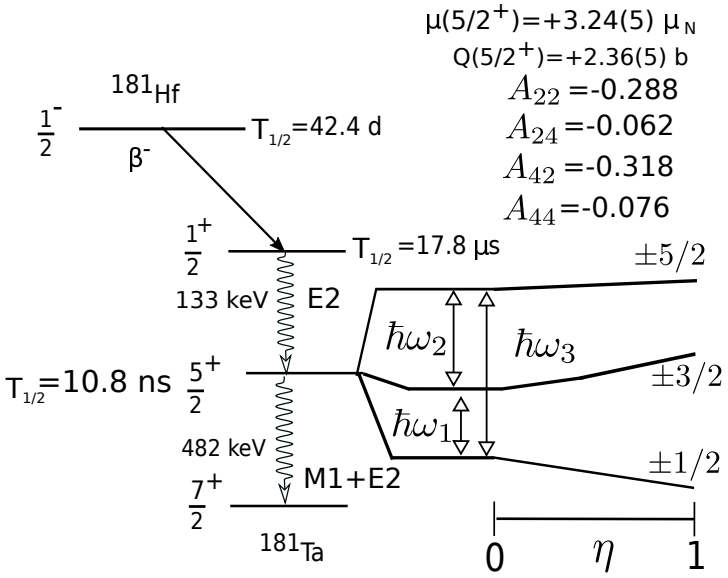

Figure 2.5: Electric hyperfine interaction for the probe nucleus ^{181}Hf.

2.5 Perturbation function for electric hyperfine interaction for polycrystalline sample

For the PAC measurement, I have used ^{181}Hf probe isotope. The decay scheme for ^{181}Hf PAC probe is shown in Figure 2.5. For this probe nucleus $A_{22} \gg A_{44}$ and, therefore, the angular correlation function for a polycrystalline sample can be simplified to the following form [2]

$$W(\theta, t) = 1 + A_{22}G_{22}(t)P_2(cos\theta). \tag{2.72}$$

Commonly, the coefficient A_{22} and G_{22} are referred as A_2 and G_2, respectively as no interference terms appear here. The perturbation function $G_2(t)$ for electric quadrupole interaction in a polycrystalline sample with intermediate spin of the probe nucleus I=5/2 $\hbar$ can be written as

$$G_2(t) = S_{20}(\eta) + \sum_{n=1}^{3} S_{2n}(\eta)\cos(\omega_n t). \tag{2.73}$$

For the probe nuclei having intermediate state $I \neq$5/2 $\hbar$, the perturbation function can be found in the reference [83]. The S_{2n} coefficients for I=5/2 $\hbar$ are written as a

polynomial in η ($=\frac{V_{xx}-V_{yy}}{V_{zz}}$ where $|V_{zz}| \geq |V_{yy}| \geq |V_{xx}|$) [84]:

$$\begin{aligned} S_{20} =& 0.20009 - 0.00664\eta + 0.33716\eta^2 - 0.42849\eta^3 + 0.15641\eta^4 \\ S_{21} =& 0.37135 + 0.00647\eta - 0.35367\eta^2 + 0.42579\eta^3 - 0.15571\eta^4 \\ S_{22} =& 0.28568 + 0.00166\eta - 0.03854\eta^2 + 0.06943\eta^3 - 0.02379\eta^4 \\ S_{23} =& 0.14280 - 0.00149\eta + 0.05504\eta^2 - 0.06673\eta^3 + 0.02308\eta^4. \end{aligned} \tag{2.74}$$

For η=0, the values of S_{2n} are S_{20}=0.20, S_{21}=0.37, S_{22}=0.29, S_{23}=0.14. For non-zero values of η, the energy of the non-degenerate M-sublevels becomes a function of η which can be written as

$$E_{\pm 5/2} = 2\alpha \cos\beta \times \hbar\omega_Q \tag{2.75}$$

$$E_{\pm 3/2} = -\alpha(cos\beta - \sqrt{3}\sin\beta) \times \hbar\omega_Q \tag{2.76}$$

$$E_{\pm 1/2} = -\alpha(cos\beta + \sqrt{3}\sin\beta) \times \hbar\omega_Q, \tag{2.77}$$

and the transition frequencies ω_n can be written as

$$\omega_1 = \frac{E_{\pm 3/2} - E_{\pm 1/2}}{\hbar} = 2\sqrt{3}\alpha\omega_Q \sin(\frac{1}{3}\cos^{-1}\beta) \tag{2.78}$$

$$\omega_2 = \frac{E_{\pm 5/2} - E_{\pm 3/2}}{\hbar} = 2\sqrt{3}\alpha\omega_Q \sin(\frac{\pi}{3} - \frac{1}{3}\cos^{-1}\beta) \tag{2.79}$$

$$\omega_3 = \frac{E_{\pm 5/2} - E_{\pm 1/2}}{\hbar} = 2\sqrt{3}\alpha\omega_Q \sin(\frac{\pi}{3} + \frac{1}{3}\cos^{-1}\beta), \tag{2.80}$$

where $\alpha = \sqrt{28(1+\eta^2/3)}$ and $\beta = \frac{80(1-\eta^2)}{\alpha^3}$.

For any value of η, the following relation is satisfied

$$\omega_3 = \omega_1 + \omega_2. \tag{2.81}$$

Here, quadrupole frequency ω_Q is expressed in units of Mrad/s, which is related to the maximum component of electric field gradient (i.e. V_{zz}) by the following relation:

$$\omega_Q = \frac{eQV_{zz}}{4I(2I-1)\hbar}. \tag{2.82}$$

Electric field gradient (V_{zz}) is sometimes expressed in term of quadrupole coupling constant ν_Q as

$$\nu_Q = \frac{eQV_{zz}}{h}. \tag{2.83}$$

Due to inhomogeneity or lattice imperfections (e.g. point defects, dislocations) in the sample, the probe nuclei do not experience a unique hyperfine interaction and a distribution of frequencies are observed. This phenomena is called inhomogeneous broadening. As a result, amplitude of the angular precession gets attenuated. For practical purposes, the perturbation function is fitted with a single linewidth of transition frequencies which is the average of the distribution frequencies for the different ω_n. The linewidth δ is defined as

$$\delta = \frac{\Delta V_{zz}}{V_{zz}}. \tag{2.84}$$

As the linewidth δ increases, the more the amplitude of oscillation of angular correlation gets attenuated with time. Generally, Gaussian or Lorentzian type distribution is used for fitting of PAC spectrum [2]. The expression for perturbation function becomes

$$G_2(t) = S_{20}(\eta) + \sum_{n=1}^{3} S_{2n}(\eta)\cos(\omega_n t)\exp\left[-\frac{1}{p}(\delta\omega_n t)^p\right]. \tag{2.85}$$

When $p = 1$, it is called Lorentzian distribution and for p=2, it is Gaussian distribution. In our PAC measurements, we have fitted the PAC spectra with Lorentzian distribution

function. When ω_n is smaller than $1/\tau_R$, no dependence of the perturbation function on the resolution of the detector (τ_R) is found. But, for the cases where ω_n is comparable with $1/\tau_R$, the perturbation function is dependent on the prompt time-resolution of the experimental set up which can be written as [85]

$$G_2(t) = S_{20}(\eta) + \sum_{n=1}^{3} S_{2n}(\eta)\cos(\omega_n t)\exp\Big[-\delta\omega_n t\Big]\exp\Big[-\frac{1}{2}(\omega_n\tau_R)^2\Big]. \tag{2.86}$$

For an axially symmetric EFG, the transition frequency ω_n are the integer multiple of the lowest transition frequency ω_Q^0 i.e. $\omega_n = n\omega_Q^0$. For the probes with half-integer spin, $\omega_Q^0 = 6\omega_Q$ and for integer spin the relation is $\omega_Q^0 = 3\omega_Q$. Thus, for ^{181}Hf probe, ω_1=ω_Q^0=$6\omega_Q$, $\omega_2 = 12\omega_Q$ and $\omega_3 = 18\omega_Q$ (i.e. $\omega_1 : \omega_2 : \omega_3$=1 : 2 : 3) for η=0. Thus, the perturbation is periodic and harmonic for η=0. For asymmetric EFG ($\eta \neq$0), the perturbation function is periodic but not harmonic. For nuclear quadrupole interaction in polycrystalline sample, as the crystallites are oriented randomly, the nuclear spin precession is averaged over all field directions. Despite of this fact, the nuclear spin precession remains observable because the oscillation frequency of angular correlation of γ-rays depends on the magnitude of the EFG and not on the direction of EFG.

Now, if different fractions of probe nuclei are exposed to different HFI due to different crystal environment in the same sample, the total perturbation function can be written as a sum of all the different perturbation functions:

$$\begin{aligned} G_2(t) &= \sum_i f_i G_2^i(t) \\ \sum_i f_i &= 1. \end{aligned} \tag{2.87}$$

where f_i is the fraction of atoms in the ith site and $G_2^i(t)$ is the corresponding perturbation function.

2.6 Nuclear spin-relaxation

When the charge density surrounding to the probe nucleus changes with time, i.e. the probe nuclei are exposed to a fluctuating electromagnetic field in the host lattice, a rapid disappearance of γ-γ correlation is observed. This phenomena is called nuclear spin-relaxation [80]. In liquid samples, time dependent hyperfine interactions are observed due to continuously changing environment surrounding the probe atom. In soild materials also, time dependent HFI can occur due to jump diffusion of vacancies which reorients EFG through large angles. The probe nuclei experience a fluctuating EFG or magnetic field as the nuclear spin continuously re-orients with time due to random collision of molecules in liquid samples. The hyperfine field axis reorients continuously with time within the lifetime of the intermediate level of the probe nucleus which produces smearing or damping in the angular correlation of γ-γ-cascade. The rate of reorientation of nuclear spin depends on nuclear electric quadrupole moment, mean EFG or magnetic field and the correlation time τ_c which is defined as the time up to which the system retains its identity. This nuclear relaxation effect depends on the relative strength of the three characteristic times 1) correlation time τ_c; 2) interaction time $\tau^{int}= < \omega^2 >^{1/2}$; 3) time of observation t. However, at any instant, a local configuration can be presumed to be stationary at the vicinity of the probe nucleus. Two different models are used to calculate the relaxation effect, 1) diffusion model; 2) strong collision model. In diffusion model, it is assumed that the molecular axis changes its direction with very small angular steps. There is a strong correlation of orientation before and after the collision. On the other hand, in strong collision model, there is no correlation of orientations before and after any collision and every orientation is equally probable after each collision. The strong collision model is called also as rapid phase approximation (RPA). Diffusion model has been widely used by experimentalists to explain the PAC results. In this model, perturbation function can be calculated for two processes a) fast relaxation ($\langle\omega^2\rangle^{-1/2}\tau_c \ll 1$) b) slow relaxation ($\langle\omega^2\rangle^{-1/2}\tau_c \gg 1$). Here, ω_Q=ω for pure electric quadrupole and

ω=ω_L for pure magnetic dipole relaxation. The correlation time τ_c depends on the molecular size, mass and on the viscosity of the solvent in liquid sample which can be calculated by Einstein-Stokes model. The correlation time τ_c can be approximately written as

$$\tau_c = \frac{4}{3}\pi r^3 \frac{\mu_\nu}{kT}, \tag{2.88}$$

where r is the radius of the molecule and μ_ν is the viscosity of the solvent at temperature T. Abragam and Pound [86] developed the perturbation theory for fast relaxation and adiabatic approximation is employed to describe the slow-relaxation process.

a) Abragam-Pound Model: fast relaxation

For fast relaxation, the correlation time $\tau_c \ll \langle\omega^2\rangle^{-1/2}$ where, $\langle\omega^2\rangle^{-1/2}$ represents the mean interaction time τ^{int}. The fast fluctuation model is valid when fluctuation occurs within $\sim 10^{-11}$s. If the time of observation $t \gg \tau_c$, then, the perturbation function can be expressed by a simple exponential relation

$$G_k(t) = \exp(-\lambda_k t), \tag{2.89}$$

where λ_k is the relaxation constant which, for a fluctuating EFG, is defined by the following relation:

$$\lambda_k = \frac{3}{5}\left\langle\omega_Q^2\right\rangle \tau_c k(k+1)[4I(I+1)-k(k+1)-1]; \quad \left\langle\omega_Q^2\right\rangle = \frac{e^2Q^2}{16\hbar^2 I^2(2I-1)^2}\left\langle V_{zz}^2\right\rangle. \tag{2.90}$$

For a fluctuating magnetic field, λ_k is given by

$$\lambda_k = \frac{1}{3}k(k+1)\left\langle\omega_L^2\right\rangle \tau_c; \quad \langle\omega_L^2\rangle = \frac{g^2\mu_N^2}{\hbar^2}\left\langle B_{hf}^2\right\rangle. \tag{2.91}$$

Here, B_{hf} is the magnitude of the magnetic field at the probe site, i.e. hyperfine magnetic field.

b) Adiabatic approximation: slow relaxation

Slow relaxation occurs due to slow rotational motion of large tumbling molecules in liquid or small molecule in viscous medium where the correlation time $\tau_c \gg \langle w^2 \rangle^{-1/2}$. The model is developed by Marshall and Meares [87] which considers an adiabatic change of local configuration with time. The perturbation function in the case of slow relaxation can be written as

$$G_k(t) = \exp(-\lambda_k t) G_k^{\text{static}}(t). \tag{2.92}$$

Here, G_k^{static} represents the random static hyperfine interaction. For spherically symmetric molecule, the rotational diffusion coefficient D is relation to the relaxation constant as

$$\tau_k = \frac{1}{\lambda_k} = \frac{1}{k(k+1)D}. \tag{2.93}$$

Slow-fluctuation model is valid if fluctuation of any atom/molecule occurs in $\geq 10^{-7}$s. In solid material, if any ion near the probe atom jumps from one vacancy site to the next-nearest vacancy site by crossing the potential barrier, the rate of fluctuation can be obtained from the Arrhenius relation [88]:

$$\begin{aligned} \lambda_k^{\text{fast}} &= \lambda_k^{+} \exp\left(\frac{\Delta E_{\text{high}}}{kT}\right) \\ \lambda_k^{\text{slow}} &= \lambda_k^{-} \exp\left(-\frac{\Delta E_{\text{low}}}{kT}\right). \end{aligned} \tag{2.94}$$

The relaxation constant λ_k^{fast} is the jump frequency in the fast fluctuation regime where ΔE_{high} is the activation energy, and λ_k^{slow} is the jump frequency in the slow fluctuation regime where ΔE_{low} is the activation energy. Due to this nuclear spin-relaxation, a damping in the PAC spectrum is observed and as the value of relaxation constant increases, the amplitude of modulation of angular correlation gets attenuated with time. In the fast fluctuation regime, the damping in the angular correlation decreases as the fluctuation rate increases and after a certain high value of fluctuation rate, the nuclear spin precession is no more observable and a static hyperfine interaction is observed. This

phenomena is called "motional narrowing". Lattice vibration may cause such phenomena where the fluctuation occurs in less than 10^{-11}s. In the slow fluctuation regime, the attenuation of the correlation function increases as the rate of fluctuation increases. The attenuation of the modulation of angular correlation reaches to a maximum at an intermediate fluctuation rate depending on the relative strengths of static and fluctuating components.

CHAPTER 3

Experimental details

3.1 Experimental set up for PAC measurements

To observe the hyperfine interaction through time differential perturbed angular correlation technique, it is required to measure the time development of angular correlation of γ-rays by detecting the two gamma rays in coincidence at angular separation of 180° and 90°. The time resolution of the detector combination sets the lower time limit and genuine to accidental coincidence count rate ratio sets the upper time limit in measuring the nuclear spin precession. Scintillation detectors as well as semiconductor detectors are mainly used for gamma-ray spectroscopic measurements. However, the semiconductor detectors produce poor time resolution (typically 5-10 ns) although it shows very good energy resolution (R$\sim$0.1% for germanium semiconductor detector whereas it is $\sim$7% for NaI scintillation detector at typically 1 MeV γ ray energy [89]). Thus, the semiconductor detectors are not generally used for PAC measurement as the probe nuclei that are commonly used usually have lifetime $\sim$ 10-100 ns. So, the detector used for PAC measurements ideally requires $\sim$1 ns time resolution. Some of the inorganic scintillation detectors viz. $LaBr_3$(Ce), BaF_2, LSO (Lu_2SiO_5) coupled with fast PMT (photo-multiplier tube) are mostly used. These detectors produce a prompt time reso-

lution (FWHM) $\sim$ few hundred ps for gamma ray energies >500 keV. These inorganic scintillators have high γ detection efficiency due to their high effective atomic number (Z_{eff}). A comparison of characteristic features of some inorganic scintillation detectors has been summarized in the Table 3.1. Plastic scintillation detectors also show good time resolution but are not used for PAC spectroscopic measurement due to their poor energy resolution and lower detection efficiency. In BaF_2, two decay components are observed. Approximately 20% of the light yield of this scintillator originates from fast decay component and rest $\sim$ 80% stems out from the slow component. A sub nanosecond prompt time resolution of BaF_2 detector is found due to its fast decay component with decay constant ~0.6-0.8 ns. The slower component has a decay constant of 630 ns. The $LaBr_3$(Ce) scintillation detector also produces a sub nanosecond prompt time resolution due to its high light yield (~63 photons/keV). Due to its very high light output compared to any other scintillator, it produces the best energy resolution (~3-4% at 662 keV) and a prompt time resolution comparable to BaF_2 detector although it has a much longer decay time of 16 ns. Time walk and jitter are significantly minimized for high amplitude pulses which improves the time resolution of $LaBr_3$(Ce) scintillation detector. Another advantage of $LaBr_3$(Ce) is that the wavelength of maximum emission occurs near visible region (at 380 nm) and a glass window PMT can be used for collecting scintillating light. In BaF_2 scintillation detector, as the fast component shows maximum emission at wavelength of ultraviolet region (Table 3.1), a quartz window PMT is required to collect signal from BaF_2 scintillator. For our PAC measurements, two TDPAC spectrometers have been employed. These are a four detector $LaBr_3$(Ce)-BaF_2 and a BaF_2-BaF_2 set-ups developed in our laboratory. For each of the set-ups, the detectors are placed on a horizontal table as shown in Figure 3.1. The schematic diagram of the $LaBr_3$(Ce)-BaF_2 and BaF_2-BaF_2 set-ups are shown in the Figure 3.2 and Figure 3.3, respectively.

Table 3.1: Characteristics of some inorganic scintillation detectors

Scintillators	Light yield (photons/keV)	1/e Decay time (ns)	Wavelength of maximum emission (nm)	Refractive index (gm/cm^3)	Density	Z_{eff}	Hygroscopic
$LaBr_3$(Ce)	63	16	380	~1.9	5.08	45.22	yes
BaF_2 (fast component)	1.8	0.6-0.8	220	1.54	4.88	50.96	slightly
(slow component)	10	630	310	1.50			
NaI(Tl)	38	250	415	1.85	3.67	50.6	yes
LSO	32	41	420	1.81	7.1	65.5	no

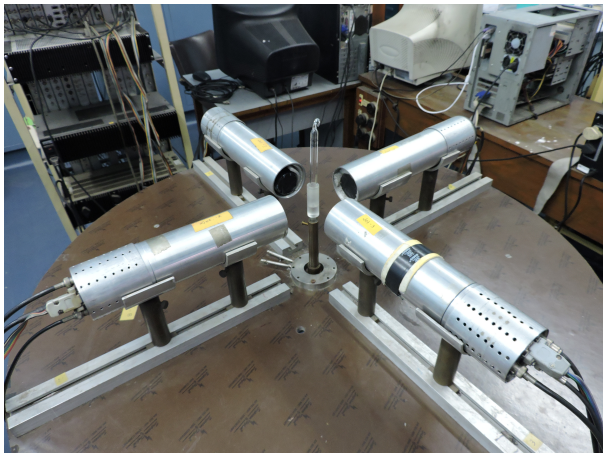

Figure 3.1: $LaBr_3$(Ce)-BaF_2 detector set up in our laboratory.

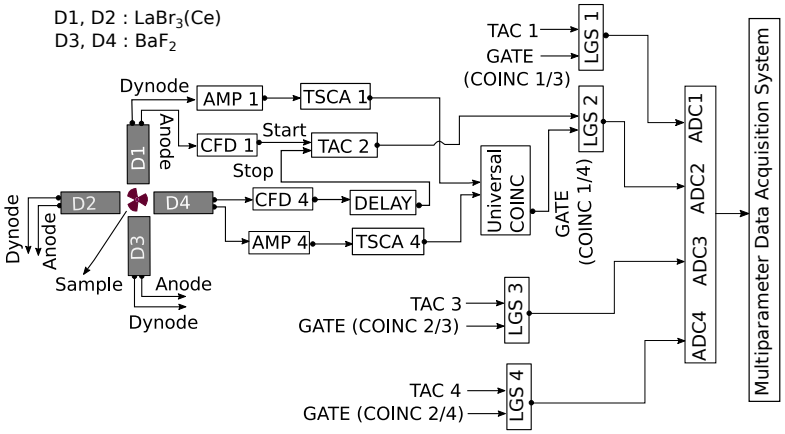

Figure 3.2: Schematic diagram of the four detector $LaBr_3$(Ce)-BaF_2 PAC set up.

3.1.1 $LaBr_3$(Ce)-BaF_2 PAC spectrometer

In the $LaBr_3$(Ce)-BaF_2 set-up, two $LaBr_3$(Ce) and two BaF_2 have been employed in a slow-fast coincidence assembly (Figure 3.1). The crystal sizes are 38.1(dia)×25.4(ht) mm^2 and 50.8(dia)×50.8(ht) mm^2 for $LaBr_3$(Ce) and BaF_2 scintillators, respectively.

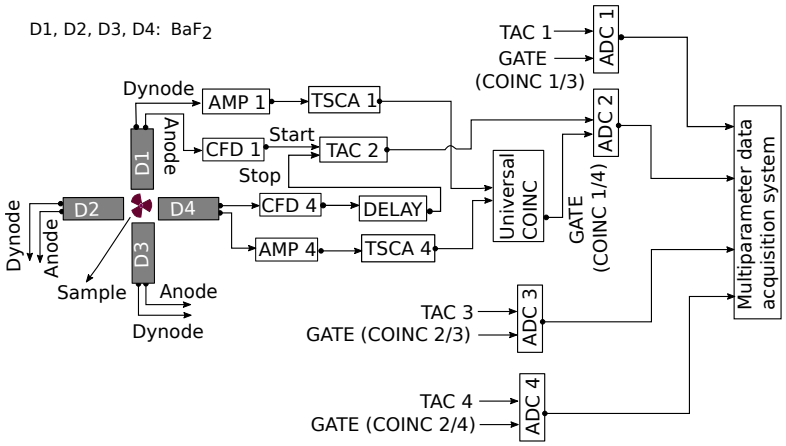

Figure 3.3: Schematic diagram of the four detector BaF_2-BaF_2 PAC set up.

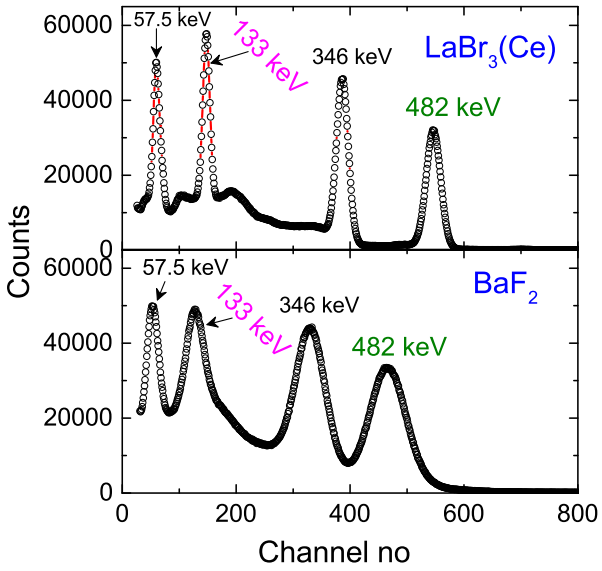

Figure 3.4: Energy spectrum of ^{181}Hf obtained from $LaBr_3$(Ce) (top) and BaF_2 (bottom) scintillation detectors. The 57.5 keV peak is the K_α X-ray of Hafnium.

The energy resolutions of the $LaBr_3$(Ce) [38.1(dia)×25.4(ht) mm^2] and BaF_2 (50.8×50.8 mm^2) detectors used in this set up have been found to be $\sim$ 4% and 14%, respectively at 662 keV γ ray energy of ^{137}Cs. The spectra of ^{181}Hf in $LaBr_3$(Ce) [38.1×25.4 mm^2] and BaF_2 (50.8×50.8 mm^2) scintillation detectors are shown in Figure 3.4. The two γ-rays that we are concerned about viz. 133 keV and 482 keV, are distinctly separated in the energy spectra obtained in both the scintillation detectors. Due to superior energy resolution of $LaBr_3$(Ce) detectors, the 133 keV gamma rays have been selected in

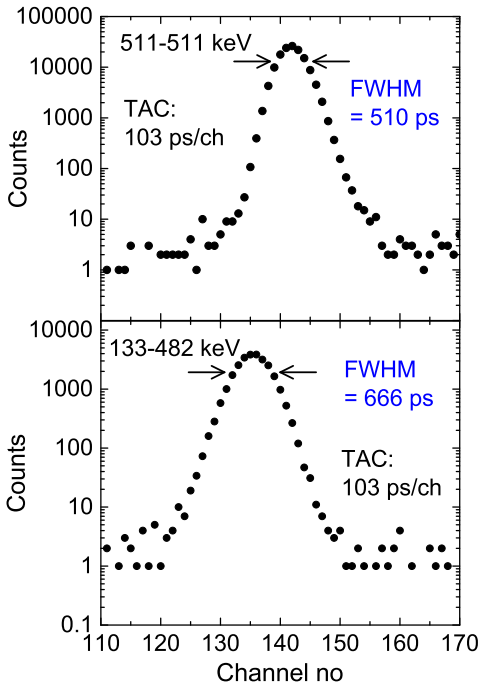

Figure 3.5: Time resolutions in a $LaBr_3$(Ce)-BaF_2 set up using ^{22}Na source at 511-511 keV (top) and 133-482 keV (bottom) energy selections.

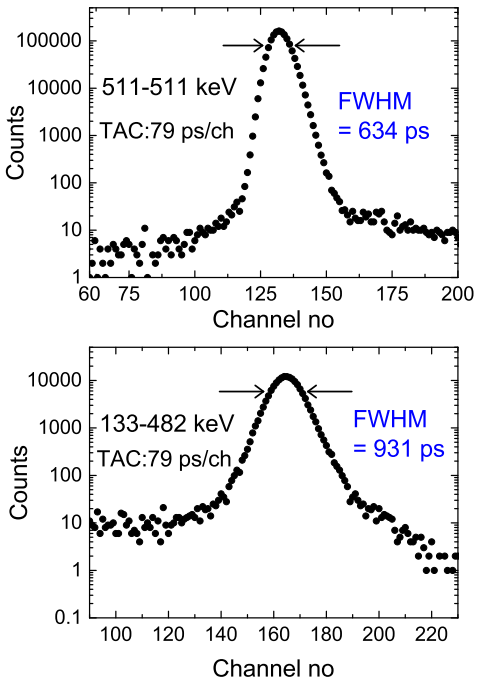

Figure 3.6: Time resolutions in a BaF_2-BaF_2 set up using ^{22}Na source at 511-511 keV (top) and 133-482 keV (bottom) energy selections.

$LaBr_3$(Ce) detector. This will reduce the Compton contribution of higher energy gamma rays falling within this energy window and BaF_2 detectors have been used to detect 482 keV γ-rays of the probe nucleus ^{181}Hf. Using these detectors, four conventional slow-fast coincidences have been made, two at 90° and two at 180°. In this set-up, all the coincidence combinations comprise of one $LaBr_3$(Ce) and one BaF_2 detector. The prompt time resolutions for the $LaBr_3$(Ce)-BaF_2 set up have been found $\sim$ 510 ps at the 511 keV gamma ray energies and $\sim$ 666 ps for 133-482 keV energy window selection using 511 keV prompt annihilation gamma rays of ^{22}Na (Figure 3.5). The four coincidences can be labeled as 1/3, 1/4, 2/3, 2/4, where detectors marked as 1 and 2 are $LaBr_3$(Ce) detectors and these detectors subtends an angle of 90° at the source position with each other (Figure 3.2). The detectors marked as 3 and 4 are the BaF_2 detectors which also subtends an angle of 90° with each other. The $LaBr_3$(Ce) and BaF_2 detectors are also placed at an angle of 90° with each other with respect to the sample position. The

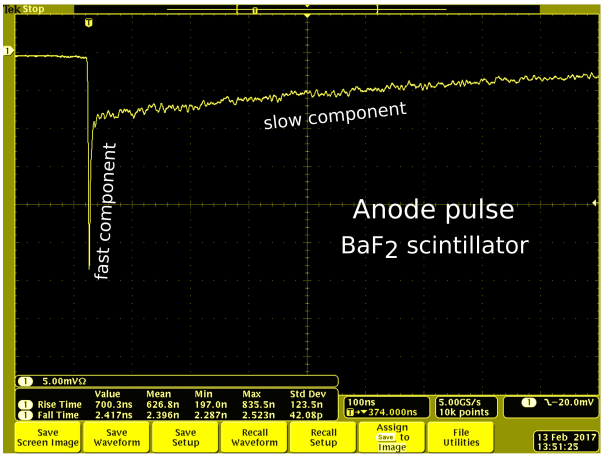

Figure 3.7: Anode pulse in a BaF_2 scintillator.

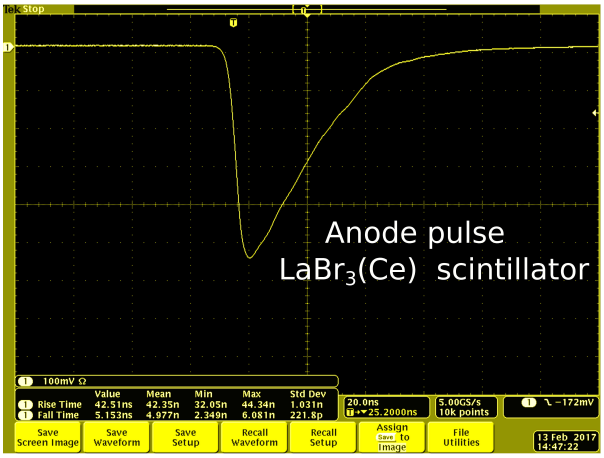

Figure 3.8: Anode pulse in a $LaBr_3(Ce)$ scintillator.

combinations 1/4, 2/3 are the coincidences where the two detectors are at 90° with each other and 1/3, 2/4 are the coincidences where the detectors are at 180° with each other. From each of the detectors, two signals have been taken out, one is from the anode and another is from the last dynode. The signal from the last dynode is used for energy selection of the desired γ-ray. The pulse from the anode is used for timing purposes. A typical anode pulses from BaF_2 and $LaBr_3(Ce)$ detectors have been shown in the Figure 3.7 and Figure 3.8, respectively. The fast and slow decay component can be distinctly observed in the anode pulse of the BaF_2 scintillator. The anode pulse is directly fed to the fast timing discriminator (ORTEC 584) in the constant fraction (CF) triggering mode [constant fraction discriminator (CFD)]. The main function of the CFD is to register the time of arrival of the detected events with maximum precision. In CFD, the analog pulse is first divided into two parts; one part is inverted and attenuated upto some constant fraction of the actual pulse, and another part is delayed. Finally the two parts of the signal are added which eliminates the dependence of the time of arrival of any signal on its amplitude and rise time. The negative logic pulse of the CFDs are directly fed to the time-to-amplitude converter (TAC). The CFD signals from the $LaBr_3(Ce)$ detectors are used as start in the TAC and the CFD signals from the BaF_2 detectors are used as stop with appropriate delay. In the TAC, a ramp pulse is

generated as soon as the start pulse appears in the TAC and the ramp is stopped by the stop signal. The amplitude of the analog output pulse from the TAC is proportional to the time differences between the start and stop pulse. The range of the TAC is generally set to 5-10 times the lifetime of the intermediate level of the probe nucleus. We have set the TAC range to 100 ns as the half-life of the intermediate level of ^{181}Hf probe nucleus is 10.8 ns. It is expected that within this time range of 100 ns almost all stop pulses will be generated. The dynode pulse is fed to the spectroscopic amplifier where the signal is processed by a pulse shaping network. The signal is allowed to pass through a CR high pass filter followed by a RC low pass filter in the amplifier. The shaping times of spectroscopic amplifiers are set to 1 μs. The output analog pulses from the amplifier are fed to the timing single channel pulse-height analyzer (TSCA). The desired γ-ray energy is selected here. The TSCA connected with $LaBr_3$(Ce) detectors are set to select 133 keV gamma rays and the TSCA connected with BaF_2 detectors are set to select 482 keV gamma rays. The two logic pulses from TSCA in a particular combination are fed to a Universal Coincidence unit after matching their delays. In the coincidence unit, the resolving time is set to few μs, which is much larger than the TAC window to reduce the loss of genuine coincidence event. The output signal from TAC is then gated with the coincidence output for a particular coincidence combination in a linear gate stretcher (LGS) unit. The output analogue pulses from the LGSs are then fed to the analogue to digital converter (ADC) units which are further processed by a multiparameter data acquisition system (Canberra Multiport II). All ADCs are set to 1K channel. Details of functional properties of the electronic modules used in this set up can be found in the references [89, 90].

We have used four TACs and four ADCs for obtaining the four coincidence spectra. As all the TACs have different time calibration, a common time calibration is needed to combine the data obtained from two coincidence spectra at 90° and two at 180°. A Time Calibrator unit (ORTEC 462) is used to calibrate all the TACs. Using a prompt source, e.g. ^{60}Co (emits 1173-1332 keV coincident γ rays), the time zero channels of the

TACs corresponding to four different coincidence combinations were obtained. With the common time calibration of the TACs and by noting all the time zero channels for the individual TACs, coincidence counts registered in the corresponding ADCs have been used to get the PAC spectra i.e. $A_2G_2(t)$ vs t.

3.1.2 BaF_2-BaF_2 PAC spectrometer

In the BaF_2-BaF_2 PAC spectrometer, four BaF_2 detectors have been used, two having sizes 38.2×25.4 mm^2 and other two having sizes 50.8×50.8 mm^2. Smaller sized BaF_2 crystal (38.1×25.4 mm^2) shows better energy resolution (∼10%) than for a BaF_2 crystal (∼14%) with larger sizes (50.8×50.8 mm^2) at 662 keV γ ray energy of ^{137}Cs. Probably, trapping of photons worsens the energy resolution for the larger sized BaF_2 scintillator. The smaller BaF_2 crystals have been employed to detect 133 keV γ-ray due to its better energy resolution and the BaF_2 scintillators with crystal sizes 50.8×50.8 mm^2 have been used to detect 482 keV γ ray. Four similar coincidences are formed in this set-up also. The coincidences are 1/3, 1/4, 2/3, 2/4, where 1 and 2 are the smaller BaF_2 crystals and 3 and 4 are the BaF_2 scintillators having higher dimension (Figure 3.3). The detectors 1 and 2 are placed at 90° with each other and detectors 3 and 4 also subtend an angle of 90° with each other with respect to the sample position. Detectors 2 and 3 are at 90°, and detectors 1 and 4 are placed also at 90° with each other. So, 1/3 and 2/4 are 180° coincidence combinations and 1/4, 2/3 are the 90° coincidence combinations. All the coincidences formed has one BaF_2 detector with dimension 38.1×25.4 mm^2 and another BaF_2 with dimension 50.8×50.8 mm^2. The prompt time resolutions for the BaF_2-BaF_2 detector combination have been found ∼ 634 ps at 511 keV γ-ray energy and ∼ 931 ps for 133-482 keV energy window selection using prompt annihilation gamma rays of ^{22}Na (Figure 3.6). Here, the TAC output and gate from universal coincidence unit for each of the coincidence combination have been fed to the analog to digital converter (ADC-FAST ComTec 7070) directly (Figure 3.3) and the data are collected by a multiparameter data

acquisition system (FAST ComTec).

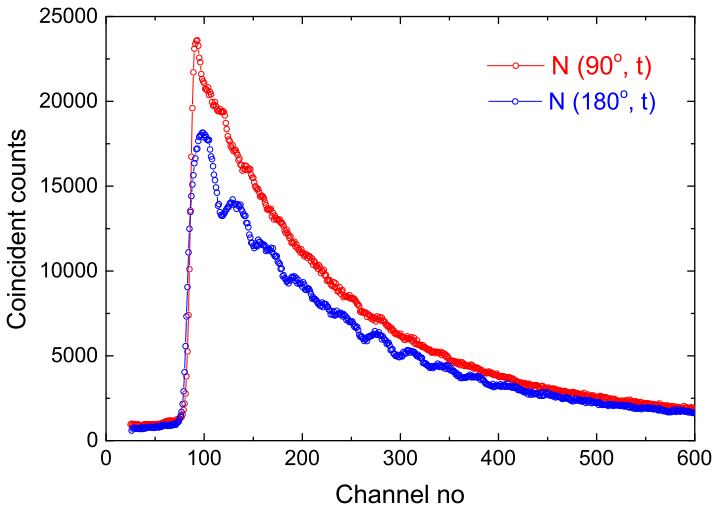

Figure 3.9: Typical coincidence data at 90° and 180° using a $LaBr_3$(Ce)-BaF_2 set up in crystalline $HfF_4{\cdot}3H_2O$. TAC calibration is 0.4 ns/ch.

3.2 Data reduction

We consider a radioactive source with activity N_0 emits coincident gamma rays and the first γ-ray is detected by the detector labeled by i and the second detector labeled by j detects the second γ-ray. The genuine coincidence count rate between these two detectors i and j can be written as [1]

$$N_{ij} = N_0 \epsilon_i \epsilon_j \Omega_i \Omega_j, \tag{3.1}$$

where ϵ_i, Ω_i are the efficiency of the detector designated by i, which detects the γ_1 of the γ-γ cascade and solid angle subtends by the detector at the source position, respectively. Similarly, ϵ_j and Ω_j are the efficiency and solid angle subtended by the detector designated by j at the source position, respectively. The random coincidence counts, arising from the detection of γ_1 and γ_2 in the detectors i and j, respectively,

emitted from different nuclei can be written as

$$N_{ij}^{random} = N_0^2 \epsilon_i \epsilon_j \Omega_i \Omega_j \tau_R, \tag{3.2}$$

where τ_R is the time resolution of the coincidence system. So, the ratio of genuine to random coincidence count rate becomes:

$$\frac{N_{ij}}{N_{ij}^{random}} = \frac{1}{N_0 \tau_R}. \tag{3.3}$$

The γ-γ cascade of the probe nuclei used for PAC measurements passes through an intermediate nuclear energy level of mean-lifetime τ_N. Then, the differential coincidence count rate is expressed as [1, 80]

$$\begin{aligned} N'_{ij}(\theta, t) =& N_{ij}(\theta, t) + N_{ij}^{random}(t) = N_0 \exp(-t/\tau_N) \epsilon_i \epsilon_j \Omega_i \Omega_j W(\theta, t) + N_{ij}^{random}(t); \\ N_{ij} =& N'_{ij} - N_{ij}^{random}, \end{aligned} \tag{3.4}$$

where t is the time difference between the detection of γ_1 and γ_2. The random subtracted coincidence count rate is expressed by N_{ij}. We have used ^{181}Hf probe whose activity was typically 50-100 μCi. The range of all the TACs were set to 100 ns (which is approximately 10 times the lifetime of the intermediate nuclear level of ^{181}Ta) in both the set-ups. In this configuration, the genuine to random coincidence count rate ratio at the peak position ∼50-100. Now, to get rid of the detector efficiencies, solid angles and exponential nuclear decay term, a conventional count rate ratio is formed. In both $LaBr_3$(Ce)-BaF_2 and BaF_2-BaF_2 set-ups, we have formed four coincidence combinations. The count rate ratio can be expressed as [1, 80, 91]

$$R(t) = \frac{2}{3} \left[\sqrt{\frac{N_{13}(180^\circ, t) N_{24}(180^\circ, t)}{N_{14}(90^\circ, t) N_{23}(90^\circ, t)}} - 1 \right]. \tag{3.5}$$

Here, $N_{13}(180°, t)$ is the coincidence count rate for the pair of detectors indicated by 1 and 3 which subtend an angle 180° at the source position and $N_{24}(180°, t)$ is the coincidence count rate for pair of detectors marked by 2 and 4 which subtends the same angle 180° at the source position. Similarly, the $N_{14}(90°, t)$ and $N_{23}(90°, t)$ are the coincidence count rate for 90° detector combinations. Detector efficiencies and the soild angle subtended by the detectors at the source position do not appear in the expression of $R(t)$ as the numerator as well as denominator contain contributions from all the four detectors. A typical coincidence count rate at 90° and 180° have been shown in Figure 3.9. For $A_4 \ll A_2$ (as in the case of ^{181}Hf probe), the angular correlation can be written as

$$W(\theta, t) = 1 + A_2 G_2(t) P(cos\theta). \tag{3.6}$$

The perturbation function $G_2(t)$ is related to $R(t)$ by the following relation [92]:

$$A_2 G_2(t) = \frac{R(t)}{1 + R(t)/2}. \tag{3.7}$$

A detailed description of data reduction in the PAC spectroscopy can be found in the reference [91]. The PAC data have been fitted by the WINFIT software. It is based on χ^2 minimization procedure. In the first step, one has to provide initial guess values of ω_Q, η, δ, S_{2n} and amplitude (f_i) of the corresponding perturbation function. In WINFIT software, the theoretical perturbation functions can be subtracted and the residual of the fitting can be observed. This software also allows to fit the spectrum where nuclear relaxation is observed. A Fourier cosine transform of the perturbation function can be viewed also where, the transition frequencies of the perturbation function are indicated in the Fourier spectrum. For initial guess values of these parameters, a nice review article can be found in the reference [93].

CHAPTER 4

Computational details

Due to enormous advancement of band structure calculations, it has become possible to calculate reliably the electric field gradient (EFG) by full potential linearized augmented plane wave (FP-LAPW) method within the framework of density functional theory (DFT) as implemented in WIEN2k simulation package. A brief overview on the calculation of EFG through density functional theory by WIEN2k code is presented here.

4.1 Density functional theory to solve quantum many body problem

A system of electromagnetically interacting particles consisting of N nuclei and ZN no of electrons in a solid form a many body quantum mechanical problem. The Hamiltonian of this quantum many body system can be written as

$$H = -\frac{\hbar^2}{2}\sum_i \frac{\boldsymbol{\nabla}^2_{\vec{R}_i}}{M_i} - \frac{\hbar^2}{2}\sum_i \frac{\boldsymbol{\nabla}^2_{\vec{r}_i}}{m_e} - \frac{1}{4\pi\epsilon_0}\sum_{i,j}\frac{e^2 Z_i}{|\vec{R}_i - \vec{r}_j|} + \frac{1}{8\pi\epsilon_0}\sum_{\substack{i,j \\ i\neq j}}\frac{e^2}{|\vec{r}_i - \vec{r}_j|} + \frac{1}{8\pi\epsilon_0}\sum_{\substack{i,j \\ i\neq j}}\frac{e^2 Z_i Z_j}{|\vec{R}_i - \vec{R}_j|}, \tag{4.1}$$

where M_i denotes the mass of nuclei at $\vec{R}_i$ and m_e is the mass of the electron at $\vec{r}_i$. The first term denotes the kinetic energy (K.E.) of the nuclei and second term denotes the

K.E. of the electrons. Third term describes the Coulomb interaction between the protons and electrons. Fourth term shows the Coulomb interaction between the electrons. The last term in the above equation shows the Coulomb repulsion between the protons of different nuclei in the system. Born-Oppenheimer approximation [10] states that nuclei are much heavier than the electrons and they hardly move as compared to the electrons. So, nuclei in solid can be thought of as a source of positive charge at fixed positions and the NZ electromagnetically interacting electrons move in the external potential of nuclei. Consequences of the Born-Oppenheimer approximation is that we can drop the K.E. term due to nucleons in the equation 4.1 and the coulomb repulsion term between the nuclei with other nuclei becomes a constant. So the many-body Hamiltonian equation reduces to the following form:

$$\hat{H} = \hat{T} + \hat{V} + \hat{V}_{\text{ext}}, \tag{4.2}$$

where T and V are the kinetic energy (K.E.) and potential energy (P.E.) of electromagnetically interacting electrons and these electrons move in a external potential created by the coulomb repulsion between nuclei and electrons. Although the difficulty in solving the many-body Hamiltonian reduces to a large extent by implementing Born-Oppenheimer approximation, it is still very difficult to solve the Hamiltonian. So, further judicial approximations are needed to solve this Hamiltonian. Density functional theory (DFT) is a very advanced technique in this purpose. The DFT is formally established by the two theorems of Hohenberg and Kohn which are:

Theorem 1: There is one-to-one correspondence between the ground state density ($\rho(\vec{r})$) of a many-electron system and the external potential V_{ext}. An immediate consequence is that the ground-state expectation value of any observable ($\hat{O}$) is a unique functional of the exact ground-state electron density

$$\langle \Psi | \hat{O} | \Psi \rangle = O[\rho]. \tag{4.3}$$

Theorem 2: For $\hat{O}$ being the is the Hamiltonian $\hat{H}$, the ground state total energy functional $H[\rho] \equiv E_{V_{\text{ext}}}[\rho]$ is of the form:

$$\begin{aligned} E_{V_{\text{ext}}}[\rho] =& \langle \Psi | \hat{T} + \hat{V} | \Psi \rangle + \langle \Psi | \hat{V}_{\text{ext}} | \Psi \rangle \\ =& F_{HK}[\rho] + \int \rho(\vec{r}) V_{\text{ext}}(\vec{r}) d\vec{r}, \end{aligned} \tag{4.4}$$

where the Hohenberg-Kohn density functional F_{HK} is universal for any many-electron system. $E_{V_{\text{ext}}}[\rho]$ reaches its minimal value (equal to the ground-state total energy) for ground-state density corresponding to V_{ext}.

Kohn-Sham (KS) expressed the total energy functional in terms K.E and P.E. of non-interacting electrons which are subjected to two external potentials, one due to nuclei and another due to exchange and correlation effects of electrons. The KS equation established DFT as a practical tool to solve the many-electron system

$$\begin{aligned} \hat{H}_{KS} = E_{V_{\text{ext}}}[\rho] =& F_{HK} + V_{\text{ext}}[\rho] \\ =& T_0[\rho] + V_H[\rho] + V_{xc}[\rho] + V_{\text{ext}}[\rho] \\ =& -\frac{\hbar^2}{2m_e} \boldsymbol{\nabla}_m^2 + \frac{e^2}{4\pi\epsilon_0} \int \frac{\rho(\vec{r}') d\vec{r}'}{|\vec{r} - \vec{r}'|} + V_{xc} + V_{\text{ext}}, \end{aligned} \tag{4.5}$$

where $T_0[\rho]$ and $V_H[\rho]$ are the K.E. and P.E. of the non-interacting electron gas, respectively. The term $V_{xc}[\rho]$ is the exchange-correlation potential. Exchange-correlation potential is obtained by taking derivative of the V_{xc} with respect to the ground state electron density

$$\hat{V}_{xc} = \frac{\delta V_{xc}[\rho]}{\delta \rho}. \tag{4.6}$$

The exact ground state density $\rho(\vec{r})$ of N-electron system can be expressed as

$$\rho(\vec{r}) = \sum_{m=1}^{N} \phi_m(\vec{r}) \phi_m^*(\vec{r}). \tag{4.7}$$

Here, $\phi_i(\vec{r})$ are the non-interacting single-particle wavefunction of the Kohn-Sham Hamil-

tonian H_{KS}

$$\hat{H}_{KS}\phi_m(\vec{r}) = \epsilon_m\phi_m(\vec{r}). \tag{4.8}$$

These $\phi_m(\vec{r})$ are not the single electron wavefunction and can be thought of as quasi-particle wavefunction which does not have any physical meaning but, the density corresponding to this ground state wavefunction is equal to the true electron density and single-particle energies ϵ_m are not same as single electron energies. Now, to construct the Hamiltonian, we need to know $V_{xc}[\rho]$ and $V_{\text{ext}}[\rho]$ which can only be constructed only if the electron density $\rho(\vec{r})$, which are being searched for, is known. We are now stuck with a self consistency problem. An iterative procedure is needed to get out of this paradox. If we start with a density ρ_0 and construct the Hamiltonian H_{KS1}, and solve the eigenvalue problem, we will get another density ρ_1. In most cases, ρ_1 will differ from ρ_0 and using ρ_1, we can construct H_{KS2}. In this way, this iterative procedure goes on until the density converges to a final density ρ_f which is consistent with the Hamiltonian.

4.1.1 Exchange-correlation functional

In the Kohn-Sham equation, the exact form of exchange-correlation functional $V_{xc}[\rho]$ is still unknown. Kohn and Sham [94] proposed an approximation called *local density approximation* (LDA) which is widely accepted to define the exchange-correlation functional. Here, the entire space is divided into infinitesimal volume element ($\rho(\vec{r})d\vec{r}$) and the exchange correlation contribution of that infinitesimal volume is obtained by assuming constant homogeneous electron density in that volume, which is same as the density of the original volume. Thus, the exchange-correlation functional can be written as

$$V_{xc}^{LDA}[\rho] = \int \rho(\vec{r})\epsilon_{xc}(\rho(\vec{r}))d\vec{r}, \tag{4.9}$$

where the function $\epsilon_{xc}(\rho)$ (not functional) is the exchange correlation energy of a homogeneous electron gas. For interacting electrons, the total energy can be obtained by

quantum Monte Carlo [10]. Subtracting the non-interacting K.E. and Hatree energy (V_H) from this total energy, the $\epsilon_{xc}(\rho)$ can be obtained numerically. This approximation works very well for many systems. A next step to improve the exchange-correlation functional is to incorporate the spatial variation of density (gradient of density) to define the exchange-correlation functional. This approximation is called *generalized gradient approximation* (GGA) which is parametrized by Perdew-Burke-Ernzerhof (PBE) [95] and can be defined by

$$V_{xc}^{GGA}[\rho] = \int \rho(\vec{r}) F(\rho(\vec{r}), \Delta\rho(\vec{r}))d\vec{r}. \tag{4.10}$$

4.1.2 Solving Kohn-Sham equation numerically

We have to solve the Kohn-Sham equation (equation 4.8) to get the single particle wavefunction ($\phi(\vec{r})$) which gives the ground state electron density $\rho(\vec{r})$ from the equation 4.7. For this purpose, the wavefunction must be expanded in a given basis set ϕ_p^b as

$$\phi_m = \sum_{p=1}^{P} c_p^m \phi_p^b, \tag{4.11}$$

where coefficients c_p^m have to be determined. Now, to get the exact single-particle wavefunction in a function space which has infinite dimension, P should be infinite. For practical purposes, a finite basis set is chosen. So, by substituting the equation 4.11 in equation 4.8, we arrive at the following eigenvalue problem

$$\begin{bmatrix} \cdots & \cdots & \cdots \\ \vdots & \left\langle \phi_i^b \right| \hat{H} \left| \phi_j^b \right\rangle - \epsilon_m \left\langle \phi_i^b | \phi_j^b \right\rangle & \vdots \\ \cdots & \cdots & \cdots \end{bmatrix} \begin{bmatrix} c_1^m \\ \vdots \\ c_P^m \end{bmatrix} = \begin{bmatrix} 0 \\ \vdots \\ 0 \end{bmatrix}. \tag{4.12}$$

Diagonalizing the matrix, we obtain P eigenvalues with P sets of coefficients which describe P eigenfunctions in the given basis. Two thumb rules are there to choose the basis set. One is that the basis set should be efficient i.e. fewer no of basis functions

to describe the eigenfunction which reduces the matrix size. Another is that the basis set should be unbiased i.e. P should not be so small that the approximation enters by this choice of P carries much properties of the basis function to define a approximated eigenfunction.

4.1.3 Basis sets

From Bloch's theorem [96], one can write the wavefunction of any electronic state for a Hamiltonian having the periodicity of the lattice as

$$\psi_{\vec{k}}^{n}(\vec{r}) = \sum_{\vec{K}} c_{\vec{K}}^{n,\vec{k}} e^{i(\vec{k}+\vec{K})\cdot\vec{r}}, \tag{4.13}$$

where $\vec{K}$ is the reciprocal lattice vector, the $\vec{k}$ is the wave vector in the first Brillouin zone and n is the band index [10, 96]. The set of coefficients $c_{\vec{K}}^{n,\vec{k}}$ are to be determined to describe the state. The summation index m in the single-particle Kohn-Sham equation can be thought of as $(n, \vec{k})$ and p stands for $\vec{k} + \vec{K}$. So, by comparing with equation 4.11, basis function can be written as

$$\phi_{\vec{K}}^{\vec{k}}(\vec{r}) = e^{i(\vec{k}+\vec{K})\cdot\vec{r}}. \tag{4.14}$$

All the eigenfunction $\psi_{\vec{k}}^{n}$ with same k but different band index are described by the basis set with that same $\vec{k}$ and the eigenstates with different $\vec{k}$ will be expressed by another basis set with that $\vec{k}$. This process will be repeated for that many $\vec{k}$ values for densely enough sampling of the first Brillouin zone. For practical purposes, we can not work with infinite basis set. For plane wave basis set, this can be done by choosing a sphere of radius K_{max}. Many a time, this K_{max} is expressed in terms of the free electron energy

$$E_{cut} = \frac{\hbar^2 K_{max}^2}{2m_e}. \tag{4.15}$$

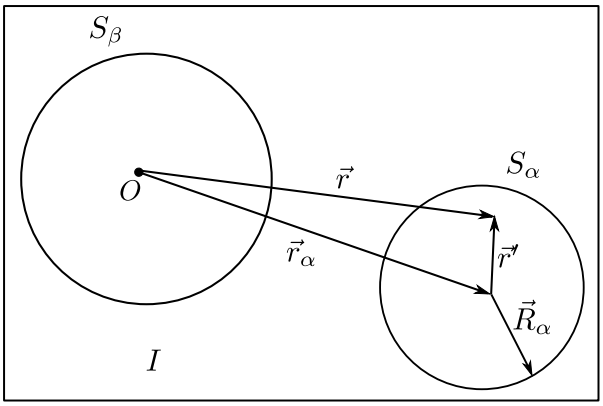

Figure 4.1: Muffin-tin region and interstitial region inside a unit cell. O is the origin of the co-ordinate system [10].

Plane wave (PW) basis set is very simple to work with but the major problem to work with plane wave basis set is that the basis set is not very efficient. The computation time is mainly determined by the time required for matrix diagonalization and the time scales as third power of the dimension of the basis set [10]. A more efficient basis set is Augmented Plane Wave (APW). The basic idea of the APW basis set is: the electrons that are close to the nuclei behave as they are in a free atom which can be more accurately described by the atomic like wavefunction and electrons that are far away from the nucleus, i.e. valance electrons behave as free particles which can be described by plane wave basis set. Surrounding each atom, a sphere is drawn with radius $\vec{R}_\alpha$, called the *muffin-tin (MT) sphere* (S_α) (Figure 4.1). All the MT sphere (S_α, S_β) in a unit cell construct the *MT-region* and the remaining space inside the unit cell is called the *interstitial region* (I). Any point inside the MT-sphere is described with respect to the center of the sphere ($\vec{r}' = \vec{r} - \vec{r}_\alpha$), and the angles θ', ϕ' describe the direction of $\vec{r}'$ in spherical harmonics. The basis set can be written as

$$\phi_{\vec{K}}^{\vec{k}}(\vec{r}, E) = \begin{cases} \frac{1}{\sqrt{V}} e^{i(\vec{k}+\vec{K})\cdot\vec{r}} & \vec{r} \in I \\ \sum_{l,m} A_{lm}^{\alpha,\vec{k}+\vec{K}} u_l^\alpha(r', E) Y_l^m(\hat{r}') & \vec{r} \in S_\alpha. \end{cases} \tag{4.16}$$

Here, $u_l^\alpha(r', E)$ is the solution of the radial part of the Schrödinger equation for atom α, $Y_l^m(\hat{r}')$ is the spherical harmonics and V is the volume of the unit cell. The major drawback of this basis set is that the radial wavefunctions are evaluated at an energy E (=the energy eigenvalue $\epsilon_{\vec{k}}^n$) which is being searched for. A similar kind of wavefunction with a linearization criterion solves this problem. Here, the function $u_l^\alpha(r', E)$ is constructed at some energy E_0 and by Taylor expansion, the function u_l^α at an energy not far away from E_0 is constructed

$$u_l^\alpha(r', \epsilon_{\vec{k}}^n) = u_l^\alpha(r', E_0) + (E_0 - \epsilon_{\vec{k}}^n)\frac{\partial u_l^\alpha(r', E)}{\partial E}\Big|_{E=E_0} + O(E_0 - \epsilon_{\vec{k}}^n)^2. \tag{4.17}$$

But, from this expansion, we get another unknown term $(E_0 - \epsilon_{\vec{k}}^n)$. So, the basis set in linearized augmented plane wave (LAPW) method can be written as

$$\phi_{\vec{K}}^{\vec{k}}(\vec{r}) = \begin{cases} \frac{1}{\sqrt{V}} e^{i(\vec{k}+\vec{K})\cdot\vec{r}} & \vec{r} \in I \\ \sum_{l,m}\left(A_{lm}^{\alpha,\vec{k}+\vec{K}} u_l^\alpha(r', E_0) + B_{lm}^{\alpha,\vec{k}+\vec{K}} \dot{u}_l^\alpha(r', E_0)\right) Y_l^m(\hat{r}') & \vec{r} \in S_\alpha. \end{cases} \tag{4.18}$$

Now, if any orbital of atom α has predominantly d-character, it will be useful to choose the value of E_0 near the center of d-band. It will be beneficial if we choose its value according to the different l-character ($l = 0, 1, 2, 3$) instead of fixing the energy value E_0 for all atoms. So, instead of E_0, we choose a set of E_l^α and the basis set can be written as

$$\phi_{\vec{K}}^{\vec{k}}(\vec{r}) = \begin{cases} \frac{1}{\sqrt{V}} e^{i(\vec{k}+\vec{K})\cdot\vec{r}} & \vec{r} \in I \\ \sum_{l,m}\left(A_{lm}^{\alpha,\vec{k}+\vec{K}} u_l^\alpha(r', E_l^\alpha) + B_{lm}^{\alpha,\vec{k}+\vec{K}} \dot{u}_l^\alpha(r', E_l^\alpha)\right) Y_l^m(\hat{r}') & \vec{r} \in S_\alpha. \end{cases} \tag{4.19}$$

Accuracy of this basis set can be judged by the product $R_{MT}^{min} K_{max}$, where R_{MT}^{min} is the radius of the smallest muffin-tin sphere and K_{max} is the magnitude of the largest reciprocal lattice vector. The typical value of the cut-off parameter $R_{mt}^{min} K_{max}$ ~6 - 9. The coefficients $A_{lm}^{\alpha,\vec{k}+\vec{K}}$ and $B_{lm}^{\alpha,\vec{k}+\vec{K}}$ are determined by the condition that the function

inside the MT-sphere should match with the plane wave in the interstitial region in value and slope at the sphere boundary.

A question arises here that which states should be described by LAPW basis set. The core states are strongly bound to the nucleus and these states do not participate in chemical bonding. Core states are entirely contained within muffin-tin sphere. The valance states which leaks out of the muffin-tin sphere participate in chemical bonding. They are described by LAPW basis sets. Core states are defined by the atomic like wavefunction that are subjected to the potential created by the valance states. Now, the situation may occur when electronic orbitals with different principal quantum number n but same l value both behave as valance states due to hybridization or any other reasons. One of these states has a greater contribution in defining the character of the valance state of that atom, then the state with lower principal quantum number is called semi-core states. But, where to choose the E_l in these type of situations? This dilemma is solved ay adding another type of function called Local Orbitals (LO) to LAPW basis set. The LAPW+LO basis set can be defined as

$$\phi_{lm}^{\alpha,LO}(\vec{r}) = \begin{cases} 0 & \vec{r} \notin S_\alpha \\ \Big(A_{lm}^{\alpha,LO} u_l^\alpha(r', E_{1,l}^\alpha) + B_{lm}^{\alpha,LO} \dot{u}_l^\alpha(r', E_{1,l}^\alpha) + C_{lm}^{\alpha,LO} u_l^\alpha(r', E_{2,l}^\alpha)\Big) Y_l^m(\hat{r}') & \vec{r} \in S_\alpha. \end{cases} \tag{4.20}$$

Local orbitals are defined for a particular l, m and atom α. Local orbitals are not connected to the plane waves in the interstitial region. This basis sets are $\vec{k}$ or $\vec{K}$ independent. The energy $E_{1,l}^\alpha$ is chosen near the center of the valance band and the linearization energy $E_{2,l}^\alpha$ is chosen near the center of the semi-core state. The coefficients $A_{lm}^{\alpha,LO}$, $B_{lm}^{\alpha,LO}$and $C_{lm}^{\alpha,LO}$ are obtained by the normalization condition, zero value and slope of the LO basis set at the sphere boundary. Thus, the LO does not leak out of the MT sphere. Now, if the number of atoms in a unit cell increases, more number of LO have to be added which increases the computational time. This is solved by adding another type of local orbitals (lo) which is different from the previously defined Local Orbitals

(LO) to LAPW basis sets and are called (L)APW+lo basis set:

$$\phi_{lm}^{\alpha,lo}(\vec{r}) = \begin{cases} 0 & \vec{r} \notin S_\alpha \\ \Big(A_{lm}^{\alpha,lo} u_l^\alpha(r', E_{1,l}^\alpha) + B_{lm}^{\alpha,lo} \dot{u}_l^\alpha(r', E_{1,l}^\alpha)\Big) Y_l^m(\hat{r}') & \vec{r} \in S_\alpha. \end{cases} \tag{4.21}$$

The coefficients $A_{lm}^{\alpha,lo}, B_{lm}^{\alpha,lo}$ are obtained by the conditions that the basis set is normalized and local orbitals match in value at the sphere boundary.

The (L)APW method can be extended to full potential where the potential in the interstitial region is no more constant (V_I^0), due to the incorporation of wrapped potential ($\sum_{\vec{K}} V_I^{\vec{K}} e^{i\vec{K}\cdot\vec{r}}$) and spherically symmetric potential inside the MT-sphere as implemented in APW method, is now modified with non-spherical terms inside the MT sphere. The potential in full potential (linearized) augmented plane wave (FP-(L)APW) method can be written as

$$V(\vec{r}) = \begin{cases} \sum_{\vec{K}} V_I^{\vec{K}} e^{i\vec{K}\cdot\vec{r}} & \vec{r} \in I \\ \sum_{lm} V_{lm} Y_l^m(\hat{r}) & \vec{r} \in \text{MT sphere.} \end{cases} \tag{4.22}$$

4.2 Calculation of EFG by WIEN2k

In WIEN2k code [7], calculations are done using full potential (linearized) augmented plane wave (FP-(L)APW) method. Certain orbitals are also treated by Local Orbitals (LO) or local orbitals (lo) which increases the accuracy of calculation at the cost of computational time. The cut-off parameter in limiting the basis function is $R_{MT}^{min} K_{max}$. In this method, as the R_{MT}^{min} increases, the computation becomes faster at the cost of accuracy of calculation. Plane wave basis set is more accurate but demands more computational time. The radii of MT sphere of different atoms in the unit cell should not be too different with one another (within 20%). The number of $\vec{k}$ vectors must be limited as the diagonalization of the Hamiltonian matrix is repeated for every $\vec{k}$ vectors but at the same time, it should be able to densely enough sample the first Brillouin zone.

The calculation of EFG were performed by using the method developed in reference [97] which is implemented in WIEN2k code. All the calculations refer to zero temperature.

Electric field gradient (EFG) is a traceless, symmetric tensor of rank 2 (3×3 matrix) and it is expressed as the second derivative of the electrostatic potential at the nuclear site. Thus, EFG is expressed by five independent components. The EFG in the cartesian coordinate in define by the equation 2.30 as

$$V_{ij} = \frac{\partial^2 \Phi(\vec{r})}{\partial x_i \partial x_j}\Big|_{\vec{r}=0}. \tag{4.23}$$

Coulomb potential is expressed by the following expression

$$V_c = \frac{e^2}{4\pi\epsilon_0} \int \frac{\rho(\vec{r}')}{|\vec{r} - \vec{r}'|} d\vec{r}'. \tag{4.24}$$

This tensor can also be expressed by five angular momentum components in spherical co-ordinate system (i.e. L=2, M=-2,-1,0,1,2). In WIEN2k code, the EFG is expressed in spherical co-ordinates due to the fact that the potential is also evaluated in spherical co-ordinates. The Cartesian components are related to the spherical components by the following relation

$$V_{ij} = \sqrt{\frac{15}{16\pi}} \lim_{r\to 0} \frac{1}{r^2} \cdot \begin{bmatrix} V_{22}(r) - \frac{1}{\sqrt{3}} V_{20}(r) & V_{2,-2}(r) & V_{21}(r) \\ V_{2,-2}(r) & -V_{22}(r) - \frac{1}{\sqrt{3}} V_{20}(r) & V_{2,-1}(r) \\ V_{21}(r) & V_{2,-1} & \frac{2}{\sqrt{3}} V_{20}(r) \end{bmatrix}. \tag{4.25}$$

Now, from earlier discussions on the EFG, we know that the most significant component of EFG in Cartesian coordinate is V_{zz} which is equivalent to V_{20} component in spherical coordinate. The component V_{zz} is expressed by

$$V_{zz} \propto \int \rho(\vec{r}) \frac{Y_2^0}{r^3} d^3r. \tag{4.26}$$

The main contribution in V_{zz} comes from the electrons inside the MT sphere. The density

$\rho(\vec{r})$ can also be expanded in lattice harmonics by the following equation

$$\rho(\vec{r}) = \sum_{LM} \rho_{LM}(\vec{r}) Y_L^M(\hat{r}). \tag{4.27}$$

Now, V_{zz} can be spatially decomposed to two components arising from muffin-tin sphere and interstitial region:

$$\begin{aligned} V_{zz} &\propto \int_{sphere} \sum_{LM} \frac{\rho_{LM}(\vec{r}) Y_L^M Y_2^0}{r^3} d^3r + \int_{interstitial} \frac{\rho(\vec{r}) Y_{20}}{r^3} d^3r \\ &= \int_{sphere} \frac{\rho_{20}(\vec{r})}{r^3} d\vec{r} + interstitial. \end{aligned} \tag{4.28}$$

For metallic samples, the local electronic charge density due to valance and semi-core states dominates. Now, spherical component of the electronic charge density inside the MT sphere $\rho_{LM}(\vec{r})$ is expressed by lattice harmonics as

$$\rho_{LM}(\vec{r}) = \sum_{\epsilon_{\vec{k}}^n < E_F} \sum_{lm} \sum_{l'm'} R_{lm}(\epsilon_{\vec{k}}^n, \vec{r}) R_{l'm'}(\epsilon_{\vec{k}}^n, \vec{r}) G_{Ll'}^{Mmm'}, \tag{4.29}$$

where R_{lm} is the radial function of non-core electronic states and are restricted by the condition $\epsilon_{\vec{k}}^n < E_F$, E_F is the Fermi energy. The G is the Gaunt number which is basically an integral over the product of spherical harmonics. Now, for $L = 2$ and $M = 0$, the terms with $l = l' = 1$ (p-p) and $l = l' = 2$ (d-d) give non-zero Gaunt numbers although a minor contribution can be found for $l = 0, l' = 2$ (s-d) and $l = 1, l' = 3$ (p-f). So, V_{zz} can can be decomposed to different sets of orbital quantum numbers as

$$\begin{aligned} V_{zz} &= V_{zz}^{pp} + V_{zz}^{dd} + ... + Interstitial \\ V_{zz}^{pp} &= \left\langle \frac{1}{r^3} \right\rangle_p \left[\frac{1}{2}(p_x + p_y) - p_z \right] \\ V_{zz}^{dd} &= \left\langle \frac{1}{r^3} \right\rangle_d \left[d_{xy} + d_{x^2-y^2} - \frac{1}{2}(d_{xz} + d_{yz}) - d_{z^2} \right]. \end{aligned} \tag{4.30}$$

Thus, the EFG is found to be proportional to the differences of orbital occupancies. Now, all the occupancies are same for cubic crystals which gives V_{zz}=0 and crystals which have

axial symmetry (hexagonal, tetragonal) give p_x=p_y.

For calculation of EFG, a supercell appraoch is most commonly used. The probe atom resides at the center of the supercell which is large enough to allow significant relaxation [94]. A detailed description of calculation of EFG can be found in the reference [98]. The combination of PAC measurements and DFT calculations can be very useful for the microscopic investigation of materials. The preferential site occupation of the probe atoms in the investigated material can be identified by comparing the measured EFG value from PAC with the calculated one using WIEN2k code.

CHAPTER 5

PAC results and ab-initio calculations

PAC measurements have been carried out on mainly two types of samples a) chemical samples (Zr/Hf-RbF-HF) b) intermetallic samples (Zr/Hf-Ni). Ab-initio calculations have been carried out for the intermetallic binary alloys by WIEN2k code to compare the calculated values of EFG with the PAC results. Structural properties of Hf metal with nominal amount of Zr impurity has been studied by PAC technique to test our PAC set up as Hf metal was studied earlier by many authors.

5.1 Studies on hafnium metal with a few at% zirconium

5.1.1 Introduction

Previous studies in Hf and Zr metals by perturbed angular correlation (PAC) [99] produced results which are not yet fully resolved. These studies were performed mostly with few at% impurities and produced non-zero values of asymmetry parameter as well as damping in the PAC spectra. The metals Hf and Zr have very similar chemical and structural properties and it is very difficult to separate completely one from the other. The crystal structures of Hf and Zr are hexagonal close-packed (hcp) with axial symmetry. Hf metal has lattice constants a=320.0 pm, c=506.2 pm (c/a=1.582) and for Zr, the lattice constants are a=323.1 pm, c=514.8 pm (c/a=1.59). The ideal packing ratio c/a is 1.633. The PAC spectra in Hf and Zr metals are, therefore, expected to produce an asymmetry parameter η=0. Rasera et al. [100], studied both Hf and Zr for different impurity concentration and concluded that non-zero values of η in these metals arise due to presence of Zr or Hf impurities. In a pure Zr metal (Hf concentration 390 ppm), these authors [100] found an almost undamped PAC spectrum with a value of $\eta \sim 0$. It was shown that the asymmetry parameter and damping of the spectrum increased with increase in impurity concentration. These authors also showed that PAC spectra in these metals with few at% impurities produced two frequency components. A fraction appeared due to all similar atoms surrounding the probe as nearest neighbor (NN) giving $\eta \sim 0$, $\delta \sim 0$ and found another fraction due to the formation of probe-impurity pair by attracting one Zr impurity atom to the probe producing non-zero value of η.

In the previous studies with few at% impurities [100], the pure component fraction observed for a particular impurity concentration was found to be significantly lower than the statistical model calculation. For an impurity concentration of only 1.1 at%,

the pure hcp fraction was found to be significantly low (∼65%) and it is difficult to understand that this low impurity concentration influences the pure hcp fraction to such a large extent whereas from statistical model calculation, this fraction was predicted to be 88%. The experimentally observed fractions for pure hcp were found to be lower than statistical model calculations for all values of impurity concentrations [100]. Also, the behaviors of component fractions with temperature for pure hcp and probe-impurity pair were not studied in earlier investigations [100]. Only, the behavior of the two fractions with impurity concentration was studied. In a Zr metal, however, the evolution of the pure hcp fraction with temperature for a particular Hf impurity concentration was reported recently [101]. At room temperature, the major fraction was found to be produced due to probe-impurity interaction and only ∼16% was due to the pure hcp fraction [101]. Interestingly, the pure fraction was found to increase with temperature and this fraction enhanced to ∼ 55% at a temperature of 773 K. For an ultrapure metal, on the other hand, no component due to the probe-impurity fraction was found. From our recent measurement in an ultrapure Hf metal with 110 ppm Zr [102], only the pure component fraction was found. The corresponding PAC spectrum was found to be undamped up to 110 ns and produced a value of $\eta \sim 0.048(2)$. Considering above facts, it is worthwhile to reinvestigate the temperature dependent PAC measurements in Hf metal with a few at% Zr impurity, particularly, i) to find the pure hcp and 1 NN Zr impurity fractions more accurately at room temperature in order to compare with the statistical model calculation and ii) to determine the behavior of these two component fractions with temperature by using a four detector $LaBr_3$(Ce)-BaF_2 set up. The $LaBr_3$(Ce) detector has the best energy resolution (∼ 4% at 662 keV γ-ray) among the inorganic scintillators [103] due to its very high light output and also produces a sub nanosecond time resolution, comparable to that of a BaF_2 detector [104].

It is known that a very small impurity concentration drastically changes the properties of metals and alloys, and therefore, the microscopic investigation of the impurity interaction may be of practical interest. Studies by hyperfine interaction give direct

information on the local environment of the investigated impurity. In a metal with a definite crystal structure, an impurity destroys the crystalline symmetry and gives rise to an electric field gradient (EFG) which interacts with the nuclear quadrupole moment of the probe atom. The EFG depends on the probe-impurity distance. If the interaction between the probe and impurity atoms favors their specific configuration in the lattice, the EFG corresponding to a given probe-impurity distance can be measured and a fraction of probes experiencing this EFG can also be determined. In particular, a number of the nearest neighbor probe-impurity pairs indicate directly the attractive or repulsive character of the impurity interaction.

In our previous report [101] in Zr metal with a few at% Hf, the number of probe-impurity pairs was studied with variation of temperature. From the temperature dependent behavior of probe-impurity fraction, values of binding energy for the probe-impurity pair and its formation entropy was determined using the Arrhenius relation described by Hrynkiewicz et al. [105]. Following our previous studies in Zr metal with a small Hf impurity, present studies in Hf metal with a few at% Zr have been carried out to determine the probe-impurity fraction and its variation with temperature. It is also aimed to relate the temperature dependent behaviors of the probe-impurity and pure hcp fractions with the Arrhenius relation [105]. This can be used to determine the entropy of formation and binding energy for the probe-impurity interaction in Hf metal similar to that used in Zr metal [101].

5.1.2 Sample preparation

For perturbed angular correlation measurements, the probe ^{181}Hf present in the sample has been used. A natural Hf wire with ∼3 wt% Zr (6 at%)), procured from Alfa Aesar, was used for the present measurements. This was activated to ^{181}Hf by thermal neutron capture (flux $\sim 10^{13}/\text{cm}^2/\text{sec}$) for 7 days in the Dhruba reactor, Mumbai. The natural Hf sample used here contains ^{180}Hf ($\sim$ 30%) having a thermal neutron capture cross section

of 14 b. The four detector $LaBr_3$-BaF_2 PAC spectrometer has been used to acquire four coincidence spectra at a time (two at 180° and two at 90°). PAC measurements at 373 K and above have been carried out using a resistive furnace placed at the centre of the detectors. For high temperature measurements, the sample was sealed in an evacuated quartz tube. For measurement at 77 K, the sample was immersed in a liquid nitrogen bath.

5.1.3 Results

The TDPAC spectrum at room temperature in present Hf sample is shown in Figure 5.1. The spectrum is analyzed by considering free S_{2n} coefficients (equation 2.74) as the sample is found to have texture effects and it does not behave as a perfect polycrystalline sample. A best fit to the PAC spectrum (up to 60 ns) at room temperature with good statistics actually produces five frequency components. In this case, component 2 with a site fraction of (f) ∼33% gives values of quadrupole frequency ω_Q=46.8(2) Mrad/s, asymmetry parameter η=0 and frequency distribution width δ=0. This can be compared with component 1 (∼ 33%) which gives values of ω_Q=51.6(3) Mrad/s, η=0.20(5) and δ=0. The component 2 can be identified as the fraction arising from a pure hcp configuration and the component 1 as due to the configuration of 11 nearest neighbor Hf plus one Zr impurity surrounding the probe atom. These assignments are due to the fact that the component 2 produces a somewhat lower value of quadrupole frequency compared to component 1 and it gives an axially symmetric EFG (η=0) while the component 1 produces a non zero value of η and a slightly higher value of ω_Q. The values of quadrupole frequencies for these two components are in good agreement with the earlier reported results [100]. However, in the present case, both pure hcp and Zr impurity frequency components produce no damping ($\delta \sim 0$) at room temperature. A comparatively higher value of quadrupole frequency for the configuration with one nearest neighbor Zr surrounding the probe compared to the pure configuration was found

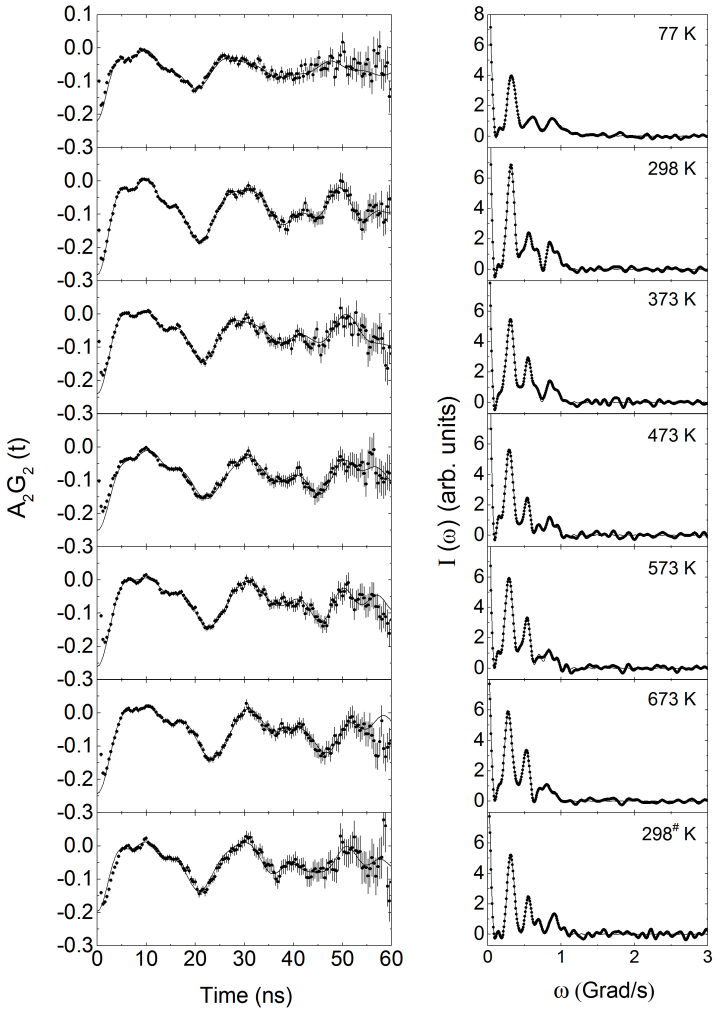

Figure 5.1: TDPAC spectra in Hf metal at different temperature during initial heating up to 673 K. Left panel shows the time spectra and the right panel shows the corresponding Fourier cosine transforms. The PAC spectrum at room temperature designated by 298$^{\#}$ K is taken after the measurement at 673 K.

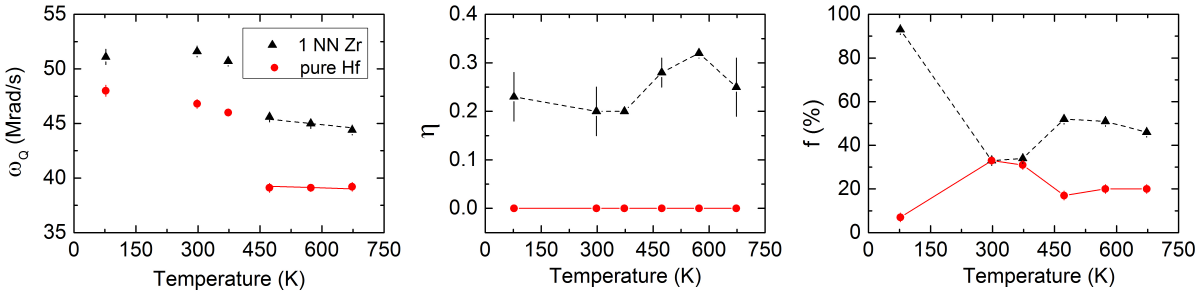

Figure 5.2: Variations of ω_Q, η and site fractions (f) with temperature during initial heating up to 673 K for the pure hcp and the Zr impurity component.

from previous studies [100] also. At room temperature, the site fractions for both pure hcp and probe-impurity were found to be the same. These results may change with Zr impurity concentration. However, apart from these two components, a third component fraction (∼15%) was found which probably arises due to trapping of oxygen in the interstitial site because of strong affinity of hafnium for oxygen [106]. Components 4 and 5 with site fractions 14 and 5%, respectively, are probably due to some other trapping of defects. Since, after neutron irradiation, no thermal treatment at high temperature was done in the sample, these defects probably arise due to irradiation effects. Component 4 producing values of ω_Q=56.4(4) Mrad/s, η=0 was also found in ultrapure Hf metal [102].

At 373 K, all five components are found to be present and no appreciable change of results are found at this temperature. However, at 473 K, a drastic change of results is found where the site fraction for the impurity fraction is enhanced abruptly to $\sim$ 50% and the pure fraction reduces to ∼17% (Figure 5.2). Component 4 with $\omega_Q \sim$ 56 Mrad/s, η=0 was not found at 473 K which probably indicates a defect nature of this component. But interestingly, it is found that quadrupole frequencies for both pure hcp and Zr impurity components decrease abruptly from the values at 373 K (Figure 5.2). This indicates that a microstructural change has occurred at 473 K. PAC measurements at 573 and 673 K have also been performed. It is found that above 473 K, the quadrupole frequencies for these two components decrease slowly and almost linearly with temperature (Figure 5.2). The asymmetry parameter for the impurity component, on the other hand, shows an increasing tendency with temperature. The site fractions for the pure and Zr impurity component do not change appreciably (Figure 5.2) in the temperature range 473-673 K. After measurement at 673 K, a re measurement at 298 K has been performed to find the reversibility of the results. This time we have found four components. The first two components give values of ω_Q which are almost identical to those found in the pristine sample. Interestingly, in this case, both the pure and Zr impurity components produce η=0, δ=0 while before heating the sample it produced η=0.20 for the impurity component. A re measurement at 373 K also produces η=0 for the impurity component.

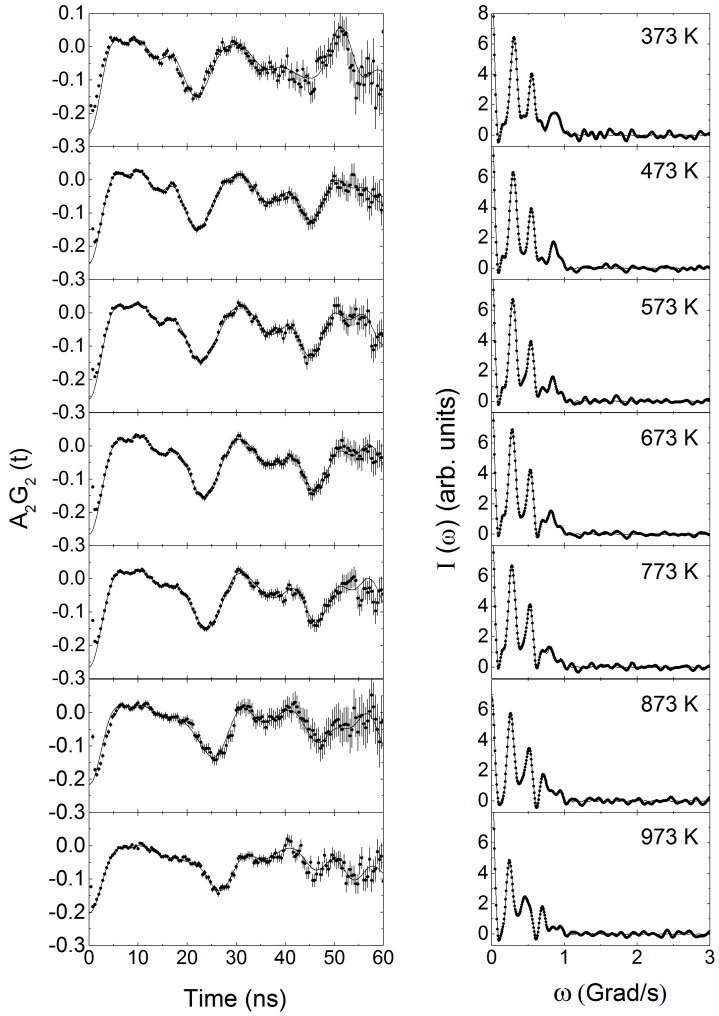

Figure 5.3: TDPAC spectrum in Hf metal re-measured at room temperature and then up to 973 K after the sample is measured at 298$^{\#}$ K. The Fourier cosine transform is shown in the right panel.

These results indicate that a Zr impurity atom in the Hf lattice does not break the axial symmetry, in general, and the axial asymmetry in case of 1 NN Zr impurity depends on the thermal history of the sample and also on temperature. At higher temperature, it always produces an asymmetry of the EFG. When the sample is re measured at 298 K, the component with ω_Q=57 Mrad/s re appears but, the component with ω_Q=35 Mrad/s is not found any more. This indicates that this is also probably a defect component. However, the component fractions for the impurity and pure hcp fractions are found to be completely reversible.

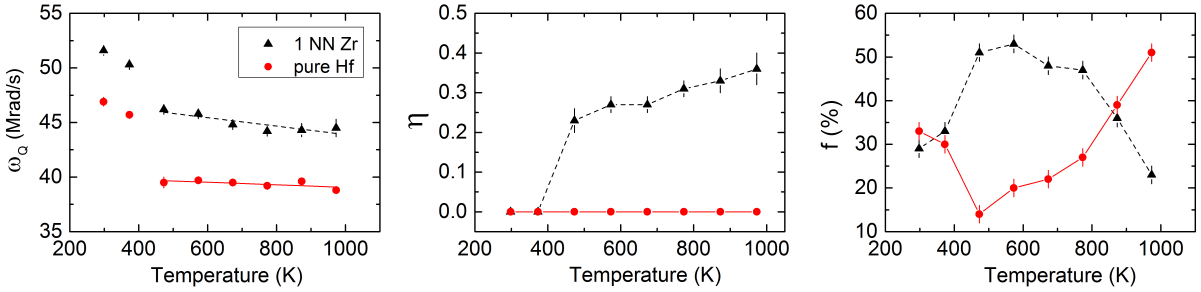

Figure 5.4: Variations of ω_Q, η and site fractions (f) with temperature for re measurements (298 to 673 K) and new measurements up to 973 K.

Table 5.1: Calculated probabilities (p) of pure component fraction for finding no dissimilar atom in the nearest neighbor to the probe

At% Zr	p(%)
1.1	88
1.5	85
2.0	81
3.0	75
4.0	70
6.0	65
8.0	63

At 77 K, the PAC spectrum (Figure 5.1) gives two frequency components only. These can be identified as the probe-impurity fraction (∼93%) and pure hcp fraction (∼7%). But, in this case, the impurity fraction produces a large damping (δ ∼10%). Three other components which do not appear at 77 K can indeed be attributed to defects. The frequency distribution width for the impurity fraction, probably, increases as a manifestation of the irregular defect components not observed at 77 K but, were found at 298 K.

After initial measurements, re measurements up to 673 K and new measurements up to 973 K in the same sample have been performed at an interval of 100 K (Figure 5.3). By comparing with the results of initial measurements, most of the results are found to be repeated, particularly, for the pure hcp and the Zr impurity component. Here also, it is found that at 473 K, the sample produces an abrupt change in microstructural configuration. At this temperature, the impurity fraction increases abruptly to ∼51%

and the pure hcp fraction is reduced to ∼14%. The fractional behaviors of these two components up to 973 K are shown in Figure 5.4. It is found that the pure fraction increases with temperature and reaches its maximum value (51%) at 973 K where the Zr impurity fraction reduces to ∼23%. The asymmetry parameter for the impurity component clearly increases with temperature (Figure 5.4). The values of quadrupole frequencies for the pure and Zr impurity components again show abrupt discontinuities at 473 K and then vary slowly with temperature. The component with ω_Q=57 Mrad/s (component 4) is not found at 673 K and above. For component 5, the quadrupole frequency is found to change its value suddenly at 473 K from the value found at 373 K and this component does not appear at 873 and 973 K. Detailed results of temperature dependent PAC measurements in this sample can be found in the reference [21].

Electric field gradient (V_{zz}) or the electric quadrupole frequency (ω_Q) in non-cubic metals generally decreases with temperature following T or $T^{3/2}$ temperature dependent relationship [1, 107, 108]. The thermal expansion can not be solely accounted for this temperature dependence. Although the reason behind the temperature dependence is not very well established in literature, it can be qualitatively said that the major contribution of the EFG or ω_Q originates from lattice vibration:

$$V_{zz}(T) = V_{zz}(0)[1 - A \cdot \langle u^2 \rangle]. \tag{5.1}$$

Here, $\langle u^2 \rangle$ is the means square atomic displacement. In the Debye model, the lattice vibration is measured in terms of means square atomic displacement $\langle u^2 \rangle$ which has T^2 temperature dependence for $T \ll T_D$ (T_D: Debye temperature) and linear temperature dependence for $T \gg T_D$ [1]. This approximately leads to $T^{3/2}$ temperature dependence of means square atomic displacement. Thus, $T^{3/2}$ temperature dependence of EFG stems out from the $T^{3/2}$ temperature dependence of the lattice vibration. In the present study, the quadrupole frequency for both pure Hf and Hf+1 NN Zr components showed a drastic change at 473 K. So, only ω_Q in the temperature range 473-973 K has been fitted for

both pure and impure components by

$$\omega_Q(T) = \omega_Q(0)(1 - \alpha T). \tag{5.2}$$

where $\omega_Q(0)$ is the extrapolated value of $\omega_Q(T)$ at 0 K. The results for $\omega_Q(0)$ and α are found to be 47.8(8) Mrad/s and $0.8(4)\times10^{-4}$/K respectively for the Zr impurity component and for the pure component, these are found to be $\omega_Q(0)$=40.2(5) Mrad/s and α=$0.3(2)\times10^{-4}$/K. In the lower temperature region (77-473 K), the values of $\omega_Q(T)$ (Figure 5.2) will give different results for $\omega_Q(0)$ and in this region, probably, the temperature dependent behaviors of ω_Q will be different. Data in this low temperature region are not fitted due to insufficient data points.

5.1.4 Discussion

In our Hf metal sample, the Zr impurity was quoted to be nominal 3%. For a particular Zr impurity concentration, the probability that the probe has twelve nearest Hf neighbor can be calculated from Poisson statistical consideration. This probability will be increased with lowering of impurity concentration. For different impurity concentrations, the probability of pure hcp fraction is shown in Table 5.1. For the present sample of nominal 3 wt% (6 at%) Zr impurity concentration, the probability that the probe has all the twelve nearest neighbor Hf is ∼65% and the probability of the probe atom being surrounded by 11 NN Hf + 1NN Zr atom (probe impurity component) is ∼35%. From two independent measurements, we have obtained a fraction of 33% at room temperature as the pure component fraction where the probe atom has no dissimilar atoms in its nearest neighbor and a site fraction of ∼33% for the probe impurity (1NN Zr) component. Thus, the probe-impurity fraction (∼33%) at room temperature agrees well with Poisson's statistical calculation (∼35%). Above 373 K, the pure fraction increases with temperature ∼50% at 973 K. This site percentage is very close to the value found from statistical consideration (∼65%). However, the pure site percentage fraction shows

an increasing trend with temperature (Figure 5.4).

For a particular impurity concentration, the probe-impurity fraction in thermal equilibrium can be described following the thermodynamical consideration described by Hrynkiewicz et al. [105]. It was found that in thermal equilibrium at a temperature T, the ratio $f^i/f^p c^i$ follows the Arrhenius behavior and is given by

$$\frac{f^i}{f^p c^i} = \beta \cdot exp(-B'/kT), \tag{5.3}$$

where f^i is the no. of probe-impurity fraction, f^p is the fraction where probe nuclei have no impurity at the nearest neighbor sites and c^i is the atomic impurity concentration. Here, β is the entropy factor and is given by

$$\beta = z \cdot exp(\Delta S/k); \tag{5.4}$$

z being the coordination number of the lattice (for the fcc and hcp lattices, z=12) and ΔS is the difference in the vibrational entropies for the impurity pair and for the isolated impurity atoms. Thus, the ratio $f^i/f^p c^i$ is the ratio of the concentration of the Ta probe bound with one Zr impurity to the concentration of Ta atoms surrounded by the host Hf atoms multiplied by the impurity concentration. The binding energy for the probe-impurity pair B is given by B=-B'. From present measurements in the temperature range 298-973 K, the ratio f^i/f^p is determined as described in reference [105]. It is found that the Arrhenius behavior for $f^i/f^p c^i$ is valid in the intermediate temperature region (473-773 K). In the temperature range 773-973 K, this ratio gives a change in slope and the same exponential behavior is not valid in this region. In the low temperature region (below 473 K) also, the results show deviation from the Arrhenius relation. The deviation at low temperature is expected considering the fact that the sample must be kept at a minimum temperature to allow the diffusing impurity atoms be trapped into pairs. This imposes a lower limit of the Arrhenius behavior. For Hf metal, this

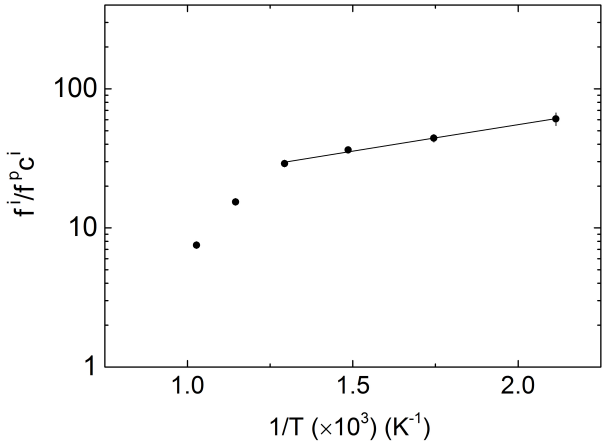

Figure 5.5: Logarithmic plot of the ratio of the probe-impurity fraction (f^i) to the product of pure hcp fraction (f^p) and impurity concentration (c^i) with temperature.

temperature is 473 K. There is a high temperature limit also which is set by the lifetime of the intermediate state of the probe nucleus. The lifetime of the pairs created can not be shorter than that lifetime. In Hf metal, the upper temperature limit for Arrhenius behavior is found to be 773 K.

Employing the Arrhenius relation, values of entropy formation factor and binding energy for the probe-impurity pair are determined and values of β=9.6(7) and B'=-0.075(4) eV are obtained from the results in the temperature range 473-777 K. The binding energy for the probe-impurity pair is thus found to be B=0.075(4) eV. These values of B and β in dilute Hf alloy with Zr impurity are comparable to the values found in other dilute alloys of Cu, Ag and Au with Pt impurity [105].

5.1.5 Conclusion

As shown in this work, Hf metal with a few at% Zr, produces five frequency components and a two component model found earlier [100] can be used to describe the microstructural configuration of this metal. It is found that Hf metal ($\sim$ 3 wt% Zr) produces both 11 NN Hf plus 1 NN Zr atom and pure 12 NN Hf with distinct values of quadrupole frequencies. The site fractions for these two types of configurations depend strongly on

temperature. At 77 K, the impurity fraction is found to be maximum (∼93%) but, it reduces to 33% at room temperature, increases to ∼53% at 573 K and then decreases again steadily with temperature. On the other hand, the pure 12 NN Hf fraction exhibits its minimum site fraction (∼7%) at 77 K. It increases to ∼33% at room temperature and then decreases to ∼14% at 473 K. But, above this temperature, the pure fraction increases steadily with temperature. In fact, the temperature dependent variations for both these site fractions show somewhat irregular behavior (Figure 5.4). A drastic change in microstructural configuration has been found at 473 K where the quadrupole frequencies for both these fractions show abrupt changes along with abrupt changes of site fractions. This interesting behavior of Hf metal at a particular temperature is observed in this report only. For the first time, to the best of our knowledge, the temperature dependent behaviors of quadrupole frequencies in a metal show clear discontinuities at a particular temperature and it is found that the values of ω_Q at different temperatures in the range 77-973 K can not be fitted by a linear T or $T^{3/2}$ relationship in this whole temperature range. From 473 K and above, however, the results show linear T dependence. It is found that the ratio $f^i/f^p c^i$ does not show the same Arrhenius behavior in the whole temperature region 77-973 K. There is a deviation above 773 K and it is found that Arrhenius behavior is not valid in the low temperature region (below 473 K). It is observed also that above 773 K, the pure 12 NN Hf fraction increases with temperature instead of showing a limiting value. It seems that at high enough temperature (above 973 K), the entire site fraction will be the pure hcp and is just opposite to what is found at very low temperature (77 K) where the major sites (∼93%) are found to be the Zr impurity. It is shown that asymmetry parameter for both Zr impurity and pure fraction can show the highest symmetry (η=0). While the pure fraction always exhibits a value of η=0, the asymmetry parameter for the impurity component depends on temperature. Our results and analysis indicate that the parameter η, particularly for the impurity fraction, depends on thermal history of the sample and it is not generally true that Zr impurity atom breaks the crystal symmetry. The three defect components found at different

temperatures are characterized also by PAC.

From present measurements at different temperature, entropy of formation and binding energy for the probe-impurity pair have been determined following the Arrhenius behavior described by Hrynkiewicz et al. [105]. These are found to be quite reasonable by comparing with earlier reported values in some other dilute alloys.

5.2 Crystal structure properties of hafnium and zirconium tetrafluoride trihydrates

5.2.1 Introduction

The compounds of hafnium and zirconium with identical chemical compositions are expected to produce the same crystal structure due to very similar chemical properties of Hf and Zr and their identical crystal structures. It was found also that all compounds of hafnium and zirconium with same chemical compositions produce the same crystal structures. The only exception was in the case of hafnium tetrafluoride trihydrate and its analogue zirconium tetrafluoride trihydrate. In all other hafnium and zirconium compounds, similar values of quadrupole frequencies and asymmetry parameters were reported [109] from time-differential perturbed angular correlation (TDPAC) measurements which indicated their isostructural crystalline properties. Considering the compounds of hafnium and zirconium tetrafluoride trihydrates, a monoclinic polymeric structure was found for $HfF_4{\cdot}3H_2O$ [110]. On the other hand, the crystal structure of $ZrF_4{\cdot}3H_2O$ [111] was found to be triclinic and is formed from discrete dimeric $Zr_2F_8(H_2O)_6$ groups in which the Zr atoms share the $F\cdots F$ common edge. In the polymeric structure of $HfF_4{\cdot}3H_2O$, one of the H_2O molecules is not directly linked to the central Hf atom but is located between the chains [3]. The different crystal structure properties of these two trihydrate compounds of Hf and Zr are not understood and, therefore, it is of high interest to resolve the structure of these compounds. Considering this fact, further studies in the two trihydrate compounds of hafnium and zirconium are worth spending. In this respect, TDPAC studies are useful where the electric field gradient (EFG) at the ^{181}Hf probe nuclear site can be determined with sufficient accuracies. The crystal structure environment surrounding the probe atom generates an EFG at the probe nuclear site if the crystal structure has a non-cubic symmetry. For a cubic symmetry, it produces zero

EFG. Now, for the compounds of Hf and Zr, if nearly same values of EFG are produced at the probe site it indicates that these have same crystal structure environment. Thus, by comparing the TDPAC results, the iso-structurality of the two compounds of Hf and Zr can be checked easily. Also, TDPAC is a sensitive technique to find any small EFG and very much helpful to determine the crystal structure with sufficient accuracy. Study of temperature dependence of EFG in a material is an excellent tool to determine the electron density that depends on chemical composition of materials.

The X-ray diffraction (XRD) method can also be employed for the crystal structure information quite accurately. XRD measurements in the hafnium tetrafluoride compounds were done earlier by Rickard and Waters [112]. From their measurements it was found that neither $HfF_4{\cdot}3H_2O$ nor $HfF_4{\cdot}H_2O$ are isostructural with the analogous zirconium compounds. But, from recent XRD studies [3], a monoclinic modification of $ZrF_4{\cdot}3H_2O$ (β-$ZrF_4{\cdot}3H_2O$) is reported and it is shown that this monoclinic form of $ZrF_4{\cdot}3H_2O$ gives identical crystal structure parameters to that found in monoclinic $HfF_4{\cdot}3H_2O$.

Previous TDPAC measurements [113–115] in these two Zr and Hf compounds reported widely different values of quadrupole frequency and asymmetry parameter. The compound $HfF_4{\cdot}3H_2O$ produced values of ω_Q=203 Mrad/s, η=0.35 [113] and these correspond to the monoclinic crystal structure (β-$HfF_4{\cdot}3H_2O$). The compound $ZrF_4{\cdot}3H_2O$, on the other hand, produced values of quadrupole frequency ω_Q ~183 Mrad/s and asymmetry parameter η ~0.83 [114, 115] and these were attributed to the triclinic crystal structure (α-$ZrF_4{\cdot}3H_2O$). Therefore, previous results from TDPAC clearly indicate that $ZrF_4{\cdot}3H_2O$ and $HfF_4{\cdot}3H_2O$ have different crystal structures. In $ZrF_4{\cdot}3H_2O$, no signal corresponding to its monoclinic structure was observed from earlier PAC measurements [114, 115]. The XRD results by Davidovich et al. [3], however, indicate that both $ZrF_4{\cdot}3H_2O$ and $HfF_4{\cdot}3H_2O$ can have monoclinic structures and they really do not have different crystal structures as reported earlier. But, to the best of our knowledge, there is no report of triclinic structure in $HfF_4{\cdot}3H_2O$ (α-$HfF_4{\cdot}3H_2O$). Since, finding the tri-

clinic structure of $HfF_4{\cdot}3H_2O$, if any, is of great importance to resolve the structures of $HfF_4{\cdot}3H_2O$ and $ZrF_4{\cdot}3H_2O$, we have performed detailed TDPAC measurements in both these compounds. If the triclinic modification of $HfF_4{\cdot}3H_2O$ is also found, the isostructurality of these two tetrafluoride trihydrates like other Hf and Zr compounds will be confirmed.

Apart from structural importance of $HfF_4{\cdot}3H_2O$ and $ZrF_4{\cdot}3H_2O$, the anhydrous HfF_4 and ZrF_4 are shown to be optical coating materials [4] with excellent and stable transmission properties over the infrared region. It is, therefore, interesting to study the dehydration properties of these trihydrate materials with temperature and to check the stability of HfF_4 and ZrF_4 at room temperature. The temperature dependent PAC measurements are useful to find any structural phase transition or any chemical change in the sample with temperature.

5.2.2 Sample preparation

The samples $ZrF_4{\cdot}3H_2O$ and $HfF_4{\cdot}3H_2O$ have been synthesized chemically. For the preparation of tetrafluoride zirconium compound, few milligrams of Zr (with ∼5% Hf) procured from Alfa Aesar is dissolved in hydrofluoric acid, HF (40%) to form a clear solution. A tiny drop of active Hf metal (^{181}Hf) in HF is added to this solution and it is slowly dried at room temperature (∼25^{o}C). Similarly, for the preparation of hafnium tetrafluoride trihydrate compound, a small piece of wire (∼5 mg) of natural Hf metal (with 3-5% Zr) is dissolved in concentrated HF. A very small quantity of active solution of ^{181}Hf in HF is added to it. This solution is dried slowly at room temperature till the solid crystal is formed. The Hf metal was activated in a similar manner as described in section 5.1.2. For measurements at different temperatures in the range 308-333 K, a close cycle refrigerating unit made of Julabo, Germany has been used in flowing mode. This system produces a temperature stability of better than ±1°C. The sample taken in a plastic vial was put in close contact with the flowing liquid, through a copper tube segment. Water

was used as circulating liquid for measurements above room temperature.

5.2.3 Results and discussion

5.2.3.1 $HfF_4 \cdot 3H_2O$

The TDPAC measurement in the dried sample of Hf metal in concentrated hydrofluoric acid, HF at room temperature is carried out to look into the crystallized components. The PAC spectrum at room temperature (Figure 5.6) shows an almost undamped periodic structure up to 50 ns which indicates a good crystalline nature of the sample. A fitting to the spectrum gives two quadrupole interaction frequency components. The dominant component (∼80%) produces values of quadrupole frequency ω_Q=183.2(2) Mrad/s, asymmetry parameter η=0.843(2) with a frequency distribution width δ=0.9(1)%. For the minor component (∼20%), the values are found to be ω_Q=203.7(8) Mrad/s, η=0.377(8) and δ=1.0(4)%. The values found for the minor component can be compared with the previously reported values in $HfF_4 \cdot 3H_2O$ [113]. Similar values found for the minor component in the present sample and those in $HfF_4 \cdot 3H_2O$ reported earlier [113] (ω_Q=203 Mrad/s, η=0.37) indicates that the present sample is hafnium tetrafluoride trihydrate. In the earlier work [113], only monoclinic component of $HfF_4 \cdot 3H_2O$ was observed. In our measurements, we have found two frequency components. One component gives similar PAC parameters to those reported earlier for the monoclinic component. The appearance of the predominant component in present sample is interesting and this provides an important information. The values of ω_Q and η for this component fraction in $HfF_4 \cdot 3H_2O$ are found to be similar to the values found in $ZrF_4 \cdot 3H_2O$ which has a triclinic structure. For the compound $ZrF_4 \cdot 3H_2O$, values of ω_Q=183 Mrad/s, η=0.83 were reported [114] and these were supported from our recent measurement [115] also. The predominant component of $HfF_4 \cdot 3H_2O$ in present sample, therefore, corresponds to the triclinic structure and the minor component corresponds

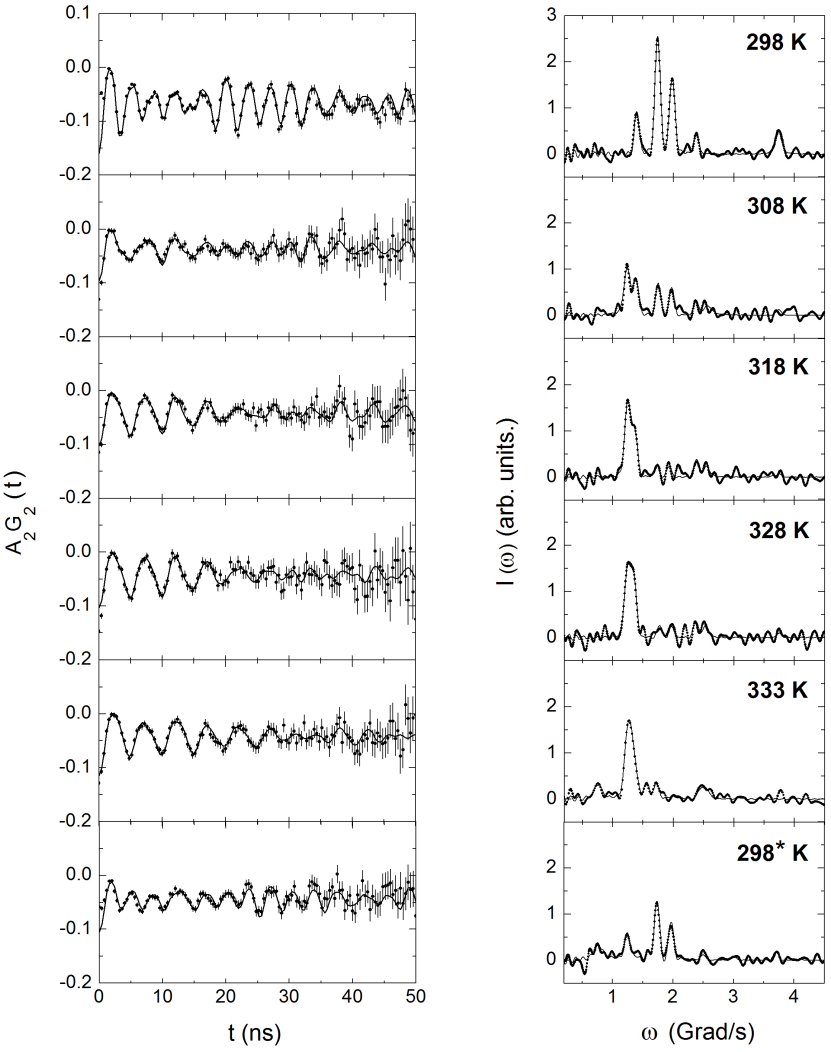

Figure 5.6: Time differential perturbed angular correlation spectra in $HfF_4 \cdot 3H_2O$ at different temperatures. Left panel shows the time spectra and the right panel shows the corresponding Fourier cosine transforms. The PAC spectrum at room temperature designated by 298* K is taken after the measurement at 333 K.

to the monoclinic structure.

This also gives the information that the hafnium tetrafluoride trihydrate can have both the monoclinic and triclinic structures. In the present sample of $HfF_4 \cdot 3H_2O$, the population fraction for the triclinic structure is found to be more at room temperature compared to the monoclinic fraction and was quite unexpected where only the monoclinic structure of it was found from previous investigations. It seems quite strange also that the triclinic structure which is predominant in present sample was not observed from

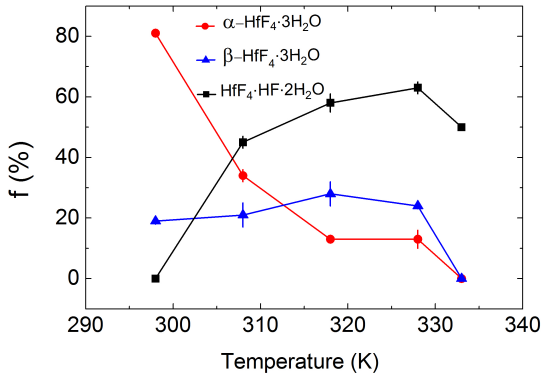

Figure 5.7: Variations of site percentages with temperature for different components produced in $HfF_4{\cdot}3H_2O$.

previous PAC measurements and this structure was unknown for this compound. The site fractions for the two structures remain almost unchanged at room temperature. To investigate the stability of the triclinic fraction and the changes in population fractions with temperature, PAC measurements have been performed at higher temperatures.

At 308 K, apart from the triclinic and monoclinic fractions, a new component appears with a site fraction ∼45%. The PAC spectrum at 308 K is shown in Figure 5.6. The values for the new component are found to be ω_Q=124(2) Mrad/s, η=0.91(3) and δ=2(1)%. This component appears at the expense of the triclinic fraction which is reduced to 34% while the monoclinic fraction remains almost unchanged. The new component fraction can be assigned to HF adducted hafnium tetrafluride ($HfF_4{\cdot}HF{\cdot}2H_2O$) by comparing the values obtained from previous PAC measurements [116, 117] in $HfF_4{\cdot}HF{\cdot}2H_2O$. In this compound, results at room temperature from two different measurements were reported to be ω_Q=126.7(4) Mrad/s, η=0.9243(4) [116] and ω_Q=126.86(31) Mrad/s, η=0.927(1) [117]. A close agreement of the present results with the results reported earlier indicates that, the sample is partially transformed to $HfF_4{\cdot}HF{\cdot}2H_2O$ at 308 K.

Results at 318 K also show these three components but with different site fractions compared to that found at 308 K. It is found that the component fraction for $HfF_4{\cdot}HF{\cdot}2H_2O$ increases to 58% while the triclinic $HfF_4{\cdot}3H_2O$ fraction is reduced more but its monoclinic fraction is slightly enhanced at this temperature (Figure 5.6).

Present results at 328 K show that the site fraction corresponding to the monoclinic $HfF_4 \cdot 3H_2O$ reduces slightly (triclinic fraction remaining same) while the fraction for $HfF_4 \cdot HF \cdot 2H_2O$ increases to 63%. The site fractions for these three fractions at different temperatures are shown in Figure 5.7. It seems there is a competition between these three site fractions and these components vary almost smoothly with temperature. Measurement at 333 K shows that component fraction for $HfF_4 \cdot HF \cdot 2H_2O$ decreases again compared to the fraction found at 328 K and the $HfF_4 \cdot 3H_2O$ starts to dehydrate. At this temperature, both the monoclinic and triclinic structures of $HfF_4 \cdot 3H_2O$ disappear. Here, apart from $HfF_4 \cdot HF \cdot 2H_2O$, three other new components are observed. These components can be assigned to $HfF_4 \cdot H_2O$ (ω_Q=212(2) Mrad/s, η=0.48(2)), $Hf_2OF_6 \cdot H_2O$ (ω_Q=156(1) Mrad/s, η=0.74(2)) and anhydrous HfF_4 (ω_Q=106(7) Mrad/s, η=0.43(9)) by comparing the present measured values of ω_Q and η with the earlier reported results [113, 115–117] for these components. Site fraction for $HfF_4 \cdot H_2O$, $Hf_2OF_6 \cdot H_2O$ and anhydrous HfF_4 were found to be ∼14%, ∼16% and ∼19%, respectively. The monohydrate $HfF_4 \cdot H_2O$ gives values of ω_Q and η closer to those found in monoclinic $HfF_4 \cdot 3H_2O$. It was found earlier [112] that crystal structures of the trihydrate $HfF_4 \cdot 3H_2O$ and monohydrate $HfF_4 \cdot H_2O$ are same. Present results indicate that $HfF_4 \cdot H_2O$ is isostructural with the monoclinic β-$HfF_4 \cdot 3H_2O$. The fitting of PAC spectrum with four components in $HfF_4 \cdot H_2O$ at 333 K was done by floating all the values of ω_Q, η and δ initially. We fixed the value of delta to zero when the fitting produced δ <0.5% for any of the components.

Measurement at room temperature is now repeated after the measurement at 333 K. The corresponding spectrum is shown in Figure 5.6. The component $HfF_4 \cdot HF \cdot 2H_2O$ is not found now and instead of this, the triclinic $HfF_4 \cdot 3H_2O$ reappears. But, interestingly, no fraction for the monoclinic $HfF_4 \cdot 3H_2O$ is observed here. This means, when the temperature is reduced back to 298 K, the sample is partially hydrated to $HfF_4 \cdot 3H_2O$ (53%) but it exhibits its triclinic structure only. On the other hand, the monoclinic structure which was known to be the crystal structure of $HfF_4 \cdot 3H_2O$ is not observed any more. The other components are found to be anhydrous HfF_4 (∼24%), $Hf_2OF_6 \cdot H_2O$

(15%) and $HfF_4{\cdot}H_2O$ (8%). The presence of monoclinic and triclinic structures in this trihydrate compound is probably sample dependent. In present sample, the co-existence of two phases are possibly due to incomplete crystallization induced by the local defects or thermal history while in samples of previous measurements only one crystalline phase (β-$HfF_4{\cdot}3H_2O$) was produced. Detailed results of temperature dependent PAC measurements in this sample can be found in the reference [38].

5.2.3.2 $ZrF_4{\cdot}3H_2O$

The PAC spectrum in the crystallized sample of $ZrF_4{\cdot}3H_2O$ (sample 1) at room temperature is shown in Figure 5.8. At room temperature, an almost undamped periodic time spectrum up to 50 ns is observed. This spectrum gives a predominant frequency component (83%) with values of ω_Q=183.2(4) Mrad/s, η=0.839(3), δ=0.9(2)% along with two other minor components. This component corresponds to the triclinic structure of $ZrF_4{\cdot}3H_2O$ as reported earlier for this compound. Appearance of the second minor component, however, is significant. It gives values of ω_Q=203(2) Mrad/s, η=0.35(2) with a value of δ=0. The site fraction for this component is found to be $\sim$10%. Comparing these values of ω_Q and η with those found in $HfF_4{\cdot}3H_2O$ reported in reference [113] and also in present report, this minor component can be identified as β-$ZrF_4{\cdot}3H_2O$. The monoclinic structure of $ZrF_4{\cdot}3H_2O$ is found at room temperature from repeated measurements and is always produced as a minor component (7-10%). However, no such component was [114, 115] found from PAC measurements done earlier. Probably, this was not crystallized in earlier samples or not identified because of its small site fraction. But, the presence of this component in present sample indicates that $ZrF_4{\cdot}3H_2O$ also has both triclinic and monoclinic crystal structures. Although the monoclinic structure was not found from previous PAC measurements, this structure is reported from a recent X-ray diffraction measurement [3]. Present PAC measurements in $ZrF_4{\cdot}3H_2O$, therefore, support the XRD results about the existence of its monoclinic structure. The third minor

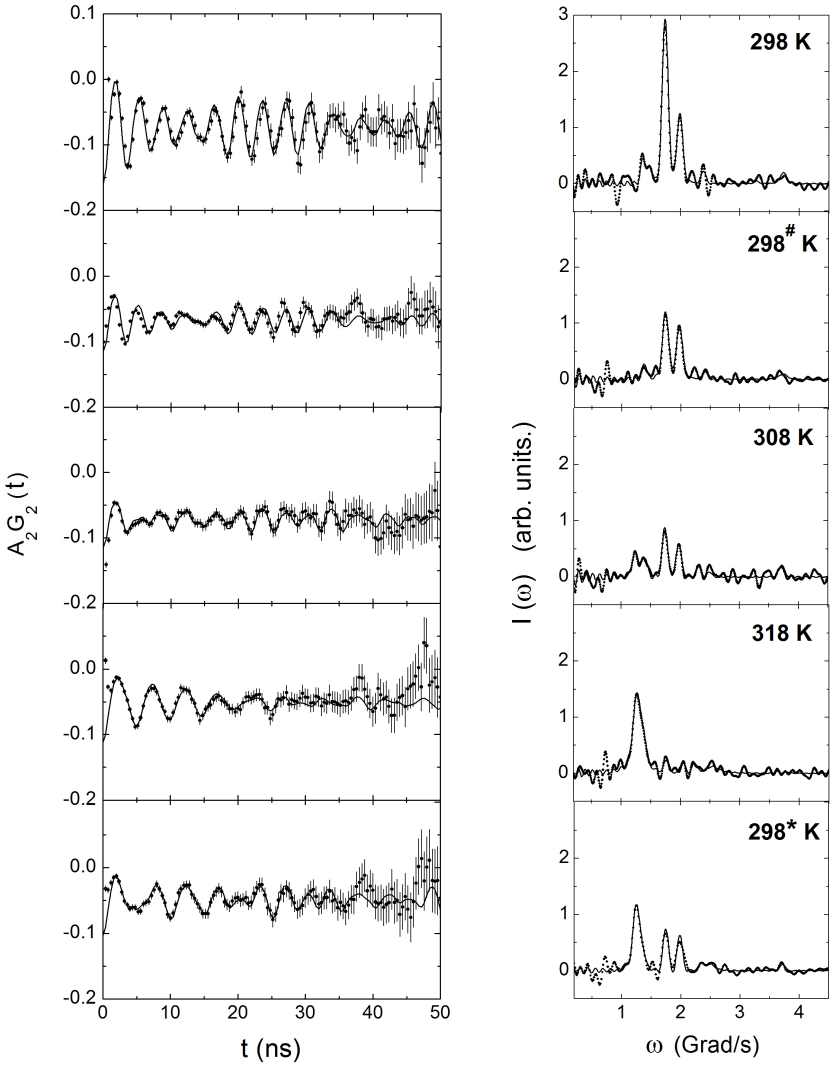

Figure 5.8: Time differential perturbed angular correlation spectra in $ZrF_4{\cdot}3H_2O$ at different temperatures. Left panel shows the time spectra and the right panel shows the corresponding Fourier cosine transforms. Here, the PAC spectrum at room temperature designated by $298^{\#}$ K is for the recrystallized sample. Spectra shown at higher temperatures are taken in this recrystallized sample. The PAC spectrum at room temperature designated by 298^{*} K is taken after the measurement at 318 K.

component (7%) with values of ω_Q=164(3) Mrad/s, η=0.76(3) and δ=0 can be attributed to $Zr_2OF_6{\cdot}H_2O$ by comparing with earlier reported values in $Hf_2OF_6{\cdot}H_2O$ [116, 117]. From our previous measurement [115], similar values of ω_Q and η for $Zr_2OF_6{\cdot}H_2O$ have been reported. To reproduce the monoclinic $ZrF_4{\cdot}3H_2O$, we have recrystallized the sample by adding concentrated HF. The solution is divided into two parts and allowed to dry slowly at room temperature. One of the crystallized samples show pure triclinic

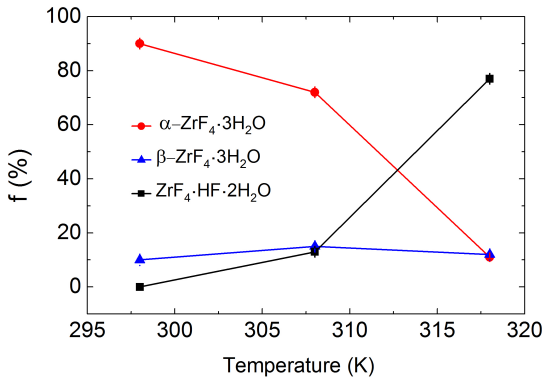

Figure 5.9: Variations of site percentages with temperature for different components produced in $ZrF_4 \cdot 3H_2O$.

$ZrF_4 \cdot 3H_2O$ (results not shown) while the second sample (sample 2) again gives a mixture of both triclinic and monoclinic structures. The monoclinic fraction in sample 2 at room temperature is also found to be relatively small (∼10%) compared to the triclinic fraction. In the recrystallized sample, however, no fraction corresponding to $Zr_2OF_6 \cdot H_2O$ appears. To investigate the temperature dependent behavior of the two structures of $ZrF_4 \cdot 3H_2O$, measurements have been performed at higher temperatures in sample 2.

At 308 K, both the triclinic and monoclinic structures are observed with site percentages of 72 and 15, respectively. Beside this trihydrated component of ZrF_4 with its two different structures, a new component (ω_Q=120(2) Mrad/s, η=0.93(2)) appears at this temperature with site fraction ∼13%. The values of ω_Q and η for this new component are found to be ω_Q=120(2) Mrad/s, η=0.93(2) and it can be attributed to $ZrF_4 \cdot HF \cdot 2H_2O$ by comparing with earlier reported results [115]. At this temperature, the fraction for monoclinic $ZrF_4 \cdot 3H_2O$ enhances while the triclinic fraction is found to be reduced. The triclinic fraction is found to be reduced drastically at 318 K (11%) and at the expense of this, the HF adducted component is enhanced much (77%). The monoclinic fraction, on the other hand, does not change appreciably. Here, site percentages for both triclinic and monoclinic structures are found to be almost same. A variation of site fractions for different components is shown in Figure 5.9. When the temperature is brought back to room temperature, the triclinic fraction again goes up (43%) and the component

due to $ZrF_4 \cdot HF \cdot 2H_2O$ reduces (46%) while the component corresponding to monoclinic $ZrF_4 \cdot 3H_2O$ is reversibly back to the original site fraction (10%). This indicates that the monoclinic $ZrF_4 \cdot 3H_2O$ is also a stable configuration like its other structural configuration. It is found that $ZrF_4 \cdot 3H_2O$ is more reversible with temperature than $HfF_4 \cdot 3H_2O$. This is duo to the fact that $ZrF_4 \cdot 3H_2O$ is heated up to a temperature of 318 K while $HfF_4 \cdot 3H_2O$ was heated up to a more higher temperature of 333 K. At 333 K, the sample $HfF_4 \cdot 3H_2O$ loses H_2O molecules and irreversibly dehydrates to HfF_4 and $HfF_4 \cdot H_2O$. Detailed results of temperature dependent PAC measurements in this sample can be found in the reference [38].

5.2.4 Conclusion

From PAC measurements in tetrafluoride trihydrate compounds of Hf and Zr, we find that both these have monoclinic and triclinic structural configurations and it is not true that their crystal structures are different viz., $HfF_4 \cdot 3H_2O$ has monoclinic and $ZrF_4 \cdot 3H_2O$ has triclinic structure. In $HfF_4 \cdot 3H_2O$, strong PAC signals for both clearly indicate presence of these structures while in $ZrF_4 \cdot 3H_2O$, the triclinic signal is more pronounced at room temperature compared to the monoclinic signal. From temperature dependent PAC measurements, it is found that the triclinic fraction of $HfF_4 \cdot 3H_2O$ decreases while the monoclinic fraction increases with temperature from room temperature up to 328 K but, the the sample composition changes at 333 K where both these structures disappear. A re-measurement at room temperature produces the triclinic structure only and the monoclinic configuration of $HfF_4 \cdot 3H_2O$ does not re-appear. This shows that, the triclinic structure of $HfF_4 \cdot 3H_2O$ is also a stable configuration as the monoclinic structure although the monoclinic form of this trihydrate compound was known only from previous X-ray diffraction and PAC measurements. Also, the monohydrate $HfF_4 \cdot H_2O$ is found to be isostructural with β-$HfF_4 \cdot 3H_2O$. In $ZrF_4 \cdot 3H_2O$, results from present measurements give a stable monoclinic structure and support the results obtained from a

recent X-ray diffraction study in this compound where the crystal structure parameters for the monoclinic modification of zirconium trihydrate tetra fluoride were reported.

5.3 Crystalline properties of Rb_2ZrF_6 and Cs_2HfF_6

5.3.1 Introduction

The previous temperature dependent perturbed angular correlation studies in Rb_2HfF_6, Rb_2ZrF_6 and Cs_2HfF_6 [5, 65–67] produced interesting results. In the crystalline compound Rb_2HfF_6, a phase transition near 740 K was reported by Martínez et al. [67] and a fluctuating electric field gradient at temperatures above 413 K was found by Vasquez et al. [65]. In Rb_2HfF_6 and Cs_2HfF_6, time-dependent relaxation effects due to the ionic motion in the crystal in presence of vacancies or other type of lattice imperfections surrounding the probe atom were observed at T $\geq$ 513 K [65, 66]. From measurements in Rb_2HfF_6 and Rb_2ZrF_6, on the other hand, no time-dependent relaxation effects were found by Martínez et al. [67] but, structural phase transitions in both these compounds around 740 K were reported. It was found [67] that Rb_2ZrF_6 produced two electric field gradients (EFG) corresponding to two different crystal structures. These were found to be V_{zz}=7.8×10^{17} V/m^2 (ω_Q=74 Mrad/s, $\eta \sim 0$) and V_{zz}=2.9×10^{17} V/m^2 (ω_Q=28 Mrad/s, $\eta \sim 0$) at room temperature with population fractions ∼94% and 6%, respectively. Similar values of EFG were found for the analogous compound Rb_2HfF_6. These authors [67] have shown that two structures of these materials change abruptly at around 740 K where the predominant structure corresponding to $\omega_Q \sim 74$ Mrad/s, $\eta \sim 0$ transforms to the second structure with $\omega_Q \sim 28$ Mrad/s, $\eta \sim 0$. From our recent measurement in Rb_2HfF_6 [5], in addition to above two components, a new structure corresponding to the frequency component with values of $\omega_Q \sim 25$ Mrad/s, $\eta \sim 0.55$ was found which was not observed from previous investigations. This new structure was found to be produced instantaneously at a particular temperature (room temperature or slightly above) or developed gradually with temperature due to rotation of the $HfF_6{}^{2-}$octahedral ionic group about the principal axis. It is known [118] that materials of type R_2MX_6 and RMX_3 (R=K^+, Rb^+ and Cs^+; X=halide) with cubic antifluorite and perovskite structures re-

spectively, undergo phase transitions of tilting variety at lower temperatures. Our earlier report in Rb_2HfF_6 [5] demonstrates this phase transition from detailed measurements in its different samples and with varying temperatures. Present investigations in Rb_2ZrF_6 and Cs_2HfF_6 have been carried out to find out any such structural phase transitions in these materials also, particularly, when there is no report of any low temperature phase transitions in these materials from previous measurements. Measurements in these materials are aimed also to find any spin relaxation effects at high temperature duo to atomic or ionic fluctuation near the probe atom in presence of vacancies or any other lattice imperfections.

5.3.2 Sample preparation

5.3.2.1 Rb_2ZrF_6

Four different samples of Rb_2ZrF_6 have been prepared by chemical synthesis. A tiny piece (∼2 mg) of Hf metal was activated in a similar manner as described in section 5.1.2. The active Hf metal piece was dissolved in concentrated HF. A very small quantity of this solution was added to each sample of Rb_2ZrF_6 and Cs_2HfF_6 in solution. For the preparation of sample 1, a small piece (4.4 mg) of natural Zr metal (∼5% Hf) procured also from Alfa Aesar was first dissolved in concentrated HF (40%). Approximately 16 mg RbF (purity 99%) was dissolved in it and then activated with ^{181}Hf. The active solution was allowed to dry slowly at room temperature till the solid crystalline powder is formed. A sample 2 of Rb_2ZrF_6 was synthesized in a similar manner as in sample 1. The quantities of Zr metal and RbF in sample 2 were approximately 6.8 and 20.4 mg, respectively. A different sample (sample 3) of Rb_2ZrF_6 was prepared in a similar way as in previous samples. In this sample, the quantities of Zr metal and RbF were approximately 14 and 40 mg, respectively and it was dried at a slightly elevated temperature using the infrared radiation. Similarly, a fourth sample of Rb_2ZrF_6 was also produced where larger

quantities of Zr metal (28.4 mg) and RbF (77.7 mg) were taken and a clear solution was produced by dissolving in concentrated HF. A part (∼3/4 th) of this solution was taken separately in a plastic container before it was activated and was dried slowly at room temperature. This inactive solid part was used for XRD measurement. The rest part of the solution was activated with ^{181}Hf which was also dried slowly at room temperature and was used for TDPAC measurements. Preparation conditions for all the samples of Rb_2ZrF_6 have been summarized in a Table 5.2. For measurements at different temperatures in the range 313-363 K, the procedure described in section 5.2.2 has been utilized.

5.3.2.2 Cs_2HfF_6

For the preparation of Cs_2HfF_6, a small piece (∼ 3.8 mg) of natural Hf metal (∼5% Zr) procured from Alfa Aesar was dissolved in concentrated HF taken in a plastic vial. Approximately 10 mg of CsF was added to this solution. The active solution was allowed to dry slowly at room temperature till the solid crystalline sample was produced.

Table 5.2: Sample preparation for Rb_2ZrF_6

Sample	Zr (mg)	RbF (mg)	preparation condition
1	4.4	16	dried slowly at room temperature
2	6.8	20.4	dried slowly at room temperature
3	14	40	dried under infrared radiation
4	28.4	77.7	dried slowly at room temperature (∼25% of the sample was used for PAC measurements while ∼75% of the sample was used for XRD measurement)

5.3.3 Results and discussion

5.3.3.1 Rb_2ZrF_6

The PAC spectrum at room temperature for sample 1 (Figure 5.10) gives two interaction frequencies. A best fitting to the spectrum is obtained by considering two frequency components. The predominant component (71%) gives a value of quadrupole frequency ω_Q=74.59(6) Mrad/s, η=0 (component 1) and a value of frequency distribution width δ=0.4(1)%. By comparing these values of ω_Q and η with those found earlier [67], the crystallized sample can be identified as Rb_2ZrF_6. But, the minor component (component 2: ω_Q=26.1(3) Mrad/s, η=0.55(2)) found in present sample with site fraction ∼29% was not observed from previous measurements [67].

Interestingly, the PAC spectrum is found to change spontaneously at room temperature. After one day, the spectrum looks significantly different (Figure 5.10). It gives the same two components but with site fractions entirely different. Here, the second component appears as predominant (70%) and the original predominant component appears as a minor fraction (30%). Values of ω_Q and η for the two components remain unchanged as expected. After the initial transformation at 298 K, site fractions for these two components are found to change very little with temperature up to 353 K (Figure 5.11). The results indicate that the second component is a different structural modification of Rb_2ZrF_6 and it was not found from previous measurements [67]. For this component, values of ω_Q and η have been found to be similar to those found in Rb_2HfF_6 from our

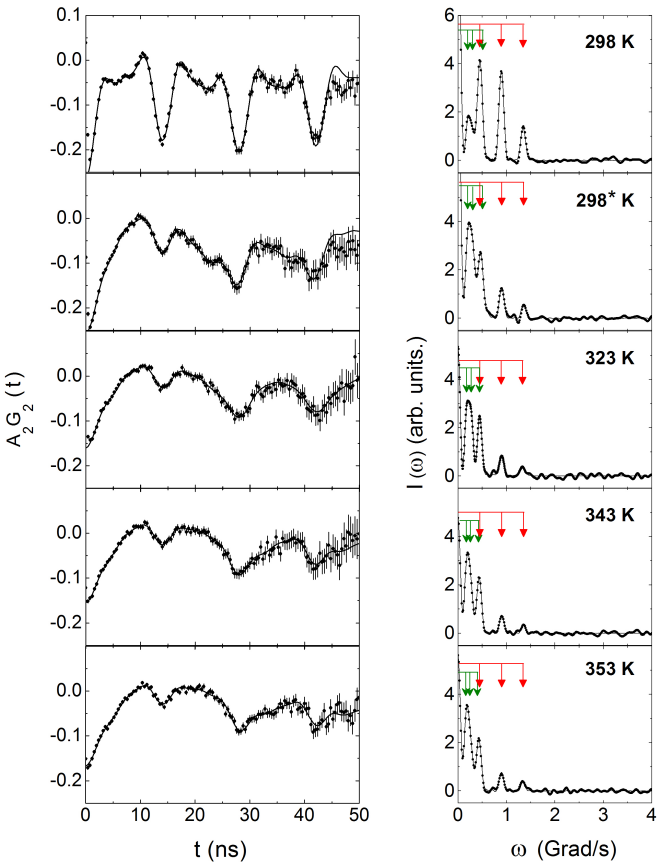

Figure 5.10: Time differential perturbed angular correlation spectra at different temperatures in Rb_2ZrF_6 (sample 1). Left panel shows the time spectra and the right panel shows the corresponding Fourier cosine transforms. The PAC spectrum designated by 298* K is taken after one day of preparation of the sample. Measurements at 298 K have been performed using the $LaBr_3$(Ce)-BaF_2 set up but for higher temperatures, the BaF_2-BaF_2 set up is used.

earlier investigations [5], which confirms that Rb_2ZrF_6 also has a structural modification that arises from rotation of the $ZrF_6{}^{2-}$ octahedron and the phase transition to this rotated structural configuration occurs spontaneously at room temperature. This new structural configuration corresponding to ω_Q=26.1 Mrad/s, η=0.55 can be assigned as component 2.

The sample 1 is recrystallized by adding a drop of concentrated HF and then slowly drying the solution at room temperature. In the TDPAC spectrum (Figure 5.12) of the recrystallized sample at room temperature, we find three frequency components of which two (component 1: ω_Q=74.53(9) Mrad/s, η=0; component 2: ω_Q=27.0(3) Mrad/s,

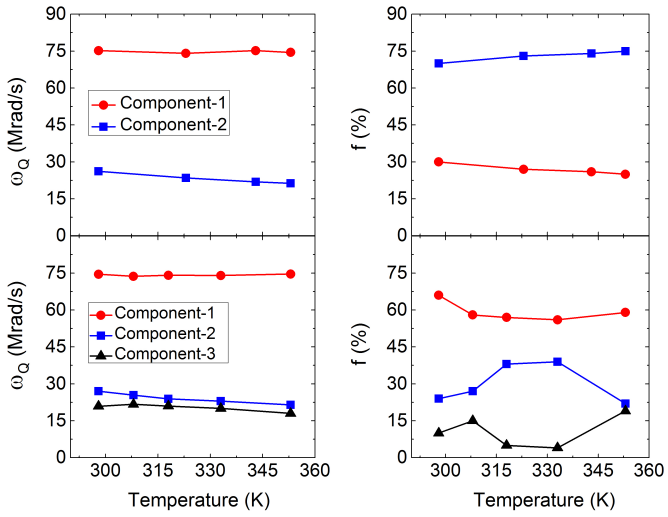

Figure 5.11: Variations of electric quadrupole frequencies and site fractions with temperature for different components in Rb_2ZrF_6. Figures in top correspond to the original sample 1 and those in bottom correspond to its recrystallized sample. Fractions for room temperature data in sample 1 are plotted corresponding to values found after one day.

η=0.56(2)) are found to be the same as in the original sample. The site fraction for component 1 and 2 were found to be ∼66% and 24%, respectively. In the recrystallized sample, there appears an additional third minor component (∼10%) with values of ω_Q=21.1(7) Mrad/s, η=0 at room temperature. This is not a defect but is shown to be a different structural modification of Rb_2ZrF_6 and we designate this as component 3. This structure of Rb_2ZrF_6 was found from previous measurements also [67]. Interestingly, no spontaneous structural change at room temperature was found in the recrystallized sample. The structural variations for the three structures with temperature are shown in Figure 5.11. It is found that component fraction for component 1 changes slowly with temperature while for the components 2 and 3, there is a competition to evolve at higher temperatures. The component 2 at first increases with temperature up to 333 K where it is found to be maximum (39%). The component 3 shows its maximum site fraction (19%) at 353 K and lowest percentage (4%) at 333 K.

Sample 2 at room temperature produces three interaction frequencies (Figure 5.13). For the predominant component (component 1), the results are found to be ω_Q=74.28(7) Mrad/s and η=0 (δ=0.9%) with site occupation f(%)=79% . Apart from this, two other

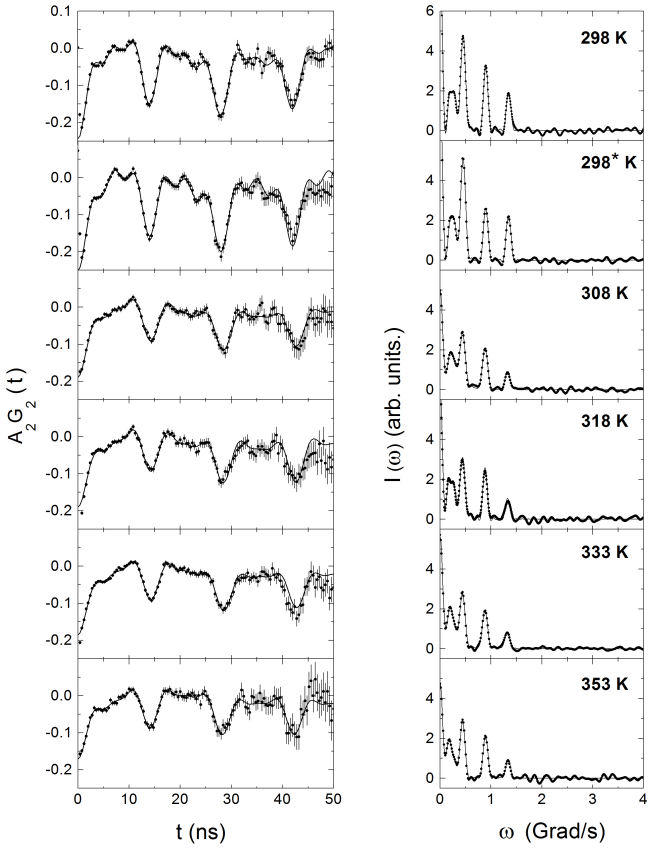

Figure 5.12: Time differential perturbed angular correlation spectra at different temperatures in the recrystallized sample of Rb_2ZrF_6. Left panel shows the time spectra and the right panel shows the corresponding Fourier cosine transforms. The PAC spectrum designated by 298* K is taken after one day of preparation of the sample. Measurements at 298 K have been performed using the $LaBr_3$(Ce)-BaF_2 set up but for higher temperatures, the BaF_2-BaF_2 set up is used.

minor components have been found where the component 2 (ω_Q=25.3(6) Mrad/s and η=0.52(4)) with site fraction ∼11% is the same as found in sample 1. The third component (component 3: ω_Q=21.1(9) Mrad/s, η=0) with site fraction ∼10%, corresponding to a different structural modification of Rb_2ZrF_6, was not observed in the original sample 1, but was present in the recrystallized sample. In this sample also, the third component is not found at room temperature when heated through 353 K but reappears at higher temperatures (393 K and above). This was also not present at 323 K and 353 K. To find the changes in relative fractions of these three components with temperature, we have performed temperature dependent PAC measurements in sample 2 in the range

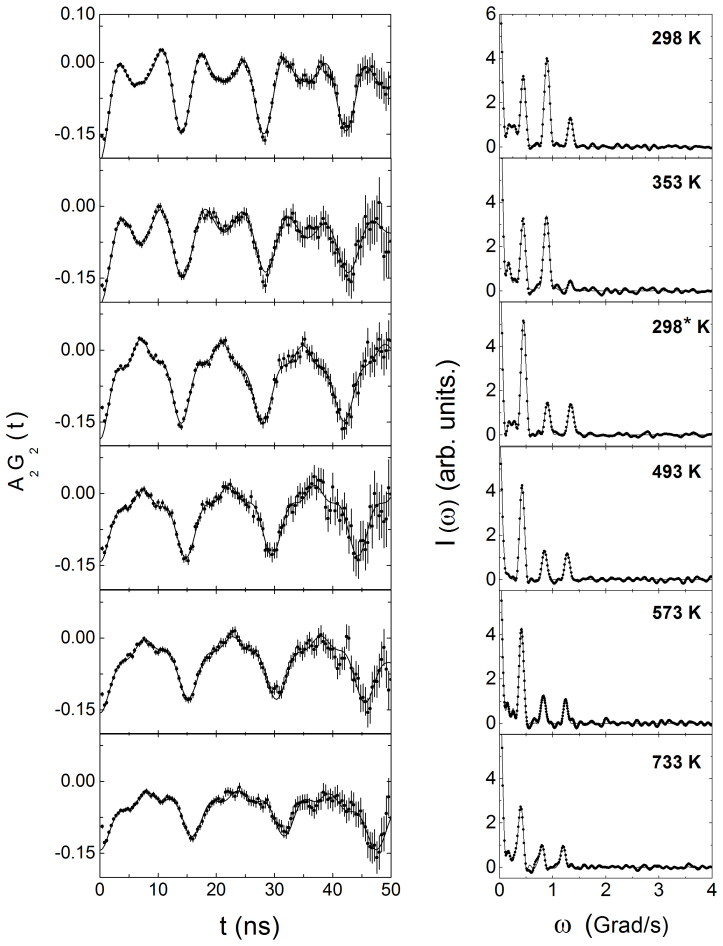

Figure 5.13: Time differential perturbed angular correlation spectra in Rb_2ZrF_6 (sample 2). Left panel shows the time spectra and the right panel shows the corresponding Fourier cosine transforms. The PAC spectrum designated by 298* K is taken after measurement at 353 K. This sample shows prominent temperature dependent texture effects. The two PAC spectra at 298 K which looks different are due to the presence of of texture effects.

298-733 K. For these measurements, the BaF_2-BaF_2 set up was used. It is found that the component 2 corresponding to the rotated fractions of $ZrF_6{}^{2-}$ disappears at 393 K and above. Up to a temperature of 393 K, it seems there is a competition between the two minor components. At 393 K, it shows the third minor component only and, probably, the component 2 transforms to component 3 at this temperature. This structure corresponding to $\omega_Q \sim 20$ Mrad/s, $\eta \sim 0$ was found from previous measurements also [67]. In the temperature range 493-733 K, the site percentage for component 3 increases (Figure 5.14) slowly with temperature at the expense of component 1. The quadrupole frequency for component 3 varies with temperature in a somewhat irregular

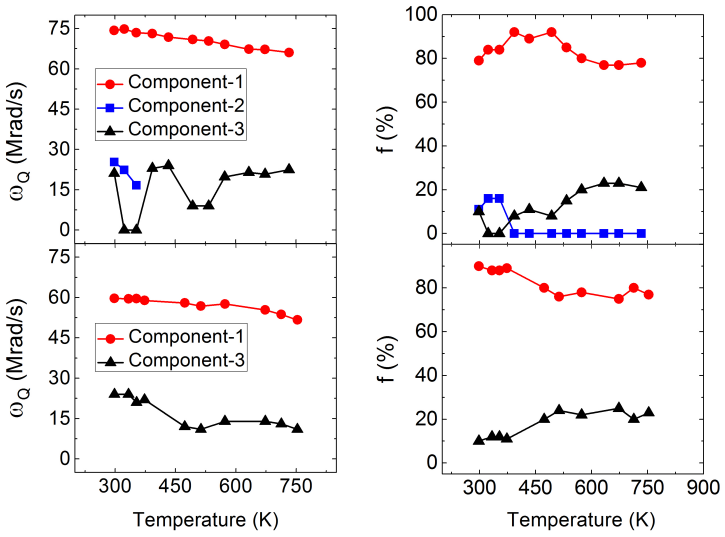

Figure 5.14: Variations of quadrupole frequencies and site fractions with temperature for different components in Rb_2ZrF_6 (sample 2) and Cs_2HfF_6. Figures in top correspond to Rb_2ZrF_6 and those in bottom correspond to Cs_2HfF_6.

manner. But, an overall increase of this component fraction at higher temperatures indicates that it is not a defect. From previous measurements [67] also, a smooth variation of quadrupole frequency with temperature was not observed.

The quadrupole frequency for component 1, on the other hand, decreases slowly with temperature almost following a linear behavior. At 733 K, we have found the component 1 as still a dominating site (78%). This means no major structural modification has occurred at high temperature and it is in disagreement with the earlier observation [67]. But the crystal structure modification in Rb_2ZrF_6 due to reorientation of ZrF_6^{2-} which is accompanied by a small distortion of the lattice is observed. In sample 2, this structure is found at low temperatures only but is not found at 393 K and above. Therefore, the temperature induced phase transition from normal to the ZrF_6^{2-} octahedron rotated structure is not clearly observed here. In Rb_2HfF_6, on the other hand, this type of structural phase transition was found [5] instantaneously at a particular temperature. This was also found to take place gradually with temperature. The exact nature of this phase transition is, therefore, not very clear and it remains as an unusual structural phase transition. Our measurements up to 733 K do not exhibit any time dependent

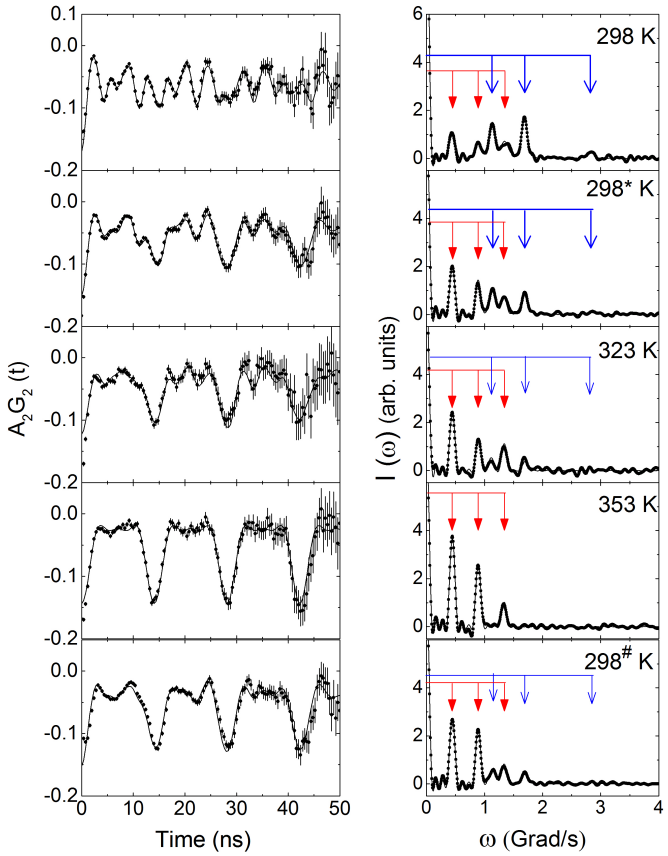

Figure 5.15: Time differential perturbed angular correlation spectra at different temperatures of Rb_2ZrF_6 (sample 3). Left panel shows the time spectra and the right panel shows the corresponding Fourier cosine transforms. The PAC spectrum designated by 298* K is taken after three weeks of measurement at 298 K. The PAC spectrum designated by 298# K is taken after measurement at 353 K.

relaxation components due to fluctuation of atoms or ions in the vicinity of the probe atom as reported in Rb_2HfF_6 [65] from previous investigations.

The TDPAC measurement in sample 3 at room temperature gives interesting results. The PAC spectrum (Figure 5.15) at room temperature shows clearly different compared to the spectra in samples 1 and 2. Here, a new high frequency component is observed as a predominant fraction (64%) with values of $\omega_Q = 148(2)$ Mrad/s, $\eta = 0.540(3)$ and $\delta = 1.2(2)\%$ (component 4) along with the frequency component usually found in Rb_2ZrF_6 which appears as a minor fraction (36%). For the minor component, the results are found to be $\omega_Q = 74.8(3)$ Mrad/s, $\eta = 0$, $\delta = 3.7(7)\%$ (component 1). The measurement at room temperature was repeated after three weeks to find any change in results. It is

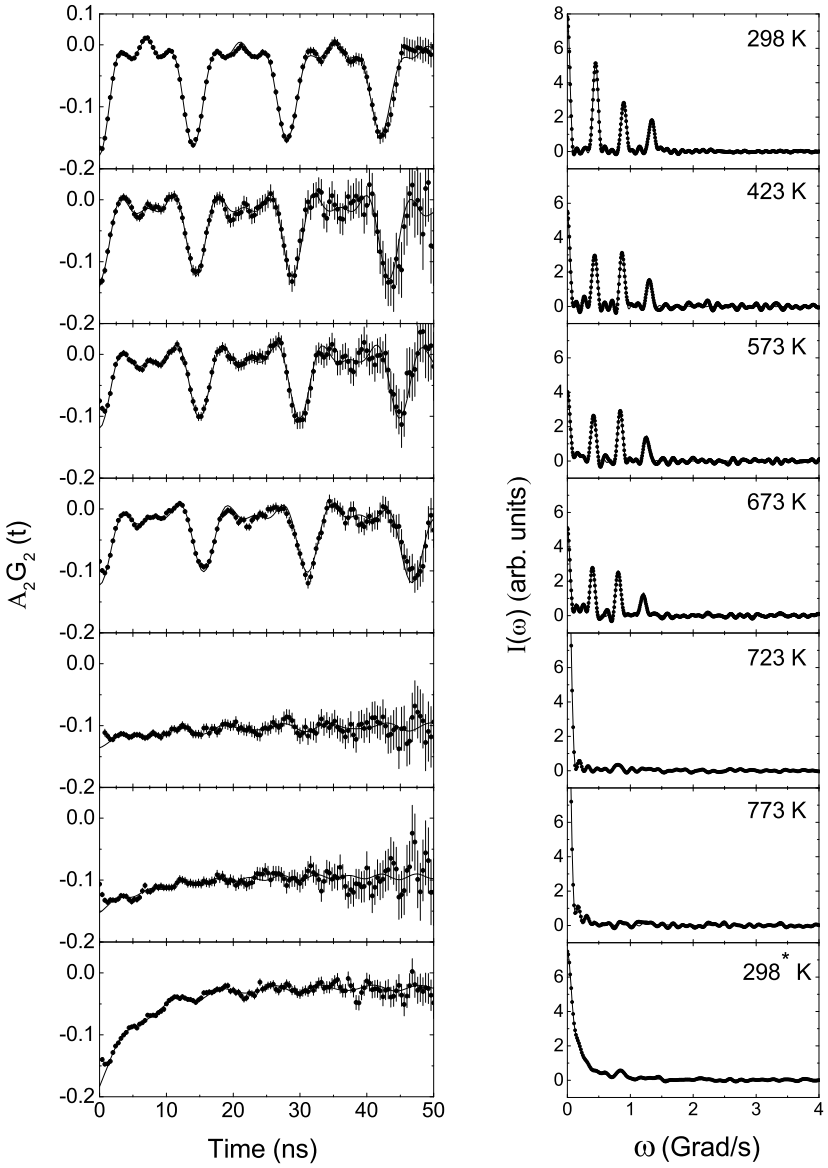

Figure 5.16: Time differential perturbed angular correlation spectra at different temperatures of Rb_2ZrF_6 (sample 4). Left panel shows the time spectra and the right panel shows the corresponding Fourier cosine transforms. The PAC spectrum designated by 298* K is taken after measurement at 773 K.

found that the site fraction for the minor component increases slowly with time at the expense of the major fraction. After approximately three weeks, the site fraction for the principal component decrease to 55% while the second component becomes relatively stronger (45%). The PAC measurement in this sample is then performed at a slightly higher temperature of 323 K. At this temperature, the higher frequency component

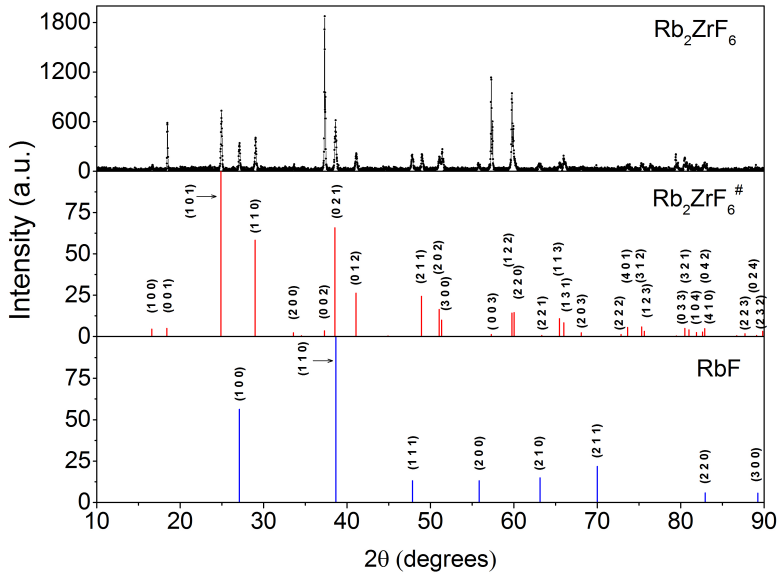

Figure 5.17: Top figure in the panel shows background subtracted X-ray diffraction pattern of Rb_2ZrF_6 which has been compared with ICDD database for trigonal crystal system Rb_2ZrF_6 (middle) and cubic RbF (bottom).

appears as a minor fraction (21%) and the lower frequency component becomes stronger (79%). Interestingly, the spectrum is found to be changed completely at 353 K where a single frequency component is observed (Figure 5.15). The results at this temperature are found to be $\omega_Q = 74.43(8)$ Mrad/s, $\eta = 0$, $\delta = 0$. The higher frequency component is found to be completely absent at 353 K. The measurement is then repeated at room temperature to find any reversibility of the results. It is found that a significant fraction of the higher frequency component reappears reversibly at room temperature as a minor fraction (30%). Initially, this component was found to be predominant.

The results in sample 3 indicate that the high frequency component is indeed a new structural modification of Rb_2ZrF_6 which was not observed earlier and also in any other sample in present measurements. A structural change at low temperature, probably, occurs in this sample. At 353 K, the structure that was found at room temperature changes to the normal structure of Rb_2ZrF_6 (component 1). Since, this structural change occurs at low temperature, probably, this can also be attributed to the rotation of the HfF_6^{2-} octahedron.

The TDPAC measurement in sample 4 gives a pure single frequency component at room temperature (Figure 5.16) with values of ω_Q = 74.60(4) Mrad/s, η = 0, δ = 0.86(9)% (component 1). The results for this frequency component indicate that the crystallized sample 4 is pure Rb_2ZrF_6. Inactive part of this sample is characterized by powder X-ray diffraction at room temperature with Cu K_α radiation using PHILIPS PW 1830 X-Ray Generator. The XRD spectrum is shown in Figure 5.17. The peaks in the spectrum were identified using ICDD database. The XRD spectrum of sample 4 shows the X-ray lines corresponding to Rb_2ZrF_6 which belongs to trigonal crystal system having a space group $P\bar{3}m1(164)$ [PDF Card No. : 01-074-0172]. In addition, it shows the lines due to RbF (PDF Card No. : 01-078-0661) which arise, probably, due to excess RbF since the quantities of Zr and RbF taken are not exactly in the stoichiometric ratio. However, temperature dependent PAC measurements in sample 4 are also carried out up to 773 K. At 323 K, no major structural change is observed in the sample. But, a minor frequency component (ω_Q = 24.2(8) Mrad/s, η = 00 with site occupation ∼8% arises at these temperature. This weak frequency component is, probably, a different structural modification of Rb_2ZrF_6 (component 3) and it increases slowly with temperature. It is found that the minor frequency component enhances to ∼16% at 673 K. A similar frequency component has been observed in sample 2 also. At 723 K, the spectrum changes drastically where the static frequency component (ω_Q=68(2) Mrad/s, η=0) becomes weak (∼30%) and it shows mainly (∼70%) a time dependent component (Figure 5.16). The probe atom, therefore, experiences a very rapid fluctuating EFG and results in a time dependent PAC spectrum which can be described by the Abragam and Pound model [119] in the fast fluctuation limit. The data can be fitted by considering the perturbation function $G_2(t) = G_2^{static} + \exp(-\lambda_2 t)$. At this temperature, probably, the fluorine anion vacancy in the ZrF_6^{2-} octahedral cage is created thermally and the fluorine atom jumps vigorously from one site to the other. An exponential fitting gives the relaxation constant λ_2 = 110(21)/μsec at 723 K. The site fraction of the dynamic component (λ_2 = 116(20)/μsec) increases to ∼83% and static component decreases to

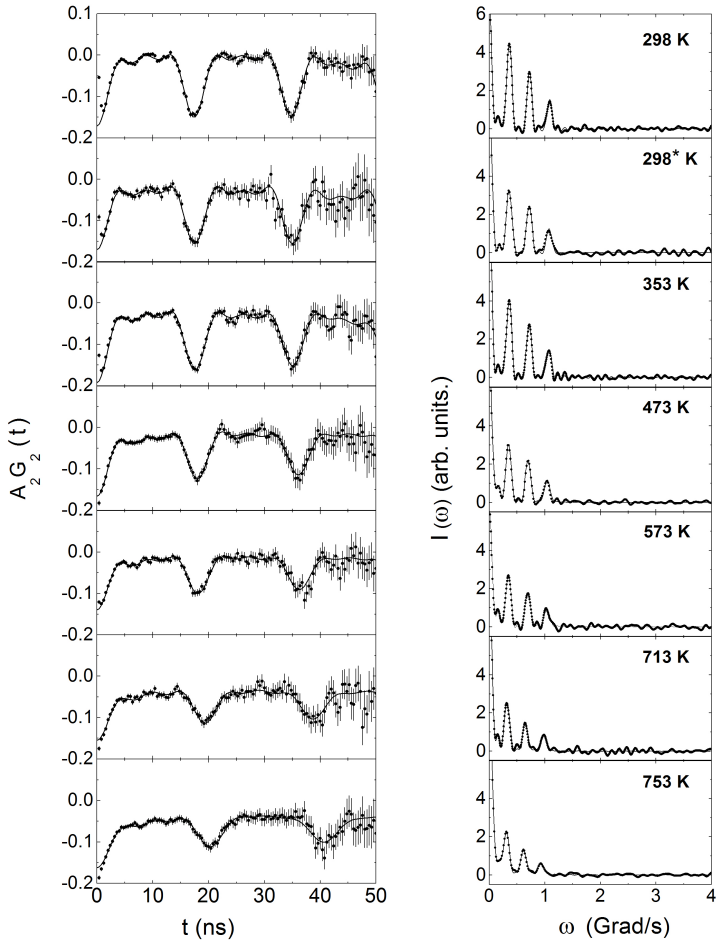

Figure 5.18: Time differential perturbed angular correlation spectra in Cs_2HfF_6. Left panel shows the time spectra and the right panel shows the corresponding Fourier cosine transforms. The PAC spectrum designated by 298* K is taken in the next day after the first measurement.

∼17% at 773 K. The value of relaxation component was found to be 116(20)/μsec at 773 K. The measurement is now repeated at room temperature where a strong (∼70%) time dependent relaxation with a higher value of λ_2 (170(15)/μsec) is observed. The static perturbation is found to be present with site fraction ∼30% at room temperature. At room temperature, a higher value of relaxation constant indicates lower fluctuation rate of fluorine atoms. The value of quadrupole frequency at room temperature (ω_Q = 70.8 Mrad/s) has been found to be slightly smaller to that found when there was no fluctuation. Detailed results of temperature dependent PAC measurements in this sample can be found in the reference [37].

5.3.3.2 Cs_2HfF_6

The PAC measurements in Cs_2HfF_6 have been performed in the temperature range 298-753 K. The spectra at different temperatures are shown in Figure 5.18. The time spectrum found at room temperature is almost periodic and undamped up to 50 ns. It produces a predominant frequency component (86%) with values of ω_Q=60.17(9) Mrad/s, η=0 and δ=0 (component 1) and a minor frequency component (component 3: ω_Q = 22.8(7) Mrad/s, $\eta = 0$) with site fraction ∼13% at room temperature. Comparing values of ω_Q and η for the predominant component with the results found in Rb_2HfF_6 and Rb_2ZrF_6 [5, 66, 67], phase of the present sample can be ascertained as Cs_2HfF_6 (component 1). For the minor component (∼13%), results are found to be ω_Q=22.8(7) Mrad/s, η=0 at room temperature. From temperature dependent measurements up to 753 K this component can be attributed to a different structural configuration of Cs_2HfF_6 (component 3). This is because, this component fraction increases slowly with temperature. In Cs_2HfF_6, we have found these two components only. The other two components corresponding to components 2 and 4, as found in Rb_2ZrF_6 are not found in the analogous compound Cs_2HfF_6 at any temperature. In this compound, the quadrupole frequencies for the two components are found to decrease slowly with temperature (Figure 5.14). The absence of components 2 and 4 indicate that the new structural modification with non-zero values of η arising due to rotation of ${HfF_6}^{2-}$ does not appear in Cs_2HfF_6. These structures, on the other hand, were found in the analogous compounds with Rb atom as one constituent. The component ω_Q=60 Mrad/s, η=0 corresponding to component 1, is always found here as a predominant component up to 753 K.

Temperature dependent PAC measurements in Cs_2HfF_6 (Figure 5.18) show no time dependent relaxation effects. The present results, therefore, are not in agreement with the results reported earlier [66]. Also, no abrupt structural phase transition in this material has been observed up to 753 K and thus is found to be again in disagreement with the results found in Rb_2HfF_6 and Rb_2ZrF_6 by Martínez et al. [67]. On the other

hand, it is found that a phase transition from component 1 to component 3 takes place slowly with temperature (Figure 5.14). Detailed results of temperature dependent PAC measurements in this sample can be found in the reference [37].

5.3.4 Summary and Conclusion

From present measurements in Rb_2ZrF_6 and Cs_2HfF_6, it is found that Rb_2ZrF_6 has four different structural modifications at room temperature. These are characterized by ω_Q=74.28(7) Mrad/s, η=0 (component 1), ω_Q=25.3(6) Mrad/s, η=0.52(4) (component 2) ω_Q=21.1(9) Mrad/s, η=0 (component 3) and ω_Q=148.7(2) Mrad/s, η=0.538(5) (component 4). The site fractions for these four structures differ from one sample to the other. In our first sample of Rb_2ZrF_6, the component 1 was found to be predominant initially (71%) and a minor fraction of 29% was observed for the component 2 while component 3 was absent in this sample. Interestingly, the site populations for these two structures reverse spontaneously at room temperature and after one day the site percentage for component 1 changes to 30% and the component 2 becomes predominant (70%). This spontaneous change in population remains almost stable and changes very little with temperature (up to 353 K). In the recrystallized sample, three structures are found to be present unlike the initially crystallized sample. In sample 2 of Rb_2ZrF_6 also, the three structures have been found at room temperature after crystallizing the sample at room temperature. In this sample, the component 1 has been found to be predominant and its site percentage remains almost unchanged in the whole temperature range of 298-733 K. The component 2 is present up to 353 K. At 393 K and above, only two components (1 and 3) are found. The quadrupole frequency and site percentage for component 3, however, vary in a peculiar manner and not smoothly. But in Rb_2ZrF_6, no drastic structural phase transition from component 1 to component 3 is found here. In sample 3, a new structural modification with ω_Q=148.7(3) Mrad/s, η=0.538(5) (component 4) is observed which is associated with component 1. The component 4 is found to be stable at room temperature but it transforms rapidly to component 1 with a slight increase in temperature. Sample 4 produces a pure static frequency component at room temperature corresponding to component 1 along with a small component duo to component 3. At 723 K, however, a strong time dependent relaxation component appears due to

fluctuation of fluorine atom in the ZrF_6^{2-} octahedral cage.

In the analogous compound Cs_2HfF_6, measurements have been performed in several samples. But, for any of these samples, the components 2 and 4 are not observed. In the present sample of Cs_2HfF_6, the component 1 is found to be the predominant component (75-90%) in the whole temperature range (298-753 K) and the component 3 appears as a minor component. In Cs_2HfF_6 also, no drastic phase transition from component 1 to component 3 has been observed in this temperature range. The component 1 remains as a predominant component in the whole temperature range.

5.4 Electric field gradients, probe site occupancy and phase components in Zr-Ni and Hf-Ni intermetallic compounds: Temperature dependent PAC measurements and DFT calculations

5.4.1 Introduction

The alloys based on Zr-Ni system have numerous technological applications. These are used as an integral part to form high temperature eutectics [120], bulk glassy alloys [121, 122], corrosion resistant material [122, 123], shape memory alloys [124], superalloys [125, 126], superconductors [127]. Magnetic properties in the transition metal based Zr_9Ni_{11} alloy was found earlier [128]. Some of the Zr-Ni binary alloys, viz. Zr_8Ni_{21}, Zr_7Ni_{10}, Zr_2Ni_7, ZrNi, Zr_9Ni_{11} and $ZrNi_3$ have received considerable attention due to their ability to absorb large amount of gaseous hydrogen and reversibility in hydrogen dissociation process. These alloys absorb gaseous hydrogen in their interstitial sites to form nickel metal hydrides (NiMH). These metal hydrides are used as negative electrode in NiMH rechargeable batteries. The electrochemical properties of these compounds were extensively studied earlier [68–75]. The Ni-MH batteries have been widely used in hybrid electric vehicles (HEV) due to their high energy density and environmentally friendly characteristics. Electrochemical capacity is found to be maximum for Zr_7Ni_{10} among Zr-Ni binary alloys by Young et al [71]. Ruiz et al [73] found that Zr_8Ni_{21} alloy had a better charge/discharge performance than Zr_7Ni_{10} and Zr_9Ni_{11}. The gaseous hydrogen storage characteristics of four intermetallic compounds in the Zr-Ni system viz. Zr_9Ni_{11}, Zr_7Ni_{10}, Zr_8Ni_{21} and Zr_2Ni_7 were compared by Joubert et al. [75]. It was found that hydrogen storage capacities in hydrogen atoms per metal atom (H/M) for these four compounds are 0.93 (10 bar), 1.01 (10 bar), 0.34 (25 bar) and 0.29 (25 bar), respectively,

at room temperature and the storage capacities for Zr_8Ni_{21}, Zr_2Ni_7 are completely reversible. The hydrogen reversible capacities for Zr_9Ni_{11} and Zr_7Ni_{10}, are 50% and 77%, respectively. In $ZrNi_3$, catalytic hydrogen activity was reported by Wright et al. [129]. It was found that the hydrogen absorption/desorption properties of many Laves phase and quaternary/ternary hydriding alloys are improved due to the presence of non-Laves Zr-Ni binary alloys [71, 72, 74, 130–132]. Recently, it has been found that the hydrogenation property of TiFe alloy is improved due to the addition of small fraction of Zr_7Ni_{10} [133]. Another recent study [134] reported improvement in hydrogenation kinetics and capacity of Ti-V-Cr body centered cubic (BCC) solid solutions when Zr_7Ni_{10} was used as an additive. Recently, hydrogen absorption/desorption properties in ZrNi alloy were investigated [132] by partial substitution of Zr with Ti for different Ti concentration. The Hf-Ni alloys also have many technological applications. Intermetallic compounds of Hf and transition metals (Fe, Co, Pd, Pt) have also hydrogen storage properties [135], with high H/M ratio at room temperature. The hafnium alloyed with nickel, niobium, and tantalum are also useful and can withstand high temperature and pressure. Hafnium alloys are useful in medical implants and devices due to their bio-compatibility and corrosion resistance [136].

The phase diagram (Figure 5.19) of Zr-Ni system [11, 137–140] shows at least eight binary compounds. From a recent study [141], all these phases were found through the interdiffusion process by annealing the Zr-Ni interface zone at different temperatures. It is found that the phases Zr_2Ni_7, Zr_2Ni, and ZrNi melt congruently while Zr_8Ni_{21}, Zr_9Ni_{11}, Zr_7Ni_{10}, and $ZrNi_5$ phases form peritectically. The phase $ZrNi_3$ is formed by peritectoid reaction. From previous studies [6], a pure single phase Zr_8Ni_{21} was not found to be produced by arc melting preparation. It was found [6] that Zr_8Ni_{21} was not formed congruently from the liquid. The Zr_2Ni_7 was first solidified from the liquid and then reacted with the remaining liquid to form Zr_8Ni_{21} alloy peritectically. The Zr_8Ni_{21} envelopes the Zr_2Ni_7 dendrite hindering further reaction of liquid with Zr_2Ni_7. During the cooling process, the remaining liquid eutectically solidifies to Zr_7Ni_{10} and Zr_8Ni_{21} phases.

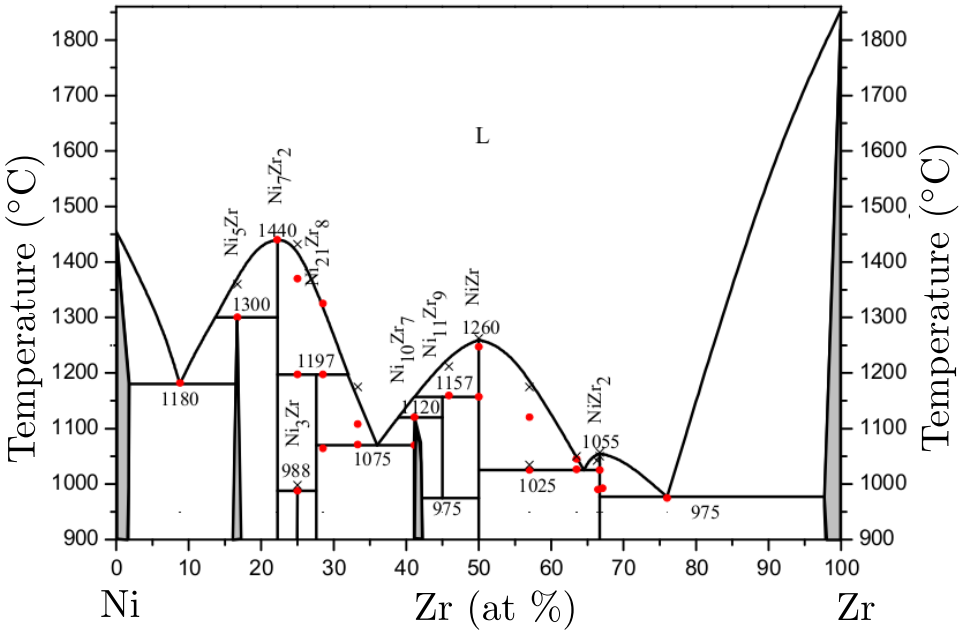

Figure 5.19: Zr-Ni phase diagram. Filled circles correspond to the onset and crosses represent the peak temperatures of differential thermal analysis (DTA) curves on heating [11].

The two other phases viz. Zr_2Ni_7 and Zr_7Ni_{10} were produced along with Zr_8Ni_{21} and were confirmed by scanning electron microscopy (SEM)/X-ray energy dispersive spectroscopy (EDS) compositional mapping and transmission electron microscopy (TEM) [6]. The ZrNi phase reacts peritectically with liquid melt to form Zr_9Ni_{11} phase at 1170°C. The phase Zr_7Ni_{10} is formed by the peritectic reaction of liquid melt with Zr_9Ni_{11} phase at 1120°C [11]. The phase Zr_9Ni_{11} was found to decompose eutectoidally to Zr_7Ni_{10} and ZrNi phases at ∼975°C [138]. Stalick et al. [76] found that the Zr_9Ni_{11} sample, prepared by argon arc melting, contained 10% of ZrNi and at 700 °C, it transformed to ZrNi (37%), Zr_7Ni_{10} (57%) and Zr_9Ni_{11} (7%). At 1000 °C, this sample reformed again to produce 90% Zr_9Ni_{11} and 10% ZrNi. According to Becle et al. [142], the $ZrNi_3$ was formed from Zr_2Ni_5 and Zr_2Ni_7 at 940°C or below by a peritectoid reaction. The stable phase of $ZrNi_3$ was obtained at room temperature by annealing the sample at ∼860°C. They found that the phase $ZrNi_3$ was not stable and decayed at 940°C following $4ZrNi_3 \rightarrow Zr_2Ni_7 + Zr_2Ni_5$. The phase $ZrNi_3$, however, was not found by other workers [137, 143, 144]. J.H.N. Van Vucht [145] also failed to produce $ZrNi_3$ by replacing Ti with Zr in $TiNi_3$. However, a

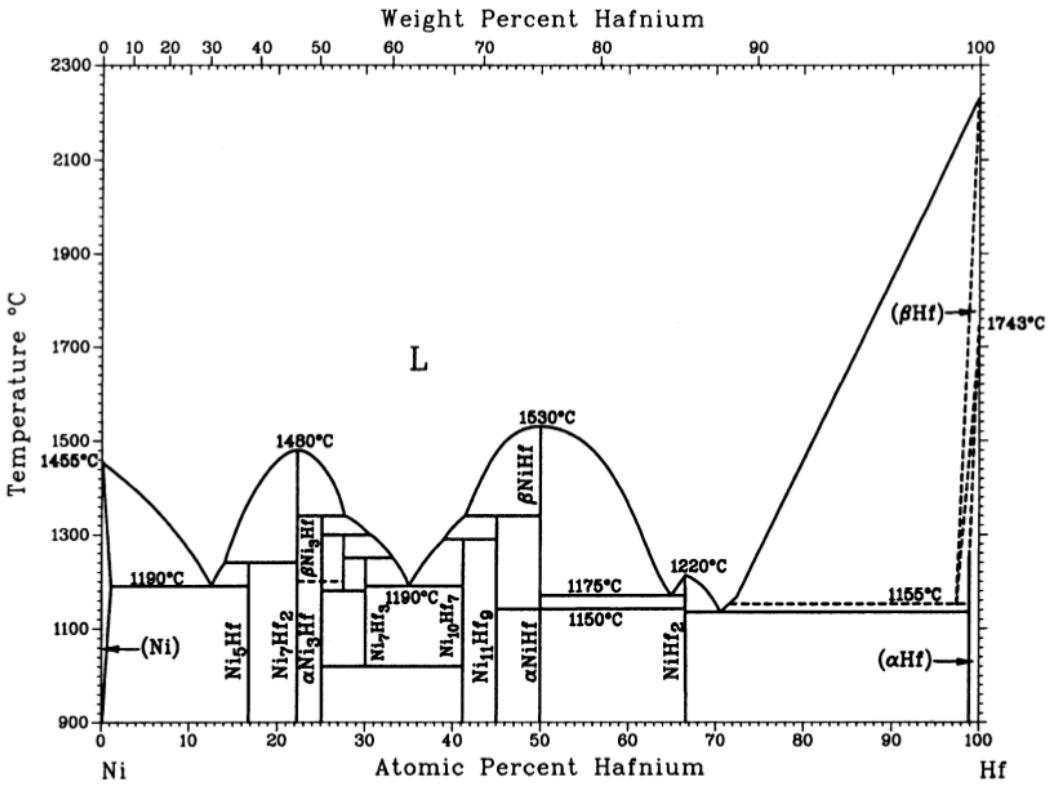

Figure 5.20: Hf-Ni phase diagram [12, 147].

different peritectoid reaction (Zr_8Ni_{21}+$Zr_2Ni_7 \leftrightarrows ZrNi_3$) was also suggested [11, 140] for the formation of $ZrNi_3$ phase at 988°C [11]. From theoretical calculations by density functional theory (DFT), the compounds $ZrNi_3$ and $HfNi_3$ were found to be highly stable alloys. Values of enthalpies of formation of these compounds were reported to be -0.36 eV/atom ($ZrNi_3$) and -0.44 eV/atom ($HfNi_3$) [146]. The formation of these Zr-Ni phases at room temperature are due to nucleation by rapid quenching from the liquid alloy [132, 139].

From the phase diagram (Figure 5.20) of Hf-Ni binary system, nine stable intermediate crystalline phases, viz., Hf_2Ni_7, HfNi, Hf_2Ni, Hf_3Ni_7, $HfNi_3$, $HfNi_5$, Hf_8Ni_{21}, Hf_9Ni_{11} and Hf_7Ni_{10} were found [12, 140, 147, 148]. The phases Hf_2Ni_7 and HfNi were reported to be congruently melting phases. All other phases are formed by peritectic reactions: L+HfNi→Hf_9Ni_{11} at 1613 K, L+Hf_9Ni_{11} →Hf_7Ni_{10} at 1563 K, L+Hf_2Ni_7 →$HfNi_3$ at 1623±20 K, L+$HfNi_3$ → Hf_3Ni_7 at 1523 K, L+HfNi→Hf_2Ni at 1473 K. The $HfNi_3$ phase

has two polymorphs, one high temperature α-$HfNi_3$ phase which is stable above 1200°C and another is low temperature β-$HfNi_3$ phase which is stable below 1200°C. The phase Hf_8Ni_{21} is stable in the temperature range 1300±20 to 1175±10°C, where it decomposes eutectoidally to Hf_3Ni_7 and $HfNi_3$. The stability of the phase Hf_3Ni_7 is limited in the temperature range of 1250±20 to 1016±3°C, where it decomposes eutectoidally to Hf_7Ni_{10} and $HfNi_3$. Three eutectic reactions are present in the phase diagram, where in one reaction liquid solidified into Hf_3Ni_7 and Hf_7Ni_{10} at 1473 K. All these reactions are reversible in nature.

The crystal structure of Zr_8Ni_{21} is known to be triclinic (space group $P\bar{1}$) [149] and is isotropic to that of Hf_8Ni_{21} [150]. The lattice parameters of Zr_8Ni_{21} are a=6.476 Å, b=8.064 Å, c=8.594 Å, α=75.15°, β=68.07° and γ=75.23° as determined by X-ray diffraction analysis. The $ZrNi_3$ is known to be a hexagonal close-packed compound of the $SnNi_3$ type with space group $P6_3/mmc$. The lattice parameters were reported to be a=5.309 Å and c=4.303 Å [142]. Crystal structure of $HfNi_3$ was also reported by L. Bsenko [151]. The crystal parameters for α and β phases of $HfNi_3$ were reported to be a=5.27 Å, c=19.2324 Å and a=5.2822 Å, c=21.3916 Å, respectively. The space group for α and β phases of $HfNi_3$ are $R\bar{3}m$ and $P6_3/mmc$, respectively. The crystal structure of Zr_9Ni_{11} is known to be body-centered tetragonal with space group $I4/m$ [11, 75, 132, 137, 138, 152–154] which is reported to be isostructural to Zr_9Pt_{11} [153, 155, 156]. The lattice parameters of Zr_9Ni_{11} were found to be a = 9.88(1) Å and c = 6.61(1) Å [152]. The Hf_9Ni_{11} was found to be isostructural to Zr_9Ni_{11}, with the lattice parameters a = 9.79 Å and c = 6.53 Å [12, 137, 157]. The crystal structure of Zr_7Ni_{10} was first reported to be a non-centrosymmetric orthorhombic structure with space group $Aba2$ by Kirkpatrick et al. [158]. Later on, Joubert et al. [159] corrected the crystal structure to be centrosymmetric orthorhombic structure with space group $Cmca$. The compound Hf_7Ni_{10} is reported to be isostructural with Zr_7Ni_{10} [12, 158, 159].

The compounds with Zr or Hf as a constituent element are very suitable for per-

turbed angular correlation (PAC) measurements using the probe ^{181}Hf. Due to chemical similarity, the probe ^{181}Hf occupies the Zr sites in the compounds with Zr. Using this technique, several studies in Hf/Zr-Ni systems were carried out earlier to investigate their EFGs and magnetic properties [160–167]. The hydrogen diffusion in the hydride alloys of Zr_2Ni were also studied earlier [56, 168–170] by PAC technique. The intermetallic compound $ZrNi_5$ was reported to have strong ferromagnetic properties by Drulis et al. [171]. A. Amamou [172] reported the electronic structure of various compounds in the Zr-Ni system, namely, Zr_2Ni, ZrNi, Zr_8Ni_{21} and $ZrNi_5$. From the studies in $ZrNi_5$ system by PAC technique [160, 173], however, no magnetic interaction was found, in contradiction with the result from previous measurements by Drulis et al. [171]. In order to help identifying the different phases produced in the investigated samples, the electric field gradients are calculated by density functional theory (DFT) and compared with the measured EFGs. The combination of PAC measurements and ab-initio calculations proved to be an excellent method to study the structural phase stabilities and the localization of the impurities in the host lattice [174, 175]. The temperature dependent PAC measurements enable us to find any structural phase transition/compositional phase changes in the material and give information on the structural stability of the compound. The secondary phases of small fractions that are produced along with the main phase can be determined quite accurately by this technique. As the EFG depends on the charge distribution of the probe-nucleus environment, the temperature evolution of the lattice properties such as crystallographic structure, imperfections or defects, can be monitored by applying PAC technique over a wide temperature range. To the best of our knowledge, there is no PAC measurement on Zr_8Ni_{21}/Hf_8Ni_{21}, $ZrNi_3/HfNi_3$, Zr_9Ni_{11}/Hf_9Ni_{11}, Zr_7Ni_{10}/Hf_7Ni_{10} binary alloys. These alloys are not generally produced in a pure single phase and multiple secondary phases were found to be produced along with the stoichiometric alloy [6, 69, 70, 75, 76]. Therefore, it is very important to study multiple phase components that are produced at high temperatures in these alloys which will help in the future development of MH with better electrochemical properties. Considering

their technological importances, these binary alloys have been studied by temperature dependent PAC measurements i) to determine the component phases in the samples from PAC, X-ray diffraction (XRD) and transmission electron microscopy/selected area electron diffraction (TEM/SAED) measurements ii) to determine the EFG for different phase components and compare the results with those obtained from theoretical calculations by density functional theory (DFT) considering the known crystal structure of the crystalline compound and iii) to determine the structural stability of the compounds with temperature from temperature dependent PAC studies. The compounds Hf_8Ni_{21}, Hf_7Ni_{10}, Hf_9Ni_{11} and $HfNi_3$ have been studied also by PAC technique to determine the isostructurality of isoformulae Zr-Ni and Hf-Ni compounds and to compare their temperature dependent properties. In Hf_7Ni_{10}, however, PAC measurements were carried out by Gil et al. [176]. These authors found five electric quadrupole frequencies from PAC measurements. But, the components were not assigned by comparing with DFT calculations.

5.4.2 Sample preparation

The intermetallic compounds Zr_8Ni_{21}/Hf_8Ni_{21}, $ZrNi_3/HfNi_3$, Zr_9Ni_{11}/Hf_9Ni_{11}, Zr_7Ni_{10}/Hf_7Ni_{10} were prepared by arc melting in an argon atmosphere. Stoichiometric amounts of high purity metals procured from Alfa Aesar were used to prepare the samples. The purity of Zr (excluding Hf), Hf (excluding Zr) and Ni metals used were 99.2%, 99.95% and 99.98% respectively. For the preparation of Zr_8Ni_{21}/Hf_8Ni_{21}, $ZrNi_3/HfNi_3$, Zr_9Ni_{11}/Hf_9Ni_{11} and Hf_7Ni_{10} compounds, the constituent metals were alloyed homogeneously by repeated melting and then activated by remelting with a tiny piece (<1 at%) of ^{181}Hf metal wire. It can be considered that addition of this very small impurity concentration will not affect stoichiometry of the samples and the sample properties. The Hf metal was activated in a similar manner as described in section 5.1.2. Barring in Hf_9Ni_{11} PAC sample, no appreciable mass loss of other samples were found during arc melting. In all cases,

shiny globule samples were formed and these were then sealed in evacuated quartz tubes for high temperature measurements. For the preparation of Zr_7Ni_{10} PAC sample, the shiny globule of Zr_7Ni_{10} was remelted with a tiny piece (<1 at%) of natural Hf metal wire. The sample was then activated to ^{181}Hf by following the similar procedure as described in section 5.1.2. Four detector $LaBr_3$(Ce)-BaF_2 PAC spectrometer were used for the PAC measurements in these alloys. For temperature dependent PAC measurements (up to 1073 K), a locally made resistive furnace was used. For measurement at 77 K, the sample is immersed in a liquid nitrogen dewar and placed at the center of the PAC table. Separate inactive stoichiometric samples of $ZrNi_3$/$HfNi_3$, Zr_9Ni_{11}/Hf_9Ni_{11} and Zr_7Ni_{10}/Hf_7Ni_{10} were prepared in similar manners for X-ray diffraction and TEM/SAED measurements. For Zr_8Ni_{21}/Hf_8Ni_{21}, different inactive samples were prepared only for XRD measurements. The X-ray powder diffraction measurements have been carried out using the Rigaku X-ray diffractometer TTRAX-III and Cu K_α radiation. Transmission electron microscopy (TEM) measurements were carried out using FEI, Tecnai G2 F30, S-Twin microscope equipped with a high angle annular dark-field (HAADF) detector, a scanning unit and a energy dispersive X-ray spectroscopy (EDX) unit to perform the scanning transmission electron microscopy (STEM-HAADF-EDX).

5.4.3 Zr_8Ni_{21} and Hf_8Ni_{21}

5.4.3.1 PAC results

Zr_8Ni_{21}

The XRD powder pattern of Zr_8Ni_{21} sample is shown in Figure 5.21. The X-ray analysis has been carried out using the known crystallographic data of Zr_8Ni_{21} [149]. Major peaks in the XRD spectrum are found due to the Zr_8Ni_{21} phase. If any small contaminating phases like Zr_7Ni_{10} or Zr_2Ni_7 are produced, it is not observed from from the present XRD powder pattern with high background noise.

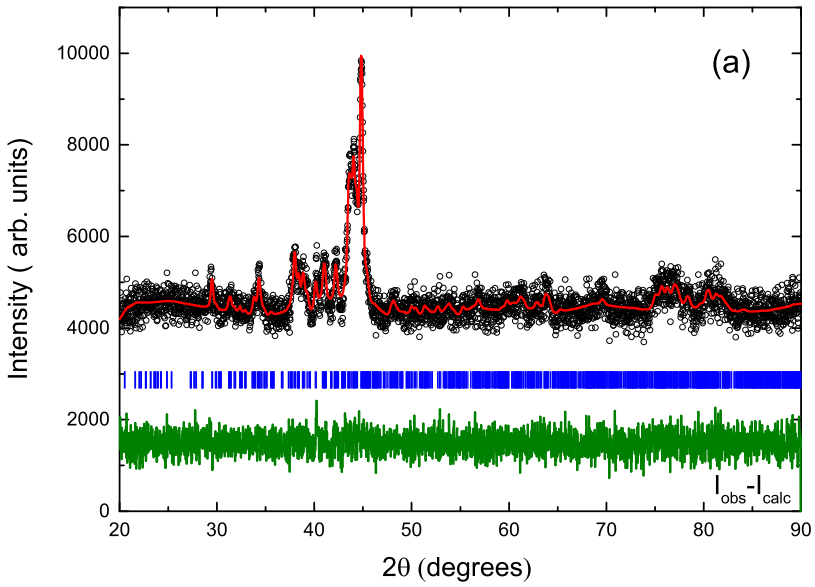

Figure 5.21: The XRD spectra in Zr_8Ni_{21} in as prepared sample. The line represents the fit to the measured data, the vertical bars denote the Bragg angles and the bottom line shows the difference between the observed and the fitted pattern.

The TDPAC spectra of ^{181}Ta in the as prepared sample of Zr_8Ni_{21} are shown in Figure 5.22. From PAC measurements, three frequency components at room temperature have been obtained. Two components ($Zr_8Ni_{21}^{(1)}$: ω_Q=75.8(2) Mrad/s, η=0.77(1) and $Zr_8Ni_{21}^{(2)}$: 100.6(8) Mrad/s, η=0.72(3)) have been attributed to Zr_8Ni_{21} by comparing with our PAC results in Hf_8Ni_{21} and results from ab-initio calculations by density functional theory (discussed later). The component $Zr_8Ni_{21}^{(1)}$ was predominantly produced (∼57%) and a minor fraction (∼15%) was observed due to $Zr_8Ni_{21}^{(2)}$ component. A secondary component (∼27%) has been attributed to Zr_7Ni_{10} (ω_Q=54.4(4) Mrad/s, η=0.69(1)). This follows from the previous X-ray EDS and SEM/TEM results reported by Shen et al. [6]. The characteristic frequency and η for this component are distinctly different than those found in Zr_2Ni_7 [166]. Moreover, assignment of this component can be supported from our PAC measurements in Zr_7Ni_{10} [177] where, a component similar to this was found. It is found that three frequency components are required to fit the spectra in the temperature range 77-373 K with no appreciable change in parameters. Variations of ω_Q, η and site fraction (f) with temperature for the two components of Zr_8Ni_{21} are

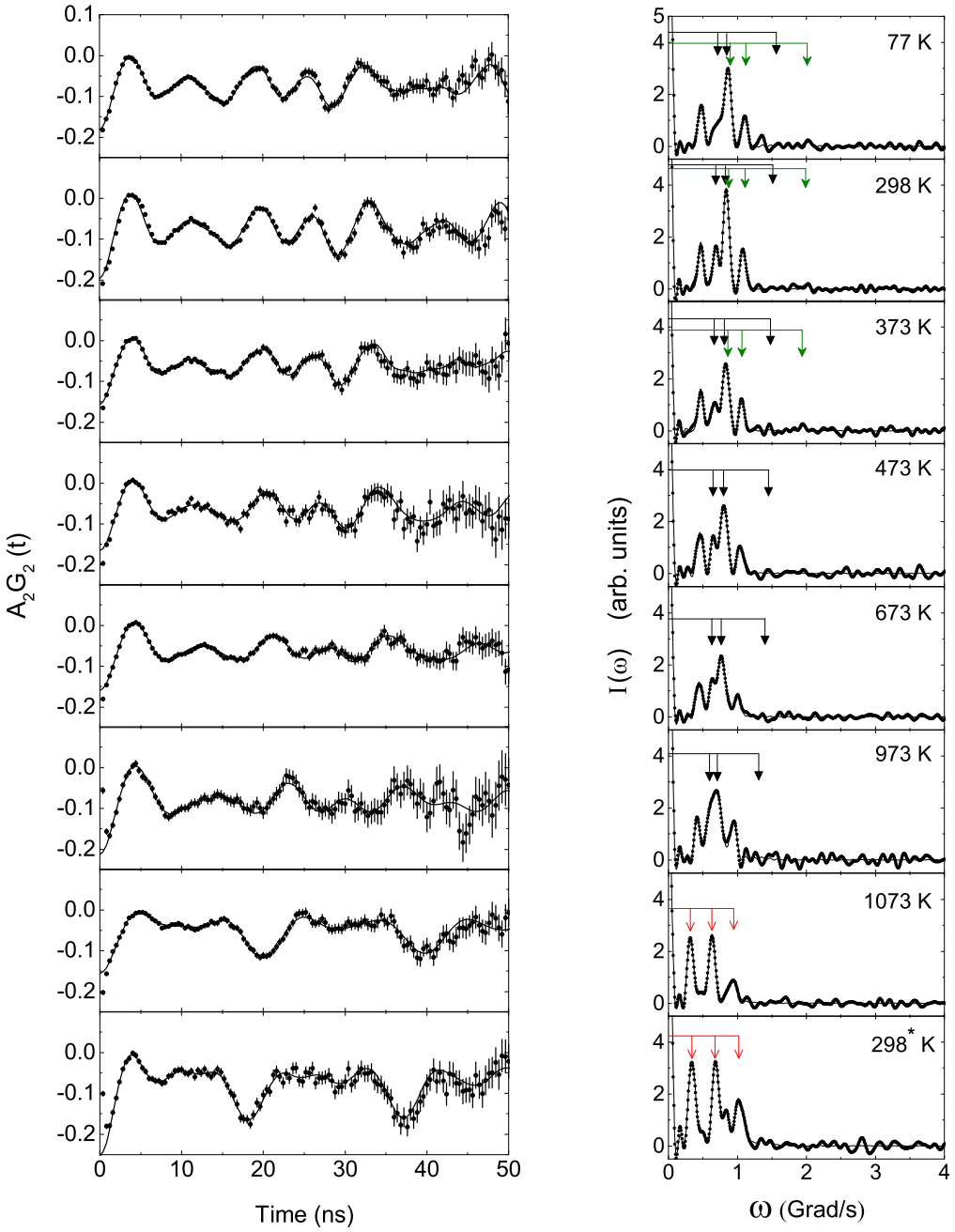

Figure 5.22: TDPAC spectra in Zr_8Ni_{21} at different temperatures. Left panel shows the time spectra and the right panel shows the corresponding Fourier transforms. The PAC spectrum designated by 298* K is taken after the measurement at 1073 K. The two sets of arrows in each Fourier spectrum (up to 373 K) correspond to two non-equivalent ^{181}Ta sites in Zr_8Ni_{21}. Arrows shown in the Fourier spectra at 1073 and 298* K correspond to Hf.

shown in Figure 5.23.

At 473 K, however, the PAC spectrum gives two components. The component $Zr_8Ni_{21}^{(2)}$

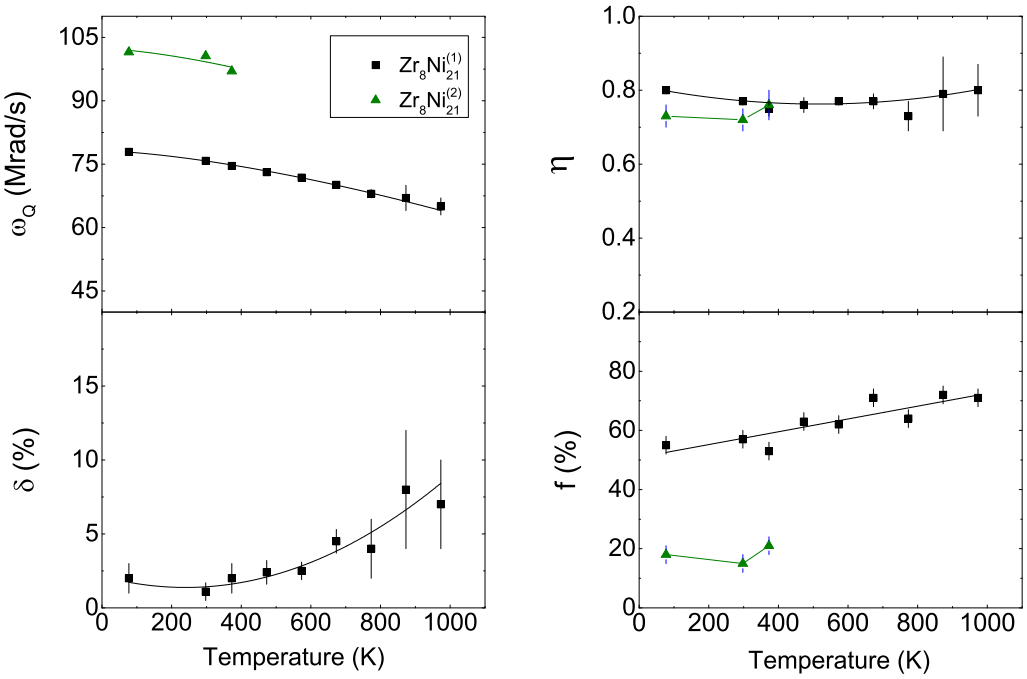

Figure 5.23: Variations of quadrupole frequency (ω_Q), asymmetry parameter (η) and site fraction $f(\%)$ with temperature for the two non-equivalent ^{181}Ta sites in Zr_8Ni_{21}. Variation of δ is shown for the component $Zr_8Ni_{21}^{(1)}$.

does not exist at this temperature. In the temperature range 473-973 K, no appreciable changes in results are observed. But at 1073 K, a drastic change in PAC spectrum is found. At this temperature, the predominant component (∼68%) produces a sharp decrease in quadrupole frequency and asymmetry parameter shows a value equal to zero. This possibly indicates a change in local environment of the probe. The component due to Zr_7Ni_{10}, on the other hand, remains almost unchanged.

To understand the change in PAC spectrum at 1073 K, we have repeated the PAC measurement at room temperature. In the re-measured spectrum at 298 K, the predominant component (∼70%) produces values of ω_Q ∼57 Mrad/s, η ∼0. At the remeasured room temperature, it is found that the major component of Zr_8Ni_{21} ($Zr_8Ni_{21}^{(1)}$) found initially at room temperature reappears with a much smaller fraction (23%). One additional new component is observed with a very small fraction (∼7%) which can be assigned to Zr_2Ni_7 (ω_Q=74(2) Mrad/s, η=0.21(10)) by comparing with the previous result in Zr_2Ni_7 [166]. From SEM/X-ray EDS measurement [6] also, Zr_2Ni_7 was found in a

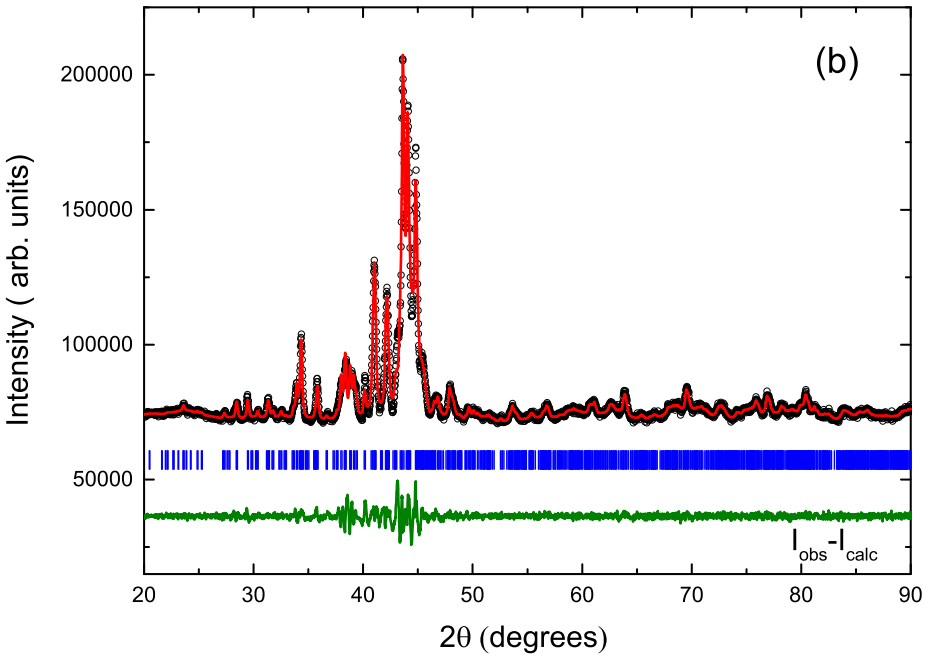

Figure 5.24: The XRD spectrum in Zr_8Ni_{21} annealed at 1073 K for two days. The line represents the fit to the measured data, the vertical bars denote the Bragg angles and the bottom line shows the difference between the observed and the fitted pattern.

sample of Zr_8Ni_{21} annealed at 1233 K. Detailed results of temperature dependent PAC measurements in Zr_8Ni_{21} can be found in the reference [22].

We have performed XRD measurement in a sample of Zr_8Ni_{21} annealed at 1073 K for two days. The XRD spectrum (Figure 5.24) shows peaks mainly due to Zr_8Ni_{21}. This indicates that no major structural or compositional phase transformation occurs at 1073 K.

Possible explanation for the predominant component observed at 1073 K and subsequently at room temperature is the following. Probably, the probe ^{181}Hf was not settled well at the position of Zr_8Ni_{21} and at 1073 K, these probe atoms got enough energy to go out from the position. The major component is, therefore, observed due to the Hf probe itself.

The electric field gradients in metal and intermetallic compound are found to vary with temperature following T or $T^{3/2}$ relationship [107]. In Zr_8Ni_{21}, it is found that

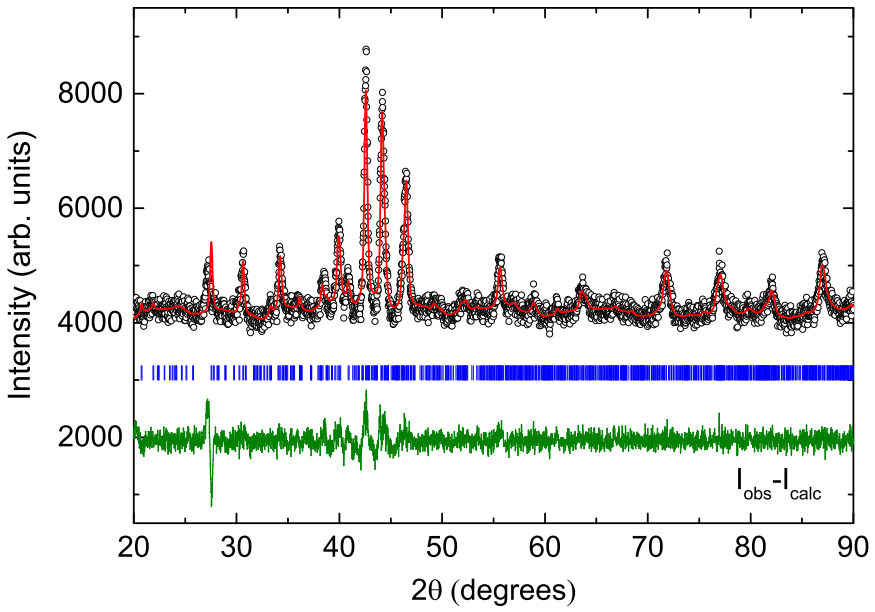

Figure 5.25: The background subtracted XRD powder pattern in Hf_8Ni_{21}. The line represents the fit to the measured data, the vertical bars denote the Bragg angles and the bottom line shows the difference between the observed and the fitted pattern.

quadrupole frequencies vary with $T^{3/2}$ for both components. For the predominant site $Zr_8Ni_{21}^{(1)}$ (present up to 973 K), the results are fitted by

$$\omega_Q(T) = \omega_Q(0)[1 - \beta T^{3/2}]. \tag{5.5}$$

A least squares fitting gives results $\omega_Q(0)$=78.2(1) Mrad/s and β=5.9(1)$\times 10^{-6}$ $K^{-3/2}$.

Hf_8Ni_{21}

The powder XRD pattern of Hf_8Ni_{21} is shown in Figure 5.25. The spectrum is fitted using the known crystallographic data of Hf_8Ni_{21} [150]. The X-ray analysis shows that there are no other peaks except for Hf_8Ni_{21} and this sample is also found to be produced in an almost pure single component phase. No contaminating phase is obtained from the XRD powder pattern.

The TDPAC spectra of ^{181}Ta in Hf_8Ni_{21} are shown in Figure 5.26. The spectrum at room temperature produces four interaction frequencies. The first two components at

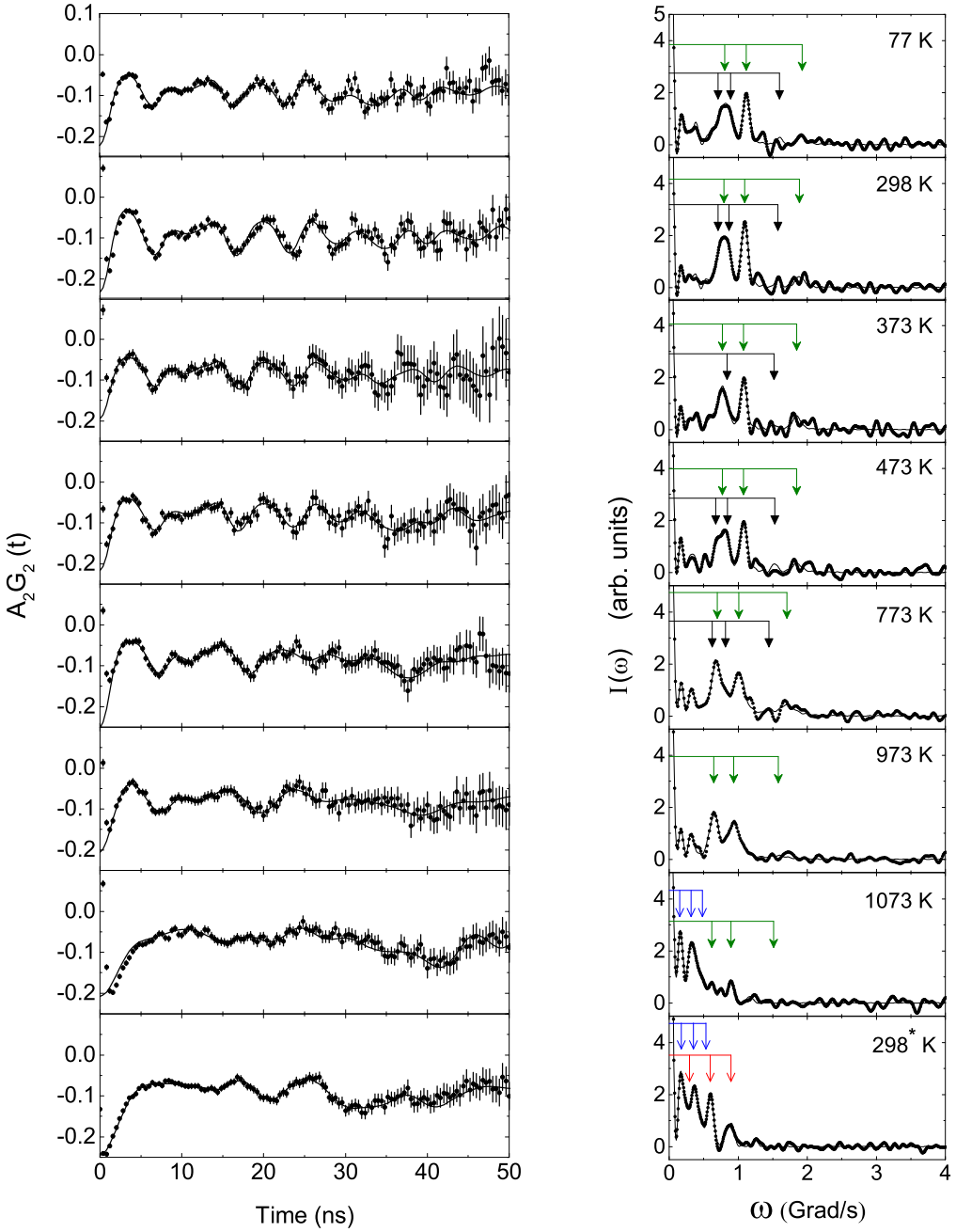

Figure 5.26: TDPAC spectra in Hf_8Ni_{21} at different temperatures. Left panel shows the time spectra and the right panel shows the corresponding Fourier transforms. The PAC spectrum designated by 298* K is taken after the measurement at 1073 K. The two sets of arrows in each Fourier spectrum (up to 773 K) correspond to two different ^{181}Ta sites in Hf_8Ni_{21}. Two sets of arrows in the Fourier spectrum at 298* K correspond to $HfNi_3$ and Hf.

room temperature with site fractions 63% ($Hf_8Ni_{21}^{(2)}$: ω_Q=97.3(3) Mrad/s, η=0.63(1)) and 21% ($Hf_8Ni_{21}^{(1)}$: ω_Q=79.1(7) Mrad/s, η=0.75(2)) are found to be quite similar to

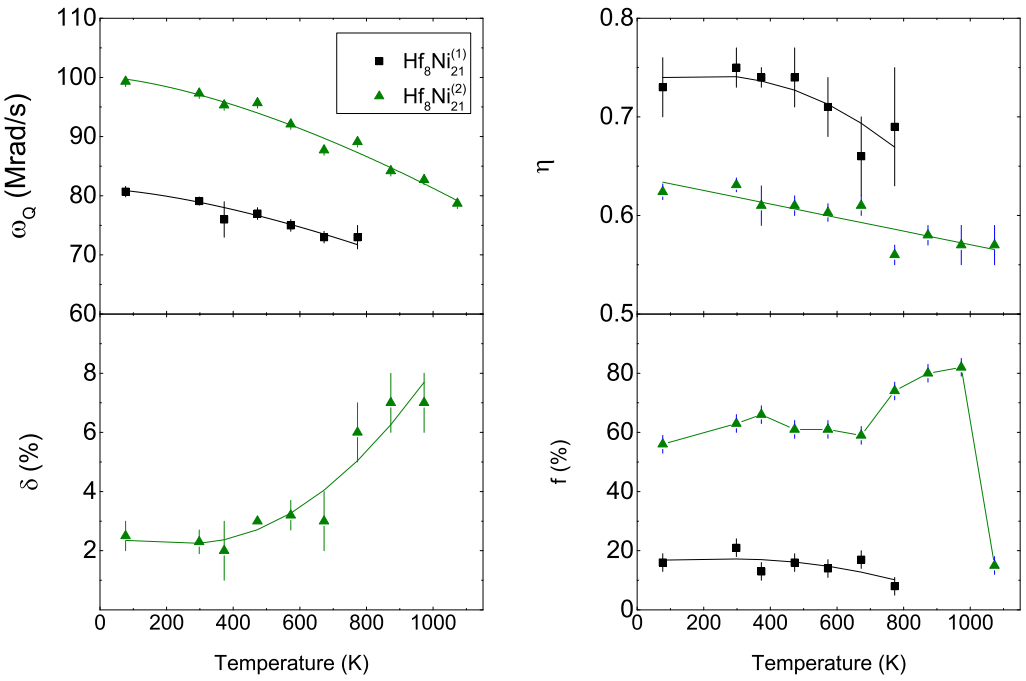

Figure 5.27: Variations of quadrupole frequency (ω_Q), asymmetry parameter (η) and site fraction $f(\%)$ with temperature for the two non-equivalent ^{181}Ta sites in Hf_8Ni_{21}. Variations of δ is shown for the site $Hf_8Ni_{21}^{(2)}$.

the components $Zr_8Ni_{21}^{(2)}$ and $Zr_8Ni_{21}^{(1)}$ found in Zr_8Ni_{21}, respectively. A weak component (∼10%) can possibly be attributed to $HfNi_3$ (ω_Q=31(1) Mrad/s, η=0) produced along with Hf_8Ni_{21} by comparing with the results obtained from our PAC measurements in $HfNi_3$ [23]. In $HfNi_3$, two non-equivalent EFG components were found and present values of ω_Q and η for the $HfNi_3$ phase match with one of its EFG components ($HfNi_3^{(1)}$). L. Bsenko [140] reported the decomposition of Hf_8Ni_{21} to $HfNi_3$ eutectoidally at 1175±10°C. This component has been found in the whole temperature range. The assignment of $HfNi_3$ in Hf_8Ni_{21} can be supported also from our PAC measurements in $HfNi_3$ [23] where a similar component to this was found. A very weak component (∼5%) found at room temperature can be attributed to Hf probe (ω_Q=50(2) Mrad/s, η=0) which is not settled in the compound. From our temperature dependent PAC measurements, it is found that all four components exist in the temperature range 77-673 K. The component due to Hf probe is not observed at 773 K and the minor site of Hf_8Ni_{21} ($Hf_8Ni_{21}^{(1)}$) disappears at 873 K. A drastic change in PAC spectrum is observed at 1073 K where the tentatively

assigned $HfNi_3$ component suddenly increases to ∼70% at the expense of Hf_8Ni_{21}. The component due to Hf_8Ni_{21} reduces to only 15%. Probably, the phase Hf_8Ni_{21} decomposed eutectoidally to $HfNi_3$ at 1073 K which is suggested from the Hf-Ni phase diagram [12]. At this temperature, a new frequency component is observed which probably can be attributed to Hf_2Ni_7 (ω_Q=63.3(9) Mrad/s, η=0.23(8)) by comparing its values with the results reported in the analogous compound Zr_2Ni_7 [166].

After measurement at 1073 K, a re-measurement at 298 K is carried out. In the re-measurement, $HfNi_3$ is found to be predominant (∼62%) which appeared as a minor fraction (∼10%) initially at room temperature. Here, no component due to Hf_8Ni_{21} is observed. A small component fraction of Hf_8Ni_{21} found at 1073 K and absence of this fraction at remeasured room temperature indicates that Hf_8Ni_{21} is not a stable phase approximately above 1000 K. It is found also that, the component due to Hf probe atom re-appears at this temperature with a higher component fraction (∼25%). The quadrupole frequency and asymmetry parameter for this component (ω_Q=50.8 Mrad/s, η=0) are very much similar to the values in a Hf metal [21]. Detailed results of temperature dependent PAC measurements in Hf_8Ni_{21} can be found in the reference [22].

Variations of ω_Q, η, δ and site fraction (f) for different components observed in Hf_8Ni_{21} in the temperature range 77-1073 K are shown in Figure 5.27. In Hf_8Ni_{21} also, the quadrupole frequencies for the two sites show $T^{3/2}$ temperature dependent behaviors. A least squares fitting (equation 5.5) for the predominant site (present up to 1073 K) gives values of $\omega_Q(0)$=100.1(5) Mrad/s, β=6.0(3)$\times10^{-6}$ $K^{-3/2}$. For the minor site (present up to 773 K), the fitted results are found to be $\omega_Q(0)$=81.2(4) Mrad/s, β=5.4(3)$\times10^{-6}$ $K^{-3/2}$. Similar values of β for both components indicate similar temperature dependent behaviors for the two sites. Also, the values of β are quite similar to the value of β in Zr_8Ni_{21} for the site $Zr_8Ni_{21}^{(1)}$.

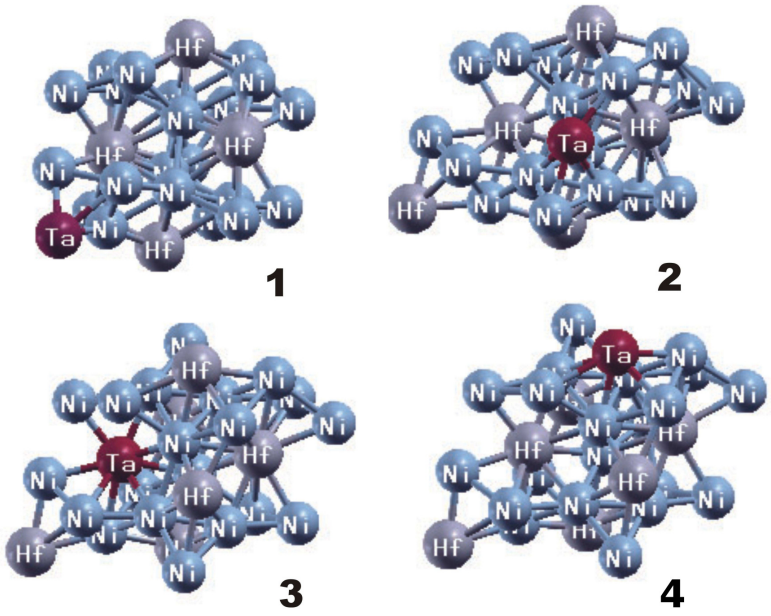

Figure 5.28: Models of four types of cells used in this study

5.4.3.2 DFT calculations

The first-principles density functional theory (DFT) calculations were performed to compare with the experimental results and to dispel the doubts existing in the interpretation of the experimental data. All the calculations were done with WIEN2k simulation package [7], based on the full potential (linearized) augmented plane waves method (FP-(L)APW). Electronic exchange-correlation energy was treated with generalized gradient approximation (GGA) parametrized by Perdew-Burke-Ernzerhof (PBE) [95]. In our calculations the muffin-tin radii for Zr, Ni and Ta (Hf) were 2.3, 2.2 and 2.4 a. u., respectively. The cut-off parameter $R_{mt}K_{max}$ for limiting the number of plane waves was set to 7.0, where R_{mt} is the smallest value of all atomic sphere radii and K_{max} is the largest reciprocal lattice vector used in the plane wave expansion.

The Brillouin zone integrations within the self-consistency cycles were performed via a tetrahedron method [178], using 18 k points in the irreducible wedge of the Brillouin zone (4×3×3 mesh). The atomic positions were relaxed according to Hellmann-Feynman

Table 5.3: Calculated EFG values in units of 10^{21} V/m^2 and asymmetry parameters

Probe	Lattice Site	EFG	η	Measured EFG extrapolated to 0 K	Measured η at 77 K
no probe (pure compound)	Zr(1) 2i 0.0691(4) 0.9052(3) 0.3147(3)	-3.5	0.82		
Zr_8Ni_{21}	Zr(2) 2i 0.2460(4) 0.4364(3) 0.0344(3)	-4.1	0.85		
	Zr(3) 2i 0.2462(4) 0.5604(3) 0.6070(3)	-5.0	0.88		
	Zr(4) 2i 0.5685(4) 0.0374(3) 0.2475(3)	-4.7	0.74		
^{181}Ta in Zr_8Ni_{21}	Zr(1) 2i 0.0691(4) 0.9052(3) 0.3147(3)	8.8	0.91	8.7(2)	0.80(1)
	Zr(2) 2i 0.2460(4) 0.4364(3) 0.0344(3)	-11.4	0.55		
	Zr(3) 2i 0.2462(4) 0.5604(3) 0.6070(3)	-12.5	0.78	11.4(1)	0.73(3)
	Zr(4) 2i 0.5685(4) 0.0374(3) 0.2475(3)	-12.3	0.56		
no probe (pure compound)	Hf(1) 2i 0.2487(3) 0.0620(3) 0.1072(3)	-11.5	0.75		
Hf_8Ni_{21}	Hf(2) 2i 0.0688(3) 0.4040(2) 0.8150(2)	-8.1	0.91		
	Hf(3) 2i 0.4312(3) 0.4633(3) 0.2543(3)	-10.8	0.69		
	Hf(4) 2i 0.2452(3) 0.9375(3) 0.5340(2)	-10.2	0.64		
^{181}Ta in Hf_8Ni_{21}	Hf(1) 2i 0.2487(3) 0.0620(3) 0.1072(3)	-13.3	0.71		
	Hf(2) 2i 0.0688(3) 0.4040(2) 0.8150(2)	9.6	0.88	9.1(1)	0.73(3)
	Hf(3) 2i 0.4312(3) 0.4633(3) 0.2543(3)	-12.5	0.60		
	Hf(4) 2i 0.2452(3) 0.9375(3) 0.5340(2)	-11.8	0.51	11.2(2)	0.62(1)

forces calculated at the end of each self-consistent cycle, with the force minimization criterion 2 mRy/a.u.. In our calculations the self-consistency was achieved by demanding the convergence of the integrated charge difference between last two iterations to be smaller than 10^{-5}. Both Zr_8Ni_{21} and Hf_8Ni_{21} crystallize in the triclinic $P\bar{1}$ type structure, which possesses 15 non-equivalent crystallographic positions [149, 150], 4 for Zr (Hf) atoms and 11 for Ni atoms. All Zr (Hf) non-equivalent positions have the same point group symmetry $2i$ and 3 Zr and 12 Ni atoms as nearest neighbors, except Zr(3), which has 2 Hf and 13 Ni. Each of the four non-equivalent Zr (Hf) atoms in the unit cell, stated in references [149, 150] was replaced by Ta subsequently (Figure 5.28, [179]) preserving the point group symmetry around original atom and then electric field gradients at thus created Ta positions were calculated using the method developed in reference [97]. The energy convergence for Hf_8Ni_{21} was between 0.00000035 and 0.00000065 Ry and for Zr_8Ni_{21}, the value was between 0.00003 and 0.00005 Ry.

The usual convention is to designate the largest component of the EFG tensor as V_{zz}. From the DFT calculations, sign as well as magnitude of the EFG is determined

whereas from PAC measurement, only magnitude of EFG is determined. The asymmetry parameter η is then given by $\eta = (V_{xx} - V_{yy})/V_{zz}$, where $|V_{zz}| \geq |V_{yy}| \geq |V_{xx}|$. The calculated EFGs in the pure compounds as well as at Ta probe positions in the investigated compounds are given in Table 5.3. It can be observed that there is not much difference in the EFG values for four non-equivalent Zr positions in the pure Zr_8Ni_{21} compound. EFG is the smallest at Zr1 and the largest at Zr3. This trend is preserved also for the electric field gradients calculated at the corresponding Ta positions, but the EFGs are now about 2.5 times larger. In the pure Hf_8Ni_{21} compound, EFG values are about doubled, as compared to the corresponding ones for Zr_8Ni_{21}, but the η values are similar. Here, also, introduction of Ta atom at one of the non-equivalent Hf sites, leads to increased EFG values.

5.4.3.3 Discussion

In the temperature range 77-373 K, Zr_8Ni_{21} PAC spectra consist of three frequency components. A uniform conversion from the measured quadrupole frequencies to the EFGs is achieved using the value of 2.36×10^{-28} m^2 [180] for the quadrupole moment of ^{181}Hf. By comparing the measured results for the EFGs and asymmetry parameters with the calculated ones (Table 5.3), two measured components are attributed to the two non-equivalent Zr sites in Zr_8Ni_{21}. The measured values of EFGs (8.7×10^{21} V/m^2 and 11.3×10^{21} V/m^2) and η (0.80 and 0.73) at 77 K are in excellent agreement with the calculated values for the two Zr sites in Zr_8Ni_{21}. However, as Ta doped Zr_8Ni_{21} has four non-equivalent crystallographic positions with similar EFG and asymmetry parameter (Table 5.3), in order to explain preferential site occupation, we performed ab initio total energy calculations for Ta doped Zr_8Ni_{21} and found that the configuration obtained when Ta replaces Zr(3) position has the lowest formation energy, about 0.013 eV lower than the structure when Ta is at Zr(1) postion. The formation energies of the remaining two configurations are about 0.1 eV higher.

At 1073 K, there is a drastic change of PAC spectrum in Zr_8Ni_{21}. At this temperature, EFG for the predominant component produces a zero value of η. A similar change in ^{181}Ta PAC spectra with increasing temperature above 650 K was observed in $TiPd_2$ compound [181] and was explained with the shift of Ta atom from Ti to Pd lattice site [181, 182], but in our case, DFT calculations excluded that possibility, as all of the non-equivalent Ni sites in Zr_8Ni_{21} has η which differs from zero. We find a resemblance of EFG and η for the major component ($\sim$70%) in Zr_8Ni_{21} at re-measured room temperature and a weak component ($\sim$5%) in Hf_8Ni_{21} at room temperature with the calculated values for Ta in pure Hf metal (6.7×10^{21} V/m^2 and $\eta = 0$).

The PAC spectrum for Hf_8Ni_{21} at room temperature consists of four components. The first two components with the EFG values 11.1×10^{21} V/m^2 and 9.0×10^{21} V/m^2 and the corresponding asymmetry parameters 0.62 and 0.73 (at 77 K) obviously correspond to the two different Hf positions in Hf_8Ni_{21} (Table 5.3). The measured results show that quadrupole frequencies for the two corresponding sites in Zr_8Ni_{21} and Hf_8Ni_{21} vary in similar manner with temperature.

5.4.3.4 Conclusion

We have presented the time differential perturbed angular correlations measurements and DFT calculations to determine the electric field gradients in Zr_8Ni_{21} and Hf_8Ni_{21} intermetallic compounds. Our results indicate that during the preparation of Zr_8Ni_{21} by arc melting, other phases like Zr_7Ni_{10} can also be formed. The same goes for Hf_8Ni_{21}, in which $HfNi_3$ compound was detected. In both Zr_8Ni_{21} and Hf_8Ni_{21}, EFGs for two non-equivalent sites of Zr/Hf, vary following $T^{3/2}$ relationship with temperature. Temperature dependent PAC measurement show that Hf_8Ni_{21} is probably not a stable phase above 1000 K.

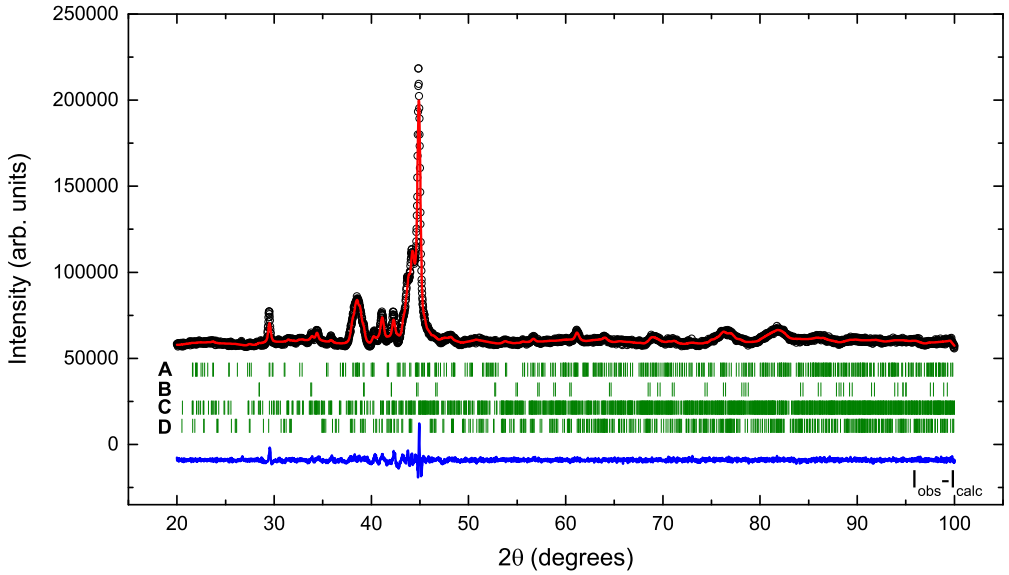

Figure 5.29: The background subtracted XRD powder pattern in the stoichiometric sample of $ZrNi_3$. The line represents the fit to the measured data. The vertical bars A, B, C and D denote the Bragg angles corresponding to Zr_2Ni_7, $ZrNi_3$, Zr_8Ni_{21} and Zr_7Ni_{10}, respectively. The bottom line shows the difference between the observed and the fitted pattern.

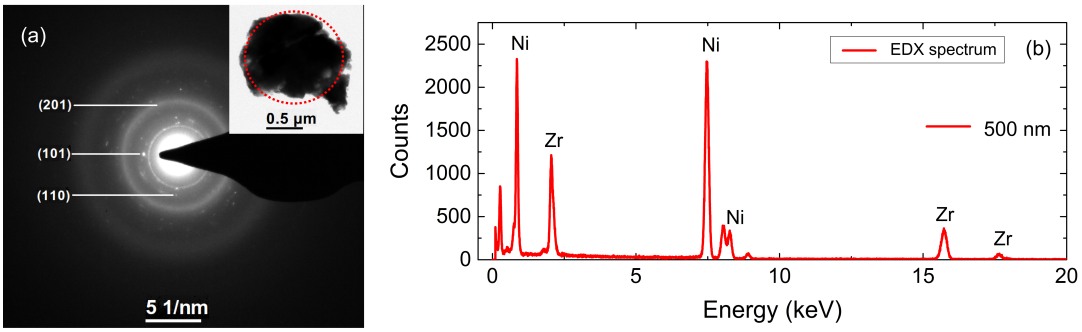

Figure 5.30: (a) Selected area electron diffraction pattern from $ZrNi_3$ particle shown in the inset. (b) Energy dispersive X-ray spectrum from the same particle.

5.4.4 $ZrNi_3$ and $HfNi_3$

5.4.4.1 PAC Results

Stoichiometric $ZrNi_3$ sample

The X-ray powder diffraction pattern found in the stoichiometric sample of $ZrNi_3$ is shown in Figure 5.29. The peaks in the spectrum were identified using ICDD database,

2009. Presence of Zr_2Ni_7 [PDF Card No.: 01-071-0543], $ZrNi_3$ [PDF Card No.: 01-029-0946], Zr_8Ni_{21} [PDF Card No.: 01-071-2622] and Zr_7Ni_{10} [PDF Card No.: 03-066-0045] phases have been found in the XRD spectrum. Analysis of the X-ray powder pattern was carried out by FullProf software package [183] using the known crystallographic parameters of Zr_2Ni_7 [184], $ZrNi_3$ [142], Zr_8Ni_{21} [149] and Zr_7Ni_{10} [159]. From present XRD analysis, refined values of lattice parameters obtained are shown in Table 5.5. The presence of $ZrNi_3$ phase in this stoichiometric sample of $ZrNi_3$ has been observed from TEM/EDX measurement (Figure 5.30) also. The atomic percentages for Zr and Ni at the indicated spot have been found to be 24.4(3) and 75.6(2), respectively. Selected area electron diffraction (SAED) pattern obtained from a region marked by a dotted circle for the same particle in the stoichiometric sample of $ZrNi_3$ is shown in Figure 5.30. Some of the measured interplaner spacings (d-spacing) from the SAED pattern are 2.07(4) Å, 2.86(4) Å and 3.60(4) Å. These measured d-spacings are very close to the (201), (110) and (101) inter-planer spacing of hexagonal $ZrNi_3$ (JCPDS # 29-0946), respectively. This further confirms the presence of $ZrNi_3$ phase in the sample.

The PAC spectrum in the stoichiometric sample of $ZrNi_3$ at room temperature is shown in Figure 5.31. The spectrum was best fitted by considering four electric quadrupole interactions. The sample produced was found to have non-random orientation of micro-crystals and the spectrum was fitted by considering free S_{2n} coefficients. The results of different components found are shown in Figure 5.32. The main frequency component ($\sim$48%) produces values of ω_Q=70.9(2) Mrad/s, η=0.25(2). This component can be assigned to Zr_2Ni_7 by comparing the values of ω_Q and η with the earlier reported results in Zr_2Ni_7 [161, 166]. From previous PAC measurements in $ZrNi_5$ also, a similar component to this was obtained and attributed to Zr_2Ni_7 [160, 173]. The $ZrNi_5$ has a cubic crystal structure and no EFG at the probe site is expected due to $ZrNi_5$. The component 2 (ω_Q=74.5(9) Mrad/s, η=0) with site percentage $\sim$13% can be attributed to $ZrNi_3$ by comparing with our calculated results from density functional theory (discussed later). The crystal structure of $ZrNi_3$ is hexagonal close-packed and, therefore, a value of η=0

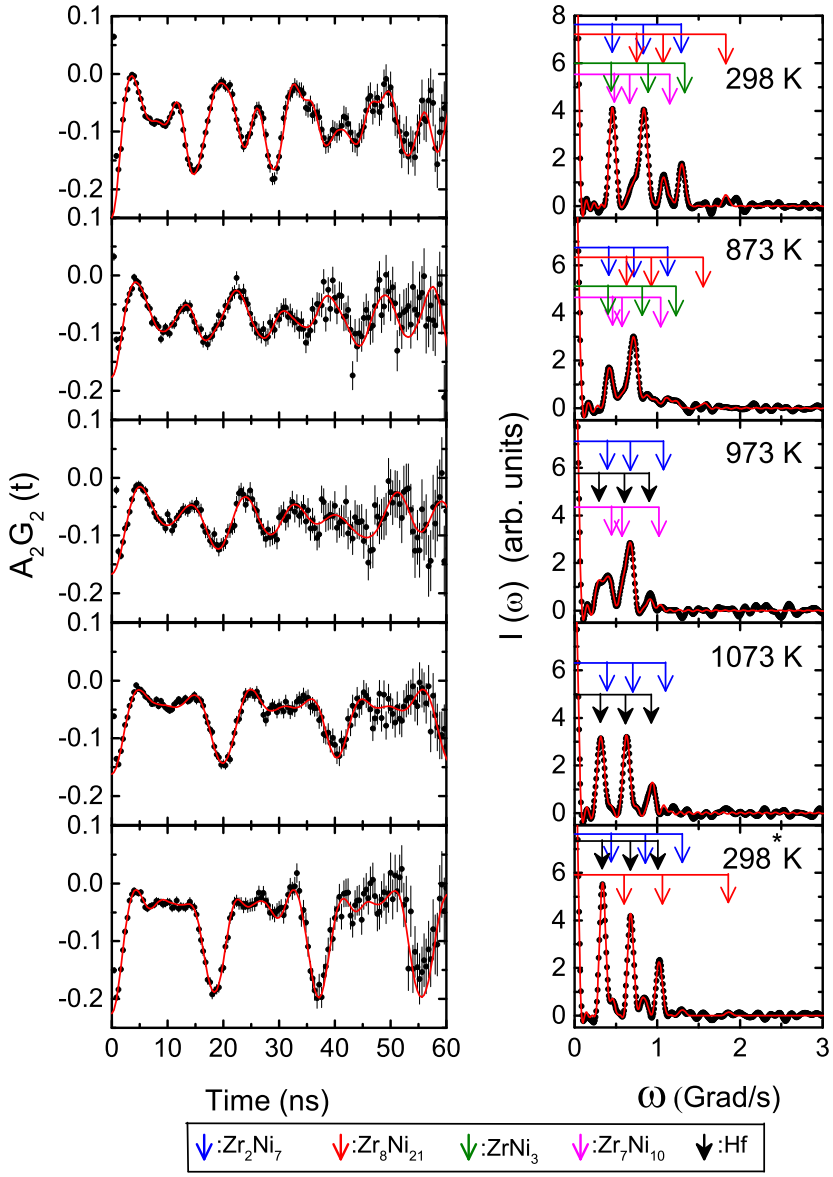

Figure 5.31: TDPAC spectra in the stoichiometric sample of $ZrNi_3$ at different temperature. Left panel shows the time spectra and the right panel shows the corresponding Fourier cosine transforms. The PAC spectrum at room temperature designated by 298* K is taken after the measurement at 1073 K. A set of three arrows indicates the three transition frequencies of a particular component.

is expected for this compound. However, this is found to be a minor phase compared to other phases produced in this sample. The results of component 3 (ω_Q=95.2(3) Mrad/s, η=0.603(8)) can be compared with our recent results in Zr_8Ni_{21} [22]. This component is found to be similar to one component of Zr_8Ni_{21} ($Zr_8Ni_{21}^{(2)}$) found from our previous measurements [22] and can, therefore, be attributed to Zr_8Ni_{21}. The component 4

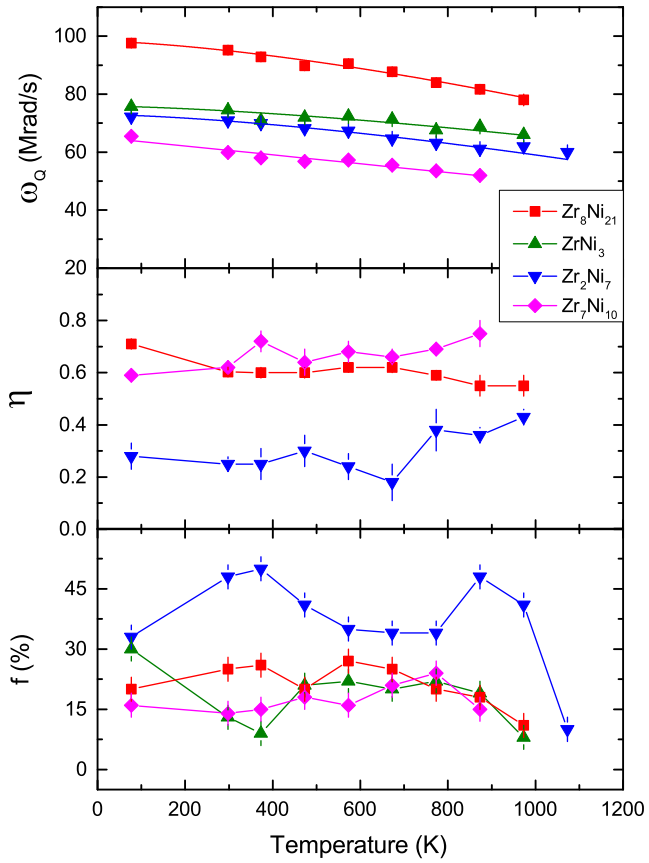

Figure 5.32: Variations of quadrupole frequency (ω_Q), asymmetry parameter (η) and site fraction $f(\%)$ with temperature for the components of Zr_2Ni_7, $ZrNi_3$, Zr_8Ni_{21} and Zr_7Ni_{10}.

(ω_Q=59.9(5) Mrad/s, η=0.62(2)) can be attributed to Zr_7Ni_{10} by comparing with the results found in Zr_7Ni_{10} [177]. A similar component to this was found in Zr_8Ni_{21} also where it was attributed to Zr_7Ni_{10} [22].

The results of temperature dependent PAC measurements in the stoichiometric $ZrNi_3$ are shown in the Figure 5.32. The corresponding TDPAC spectra are shown in Figure 5.31. It is found that the component fraction due to $ZrNi_3$ is present in the temperature range (77-973 K). At 77 K, the site fraction of $ZrNi_3$ was found to be maximum (∼30%). In the temperature range 77-873 K, four component fractions are found to be present with no appreciable change in parameters. The fractional variations of different components are shown in Figure 5.32. At 973 K, a distinct change in PAC spectrum has been observed. At this temperature, the component due to Zr_7Ni_{10} disappears. On the other

Table 5.4: Results of temperature dependent variations of ω_Q for different components in the stoichiometric samples of $ZrNi_3$ and $HfNi_3$.

Component phases	$\omega_Q(0)$ (Mrad/s)	$V_{zz}(0)$ ($\times 10^{21}$) V/m^2	α ($\times 10^{-4}$) K^{-1}	β ($\times 10^{-6}$) K$^{-3/2}$
Zr_2Ni_7	72.9(4)	8.2(1)		6.2(4)
$ZrNi_3$	76(1)	8.5(1)		4.3(6)
Zr_8Ni_{21}	98.2(5)	11.0(2)		6.5(3)
Zr_7Ni_{10}	64(2)	7.3(1)	2.3(3)	
$HfNi_3^{(1)}$	32.9(4)	3.7(1)	1.6(2)	
$HfNi_3^{(2)}$	65.7(4)	7.3(1)		7.0(4)
Hf_2Ni_7	72.2(4)	8.1(1)		5.7(2)
Hf_8Ni_{21}	99.3(6)	11.1(2)		6.6(4)
Hf	53.3(6)	6.0(1)	0.8(2)	

hand, a new frequency component with values of ω_Q=53.0(4) Mrad/s, η=0 appears. This component is similar to that found in Zr_8Ni_{21} at 1073 K [22]. The site percentage of this new component is found to be ∼39% at this temperature and it enhances abruptly at 1073 K (∼90%). At 1073 K, only two components are found to be present. The minor component found at this temperature is due to Zr_2Ni_7. At this temperature, $ZrNi_3$ and Zr_8Ni_{21} phases completely disappear. We have repeated the measurement at room temperature after the measurement at 1073 K. The remeasured spectrum at room temperature produces a strong electric quadrupole interaction (∼81%) with values of ω_Q=56.5(1) Mrad/s, η=0. This component can be recognized as the same component that appeared at 973 and 1073 K. Besides this, two other minor components are found here. The component due to Zr_8Ni_{21} reappears with a small fraction (∼8%) and the component due to Zr_2Ni_7 is also found to be present (∼10%). No component of $ZrNi_3$ at room temperature after heating the sample to 1073 K has been observed. This indicates a decomposition of $ZrNi_3$ at 1073 K. Detailed results of temperature dependent PAC measurements in $ZrNi_3$ can be found in the reference [185].

From previous XRD measurements [186], $ZrNi_3$ was found to be produced after heating ZrCrNi-H_2 system to 1024 K and a decomposition of $ZrNi_3$ to Zr_2Ni_7 was observed [186] after heating the sample to 1083 K. The results of present PAC measurements, therefore, support the results of previous XRD measurements [186]. On the other hand,

decomposition of $ZrNi_3$ at 1213 K as reported by Becle et al. [142] is not supported.

In the present Zr-Ni sample, the predominant component found at 1073 K and subsequently at room temperature can probably be assigned to Hf. At temperatures below 973 K, the probe atoms which were settled at various lattice sites come out from the lattice positions after gaining sufficient energy at high temperature. It seems that at 973 K, probe atoms have detached partially (∼39%) from the Zr-Ni compounds and at 1073 K, only a small fraction of the probe nucleus (∼10%) is attached with the compounds. A similar phenomenon was observed from our recent PAC investigation in Zr_8Ni_{21} [22].

The evolution of quadrupole frequency, asymmetry parameter and site fraction with temperature for different components observed are shown in Figure 5.32. It is found that quadrupole frequencies for the components Zr_2Ni_7, $ZrNi_3$ and Zr_8Ni_{21} vary with temperature following $T^{3/2}$ relationship. For the Zr_8Ni_{21} component, a similar temperature dependent behavior was observed from our previous PAC investigation in Zr_8Ni_{21} [22]. For these three components, values of ω_Q have been fitted using a $T^{3/2}$ temperature dependent relationship (equation 5.5). The results of η and site fraction for different components are also plotted (Figure 5.32). These results do not show large variations except the site fraction of Zr_2Ni_7 which decreases drastically at 1073 K (∼10%) compared to the fraction found at 973 K (∼41%). The fitted results are listed in Table 5.4. Contrary to these, ω_Q for the component Zr_7Ni_{10} is found to obey a linear temperature dependent behavior. In this case, we have fitted the results of $\omega_Q(T)$ using a linear temperature dependent relationship

$$\omega_Q(T) = \omega_Q(0)[1 - \alpha T]. \tag{5.6}$$

Both $T^{3/2}$ and T variations of EFG (proportional to ω_Q) for metallic and intermetallic systems are found in literature [107, 108, 187].

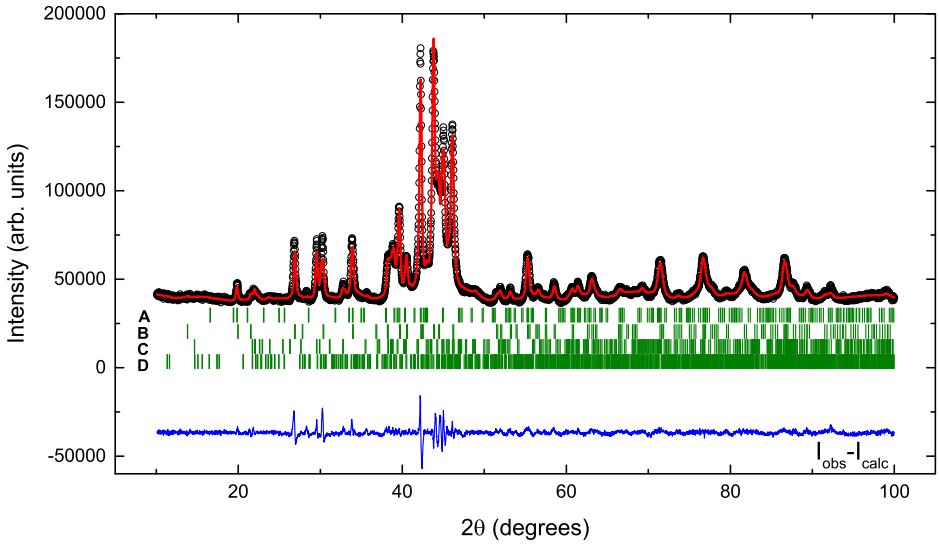

Figure 5.33: The background subtracted XRD powder pattern in $HfNi_3$. The line represents the fit to the measured data. The vertical bars A, B, C and D denote the Bragg angles corresponding to β-$HfNi_3$, α-$HfNi_3$, Hf_2Ni_7 and Hf_8Ni_{21}, respectively. The bottom line shows the difference between the observed and the fitted pattern.

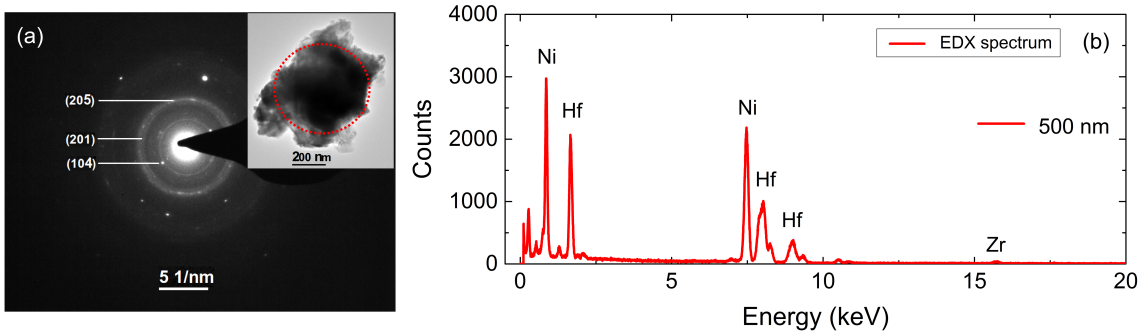

Figure 5.34: (a) Selected area electron diffraction pattern from β-$HfNi_3$ particle shown in the inset. (b) Energy dispersive X-ray spectrum from the same particle.

Stoichiometric $HfNi_3$ sample

The XRD measurement in the stoichiometric sample of $HfNi_3$ has been carried out at room temperature (Figure 5.33). The peaks in the spectrum were identified using ICDD database, 2009. Presence of β-$HfNi_3$ [PDF Card No.: 01-071-0476], α-$HfNi_3$ [PDF Card No.: 01-071-0474], Hf_2Ni_7 [PDF Card No.: 01-074-6880] and Hf_8Ni_{21} [PDF Card No.: 01-074-0476] phases have been found in the XRD spectrum. Analysis of the X-ray powder pattern was carried out by FullProf software package [183] using the known

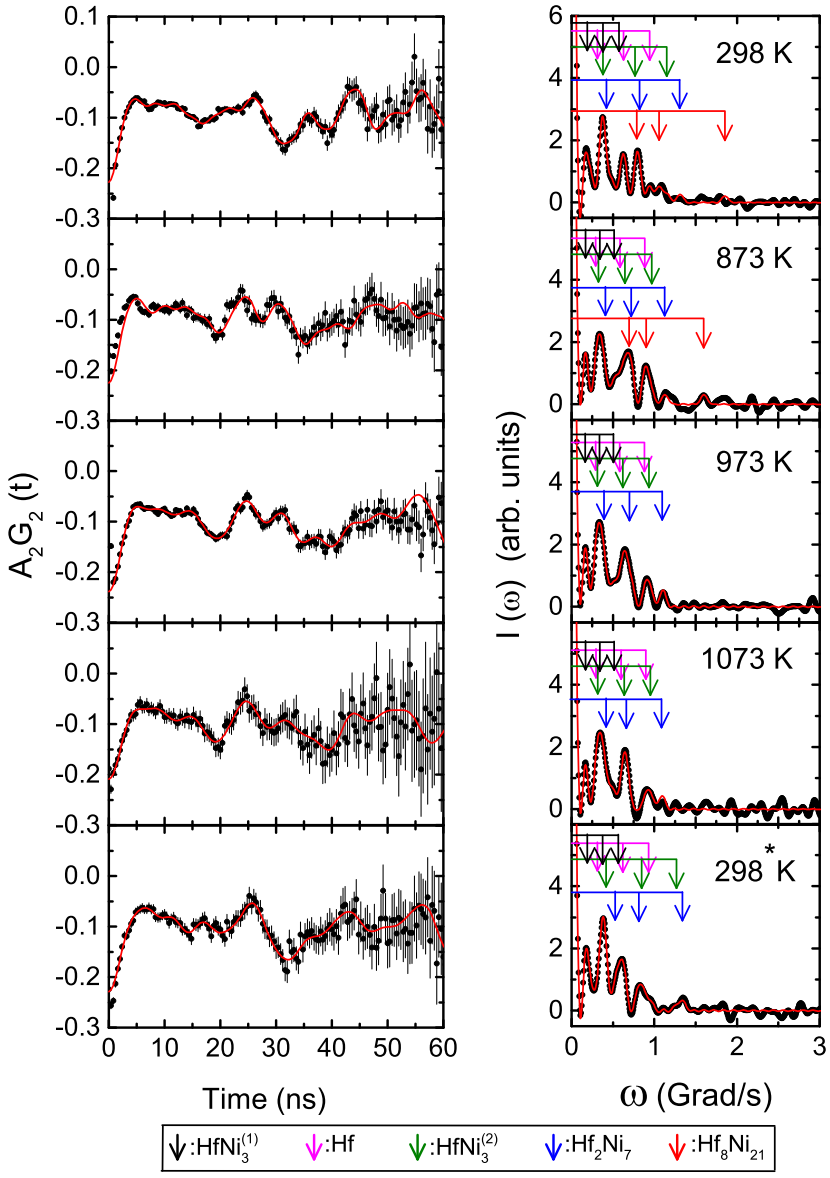

Figure 5.35: TDPAC spectra in the stoichiometric sample of $HfNi_3$ at different temperature. Left panel shows the time spectra and the right panel shows the corresponding Fourier cosine transforms. The PAC spectrum at room temperature designated by 298* K is taken after the measurement at 1073 K. A set of three arrows indicates the three transition frequencies of a particular component.

crystallographic data of β-$HfNi_3$ [151], α-$HfNi_3$ [151], Hf_2Ni_7 [188] and Hf_8Ni_{21} [150]. From present XRD analysis, refined values of lattice parameters found are shown in Table 5.5. It was reported [140] that high temperature phase of $HfNi_3$ was formed from the melt and Hf_2Ni_7 by peritectic reaction. Apart from $HfNi_3$, there are phases due to Hf_2Ni_7 and Hf_8Ni_{21}. But, no prominent peak due to Hf_7Ni_{10} was found in the XRD

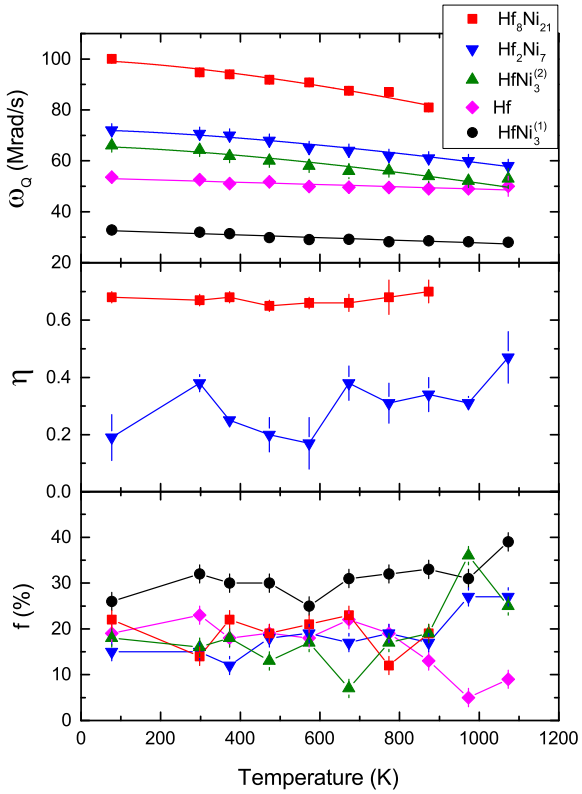

Figure 5.36: Variations of quadrupole frequency (ω_Q), asymmetry parameter (η) and site fraction $f(\%)$ with temperature for $HfNi_3^{(1)}$, $HfNi_3^{(2)}$, Hf_2Ni_7, Hf_8Ni_{21} and Hf.

spectrum. The phase $HfNi_3$ has been observed from our TEM/EDX measurement also (Figure 5.34). The atomic percentages for Hf and Ni at the indicated spot have been found to be 24.4(2) and 74.3(2), respectively. The SAED pattern obtained from a region marked by a dotted circle for the same particle in the stoichiometric sample of $HfNi_3$ is shown in Figure 5.34. Some of the measured interplaner spacings (d-spacing) from the SAED pattern are 2.06(4) Å, 2.31(4) Å and 3.41(4) Å. These measured d-spacings are very close to the (205), (201) and (104) inter-planer spacing of hexagonal β-$HfNi_3$ (JCPDS # 71-0475), respectively. This further confirms the presence of β-$HfNi_3$ phase in the sample.

The PAC spectrum observed in $HfNi_3$ at room temperature after preparing the sample in argon arc furnace is shown in Figure 5.35. It is found that five electric quadrupole frequencies are required to fit the time spectrum. Analysis was done by considering free S_{2n}

coefficients. The major component (∼32%) found with values of ω_Q=32.0(3) Mrad/s, η=0 can be attributed to $HfNi_3$ ($HfNi_3^{(1)}$) by comparing with our calculated results from DFT (discussed later). From our previous studies in Hf_8Ni_{21} [22] and Hf_7Ni_{10} [177], a component similar to this was observed and tentatively assigned to $HfNi_3$. Component 2 (ω_Q=64.3(8) Mrad/s, η=0) with site fraction ∼16% can also be attributed to $HfNi_3$ ($HfNi_3^{(2)}$) because the values of EFG and asymmetry parameter for this component are found to be in good agreement with the calculated results from DFT (discussed later). The component 3 (ω_Q=70.6(6), η=0.38(3)) with site fraction ∼15% has been attributed to Hf_2Ni_7 by comparing with the earlier reported results in Hf_2Ni_7 [160, 161]. From previous PAC measurement in $HfNi_5$, a similar component to this was also found and attributed to Hf_2Ni_7 [160]. The component 4 (∼14%) with values of ω_Q=94.8(6) Mrad/s and η=0.67(2) can be assigned to Hf_8Ni_{21}. From our recent investigation in Hf_8Ni_{21} [22], similar values of quadrupole frequency and asymmetry parameter were found. In Hf_8Ni_{21}, however, two non-equivalent Hf sites were found. But, in this stoichiometric $HfNi_3$ sample, we have found only one site of Hf_8Ni_{21} ($Hf_8Ni_{21}^{(2)}$). The other non-equivalent site of Hf_8Ni_{21} ($Hf_8Ni_{21}^{(1)}$) is not observed here. Besides these, a component with symmetric EFG (ω_Q=52.6(4) Mrad/s, η=0) was found with site fraction ∼23% which can be attributed to pure hcp Hf by comparing the values of ω_Q and η with earlier reported results [21]. Probably, this component arises due to unreacted Hf with Ni. Decrease of this component at 973 and 1073 K indicates that more Hf reacts with Ni to form compounds at high temperatures.

Temperature dependent PAC results are shown in Figure 5.36. The corresponding PAC spectra are shown in Figure 5.35. In the temperature range 77-873 K, there are no appreciable changes in the PAC spectra. At 973 K, the component Hf_8Ni_{21} disappears. The component due to Hf_8Ni_{21} does not appear at 1073 K also. But other four components are found to exist at 1073 K. However, unlike stoichiometric $ZrNi_3$, no additional component is observed at 1073 K. The PAC measurement was then repeated at room temperature. At this temperature, two components of $HfNi_3$ reappear which indicates

that $HfNi_3$ is a stable phase. The component Hf_8Ni_{21} does not appear when remeasured at room temperature. The components of Hf_2Ni_7 and Hf are found to be present when remeasured at room temperature. Detailed results of temperature dependent PAC measurements in $HfNi_3$ can be found in the reference [185].

The evolution of the quadrupole frequency, η and site fraction with temperature for the different components observed in stoichiometric $HfNi_3$ are shown in Figure 5.36. The components Hf_8Ni_{21} and Hf_2Ni_7 follow the same $T^{3/2}$ temperature dependence as found for Zr_8Ni_{21} and Zr_2Ni_7 in $ZrNi_3$. The EFG for the two components of $HfNi_3$ are found to vary different manner. The quadrupole frequency of $HfNi_3^{(2)}$ varies with temperature following $T^{3/2}$ relationship (equation 5.5). On the other hand, a linear temperature dependent behavior (equation 5.6) was found for the $HfNi_3^{(1)}$ component. Variation of the quadrupole frequency for the hexagonal Hf was also found to be linear. The fitted results are shown in Table 5.4. The variations of η and site fractions for different components do not show large changes (Figure 5.36).

5.4.4.2 DFT calculations

The first-principles density functional theory (DFT) calculations were performed with the WIEN2k simulation package [7] based on the full potential (linearized) augmented plane waves method (FP-(L)APW). Electronic exchange-correlation energy was treated with generalized gradient approximation (GGA) parametrized by Perdew-Burke-Ernzerhof (PBE) [95]. In our calculations the muffin-tin radii for Hf, Ni, Zr and Ta were 2.3, 2.1, 2.3 and 2.3 a. u., respectively. The cut-off parameter $R_{mt}K_{max}$ for limiting the number of plane waves was set to 7.0, where R_{mt} is the smallest value of all atomic sphere radii and K_{max} is the largest reciprocal lattice vector used in the plane wave expansion.

The Brillouin zone integrations within the self-consistency cycles were performed via a tetrahedron method [178], using 6-50 k points in the irreducible wedge of the Brillouin zone (4×4×2 and 8×8×8 meshes for Ta doped $HfNi_3$ and $ZrNi_3$, respectively) for the su-

Table 5.5: The parameters of the β-$HfNi_3$ and $ZrNi_3$ structure, given in Å.

	Our calculated results (WIEN 2k) [7, 189]	Previous experimental results (X-ray diffraction) [142, 151]	Earlier calculated results [190]	Present experimental results (X-ray diffraction)
β-$HfNi_3$				
a	5.285	5.2822(2)	5.267	5.282(1)
c	21.419	21.3916(18)	21.411	21.392(2)
B [GPa]	186			
Hf 2b	0 0 1/4	0 0 1/4	0 0 1/4	
Hf2 4f	1/3 2/3 0.3488	1/3 2/3 0.3488	1/3 2/3 0.3489	
Hf3 4f	1/3 2/3 0.5458	1/3 2/3 0.5458	1/3 2/3 0.5461	
Ni 6h	0.5110 0.022 1/4	0.5117 0.0234 1/4	0.5107 0.0213 1/4	
Ni2 12k	0.156 0.312 0.0514	0.156 0.312 0.0514	0.1563 0.3126 0.0512	
Ni3 12k	0.8320 0.6640 0.1495	0.8316 0.6632 0.1495	0.8322 0.6645 0.1496	
$ZrNi_3$				
a	5.319	5.3090(8)	5.267	5.308(2)
c	4.305	4.3034(12)	21.411	4.303(1)
B [GPa]	177			
Zr 2c	1/3 2/3 1/4	1/3 2/3 1/4	1/3 2/3 1/4	
Ni 6h	0.8435 0.687 1/4	0.829 0.658 1/4	0.844291 0.688581 1/4	

Table 5.6: Calculated EFG values for $HfNi_3$ in units of 10^{21} V/m^2 and asymmetry parameters

Probe	Lattice Site	EFG	asymmetry parameter (η)
no probe (pure compound)	Hf1 2b 0 0 1/4	-1.3	0
	Hf2 4f 1/3 2/3 0.3488(2)	-5.0	0
	Hf3 4f 1/3 2/3 0.5458(1)	-2.2	0
^{181}Ta	Hf1 2b 0 0 1/4	-1.7	0
	Hf2 4f 1/3 2/3 0.3488(2)	-7.1	0
	Hf3 4f 1/3 2/3 0.5458(1)	-3.5	0

percell calculations. The atomic positions were relaxed according to Hellmann-Feynman forces calculated at the end of each self-consistent cycle, with the force minimization criterion 2 mRy/a.u.. In our calculations the self-consistency was achieved by demanding the convergence of the integrated charge difference between last two iterations to be smaller than 10^{-5} e. All the calculations refer to zero temperature.

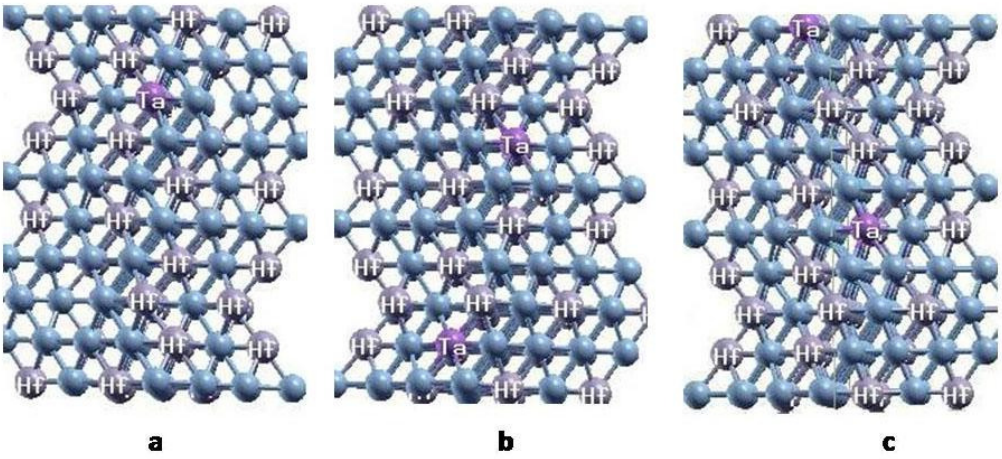

Figure 5.37: Models of cells used in the study of $HfNi_3$

$HfNi_3$

$HfNi_3$ at the temperatures below 1200°C, has the γ-Ta(Pd,Rh)$_3$-type structure, with a stacking of ten AB_3 layers in the sequence ABCBCACBCB. The space group is $P6_3/mmc$ and the unit cell dimensions are a=5.2822(2) Å, c=21.3916(18) Å at room temperature [151]. This structure contains 40 atoms in the unit cell, distributed at 6 non-equivalent crystallographic positions, 3 for Hf atoms and 3 for Ni atoms (Table 5.5).

After obtaining the optimized structural parameters, we constructed 2×2×1 supercell from periodically repeating unit cells of the host crystals. To simulate PAC measurements at Hf1 position, we replaced one Hf atom in the supercell at the position (0 0 1/4) with Ta (Figure 5.37a [179]). In the case of Ta at the Hf2 and Hf3 positions due to the complexity of the calculations, we had to replace two Hf atoms at the corresponding position with Ta, thus obtaining the cell with 50 non-equivalent atoms (Figure 5.37b and c). We checked that the two Ta atoms are sufficiently far from each other (11.1 Å) to avoid significant impurity-impurity interactions. After determing the self-consistent charge density we obtain the electric field gradient (EFG) tensor V_{ij} using the method developed in reference [97]. The usual convention is to designate the largest component of the EFG tensor as V_{zz}. The asymmetry parameter η is then given by η= (V_{xx}-V_{yy})/V_{zz}, where $|V_{zz}| \geq |V_{yy}| \geq |V_{xx}|$. All the calculations refer to zero temperature.

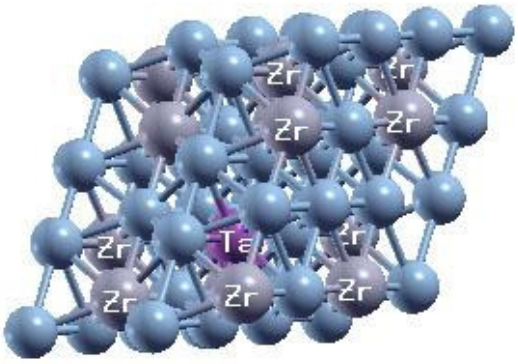

Figure 5.38: Model of cell used in the study of $ZrNi_3$

The theoretically determined cell and structure parameters for the investigated structure, along with the experimental values obtained from X-ray diffraction measurements are given in Table 5.5. The theoretical volume slightly overestimates the experimental one. The bulk modulus B_0, obtained by fitting the data to the Murnaghan's equation of state [189] is also given in Table 5.5. The calculated formation enthalpy, -0.50 eV/atom, is in good agreement with the earlier measured (-0.52 eV/atom [191]) and calculated (-0.44 eV/atom [146], -0.54 eV/atom [192]) values.

The calculated EFGs in the pure compound as well as at Ta probe position in the β-$HfNi_3$ are given in Table 5.6. It can be observed that EFG is smallest at Hf1 position and the largest at Hf2 position. This trend preserves also for the electric field gradients calculated at corresponding Ta positions, but the EFGs are now larger from 30% to 60%. We see that the calculated result for EFG at the Ta probe site replacing Hf3 atom (3.5×10^{21} V/m^2) is in excellent agreement with the measured value of EFG=$3.7(1)\times10^{21}$ V/m^2 ($\omega_Q(0)$=32.9(4) Mrad/s) for the component $HfNi_3^{(1)}$, thus confirming that the mentioned component of the measuered PAC spectra originates from $HfNi_3$. Similarly, the calculated results at the Ta probe site replacing Hf2 atom ($V_{zz}=7.1\times10^{21}$ V/m^2 and η=0) are in excellent aggrement with our measured values of $HfNi_3^{(2)}$ component ($V_{zz}(0)=7.3(1)\times10^{21}$ V/m^2 and η=0) which confirms that this component also originates from $HfNi_3$.

$ZrNi_3$

$ZrNi_3$ crystallizes in the hexagonal Ni_3Sn type structure, which possesses two non-equivalent crystallographic positions, Zr 2c and Ni 6h [142]. The optimized lattice constants, which slightly overestimate the experimental values, are given in Table 5.5. The calculated formation enthalpy, -0.41 eV/atom, agrees well with the earlier calculated (-0.36 eV/atom [146], -0.46 eV/atom [193]) values. The calculated EFG at Zr position is -3.0×10^{21} V/m^2, with zero asymmetry parameter. In order to simulate PAC measurement, we constructed 2×2×2 supercell from periodically repeating unit cell and then replaced one of the Zr atoms by Ta (Figure 5.38 [179]). The point group symmetry around the impurity Ta atom remained the same as around the original Zr atom, but the number of non-equivalent positions increased. The calculated EFG at the Ta probe atom -8.4×10^{21} V/m^2 is in excellent agreement with two mutually similar EFG values from measured PAC spectra (8.2 and 8.48×10^{21} V/m^2, corresponding to $\omega_Q(0)$= 72.9 and 76 Mrad/s, respectively). The fact that the corresponding calculated asymmetry parameter is zero, enables us to assign the 76 Mrad/s component to $ZrNi_3$ and thus definitely confirm the presence of this phase in our stoichiometric sample.

5.4.4.3 Conclusion

From TDPAC and XRD measurements, multiple phases have been found in the stoichiometric samples of $ZrNi_3$ and $HfNi_3$. The presence of $ZrNi_3$ and $HfNi_3$ in these stoichiometric samples have been confirmed from TDPAC, XRD and TEM/EDX measurements. From PAC studies, it is found that $ZrNi_3$ is produced as a minor phase while the phase $HfNi_3$ is found to be largely produced. Also, our temperature dependent PAC studies show that $HfNi_3$ is a very stable phase. In the stoichiometric samples of $ZrNi_3$ and $HfNi_3$, secondary phases due to $(Zr/Hf)_8Ni_{21}$ and $(Zr/Hf)_2Ni_7$ are found to be produced. In $ZrNi_3$, the phase due to Zr_7Ni_{10} is observed while no phase due to Hf_7Ni_{10} is found in $HfNi_3$ sample. Only one and the same crystallographic site of $(Zr/Hf)_8Ni_{21}$ is found

in present stoichiometric samples of $ZrNi_3$ and $HfNi_3$ although two non-equivalent sites were found in $(Zr/Hf)_8Ni_{21}$ [22]. The experimental values of EFG and η for $ZrNi_3$ and $HfNi_3$ are found to be in excellent agreement with the theoretically calculated values of EFG and η at ^{181}Ta impurity sites by the first-principles density functional theory based on the FP-(L)APW. From our calculation, three non-equivalent Hf sites in $HfNi_3$ have been found whereas two of these have been observed from PAC measurements. In $ZrNi_3$, on the other hand, the present DFT calculation produces one EFG corresponding to a single Zr site. From our PAC measurements in $ZrNi_3$ also, a single frequency component has been found.

The solubility of Hf in Ni is found to be less compared to Zr in Ni. The Hf solubility in Ni is found to increase with temperature and it decreases again when the temperature is lowered. In Zr-Ni compounds, the binding energy of Hf probe to the lattice sites is not strong enough at high temperature and, probably, the probe atoms are detached from the compound at 1073 K.

5.4.5 Zr_9Ni_{11} and Hf_9Ni_{11}

5.4.5.1 PAC results

Zr_9Ni_{11}

The XRD powder pattern in Zr_9Ni_{11} is shown in Figure 5.39. The peaks were identified using ICDD database, 2009. Presence of tetragonal Zr_9Ni_{11} [PDF Card No.: 00-033-0963] and orthorhombic Zr_7Ni_{10} [PDF Card No.: 01-072-3501] phases have been found in the XRD spectrum. Analysis of the X-ray powder pattern was carried out by FullProf software package [183] using the known crystallographic data of Zr_9Ni_{11} with space group $I4/m$ [152] and Zr_7Ni_{10} [194]. The presence of a minor phase Zr_7Ni_{10} in the stoichiometric sample of Zr_9Ni_{11} was also observed from X-ray diffraction measurements by Joubert et al. [75].

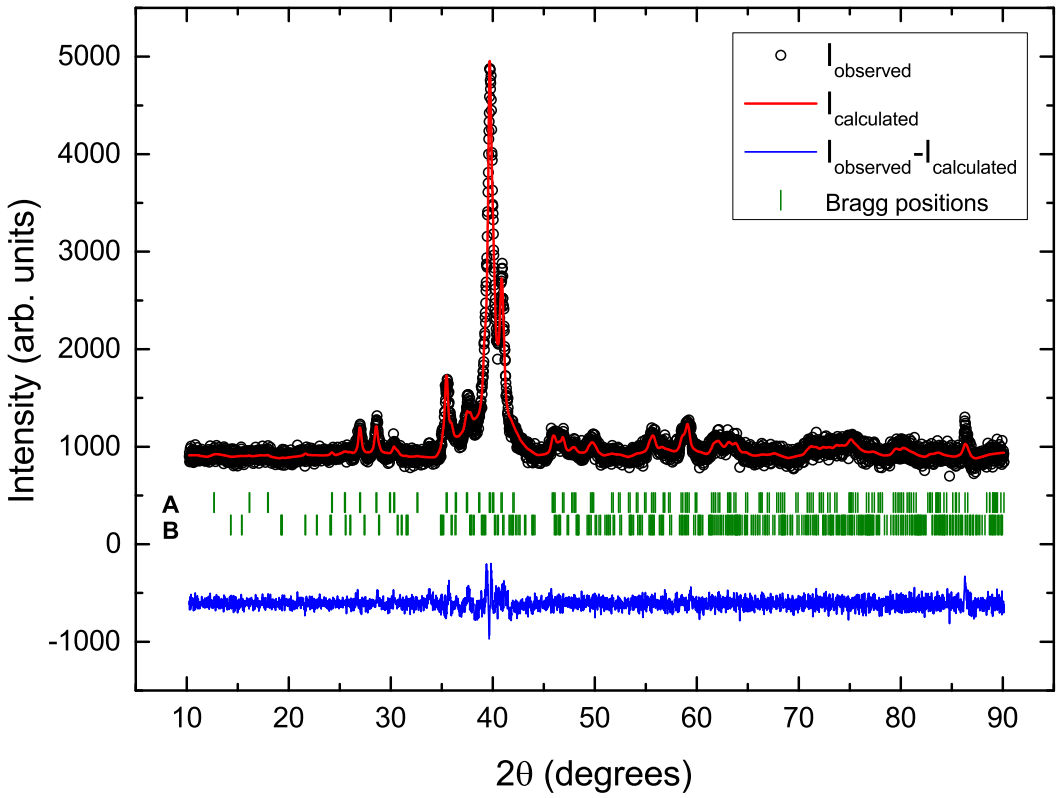

Figure 5.39: The background subtracted XRD powder pattern in the stoichiometric sample of Zr_9Ni_{11}. The line represents the fit to the measured data. The vertical bars A, B denote the Bragg angles corresponding to Zr_9Ni_{11} and Zr_7Ni_{10}, respectively. The bottom line shows the difference between the observed and the fitted pattern.

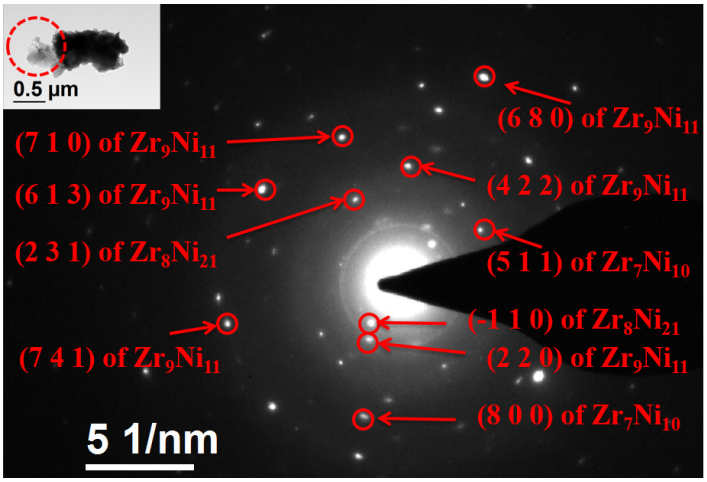

Figure 5.40: Selected area electron diffraction pattern from the stoichiometric Zr_9Ni_{11} particle shown in the inset.

The presence of Zr_9Ni_{11}, Zr_8Ni_{21} and Zr_7Ni_{10} phases in this stoichiometric sample of Zr_9Ni_{11} have been observed from TEM/SAED measurement (Figure 5.40). The SAED

pattern obtained from a region marked by a dotted circle in the stoichiometric sample of Zr_9Ni_{11} is shown in Figure 5.40. The interplanar spacing (d_{hkl}) is obtained by measuring the distance (Δq) of a particular spot from the central bright spot using the formula $d_{hkl} = 1/\Delta q$. Some of the measured d_{hkl} from the SAED pattern are 1.39 Å, 1.30 Å, 1.21 Å, 3.45 Å, 0.99 Å and 1.84 Å. These measured interplanar spacings are very close to the (710), (613), (741), (220), (680) and (422) interplanar spacings of tetragonal Zr_9Ni_{11} (JCPDS # 33-0963), respectively. This further confirms the presence of Zr_9Ni_{11} phase in the sample. Few of the measured d_{hkl} from the SAED pattern are 2.29 Å and 4.34 Å which are very close to the (231) and (-110) interplanar spacings of triclinic Zr_8Ni_{21} (ICDD PDF Card No.: 01-071-2622), respectively. The presence of Zr_8Ni_{21} phase in the sample is thus confirmed. Some of the measured interplanar spacings from the SAED pattern, 2.32 Å and 1.55 Å, are found to be very close to the (511) and (800) interplanar spacings of orthorhombic Zr_7Ni_{10} (ICDD PDF card No.:01-072-3501), respectively, which confirms the presence of Zr_7Ni_{10} phase in the stoichiometric sample of Zr_9Ni_{11}.

The PAC spectrum found at room temperature in the stoichiometric sample of Zr_9Ni_{11} is shown in Figure 5.41. The predominant component (89%) produces values of ω_Q = 39.2(5) Mrad/s ($V_{zz} = 4.4(1)\times10^{21}$ V/m^2), $\eta = 0.64(3)$ with a large frequency distribution width ($\delta = 15\%$). Apart from this, a minor component (ω_Q=77.5(7) Mrad/s, η=0.52(2)) is also observed with site fraction ∼11%. The predominant component has been assigned to Zr_9Ni_{11} by comparing the results with DFT calculations (discussed later). The minor component found can be attributed to Zr_8Ni_{21} by comparing the values of ω_Q and η with the results from our recent investigation [22] for a particular crystallographic site in Zr_8Ni_{21} ($Zr_8Ni_{21}^{(1)}$). It was found [138] that the phases Zr_2Ni_7, Zr_2Ni and ZrNi melt congruently. The phase Zr_8Ni_{21} was formed at ∼1453 K from the liquid by peritectic reaction L+Zr_2Ni_7 →Zr_8Ni_{21} [138]. Kirkpatrick and Larson [137] reported that the phase Zr_9Ni_{11} was produced peritectically by the reaction L+ZrNi→Zr_9Ni_{11} at 1443 K [138] and this phase was found to decompose eutectoidally Zr_9Ni_{11} → ZrNi+Zr_7Ni_{10} at ∼1248 K [138]. In the process of arc-melting, the production of Zr_9Ni_{11} phase at room

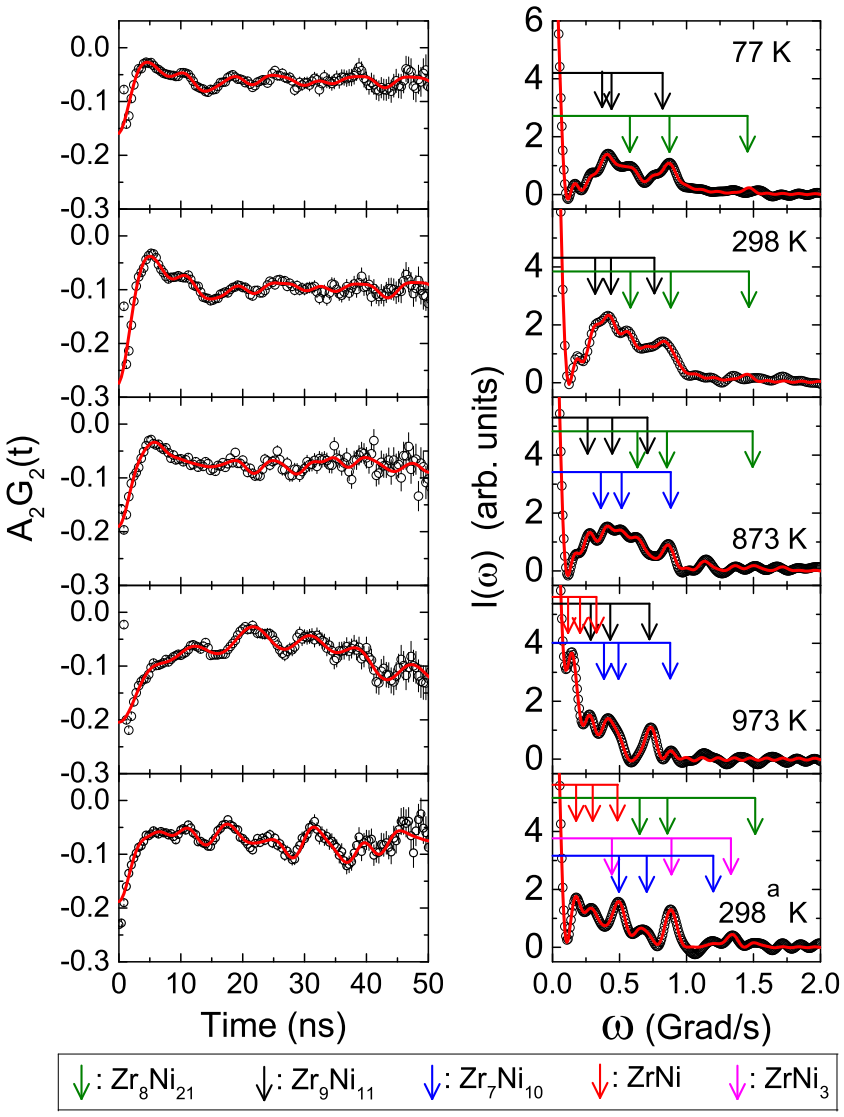

Figure 5.41: PAC spectra in the stoichiometric sample of Zr_9Ni_{11} at different temperature. Left panel shows the time spectra and the right panel shows the corresponding Fourier cosine transforms. The PAC spectrum at room temperature designated by 298^a K is taken after the measurement at 973 K.

temperature is due to rapid solidification from the liquid melt. To find any structural change in this compound or its phase stability with temperature, PAC measurements have been performed in the sample at high temperatures also (up to 973 K). The results show that up to 673 K, the phase due to Zr_9Ni_{11} remains stable and the component fractions do not change appreciably. At 773 K, however, the sample compositions change. At this temperature, a new component ($\sim$27%) appears at the expense of Zr_9Ni_{11}. This

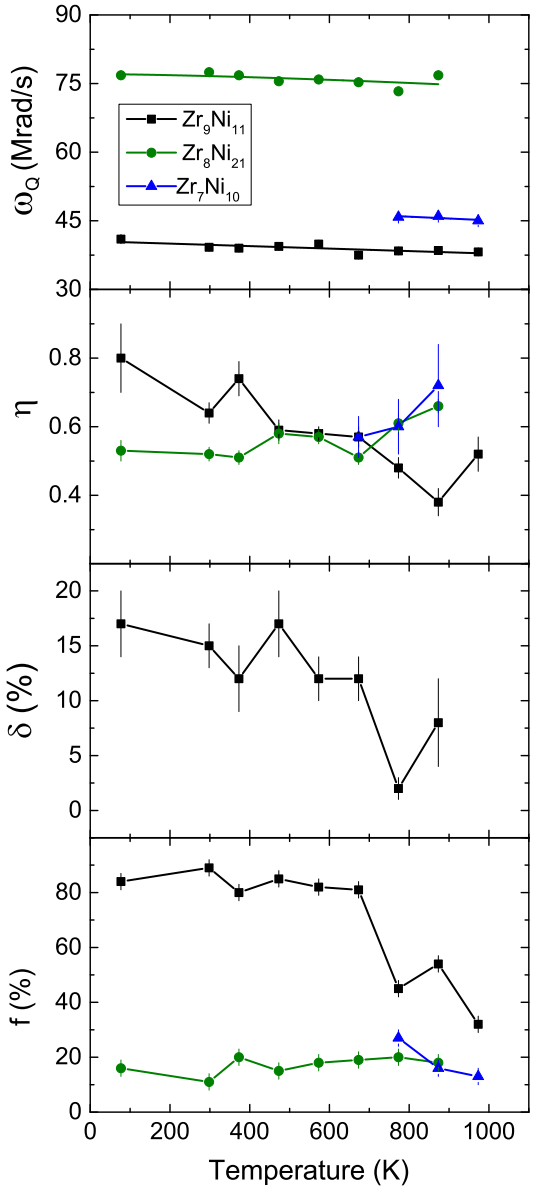

Figure 5.42: Variations of quadrupole frequency (ω_Q), asymmetry parameter (η), frequency distribution width (δ) and site fraction $f(\%)$ with temperature for the components of Zr_9Ni_{11}, Zr_8Ni_{21} and Zr_7Ni_{10}.

has been attributed to Zr_7Ni_{10} by comparing with the previous PAC results in Zr_7Ni_{10} [177]. Kosorukova et al. [11] reported that the phase Zr_7Ni_{10} was produced by peritectic reaction L+Zr_9Ni_{11} $\rightarrow$ Zr_7Ni_{10} at 1393 K. The component fraction due to Zr_8Ni_{21} at 773 K, however, does not change. Another new component (ω_Q=99(2) Mrad/s, η=0) with a small fraction ($\sim$7%) also appears which could not be assigned. At 873 K, the phase due to Zr_9Ni_{11} slightly increases to 54% at the cost of Zr_7Ni_{10} component. At a

temperature of 973 K, the sample composition changes drastically. At this temperature, the predominant component (∼55%) is found to have $\omega_Q = 17.9(6)$ Mrad/s, $\eta = 0.36(4)$, $\delta = 0$ and this can be attributed to ZrNi by comparing the results found in ZrNi from previous PAC measurements [167]. At this temperature, the Zr_8Ni_{21} phase vanishes and the Zr_9Ni_{11} phase reduces to 32%. It was reported [137,138] that the the phase ZrNi was formed by the decomposition of Zr_9Ni_{11} phase eutectoidally at ∼1248 K. We have carried out a re-measurement in the sample at room temperature after the measurement at 973 K to find the change in sample composition before and after heating the sample. In the re-measurement, a new component (∼17%) with $\omega_Q = 74.2(4)$ Mrad/s, $\eta = 0$ is found. This new component can be attributed to $ZrNi_3$ by comparing the results reported from our recent PAC investigations in $ZrNi_3$ [23]. It is known that $ZrNi_3$ was formed by the peritectoid reaction (Zr_2Ni_7+Zr_8Ni_{21} →$ZrNi_3$) at 1193 K [138] and at 1261 K [11]. The predominant phase due to ZrNi (63%) is found to be produced here which was first observed at 973 K in the sample. Appearance of ZrNi as a secondary phase in the synthesized Zr_9Ni_{11} alloy was also found earlier [75, 76, 130, 154]. The remaining phases in the sample can be identified as Zr_8Ni_{21} (∼11%) and Zr_7Ni_{10} (∼9%). Interestingly, no phase due to Zr_9Ni_{11} is found here and the sample is transformed completely. Detailed results of temperature dependent PAC measurements in Zr_9Ni_{11} can be found in the reference [195].

The Zr_9Ni_{11} compound was studied by Stalick et al. [76] earlier using transmission electron microscopy and powder neutron diffraction in the temperature range 4-1273 K. At room temperature, these authors reported a mass fraction of 90% Zr_9Ni_{11} and 10% ZrNi in Zr_9Ni_{11}. From present PAC measurements, however, no ZrNi phase is found at lower temperatures (below 873 K). The ZrNi phase is found only at 973 K. Stalick et al. [76] reported a sharp enhancement of this phase at 973 K and the production of a new phase of Zr_7Ni_{10}. The phase fractions were reported to be 37% ZrNi, 57% Zr_7Ni_{10} and 7% Zr_9Ni_{11} at 973 K [76]. We have also found phase components of ZrNi, Zr_7Ni_{10} and Zr_9Ni_{11} at 973 K with site fractions ∼55%, ∼13% and ∼32%, respectively. Although

the phase fractions found from this present study does not agree completely with the results obtained by Stalick et al. [76], the appearance of similar phase components due to decomposition of Zr_9Ni_{11} at high temperature are observed. Stalick et al. [76] found also a phase reformation at 1273 K where the sample was again 90% Zr_9Ni_{11} and 10% ZrNi. Production of Zr_7Ni_{10} and ZrNi can also be explained from the Zr-Ni phase diagram due to their proximity to Zr_9Ni_{11} phase and very small homogeneity range of this phase [75, 137, 138, 152].

The variations of ω_Q, η, δ and phase fraction (f) with temperature for the Zr_9Ni_{11}, Zr_8Ni_{21} and Zr_7Ni_{10} phases are shown in Figure 5.42. A very weak temperature dependence of quadrupole frequency for the Zr_9Ni_{11} phase is found in this compound. Values of ω_Q for the Zr_9Ni_{11} phase shows a linear variation with temperature and it is fitted using the following a linear relation with temperature (equation 5.6). The fitted results are found to be $\omega_Q(0) = 40.5(5)$ Mrad/s ($V_{zz} = 4.5(1)\times10^{21}$ V/m^2) and $\alpha = 0.7(2)\times10^{-4}$ K^{-1}. The quadrupole frequency for the Zr_8Ni_{21} phase follows $T^{3/2}$ temperature dependence (equation 5.5). The fitting produces values of $\omega_Q(0) = 77.1(8)$ Mrad/s ($V_{zz} = 8.6(2)\times10^{21}$ V/m^2) and $\beta = 1.2(6)\times10^{-6}$ K$^{-3/2}$. In our recent PAC investigation in Zr_8Ni_{21} [22], similar temperature dependence was found.

Temperature evolution of electric quadrupole frequency in metals and intermetallic compounds following a T and $T^{3/2}$ relation are generally found in literature [1, 107]. In most cases, the EFG decreases with temperature. The coefficient α depends on crystal structure and the lattice parameters. A very weak temperature dependence of EFG in Zr_9Ni_{11}, probably, indicates that lattice parameters or lattice volume does not change much with temperature.

To closely examine the phase transitions, a remeasurement of X-ray powder diffraction pattern (Figure 5.43) has been carried out after heating the sample for two days at 1073 K. Peaks in the XRD spectrum were identified using ICDD database, 2009. It is found that the sample after heating gives the phase components Zr_9Ni_{11} ([76], PDF Card No.:

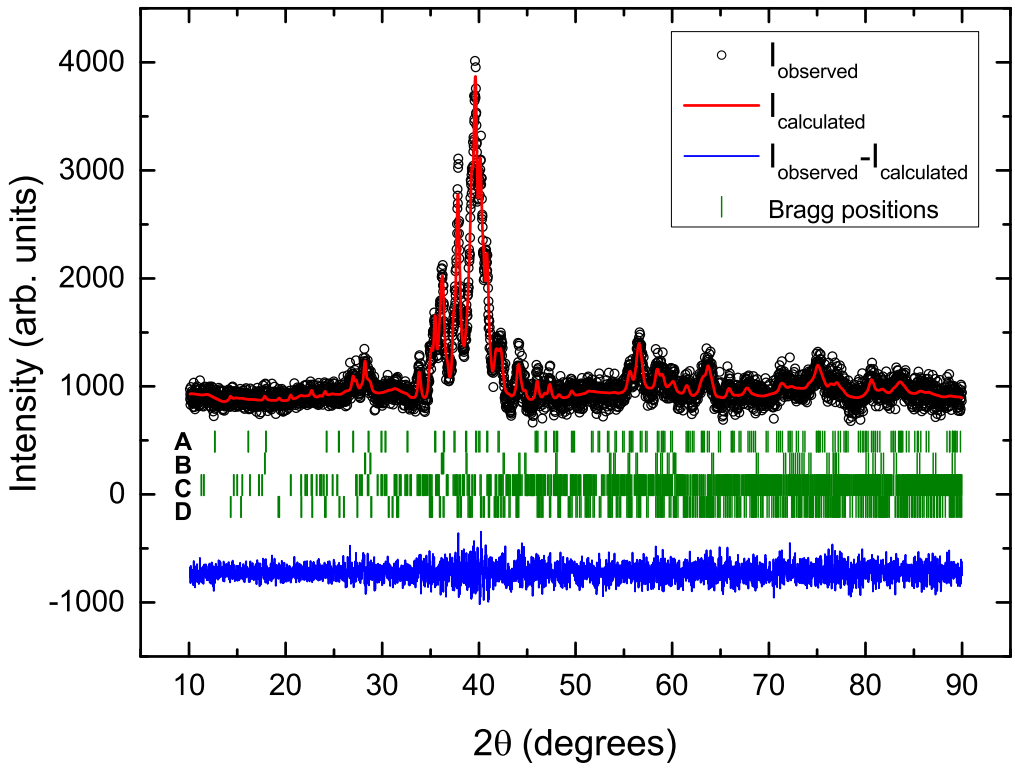

Figure 5.43: The background subtracted XRD powder pattern in the stoichiometric sample of Zr_9Ni_{11} after the sample is annealed at 800°C for two days. The line represents the fit to the measured data. The vertical bars A, B, C and D denote the Bragg angles corresponding to Zr_9Ni_{11}, ZrNi, Zr_8Ni_{21} and Zr_7Ni_{10}, respectively. The bottom line shows the difference between the observed and the fitted pattern.

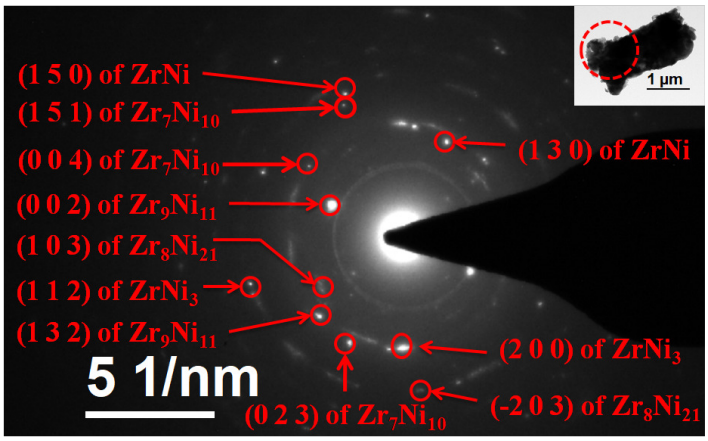

Figure 5.44: Selected area electron diffraction pattern from stoichiometric Zr_9Ni_{11} particle (after annealing at 1073 K for 2 days) shown in the inset.

00-033-0963), ZrNi ([196], PDF Card No.: 01-072-6477), Zr_8Ni_{21} ([149], PDF Card No.: 01-071-2622) and Zr_7Ni_{10} ([194], PDF Card No.: 01-072-3501) as the constituent

phase fractions. The phase transformation of Zr_9Ni_{11} found at 973 K to ZrNi, therefore, can be supported from XRD measurements also. However, from PAC measurement, no phase due to Zr_9Ni_{11} has been found at remeasured room temperature. Possibly, in this case, the phase Zr_9Ni_{11} is completely transformed to ZrNi due to prolonged heating at successive higher temperatures upto 973 K.

The presence of Zr_9Ni_{11}, ZrNi, Zr_8Ni_{21}, $ZrNi_3$ and Zr_7Ni_{10} phases in this stoichiometric sample of Zr_9Ni_{11} after annealing the sample at 1073 K for 2 days have been observed from TEM/SAED measurement (Figure 5.44). The SAED pattern obtained from a region marked by a dotted circle in the stoichiometric sample of Zr_9Ni_{11} is shown in Figure 5.44. Some of the measured interplanar spacings (d_{hkl}) from the SAED pattern are 3.32 Å and 2.27 Å. These measured d_{hkl} are very close to the (002) and (132) interplanar spacings of tetragonal Zr_9Ni_{11} (JCPDS # 33-0963), respectively. This further confirms the presence of Zr_9Ni_{11} phase in the sample. Few of the measured d_{hkl} from the SAED pattern are found to be 2.33 Å and 1.70 Å which are very close to the (130) and (150) interplanar spacings of orthorhombic ZrNi (JCPDS # 65-7465), respectively. The presence of ZrNi phase in the sample is thus confirmed. Some of the measured interplanar spacings from the SAED pattern, 2.75 Å and 1.70 Å, are found to be very close to the (103) and (-203) interplanar spacings of triclinic Zr_8Ni_{21} (ICDD PDF Card No.: 01-071-2622), respectively. This confirms the presence of Zr_8Ni_{21} phase in the sample. Few of the measured interplanar spacings (d-spacing) from the SAED pattern are 2.32 Å and 1.67 Å. These measured d_{hkl} are very close to the (200) and (112) interplanar spacings of hexagonal $ZrNi_3$ (JCPDS # 65-1968), respectively. Hence, the presence $ZrNi_3$ phase in the sample is confirmed. Measured values of some of the interplanar spacings (d-spacing) are 1.77 Å, 2.30 Å and 2.26 Å which are found to be very close to the (151), (004) and (023) interplanar spacings of Zr_7Ni_{10} (ICDD PDF Card No.:01-072-3501), respectively. Therefore, the presence of Zr_7Ni_{10} phase in this sample is confirmed.

Hf_9Ni_{11}

The powder X-ray diffraction pattern in Hf_9Ni_{11} is shown in Figure 5.45. Presence of Hf_9Ni_{11} and HfNi phases have been found in the XRD spectrum. Analysis of the X-ray powder pattern was carried out by FullProf software package [183] using the known crystallographic data of body-centered tetragonal Hf_9Ni_{11} [12,137,157] and base-centered orthorhombic HfNi ([12, 137, 196], JCPDS # 47-1414) phases. The presence of HfNi phase in this stoichiometric sample of Hf_9Ni_{11} has been observed from TEM/SAED measurement (Figure 5.46). Selected area electron diffraction (SAED) pattern obtained from a region marked by a dotted circle in the stoichiometric sample of Hf_9Ni_{11} is shown in Figure 5.46. One of the measured interplanar spacing from the SAED pattern is 2.03 Å which is found to be very close to the (002) interplanar spacing of orthorhombic HfNi (JCPDS # 47-1414). This further confirms the presence of HfNi phase in the sample. The phase Hf_9Ni_{11} could not be identified from SAED pattern in the stoichiometric sample of Hf_9Ni_{11} due to non-availability of X-ray diffraction data of interplanar spacings (d_{hkl}) and corresponding crystallographic planes (hkl) for Hf_9Ni_{11}.

The PAC spectrum at room temperature in Hf_9Ni_{11} is shown in Figure 5.47. An analysis of the spectrum produces one predominant component (∼81%) with values of $\omega_Q = 25.7(3)$ Mrad/s, $\eta = 0.37(3)$ and $\delta = 12(1)\%$ and a minor component (∼19%) with values of $\omega_Q = 39.5(5)$ Mrad/s, $\eta = 0.64(4)$, $\delta = 0$. Comparing these values with the PAC results in Zr_9Ni_{11} at room temperature, the minor component can be assigned to Hf_9Ni_{11}. Since the crystal structures of Zr_9Ni_{11} and Hf_9Ni_{11} are the same, similar values of ω_Q and η in the two compounds are expected. The predominant component, however, can be attributed to HfNi by comparing these results with the previous reported results in HfNi [197]. In the Hf-Ni phase diagram [12], nine intermediate phases have been found where the phases Hf_2Ni_7 and HfNi melt congruently, and seven other phases of Hf-Ni binary system, namely, Hf_9Ni_{11}, α/β-$HfNi_3$, Hf_8Ni_{21}, Hf_3Ni_7, Hf_7Ni_{10}, Hf_2Ni, $HfNi_5$ are formed peritectically [12]. The Hf_9Ni_{11} phase is formed by peritectic reaction from the

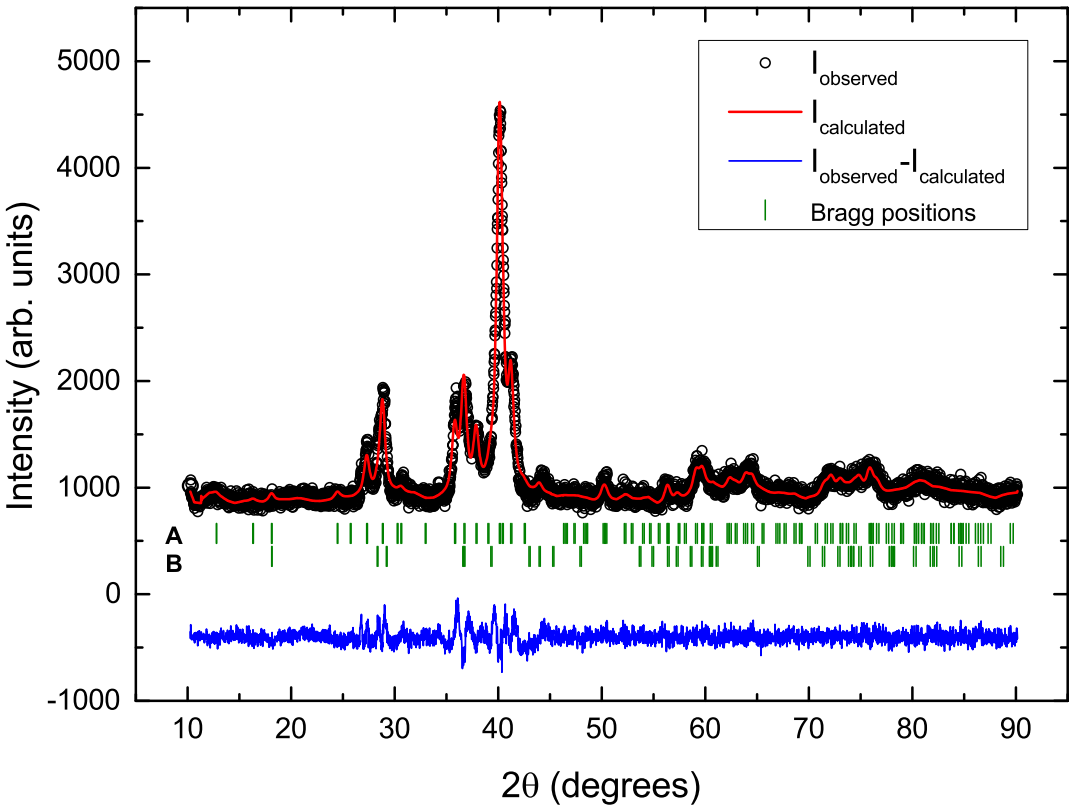

Figure 5.45: The background subtracted XRD powder pattern in the stoichiometric sample of Hf_9Ni_{11}. The line represents the fit to the measured data. The vertical bars A, B denote the Bragg angles corresponding to Hf_9Ni_{11} and HfNi, respectively. The bottom line shows the difference between the observed and the fitted pattern.

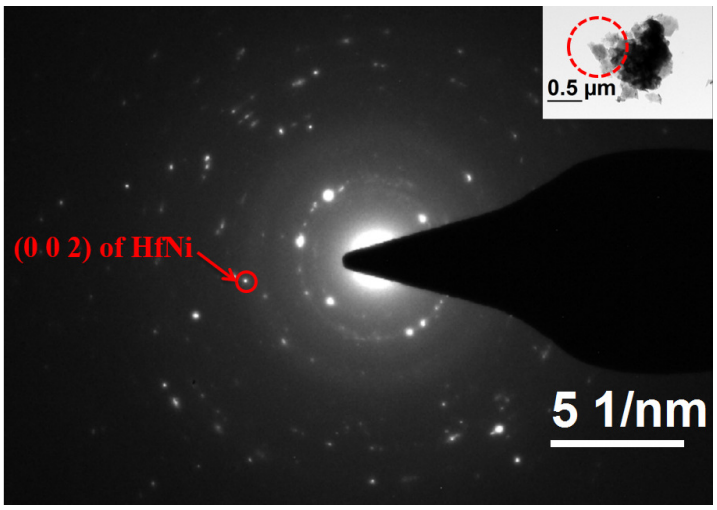

Figure 5.46: Selected area electron diffraction pattern from Hf_9Ni_{11} particle shown in the inset.

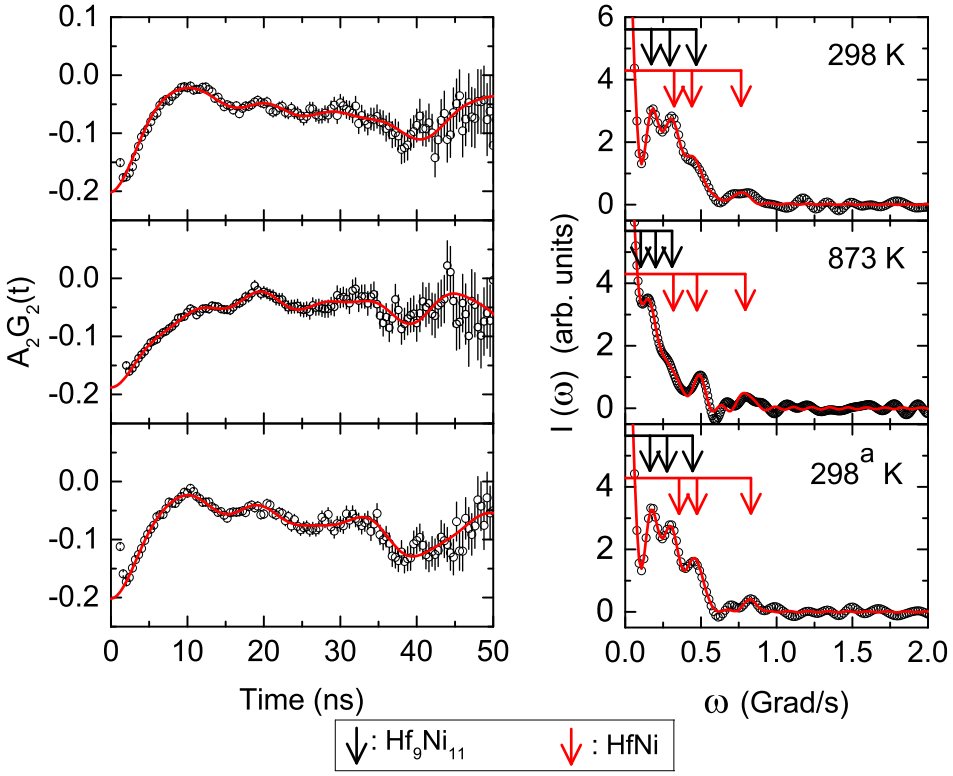

Figure 5.47: PAC spectra in the stoichiometric sample of Hf_9Ni_{11} at different temperature. Left panel shows the time spectra and the right panel shows the corresponding Fourier cosine transforms. The PAC spectrum at room temperature designated by 298^a K is taken after the measurement at 873 K.

liquid melt and HfNi at 1613 K [198,199]. Kirkpatrick and Larson [137] reported that the Hf-Ni system is analogous to Zr-Ni system. Unlike Zr_9Ni_{11}, a predominant component due to HfNi is observed in Hf_9Ni_{11}. This is, probably, due to the fact that in Hf_9Ni_{11} PAC sample, a significant mass loss (∼5.5%) of the sample was observed during its preparation in argon arc furnace. This mass loss can be considered as due to loss of Ni which has a much lower melting and boiling point compared to the other constituent Hf. So, the stoichiometry of the arc melted sample was changed and a Ni deficient compound was produced by melting. Since, the stoichiometry of Hf_9Ni_{11} (Hf/Ni ratio 1:1.22) and HfNi are not very different, the production of HfNi phase in the sample is expected. In this case, the mass loss of the sample was such that its stoichiometry comes closer to HfNi. The PAC measurements at higher temperatures have also been performed in Hf_9Ni_{11}. It is found that at 373 K, the fraction due to Hf_9Ni_{11} enhances to 45% at the expense

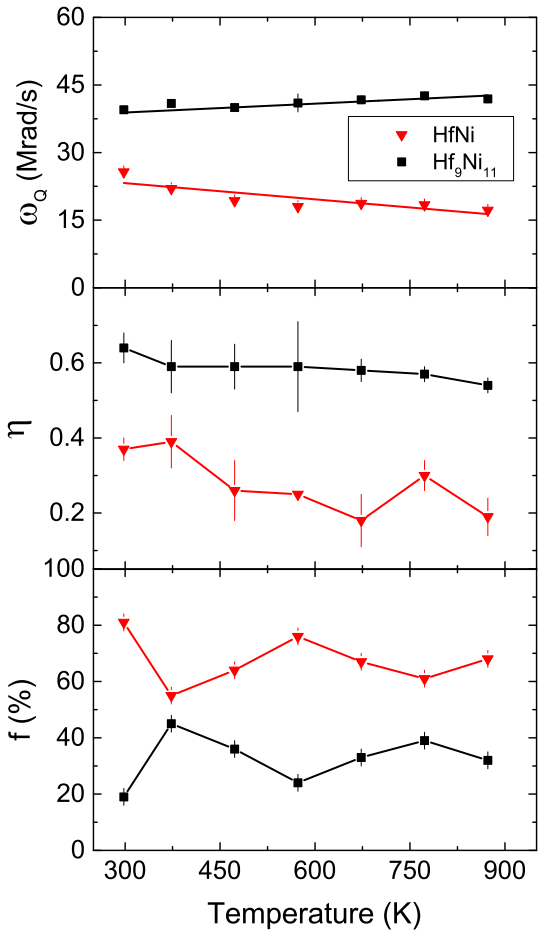

Figure 5.48: Variations of quadrupole frequency (ω_Q), asymmetry parameter (η) and site fraction $f(\%)$ with temperature for the components of Hf_9Ni_{11} and HfNi.

of HfNi which reduces to ∼55%. In the temperature range (373-873 K), the component fractions do not change much (Figure 5.48).

After heating the sample gradually up to 873 K, a re-measurement at room temperature was carried out. The results are found to be almost the same as found before heating. The frequency distribution width for the predominant component, however, decreases to zero as expected due to annealing of the sample. In this case, the values of quadrupole frequencies for the two components are found to change slightly. In the two cases, there are large changes in frequency distribution widths which probably affect the results. But unlike Zr_9Ni_{11}, no change in phases due to heating is observed in Hf_9Ni_{11} and the phases are found to be stable up to 873 K. Detailed results of temperature

dependent PAC measurements in Hf_9Ni_{11} can be found in the reference [195].

The variations of quadrupole frequency and asymmetry parameters of two phases found in the stoichiometric sample of Hf_9Ni_{11} with temperature are shown in Figure 5.48. It is found that the temperature dependence of quadrupole frequency for the Hf_9Ni_{11} phase is very weak which is similar to the temperature dependence of quadrupole frequency in Zr_9Ni_{11}. But, unlike Zr_9Ni_{11}, ω_Q for Hf_9Ni_{11} is found to increase with temperature. Although, the ω_Q for this phase is found to evolve with temperature following a linear temperature dependent relation (equation 5.6). A fitting to the equation 5.6 produces values of $\omega_Q(0)$ = 36.9(9) Mrad/s (V_{zz}=4.1(1)$\times 10^{21}$ V/m^2) and α = -1.9(3)$\times 10^{-4}$ K^{-1}. Similar unusual temperature dependence of quadrupole frequency was also found in the literature [200]. Here also, a weak temperature dependence of EFG indicates that crystal parameters do not change much with temperature. The ω_Q for the predominant HfNi component is also found to vary linearly with temperature following equation 5.6. The fitted results are found to be $\omega_Q(0)$ = 27(2) Mrad/s (V_{zz} = 3.0(2)$\times 10^{21}$ V/m^2) and α=4(1)$\times 10^{-4}$ K$^{3/2}$.

5.4.5.2 Ab initio calculations

The ab initio density functional theory (DFT) calculations were performed to compare with the experimental results by all-electron full potential (linearized) augmented plane waves plus local orbitals [FP-(L)APW+lo] method, as implemented in WIEN2k [7]. The exchange-correlation potential was calculated using the generalized gradient approximation (GGA) with the parameterization of Perdew-Burke-Ernzerhof (PBE) [95]. The cut-off parameter $R_{mt}K_{max}$ for limiting the number of plane waves, where R_{mt} is the smallest value of all atomic sphere radii and K_{max} is the largest reciprocal lattice vector used in the plane wave expansion, was set to 7.0. The Brillouin zone integration was achieved via a tetrahedron method [178]. Taking into consideration both the accuracy and the efficiency of the calculations, we have selected a 10 $\times$ 10 $\times$ 10 point mesh to

Table 5.7: The parameters of the Zr_9Ni_{11} and Hf_9Ni_{11} structure. The lattice constants are given in Å.

	Our calculated results (WIEN 2k) [7]	Previous experimental results (XRD) [11, 132, 137, 152, 157]	Present experimental results (XRD)
Zr_9Ni_{11}			
a	9.88	9.88(1) [152], 9.9778 [11]	9.881(2)
c	6.48	6.61(1) [152], 6.5809 [11]	6.613(1)
B [GPa]	144		
Hf_9Ni_{11}			
a	9.89	9.79 [137]	9.801(2)
c	6.44	6.53 [137]	6.532(2)
B [GPa]	161		

Table 5.8: The calculated and experimental values of EFG (in units of 10^{21} V/m^2) and asymmetry parameter (η) for Zr_9Ni_{11} and Hf_9Ni_{11}.

Compound	Lattice site	Calculated EFG	Calculated η	Measured EFG	Measured η
Zr_9Ni_{11} (^{181}Ta probe)	Zr1 2a	25.9	0		
	Zr2 8h	-8.4	0.30		
	Zr3 8h	-5.6	0.92	4.6(1)	0.80(10)
Hf_9Ni_{11} (^{181}Ta probe)	Hf1 2a	20.7	0		
	Hf2 8h	-8.1	0.39		
	Hf3 8h	5.0	0.72	4.7(1)	0.68(3)

sample the entire Brillouin-zone (BZ), yielding 143 points in the irreducible Brillouin-zone. The structure was relaxed according to Hellmann-Feynman forces calculated at the end of each self-consistent cycle, until the forces acting on all atoms were less than 0.03 eV/Å (2 mRy/a.u.). During this relaxation, the cell volume was kept fixed to its experimental value. Then the theoretical equilibrium volume was determined by fixing the atomic positions to their optimized values and further keeping c/a ratio fixed. A series of calculations was carried out, changing the volume within ± 5% of its experimental value and calculating the total energy as its function. Finally, the c/a ratio was optimized by changing it within ± 2% of its experimental value while keeping the optimized volume fixed. The convergence criterion for achieving self-consistency was that the integrated charge difference between last two iterations to be smaller than 5×10^{-5} electron.

We used the optimal structural parameters to construct 1 × 1 × 2 supercell and then replaced each of the Zr (Hf) nonequivalent host sites by a Ta atom successively

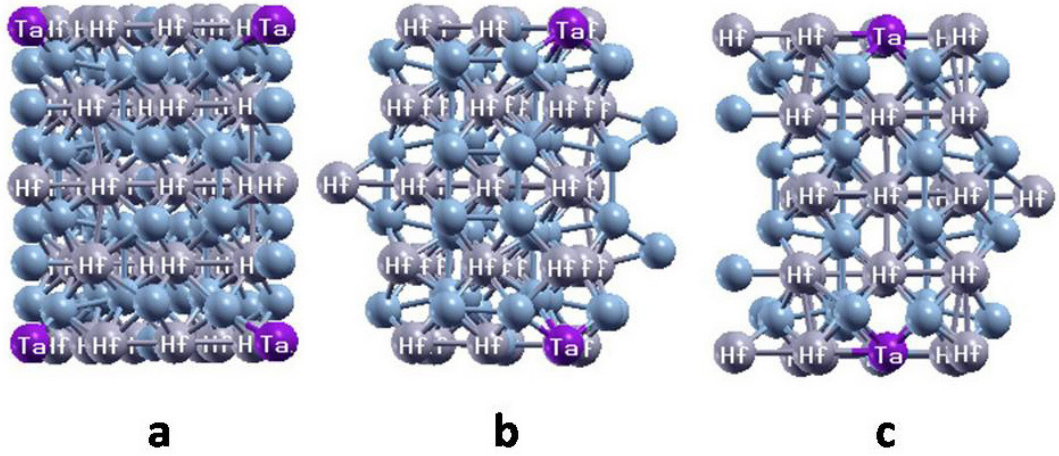

Figure 5.49: Models of cells used in DFT study.

(Figure 5.49, [179]). The point group symmetry around the Ta atom remained the same as around the original atom, but the number of non-equivalent positions enlarged to 18-50, which increased the complexity of the calculations. We used 36-64 k points in the irreducible wedge of the Brillouin zone for these calculations.

Both Zr_9Ni_{11} and Hf_9Ni_{11} have tetragonal $I4/m$ type crystal structure (space group number 87). For Zr_9Ni_{11}, $P4/m$ structure (space group no 83) was reported by Stalick et al. [76] only, but other authors found $I4/m$ structure [11, 132, 152] including two recent results by Matsuyama et al. [132] and Kosorukova et al. [11]. We have found $I4/m$ crystal structure from XRD (Table 5.7, Figure 5.39, 5.43, 5.45) and TEM/SAED (Figure 5.40, 5.44) studies in our samples. So, for DFT calculations, we have considered $I4/m$ crystal structure for both Zr_9Ni_{11} and Hf_9Ni_{11}. This structure contains 20 atoms in the primitive cell and three nonequivalent Hf (Zr) crystallographic positions. The theoretically optimized structure parameters together with the experimental values obtained from earlier [11, 152] and present X-ray diffraction measurements are shown in Table 5.7. We can see that a lattice constants overestimate the experimental ones for about 1%, while the c lattice constants underestimate the measured ones for about 2%. The bulk moduli B, obtained by fitting the data to the Murnaghan's equation of state [189] are also given in Table 5.7.

The electric field gradient (EFG) tensor V_{ij} was calculated from the obtained charge density using the method developed in reference [97]. The usual convention is to designate the largest component of the EFG tensor as V_{zz}. The asymmetry parameter η is then given by $\eta = (V_{xx} - V_{yy})/V_{zz}$, where $|V_{zz}| \geq |V_{yy}| \geq |V_{xx}|$. The calculated and experimental EFGs at the Ta probe positions in the Hf_9Ni_{11} and Zr_9Ni_{11} compounds, along with the corresponding asymmetry parameter values, are given in Table 5.8. It can be observed that the EFG values for Ta at $2a$ position are not very different in Hf_9Ni_{11} and Zr_9Ni_{11}. This is the position with largest EFG. The EFGs for Ta at the other two nonequivalent Hf(Zr) positions, $8h$, are also similar in both compounds. We see that the calculated result for EFG and η at the Ta probe replacing Zr3 atom (-5.6 $\times$ 10^{21} V/m^2 and 0.92) is in agreement with the corresponding values measured at 77 K (4.6 $\times$ 10^{21} V/m^2 and 0.80), thus confirming that the mentioned component of the measured PAC spectra originates from Zr_9Ni_{11}. The sign of V_{zz} can not be determined by PAC measurements. Therefore, absolute values of V_{zz} have been compared. In the case of Hf_9Ni_{11}, the calculated results of EFG (5.0 $\times$ 10^{21} V/m^2) and η (0.72) are in better agreement with the measured values of EFG (4.4 $\times$ 10^{21} V/m^2) and η (0.64) at room temperature. It is interesting to notice that remeasured values at room temperature after heating (4.7 $\times$ 10^{21} V/m^2 and 0.68) exhibit even better agreement with the calculated ones. Possible explanation is that the heating resulted in the better structure arrangement, which is now closer to the ideal one.

5.4.5.3 Conclusion

We have performed PAC measurements and DFT calculations to address the phase components, and phase stability in Zr_9Ni_{11} and Hf_9Ni_{11}. In both these compounds, multiphase components have been found which are assigned by comparing with the results from DFT calculations. Three non-equivalent Zr/Hf sites are found from calculations while only one site occupation (Zr3/Hf3) by the probe is obtained experimentally. In

Zr_9Ni_{11} stoichiometric sample, up to 673 K, the phase due to the Zr_9Ni_{11} is found to be predominant, with the minor phase belonging to Zr_8Ni_{21}. Above 673 K, the Zr_9Ni_{11} phase becomes unstable and Zr_7Ni_{10} appears. At 973 K, the phase due to ZrNi is produced as a dominating phase. This phase has also been found to be predominant when remeasured at room temperature after measurement at 973 K.

In the stoichiometric Hf_9Ni_{11} sample, the phase due to Hf_9Ni_{11} is produced as a minority phase and the HfNi phase is found to be predominantly produced. From our PAC measurements, isostructurality of Zr_9Ni_{11} and Hf_9Ni_{11} has been found. The phases produced in Hf_9Ni_{11} are found to be stable up to 873 K.

In both Zr_9Ni_{11} and Hf_9Ni_{11}, very weak temperature dependence of electric field gradients (EFG) have been observed which indicates that the lattice parameters do not change much with temperature. The calculated results of EFG and asymmetry parameter (η) at the Ta impurity atom positions, Zr3 8h in Zr_9Ni_{11} and Hf3 8h in Hf_9Ni_{11}, are found to be in good agreement with our experimental results, thus confirming the origin of the components of our interest in the PAC spectra.

5.4.6 Zr_7Ni_{10} and Hf_7Ni_{10}

5.4.6.1 PAC results

Zr_7Ni_{10}

The XRD powder pattern obtained in stoichiometric Zr_7Ni_{10} sample is shown in Figure 5.50. Peaks were first identified using ICDD database. The presence of orthorhombic Zr_7Ni_{10} ([159], PDF Card No.: 01-072-3501), triclinic Zr_8Ni_{21} ([149], PDF Card No.: 01-071-2622) and monoclinic Zr_2Ni_7 ([184], PDF Card No.: 01-071-0543) phases have been found from XRD analysis. The X-ray intensity profile has been fitted using FullProf software package [183]. The presence of Zr_7Ni_{10}, Zr_2Ni_7 and Zr_8Ni_{21} phases in this stoichiometric sample of Zr_7Ni_{10} have been observed from TEM/SAED measurement

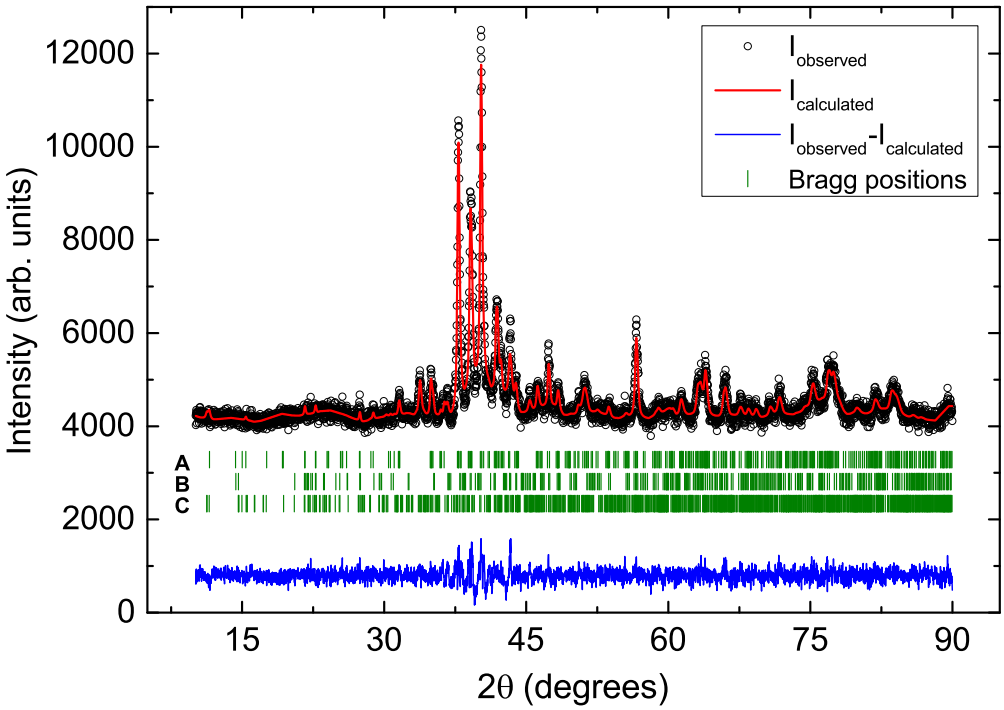

Figure 5.50: The background subtracted XRD powder pattern in the stoichiometric sample of Zr_7Ni_{10}. The vertical bars A, B and C denote the Bragg angles corresponding to Zr_7Ni_{10}, Zr_2Ni_7 and Zr_8Ni_{21} phases, respectively.

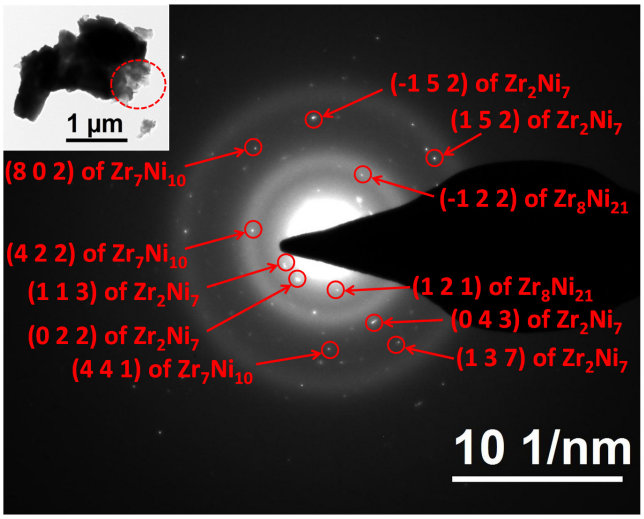

Figure 5.51: Selected area electron diffraction pattern from stoichiometric Zr_7Ni_{10} particle shown in the inset.

also (Figure 5.51). The SAED pattern obtained from a region marked by a dotted circle in the stoichiometric sample of Zr_7Ni_{10} is shown in Figure 5.51. The interplaner spacing (d_{hkl}) is obtained by measuring the distance (Δq) of a particular spot from the central

bright spot using the formula $d_{hkl} = 1/\Delta q$. Few of the measured d_{hkl} from the SAED pattern are 1.47(4) Å, 2.26(4) Å and 1.81(4) Å. These measured interplaner spacings are very close to the (8 0 2), (4 2 2) and (4 4 1) inter-planer spacings of orthorhombic Zr_7Ni_{10} (ICDD PDF Card No.:01-072-3501), respectively. This further confirms the presence of Zr_7Ni_{10} phase in the sample. Some of the measured d_{hkl} from the SAED pattern are 1.39(4) Å, 1.49(4) Å, 2.73(4) Å, 3.39(4) Å, 1.83(4) Å and 1.36(4) Å which are very close to the (-1 5 2), (1 5 2), (1 1 3), (0 2 2), (0 4 3) and (1 3 7) inter-planer spacings of monoclinic Zr_2Ni_7 (JCPDS # 65-2321), respectively. The presence of Zr_2Ni_7 phase in the sample is thus confirmed. Few of the measured interplaner spacings from the SAED pattern, 2.34(4) Å and 3.38(4) Å, are found to be very close to the (-1 2 2) and (1 2 1) inter-planer spacing of triclinic Zr_8Ni_{21} (ICDD PDF Card No.: 01-071-2622), respectively, which confirms the presence of Zr_8Ni_{21} phase in the stoichiometric sample of Zr_7Ni_{10}.

The PAC spectrum in the stoichiometric Zr_7Ni_{10} sample at room temperature is shown in Figure 5.52. The spectrum is found to be best fitted by considering five quadrupole frequencies. Texture effects are observed in the sample which indicates that the EFGs produced at the probe sites are not randomly oriented and it is not a perfect polycrystalline sample. Therefore, the spectrum is analyzed using free S_{2n} (n=0,1,2,3) parameters. At room temperature, a major component ($\sim$ 38%) is found with values of ω_Q = 72.7(3) Mrad/s, $\eta = 0.12(4)$ and $\delta = 1.1(7)$%. This component can be assigned to Zr_2Ni_7 by comparing with the results found in Zr_2Ni_7 [166]. In the stoichiometric $ZrNi_3$ [23] and $ZrNi_5$ [173] alloys also, the phase Zr_2Ni_7 was produced as a major component.

The second major component ($\sim$25%) with values of ω_Q = 58.9(3) Mrad/s, η = 0.71(1) is attributed to Zr_7Ni_{10} phase by comparing the result with our DFT calculation (discussed later). A minor component ($\sim$11%) was found to be present with values of ω_Q = 77.1(9) Mrad/s, η = 0.81(2). This component has been identified as Zr_8Ni_{21} by comparing the result with our recent PAC investigation in Zr_8Ni_{21} [22] for Zr(1)

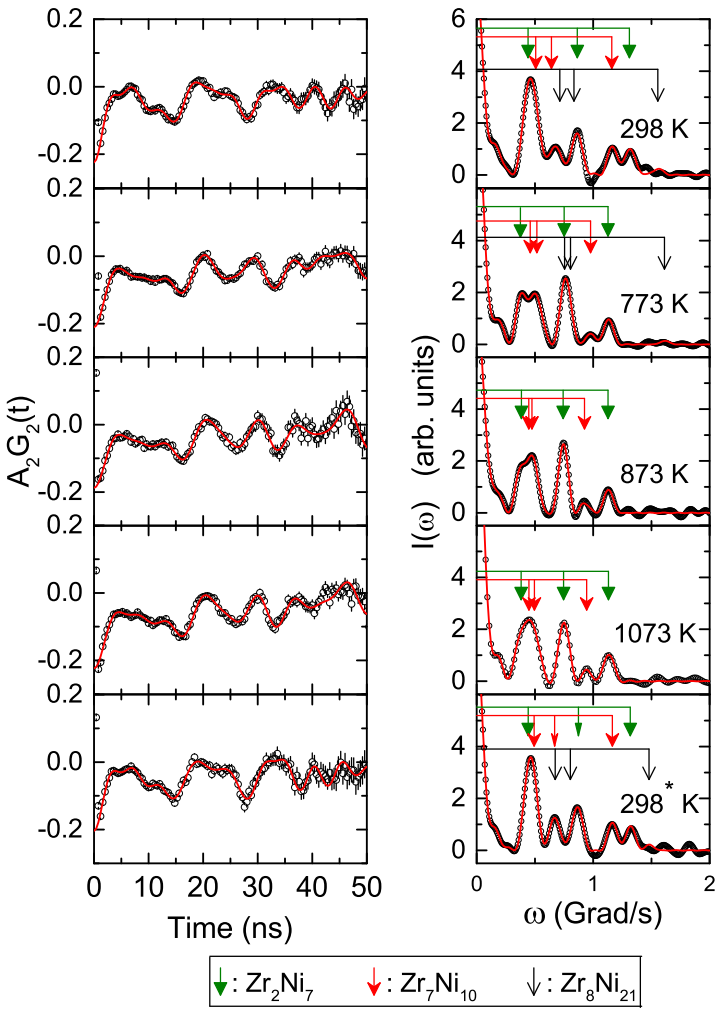

Figure 5.52: Perturbed angular correlation spectra in Zr_7Ni_{10} at different temperatures. Left panel shows the time spectra and the right panel shows the corresponding Fourier cosine transforms. The PAC spectrum designated by 298* K is taken at room temperature after the measurement at 1073 K.

crystallographic site ($Zr_8Ni_{21}^{(1)}$). Apart from these components, two other minor frequency components (component 4: ω_Q=8.0(7) Mrad/s, η=0; component 5: ω_Q=33(1) Mrad/s, η=0) have been found. These two components are attributed to defects. Since the activation of the sample was done after preparing the sample, crystalline defects can be produced by neutron irradiation [201]. From the Zr-Ni phase diagram, it is found that the phase Zr_2Ni_7 melts congruently and Zr_8Ni_{21} phase is formed peritectically from Zr_2Ni_7 and liquid melt (L+Zr_2Ni_7 → Zr_8Ni_{21}) at 1453 K [138]. The phases Zr_7Ni_{10} and Zr_8Ni_{21} are formed from liquid alloy by an eutectic reaction (L→Zr_8Ni_{21}+Zr_7Ni_{10}) [138]

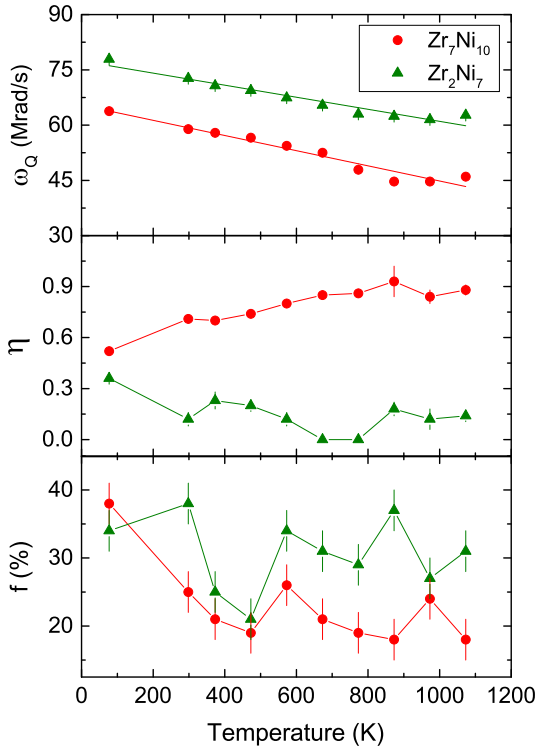

Figure 5.53: Variations of quadrupole frequency (ω_Q), asymmetry parameter (η) and site fraction $f(\%)$ with temperature for the components of Zr_7Ni_{10} and Zr_2Ni_7.

at 1333 K. The phase Zr_7Ni_{10} is also formed by peritectic reaction from Zr_9Ni_{11} and liquid melt (L + Zr_9Ni_{11} → Zr_7Ni_{10}) at 1393 K [11]. At 77 K, the Zr_2Ni_7 and Zr_7Ni_{10} phases were found only with site fractions ∼34% and ∼38%, respectively. All the three Zr-Ni phases, viz. Zr_2Ni_7, Zr_8Ni_{21} and Zr_7Ni_{10} are present in the temperature range 298-773 K. At 873 K and above, the component due to Zr_8Ni_{21} does not appear. The phases Zr_2Ni_7 and Zr_7Ni_{10}, however, remain stable up to 1073 K. The phase Zr_2Ni_7 is found to be predominant in the whole temperature range (77-1073 K) among the Zr-Ni binary phases that are produced in the stoichiometric sample of Zr_7Ni_{10}. The frequency values for the component 4 and 5 show anomalous temperature dependence and do not vary smoothly with temperature. This further indicates that these components are irregular defect components. A re-measurement is carried at room temperature after measurement at 1073 K. Here, all the three Zr-Ni phases, viz. Zr_2Ni_7, Zr_7Ni_{10} and Zr_8Ni_{21} produced with almost same fractions reversibly. Detailed results of temperature dependent PAC

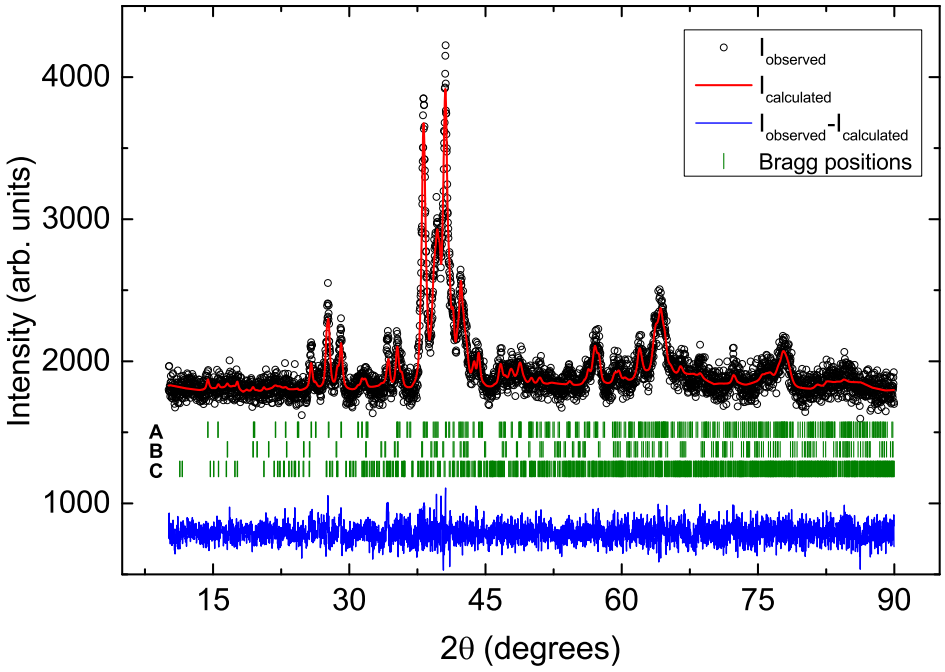

Figure 5.54: The background subtracted XRD powder pattern in the stoichiometric sample of Hf_7Ni_{10}. The vertical bars A, B and C denote the Bragg angles corresponding to Hf_7Ni_{10}, β-$HfNi_3$ and Hf_8Ni_{21}, respectively.

measurements in Zr_7Ni_{10} can be found in the reference [177].

Temperature evolution of quadrupole frequency, asymmetry parameter and site fraction for two Zr-Ni phases, viz. Zr_2Ni_7 and Zr_7Ni_{10} present in the stoichiometric sample of Zr_7Ni_{10} are shown in Figure 5.53. The asymmetry parameter of Zr_7Ni_{10} phase is found to increase with temperature. The quadrupole frequencies for both the components decrease linearly with temperature. The values of quadrupole frequencies obtained for Zr_2Ni_7 and Zr_7Ni_{10} phases in the temperature range 77-1073 K have been fitted with the following a linear relationship with temperature (equation 5.6). The fitted results give $\omega_Q(0) = 65(1)$ Mrad/s ($V_{zz} = 7.3(2)\times10^{21}$ V/m^2), $\alpha = 3.1(3)\times10^{-4}$ K^{-1} for Zr_7Ni_{10} component. For the Zr_2Ni_7 component, the results are $\omega_Q(0) = 77(1)$ Mrad/s ($V_{zz} = 8.6(2)\times10^{21}$ V/m^2), $\alpha = 2.1(2)\times10^{-4}$ K^{-1}. The linear temperature dependence of quadrupole frequency was observed in many intermetallic compounds [162, 202–207].

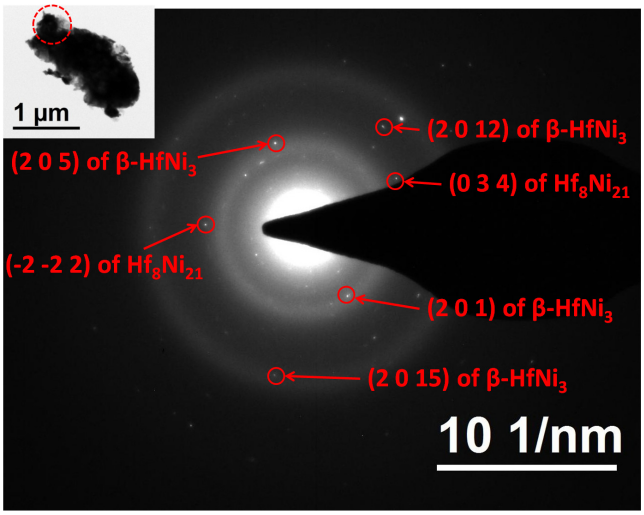

Figure 5.55: Selected area electron diffraction pattern from stoichiometric Hf_7Ni_{10} particle shown in the inset.

Hf_7Ni_{10}

The XRD powder pattern in the Hf_7Ni_{10} sample is shown in Figure 5.54. The peaks were identified using ICDD database, 2009. Presence of the hexagonal β-$HfNi_3$ ([151], PDF Card No.: 01-071-0475), orthorhombic Hf_7Ni_{10} [158], and triclinic Hf_8Ni_{21} ([150], PDF Card No.: 01-071-0476) phases are found in the stoichiometric Hf_7Ni_{10} sample. Fitting of the XRD intensity profile has been carried out using FullProf software package [183]. The space group for Hf_7Ni_{10} has been considered *Cmca* due to its isostructurality with Zr_7Ni_{10} [12, 158]. Selected area electron diffraction (SAED) pattern obtained from a region marked by a dotted circle in the stoichiometric sample of Hf_7Ni_{10} is shown in Figure 5.55. Some of the measured interplaner spacing from the SAED pattern are 1.41(4) Å, 2.27(4) Å and 2.01(4) Å which are found to be very close to the (2 0 12), (2 0 1) and (2 0 5) inter-planer spacings of hexagonal β-$HfNi_3$ (JCPDS #71-0475). This further confirms the presence of $HfNi_3$ phase in the sample. Few of the interplaner spacing from the SAED pattern are 1.70(4) Å and 1.82(4) Å. These are found to be very close to the (0 3 4) and (-2 -2 2) interplaner spacings of triclinic Hf_8Ni_{21} (JCPDS #71-0476). The phase Hf_7Ni_{10} could not be identified from SAED pattern in the stoichiometric sample of Hf_7Ni_{10} due to non-availability of X-ray diffraction data of interplaner spacings (d_{hkl})

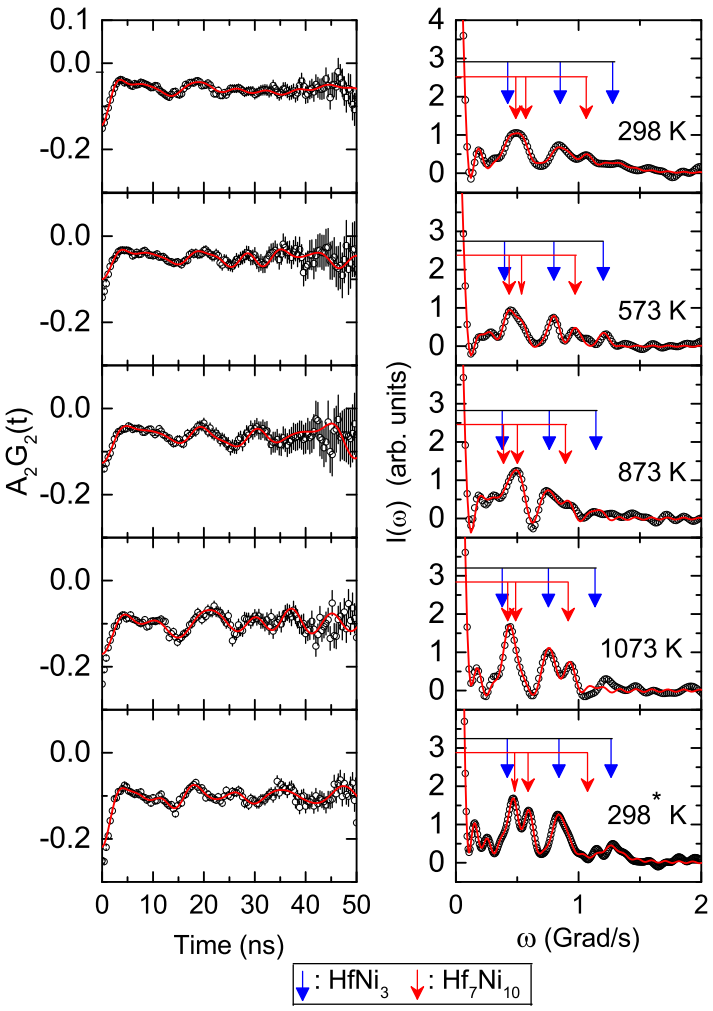

Figure 5.56: Time differential perturbed angular correlation spectra in Hf_7Ni_{10} at different temperatures. Left panel shows the time spectra and the right panel shows the corresponding Fourier cosine transforms. The PAC spectrum designated by 298* K is taken at room temperature after the measurement at 1073 K.

and corresponding crystallographic planes ($h\ k\ l$) for Hf_7Ni_{10}.

The PAC spectrum at room temperature in the stoichiometric Hf_7Ni_{10} sample is shown in Figure 5.56. Fitting of the spectrum shows the presence of three quadrupole frequency components. Analysis of the spectrum has been carried out using free S_{2n} (n=0,1,2,3) parameters as the sample is found to have texture effects. The predominant component ($\sim 62\%$) produces values of $\omega_Q = 71.4(9)$ Mrad/s, $\eta = 0$, $\delta = 11(2)\%$. This component has been assigned to β-$HfNi_3$ by comparing the values with the results from our recent PAC investigation in $HfNi_3$ sample [23] for Hf(3) crystallographic site. The second component

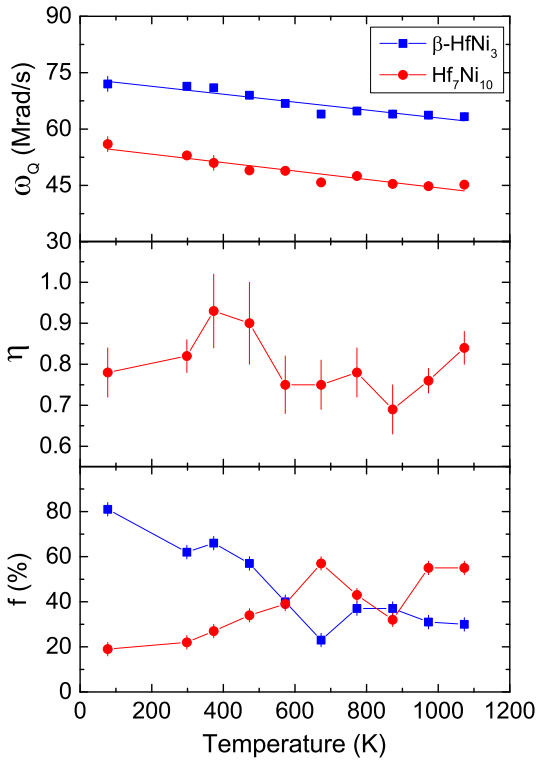

Figure 5.57: Variations of quadrupole frequency (ω_Q), asymmetry parameter (η) and site fraction $f(\%)$ with temperature for the components of Hf_7Ni_{10} and β-$HfNi_3$.

produces values of ω_Q = 53(1) Mrad/s, η = 0.82(4) with site fraction ∼ 22%. This component has been assigned to Hf_7Ni_{10} by comparing the values with the results found in the analogous Zr_7Ni_{10} phase and with the results from DFT calculations (discussed later). A minor component (∼16%) with values of ω_Q = 32(1) Mrad/s, η = 0 was also found to be present. The value of quadrupole frequency for this component varies with temperature in an irregular manner and suggests that this is a crystalline defect produced during sample preparation. In the PAC sample, however, no component due to Hf_8Ni_{21} was observed. In the Hf-Ni phase diagram, it is found that Hf_2Ni_7 and HfNi are congruently melting phases. The $HfNi_3$ has two polymorphs, one is high temperature phase (α-$HfNi_3$) which is stable above 1473 K and the other is low temperature phase (β-$HfNi_3$) which is stable below 1473 K [140]. The phase $HfNi_3$ is produced by peritectic reaction of liquid melt with Hf_2Ni_7 (L+Hf_2Ni_7 →$HfNi_3$) at 1573 K. It was reported [199] that the phase Hf_7Ni_{10} is produced by peritectic reaction L + Hf_9Ni_{11} → Hf_7Ni_{10} [199] at ∼1563 K. At 77 K, the phase fraction of β-$HfNi_3$ component enhances to ∼ 81%. The

site fraction of Hf_7Ni_{10} increases while the site percentage of β-$HfNi_3$ phase decreases up to 673 K (Figure 5.57) with the increase of temperature. However, the phase β-$HfNi_3$ was found to be predominant up to 573 K. The Hf_7Ni_{10} phase becomes predominant (∼57%) and the phase fraction of β-$HfNi_3$ decrease to 23% at 673 K. In the temperature range 773-873 K, the phase fraction of Hf_7Ni_{10} decreases and β-$HfNi_3$ increases to 37%. Major contribution (∼55%) in the PAC spectrum at 973 K and 1073 K was found due to the Hf_7Ni_{10} phase and β-$HfNi_3$ phase fraction reduces to ∼30%. The PAC measurement was carried out at room temperature after measurement at 1073 K where the site percentages for Hf_7Ni_{10} and β-$HfNi_3$ phases were found to be ∼25% and ∼58%, respectively. Similar results of phase fractions of β-$HfNi_3$ and Hf_7Ni_{10} at initial room temperature and after 1073 K show phase reversibility of the two phases. Detailed results of temperature dependent PAC measurements in Hf_7Ni_{10} can be found in the reference [177].

Variation of quadrupole frequency (ω_Q), asymmetry parameter (η) and phase fraction with temperature for β-$HfNi_3$ and Hf_7Ni_{10} phases are shown in Figure 5.57. The quadrupole frequency for β-$HfNi_3$ and Hf_7Ni_{10} phases decrease linearly with temperature following the equation 5.6. Similar temperature dependence of ω_Q was found in Zr_7Ni_{10} which shows isostructurality of Zr_7Ni_{10} and Hf_7Ni_{10}. The fitted results are $\omega_Q(0)$ = 55.9(9) Mrad/s (V_{zz}=6.2(2)×10^{21} V/m^2), α = 2.0(2)×10^{-4} K^{-1} for the Hf_7Ni_{10} phase. For β-$HfNi_3$ phase, the fitted results are $\omega_Q(0)$ = 73.5(9) Mrad/s (V_{zz}=8.2(2)×10^{21} V/m^2), α = 1.5(1)×10^{-4} K^{-1}.

5.4.6.2 DFT calculations and results

Zr_7Ni_{10} and Hf_7Ni_{10} crystallize in the orthorhombic base-centered centrosymmetric *Cmca* type structure (space group number 64) with lattice parameters a=12.381 Å, b=9.185 Å and c=9.221 Å for Zr_7Ni_{10} [159] and a=12.275 Å, b=9.078 Å, c=9.126 Å for Hf_7Ni_{10} [12]. This structure contains 34 atoms in the unit cell and possesses 7 non-equivalent crystallographic positions; 4 non-equivalent positions for Zr (or Hf) and 3 non-equivalent

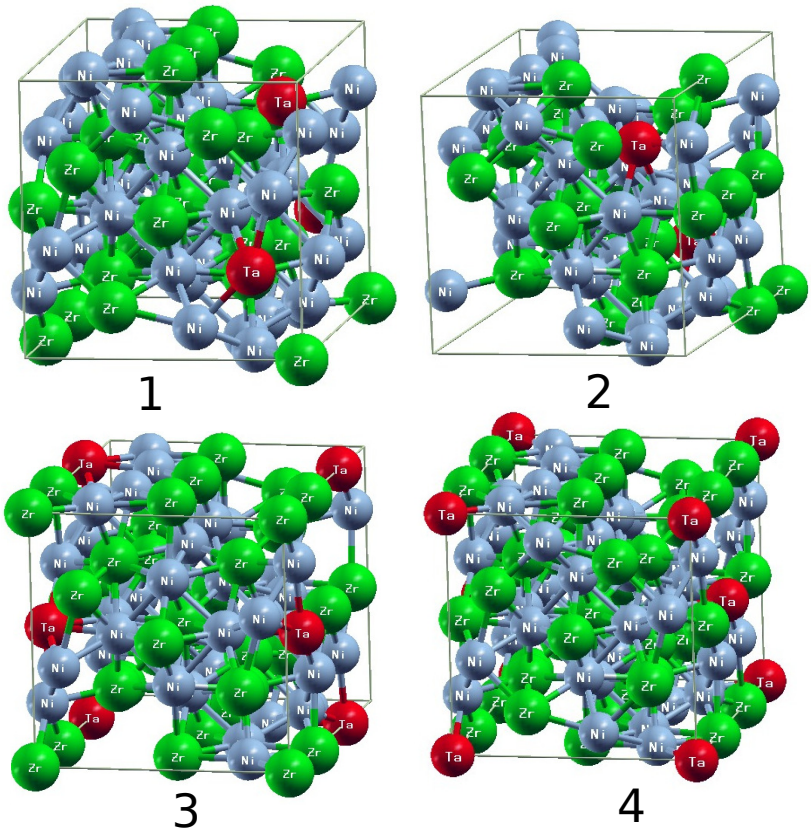

Figure 5.58: Models of cells used in DFT study. The Zr, Ni and Ta atoms are denoted by green, blue and red spheres, respectively

positions for Ni.

First we have optimized these structural parameters. The first-principles density functional theory (DFT) calculations were performed to compare with the experimental results. All the calculations were done using the full potential (linearized) augmented plane waves method [FP-(L)APW], as implemented in WIEN2k [7]. The energy convergence has been achieved by expanding the basis function up to $R_{MT} \cdot K_{max}$=7, where R_{MT} is the smallest atomic sphere radius in the unit cell and K_{max} gives the magnitude of the largest $\vec{k}$ vector in the plane wave expansion. In our calculations the muffin-tin radii for Zr, Ni and Hf(Ta) were 2.2, 2.1 and 2.15 a. u., respectively. The valence wave functions inside the spheres are expanded up to l_{max}=10 while the charge density is Fourier expanded up to G_{max}=16. The energy to separate core and valence states was set to -7 Ry. Electronic exchange-correlation energy was treated with generalized gradient approxima-

Table 5.9: The lattice constants a, b and c (given in Å) of the Zr_7Ni_{10} and Hf_7Ni_{10} *Cmca* crystal structure and the fractional coordinates of 7 crystallographic non-equivalent positions.

	Present calculated results (WIEN2k)	Experimental results [159], [12] (XRD)	Present experimental results (XRD)
Zr_7Ni_{10}			
a	12.365	12.381	12.374
b	9.172	9.185	9.173
c	9.197	9.221	9.213
Zr1	0 0.31359 0.18707	0 0.31219 0.18847	
Zr2	1/4 0.25466 1/4	1/4 0.25466 1/4	
Zr3	0.30754 0 0	0.30634 0 0	
Zr4	0 0 0	0 0 0	
Ni1	0.14438 0.01115 0.20822	0.14438 0.01115 0.20822	
Ni2	0.35507 0.29157 0.00833	0.35507 0.29157 0.00833	
Ni3	0 0.10655 0.39553	0 0.10755 0.39423	
Hf_7Ni_{10}			
a	12.281	12.275	12.279
b	9.062	9.078	9.071
c	9.151	9.126	9.120
Hf1	0 0.31439 0.1867	0 0.31219 0.18847	
Hf2	1/4 0.25504 1/4	1/4 0.25466 1/4	
Hf3	0.30645 0 0	0.30634 0 0	
Hf4	0 0 0	0 0 0	
Ni1	0.14391 0.00998 0.20874	0.14438 0.01115 0.20822	
Ni2	0.35507 0.29111 0.00665	0.35507 0.29157 0.00833	
Ni3	0 0.10699 0.39569	0 0.10755 0.39423	

tion (GGA) parametrized by Perdew-Burke-Ernzerhof (PBE) [95, 208, 209]. Taking into consideration both the accuracy and the efficiency of the calculations, we have selected a 8×8×8 *k* point mesh to sample the entire Brillouin-zone (BZ), yielding 143 points in the irreducible Brillouin-zone. The structure was relaxed according to Hellmann-Feynman forces calculated at the end of each self-consistent cycle, until the forces acting on all atoms were less than 0.068 eV/Å (5 mRy/a.u.). The relaxation method is described in reference [164]. In our calculations the self-consistency was achieved by demanding the convergence of the integrated charge difference between last two iterations to be smaller than 10^{-5}e. All the calculations refer to zero temperature.

The theoretically optimized lattice parameters *a*, *b* and *c*, and fractional coordinates of atoms together with the present and previous experimental values [12, 159] are presented in Table 5.9. From Table 5.9 it can be seen that our calculated parameters are in very good agreement with the experimental results. After obtaining the optimized structural

Table 5.10: The calculated and experimental EFG values in units of 10^{21} V/m^2 and asymmetry parameter (η) values for Zr_7Ni_{10} and Hf_7Ni_{10} *Cmca* crystal structure.

Probe	Lattice Site site	calculated EFG	calculated η	Measured EFG	Measured η (77 K)
Zr_7Ni_{10}					
no probe	Zr1	1.11	0.63		
(pure compound)	Zr2	4.05	0.10		
	Zr3	-3.02	0.37		
	Zr4	-3.38	0.41		
^{181}Ta	Zr1-Ta	1.33	0.77		
	Zr2-Ta	10.11	0.10		
	Zr3-Ta	-6.99	0.54	7.3(2)	0.52(1)
	Zr4-Ta	-10.75	0.25		
Hf_7Ni_{10}					
no probe	Hf1	-1.15	0.33		
(pure compound)	Hf2	9.48	0.18		
	Hf3	-4.96	0.82		
	Hf4	-8.94	0.32		
^{181}Ta	Hf1-Ta	1.87	0.25		
	Hf2-Ta	9.75	0.10		
	Hf3-Ta	-6.37	0.77	6.2(2)	0.78(6)
	Hf4-Ta	-10.68	0.22		

parameters, we replaced one of the host sites; i.e. one of the 4 non-equivalent positions of Zr (or Hf) by a Ta atom (preserving the point group symmetry around original atom), in order to simulate a dopant in the crystal lattice. This substitutional structures have been marked as X1-Ta, X2-Ta, X3-Ta and X4-Ta; X=Zr, Hf (Figure 5.58). For each case of the substitutional structure, we have repeated calculations again, keeping all parameters and charge convergence criteria same as in the case of the pure compounds. For example, to simulate PAC measurements at Zr1 position, we replaced one atom at position (0, 0.31359, 0.18707) with Ta atom. We checked that the two Ta atoms are sufficiently far from each other (∼8 Å) to avoid significant impurity-impurity interactions. The calculated electric field gradients (EFGs) in the pure compounds as well as at Ta probe positions in the Zr_7Ni_{10} and Hf_7Ni_{10} structures along with the values of asymmetry parameter η, are given in Table 5.10. The sign of EFG (V_{zz}) can not be determined from PAC measurement. Thus, absolute values of measured EFG (extrapolated to 0 K) and

asymmetry parameter (at 77 K) for Zr_7Ni_{10} and Hf_7Ni_{10} have been compared with the theoretical results in the Table 5.10. The calculation of EFG were performed by using the method developed in reference [97]; which is implemented in WIEN2k code. All the calculations refer to zero temperature.

We see that the calculated result for EFG at the Ta probe site replacing Zr3 atom (6.99×10^{21} V/m^2) with asymmetry parameter 0.54 is in excellent agreement with the measured value of EFG extrapolated to 0 K ($7.3(2)\times10^{21}$ V/m^2) and η (77 K)=0.52(1) for the component Zr_7Ni_{10}, thus confirming that the mentioned component of the measured PAC spectra originates from Zr_7Ni_{10}. Similarly, the calculated result for EFG at the Ta probe site replacing Hf3 atom (6.37×10^{21} V/m^2) with asymmetry parameter 0.77 is in excellent agreement with the measured value of EFG extrapolated to 0 K ($6.2(2)\times10^{21}$ V/m^2) and η (77 K)=0.78(6) for the component Hf_7Ni_{10}, thus confirming that the mentioned component of the measured PAC spectra originates from Hf_7Ni_{10}.

5.4.6.3 Conclusion

In stoichiometric Zr_7Ni_{10} sample, the phases Zr_2Ni_7, Zr_7Ni_{10} and Zr_8Ni_{21} are produced where Zr_2Ni_7 is found as a major phase and a minor phase due to Zr_8Ni_{21} is found at room temperature. In the stoichiometric Hf_7Ni_{10} sample, the phases β-$HfNi_3$ and Hf_7Ni_{10} are produced where the phase β-$HfNi_3$ is predominant at room temperature. The phase fraction of Hf_7Ni_{10} increases with temperature at the expense of β-$HfNi_3$. At temperatures $\geq 400°C$, the phase Hf_7Ni_{10} becomes predominant which indicates that it is a high temperature phase. However, these phase fractions are found to be reversible with temperature. Similar values of quadrupole frequency and asymmetry parameter indicate isostructurality of Zr_7Ni_{10} and Hf_7Ni_{10} phases. In both Zr_7Ni_{10} and Hf_7Ni_{10}, four non-equivalent crystallographic sites of Zr/Hf have been found. Our experimental results of EFG and η are in excellent agreement with the values of EFG at ^{181}Ta sites corresponding to Zr3/Hf3 positions calculated by the first-principles density functional theory based on

the full potential (linearized) augmented plane waves method [FP-(L)APW]. The origin of observed EFG in these materials can thus be explained.

CHAPTER 6

Nuclear electromagnetic moments as building block of nuclei: An example

6.1 Introduction

Important role played by the electromagnetic moments in building up of nuclear structure and many observed co-operative phenomena, directly or indirectly associated with the nuclear electromagnetic moments, are important topics of research in nuclear physics. In the previous chapters, detailed studies of the role played by the nuclear electromagnetic moments as non-interfering probe of the atomic environment in solids have been illustrated and the results obtained from such studies are elucidated. As indicated in the Chapter 1 of the thesis, the role of electromagnetic moments in the nuclear environment are to be treated in a completely different way. In this case, the dual role played by the electromagnetic moments, both as the building block as well as the nuclear probe makes the investigations complicated but challenging at the same time. Specifically, the role played by the magnetic moments of neutrons and protons belonging to different single particle states in forming the high spin states of trans-lead nuclei are investigated through in-beam experiments in nuclear spectroscopy. A few details of experimental investigation on the high spin states of proton rich astatine nucleus (^{204}At) by way of an example, are described in this chapter.

Nuclear spectroscopic experiments are carried out to explore the nuclear structure at high angular momentum and excitation energy to determine the spin-parity, excitation energy, lifetime, electromagnetic moments of nuclear energy levels and shape, deformation of nucleus by observing the emitted radiation from an unstable nucleus. The transition probability of γ-rays emitted from high spin states are related with the nuclear moments, viz. the transition probability for electric quadrupole transition are connected with the intrinsic quadrupole moment and the magnetic dipole transition probability is associated with the nuclear g-factors or the nuclear magnetic dipole moment. In a stretched γ-ray transition, the photon carries angular momentum equal to the algebraic spin difference between the initial and final state (i.e. $|J_f - J_i| = L$). The lowest possible multipole transition is favored as the total transition probability decreases with increasing L according to the relation:

$$T_{fi}(\sigma L) = \frac{8\pi(L+1)}{\hbar L[(2L+1)!!]^2}\Big(\frac{E_\gamma}{\hbar c}\Big)^{2L+1} B(\sigma L : J_i \rightarrow J_f), \tag{6.1}$$

where σ is either electric (E) or magnetic (M) transition, L is the multipolarity, E_γ is energy of the emitted photon, and $B(\sigma L : J_i \rightarrow J_f)$ is the reduced transition probability. The multipolarity of a transition is not always pure, rather there is a mixture of transitions of different multipolarities which can connect the two nuclear energy levels. The transition probability for a mixed multipolarity transition (generally restricted to $M1/E2$ decays) can be calculated by measuring multipole mixing ratio, δ, which is related to transition probability T by the expression:

$$\delta^2_{E2/M1} = \frac{T(E2 : J \rightarrow J-1)}{T(M1 : J \rightarrow J-1)}. \tag{6.2}$$

The single particle transition rates assume that the transition is due to a single nucleon changing from one shell model state to another and the most common prescription for calculation is the Weisskopf Estimates [210]. These are proportional to E_γ^{2L+1} and predict that higher order multipoles have lower transition rates. Reduced matrix element of the

magnetic dipole moment operator leads to the following expression of the reduced $M1$ transition rate (in units of μ_N^2):

$$B(M1; I \to I-1) = \frac{3}{4\pi}(g_K - g_R)^2 K^2 [1 + (-1)^{I+1/2} b] |\langle IK10|I-1\ K\rangle|^2, \tag{6.3}$$

where g_K and g_R are the single particle and collective g-factors respectively. The $\langle IK10|I-1\ K\rangle$ is the Clebsch-Gordon vector addition coefficient, b is the magnetic decoupling parameter which is non-zero for bands with $K = 1/2$. These particle and core g-factors g_K and g_R, relate to the magnetic dipole moment, μ, of a state of spin I with projection K by the expression [211]:

$$\mu = g_R I + (g_K - g_R)\frac{K^2}{I+1}. \tag{6.4}$$

The reduced matrix element of the electric quadrupole operator leads to the following expression for the reduced $E2$ transition rate (in the units of e^2b^2):

$$B(E2; I \to I-2) = \frac{5}{16\pi} Q_0^2 |\langle IK20|I-2\ K\rangle|^2, \tag{6.5}$$

where $\langle IK20|I-2\ K\rangle$ is the Clebsch-Gordan vector addition coefficient. Intrinsic quadrupole moment Q_0 is defined in the nuclear frame of reference and spectroscopic quadrupole moment is defined in the laboratory frame:

$$Q_S = \langle I, M = I|Q(\vec{r})|I, M = I\rangle, \tag{6.6}$$

where the state $|I, M = I\rangle$ defines Q_S as the maximum observable quadrupole moment. These are related by

$$Q_S = Q_0 \frac{3K^2 - I(I+1)}{(I+1)(2I+3)}. \tag{6.7}$$

Dönau and Frauendorf [212] developed a simplified geometrical model to estimate the $B(M1)$ values for a multi-quasi-particle band. For bands with no signature splitting, the

$B(M1)$ value can be estimated (in units of μ_N^2) by

$$B(M1) = \frac{3}{8\pi}\frac{K^2}{I^2}[(g^{(1)} - g_R)\Big(\sqrt{I^2 - K^2} - i_x^{(1)}\Big) - (g^{(2)} - g_R)i_x^{(2)}]^2, \tag{6.8}$$

where the g with different indices are the g-factors for specific particles and i_x is the contribution to the aligned angular momentum from that particle. The deformation aligned and rotation aligned particles are represented by the superscripts (1) and (2), respectively. In the rotational model, the $B(E2 : I \to I-2)$ is given by

$$B(E2) = \frac{5}{16\pi}Q_0^2\frac{3(I-K)(I-K-1)(I+K)(I+K-1)}{(2J-2)(2J-1)J(2J+1)}, \tag{6.9}$$

where Q_0 is the intrinsic quadrupole moment. For an unstretched $E2$ transitions, the $B(E2 : I \to I-1)$ is given by

$$B(E2) = \frac{5}{16\pi}Q_0^2\frac{3K^2(J-K)(J+K)}{(J-1)J(2J+1)(J+1)}, \tag{6.10}$$

for a transition between states of spin I and $I-1$, and K is the projection of the angular momentum along the symmetry axis. The value of K is usually taken as being equal to the spin of the lowest energy state in the band, known as the bandhead. The $\frac{B(M1)}{B(E2)}$ branching ratios (in units of $\frac{\mu_N^2}{e^2b^2}$) can be obtained by measuring the energies of the γ-ray transitions and their corresponding intensities from the expression:

$$\frac{B(M1)}{B(E2)} = 0.697\frac{E_2^5}{E_1^3}\frac{1}{1+\delta^2}\frac{I_\gamma(\Delta I = 1)}{I_\gamma(\Delta I = 2)}. \tag{6.11}$$

Here, E_1 and $I_\gamma(\Delta I = 1)$ are the energy and intensity of the dipole transition, respectively. The E_2 and $I_\gamma(\Delta I = 2)$ are the energy and intensity of the quadrupole transition.

Gamma ray spectroscopic studies in the trans-lead region ($Z > 82, N < 126$) have gained considerable interest due to observation of many exotic nuclear phenomena at high spin and excitation energies. Some of these features are: 1) abundance of isomeric

levels [213,214]; 2) magnetic rotational (MR) bands or shears bands, i.e. groups of levels that display rotational-like character connected by enhanced magnetic dipole transitions in near-spherical nuclei [215]; 3) super deformation, i.e. large deformation in the shape of the nuclei from a sphere to an ellipsoid with axes having ratio $\approx$ 2:1:1 [216] and 4) shape coexistence, i.e. the coexistence of different intrinsic shapes which are very common to collective models of nuclei. In the macroscopic limit, these shapes, belonging to different configurations, mix with each other through the residual interactions between the nucleons [217]. It is generally found that the nucleus with even number of protons and neutrons is most stable and a nucleus having odd-odd nucleons is the least stable. The nucleus with proton or neutron number 2, 8, 20, 28, 50, 82, 126 show the high stability when compared with a nucleus containing another extra proton or neutron. The doubly magic nuclei where both the number of proton and neutron are magic numbers, show highest stability. These doubly magic nuclei are generally spherical in shape such as, $^{208}_{82}$Pb. An addition of a single proton in the $^{208}_{82}$Pb results in deformation in the shape of the nucleus. The major difficulties in populating high spin states and detection of these nuclei are: 1) low cross-section ($\sim$10 mb or less) of evaporation residue (ER) formation, 2) dominant fission channel which prevents the compound nucleus to sustain large angular momenta, 3) presence of long lived isomers, 4) presence of low energy transitions with high internal conversion coefficients, etc. Gamma-rays emitted from the fission products make the gamma-ray spectroscopic studies of these ERs more difficult, particularly for short-lived high-spin states. More asymmetric target-projectile combination is generally chosen to produce these nuclei as the competing fission cross section is higher for symmetric combinations. In this trans-lead region, high spin states of neutron deficient astatine nuclei (Z=85) are less explored except ^{205}At [9], and in most of the cases, there are ambiguities in level energies, assignment of spins and parities. Partial level scheme based on systematics of the neighboring nuclei was established in ^{206}At [218].

A spectroscopic study [8] on doubly odd proton rich ^{204}At using Gammasphere and HERCULES II have been rather incomplete in establishing its level scheme extending to

high spin states. An isolated ΔI=1 band was observed, but the cross-over $E2$ transitions and yrast sequence of transitions were not observed. The linking transitions between the ΔI=1 band and the ground state transitions were not established. Assignment of spin-parity was not firmly established due to less statistics and due to the contamination from the neighboring nuclei. However, use of X-ray gating and clean up by tight gating on the time window can be effective in constructing the level scheme. Attempts for a complete study of the high spin states and isomer decays in ^{204}At have been undertaken in the present investigation.

This nucleus, with neutron number N=119 and proton number Z=85, is close to the neutron sub-shell closure at N=120 and proton shell closure at Z=82. Consequently, the nucleus is expected to exhibit small deformation in shape. Therefore, ^{204}At nucleus should have vibrational structure and level sequence for the excited states. Because of small deformation, the unpaired neutron and proton particles (or holes) will behave like single particles, and manifest a co-operative phenomenon known as magnetic rotation. This is due to precession of the unpaired valence neutrons and protons, as magnetic dipoles, around the principal axis. At low excitation energy and angular momenta, the projection of the dipoles is small along the principal axis. At increasing excitation energy and angular momenta, the dipoles close in, resulting in increase in projection along the principal axis. The characteristic of magnetic rotation is the existence of enhanced $M1$ transitions along the sequence of levels, known as the magnetic dipole band. because of near-spherical structure, the corresponding $E2$ transitions within the band are very weak or non-existent. Because of similarity of the mechanism of closing of two dipole magnets almost perpendicularly apart in orientation with that of two blades of a scissor, this is also termed as the shears mechanism and the resulting dipole band is called the shears band.

In the trans-lead region, shears band has been observed [215, 219]. The configuration is associated to the high-j valence nucleons in a weekly deformed system. The tilted-axis

cranking (TAC) model of Frauendorf [219] is one of the successful model for explanation of the origin of these bands. According to this model, as applied to the case of trans-lead nuclei in general, the high-j $h_{9/2}$ and $i_{13/2}$ protons prefer the deformation aligned coupling which leads to the minimum energy configuration with alignment along the axis, and the quasi neutrons in $i_{13/2}$ prefer the rotation aligned coupling with energy minimum alignment perpendicular to the axis. In the lowest configuration of this magnetic rotational band, the angular momentum vectors of high-j protons and neutrons are nearly perpendicular to each other. They couple and create a total angular momentum vector that does not lie on any of the principal axes [8, 215]. With the increase of excitation energy, the proton and neutron vectors close on the total angular momentum vector (similar to the closing of a pair of shears) that increases the angular momentum of the system. Now, as the closing mechanism is quantized, the spectra appears similar to that of collective rotation.

6.2 Experimental details

The gamma-ray spectroscopic measurement was done at the Indian National Gamma Array (INGA), stationed at Pelletron-LINAC facility in Tata Institute of Nuclear Physics (TIFR), Mumbai. The excited neutron deficient astatine nuclei were produced by bombarding self-supporting gold (99.99% purity) target having thickness or surface density 5.0 mg/cm^2 with ^{12}C beam at 65 and 75 MeV beam energies. Estimation of cross sections of evaporation residues (ER) and fission yield were done using Projected Angular momentum Coupled Evaporation (PACE) code [220] (Figure 6.1). Based on this statistical model code, ∼10-20% of the fusion products are estimated to undergo fission. The beam current was ∼4-5 nA. Fifteen Compton suppressed clover detectors were arranged in spherical geometry where the detector positions are as follows: 3 at 157°, 2 at 140°, 2 at 115°, 4 at 90°, 2 at 3 at 65° and 2 at 40° with respect to the beam direction. Two fold coincidence data with time stamps were collected using fast digital data acquisition

t!

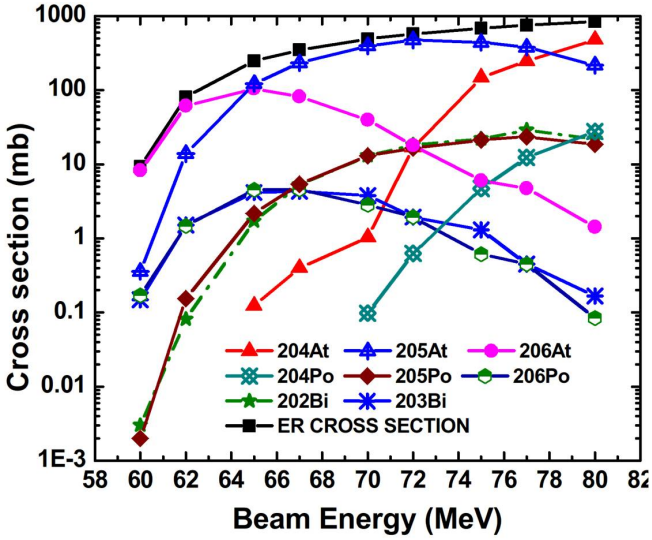

Figure 6.1: Cross-section of evaporation residue (ER) as a function of beam energy using PACE calculation for the target-projectile combination of the present experiment.

system based on Pixie-16 modules of XIA LLC [221]. The details of the array, data acquisition system and associated electronics can be found in the reference [222]. The data sorting routine Multi pARameter time-stamped based COincidence Search program (MARCOS) developed at TIFR has been used to generate γ-γ coincidence matrix and γ-γ-γ cube in Radware compatible format. Assignment of spin and parity of excited states were done by constructing angle dependent asymmetric γ-γ matrices and crystal orientation dependent polarization matrices, respectively using MARCOS. The coincident data were analyzed by INGASORT [223] and RADWARE [224] softwares.

6.3 Results and discussion

The ground state spin-parity of ^{204}At is known to be I^{π}=7^{+} and the configuration is $\pi(1h_{9/2})\otimes\nu(2f_{5/2})$ outside the ^{202}Po core. An isomeric excited state ($T_{1/2}$=108 ms) of 587 keV with spin parity 10^{-} was known previously for this nucleus with $\pi(1h_{9/2})\otimes\nu(1i_{13/2})$ configuration due to the spin gap arising from the intruder neutron orbital [225]. The main sequence of transitions including 601, 491, 717 and 537 keV gamma rays and the ΔI

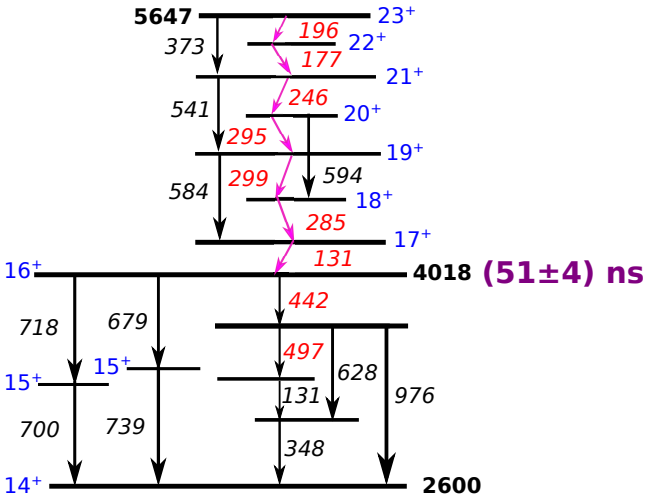

Figure 6.2: Part of the level scheme involving ΔI=1 magnetic dipole transitions. Transitions marked with red color were reported by previous workers [8].

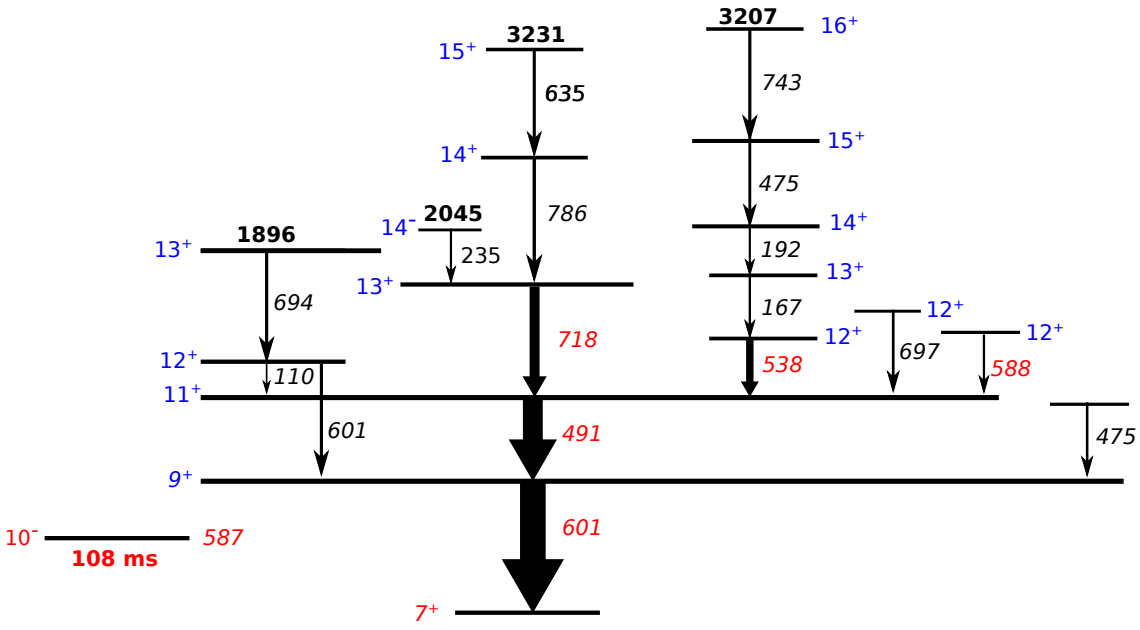

Figure 6.3: Level scheme of ^{204}At involving yrast sequence of transitions. Transitions marked with red color were reported by previous workers [8].

= 1 possible shears band-like structure consisting of transitions involving 131, 285, 299, 296 and 246 keV gamma rays were identified from angular distribution measurements by the previous workers [8]. It was reported that the ΔI=1 band is highly probable to be magnetic dipole in nature as large intensity of astatine X-rays was observed which is not possible for a $E1$ transition due to its lower internal conversion coefficient.

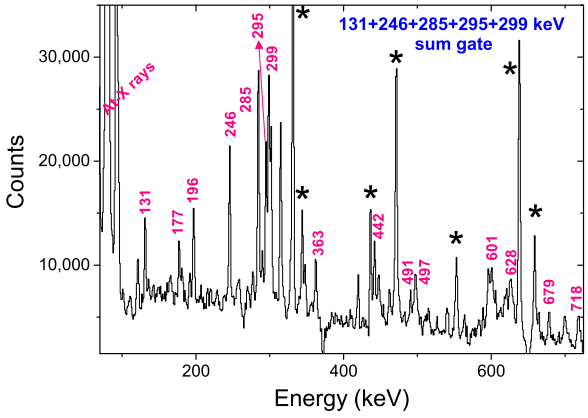

Figure 6.4: Gamma-ray coincidence spectrum in ^{204}At by gating on the sum of γ-ray transitions (131, 246, 285, 295 and 299 keV) in the $\Delta I = 1$ band. Contaminations due to the production of other nuclei, especially ^{205}At, are indicated by *.

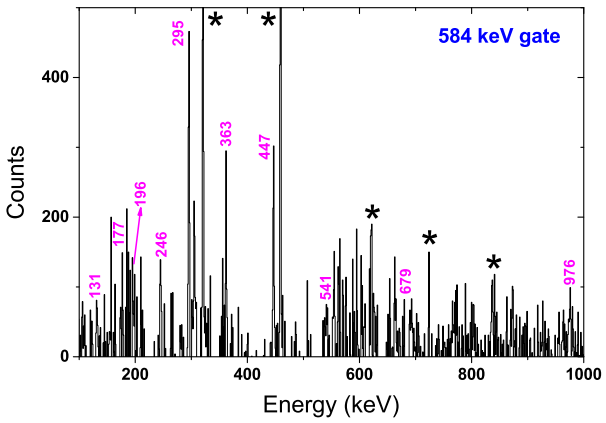

Figure 6.5: Gamma-ray coincidence spectrum in ^{204}At by gating on cross-over 584 keV γ-ray transition along ΔI=1 band.

From the on-line data taken at 65 and 75 MeV beam energies, γ-γ matrices, astatine X-ray gated γ-γ matrices, prompt and delayed γ-γ matrices and gamma gated γ-ΔT matrices were constructed to build the level scheme of ^{204}At. Identification of ^{204}At was done by astatine X-ray coincidence and by gating on the known transitions of ^{204}At [8]. A huge contamination due to ^{205}At was observed in the projection spectrum. The multipolarities of the coincident γ-ray transitions have been determined through the measurement of ratio of directional correlation of oriented nuclei (RDCO) by the data taken from the Clover detectors [226–228] placed at 157° and 90° angles using the following equation

$$\mathrm{R_{DCO}} = \frac{I_{\gamma_2} \text{ observed at } 157^\circ, \text{ gated by } \gamma_1 \text{ at } 90^\circ}{I_{\gamma_2} \text{ observed at } 90^\circ, \text{ gated by } \gamma_1 \text{ at } 157^\circ}, \tag{6.12}$$

where I is the intensity of a particular peak. Linear polarization of the coincident γ-rays was determined by using Clover detectors as Compton polarimeters [229–231] where all the four crystals of the Clover detector act as scatterer and two adjacent crystals behave as absorbers. Due to the orientation of electric and magnetic field vectors of the multipole radiation at 90° with respect to the beam axis, electric multipole radia-

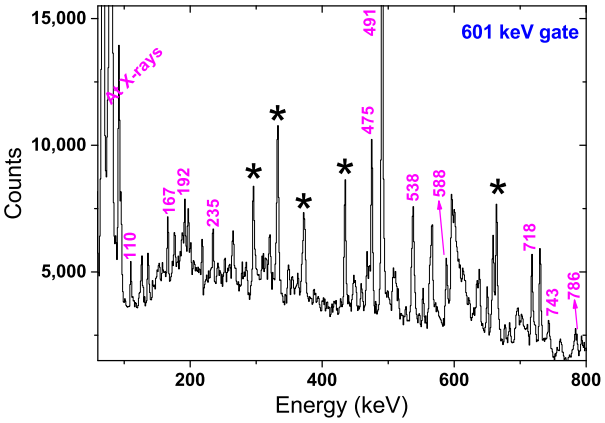

Figure 6.6: Gamma-ray coincidence spectrum by gating on 601 keV γ-ray transition above the 7^+ ground state of ^{204}At.

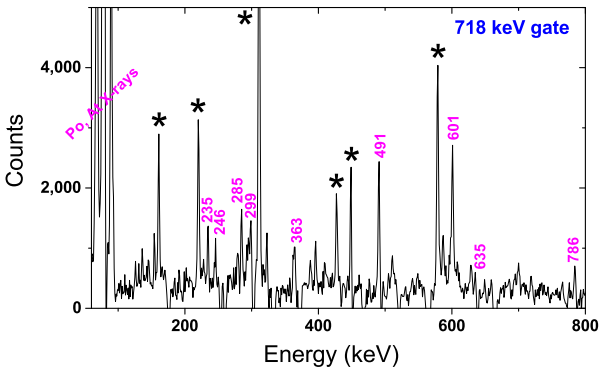

Figure 6.7: Gamma-ray coincidence spectrum in ^{204}At by gating on 718 keV transition.

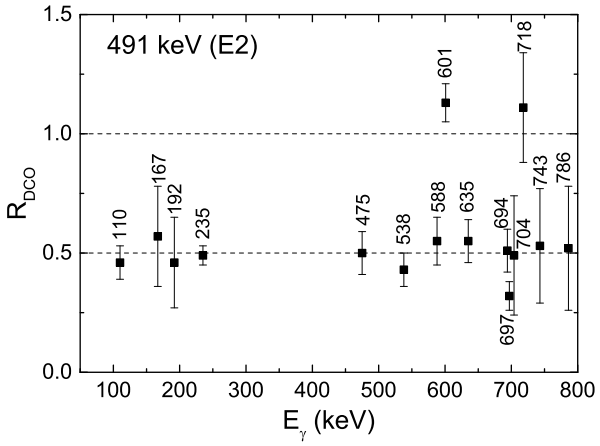

Figure 6.8: DCO plot with respect to 491 keV dipole transition of the $\Delta I = 1$ band in ^{204}At.

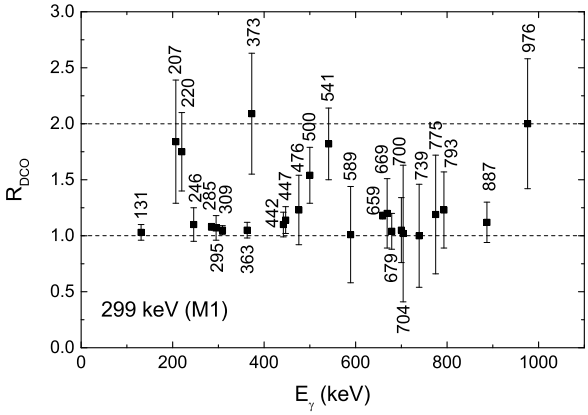

Figure 6.9: DCO plot with respect to 299 keV dipole transition of the $\Delta I = 1$ band in ^{204}At.

tion prefers perpendicular scattering and magnetic multipole radiation prefers parallel Compton scattering. Asymmetry of the Compton scattered photons or the polarization directional correlation of oriented nuclei (PDCO) can be determined by the following equation:

$$\text{PDCO} = \frac{a(E_\gamma)N_\perp - N_\parallel}{a(E_\gamma)N_\perp + N_\parallel}, \tag{6.13}$$

where $N_\parallel$ and $N_\perp$ are the intensities of a particular gamma-ray transition scattered into parallel and perpendicular segments of the Colver detectors with respect to the beam direction. The factor a is the correctional factor due to geometrical asymmetry of the

Clover crystals and it is obtained from the following formula:

$$a(E_\gamma) = \frac{N_\parallel(\text{unpolarized})}{N_\perp(\text{unpolarized})}. \tag{6.14}$$

This factor a is obtained using calibration sources viz. ^{152}Eu and ^{133}Ba.

Two sequences of transitions in the level scheme of ^{204}At, built from the present experiment are shown in Figures 6.2 and 6.3. Relevant gated coincidence spectra are shown in the Figures 6.4, 6.5, 6.6 and 6.7. Gamma ray spectra, obtained by gating on the known transitions of the $\Delta I = 1$ band, reveal four new cross-over transitions (Figure 6.5) from the present experiment. Multipolarity of the transitions, observed for the coincident gamma-rays in ^{204}At, are estimated by putting gate on 299 keV dipole transition and 491 keV quadrupole transition. These are shown in the Figures 6.8 and 6.9, respectively. The PDCO plot shown in the Figure 6.10 reveals electric/magnetic nature of transitions observed for ^{204}At. By putting gates on the 601 and 491 keV gamma rays (Figure 6.6), and also on the astatine X-rays, a significant number of new transitions were found. The 538 keV transition, which was put in coincidence with 717, 491 and 601 keV γ-rays by the previous workers [8], was not found to have any coincidence relationship with the 718 keV gamma ray (Figure 6.7). A sequence of new transitions were found above the 1630 keV level involving 167, 192, 475, 743 keV γ-ray transitions, which are in coincidence with 538 keV γ-ray decaying to 1092 keV level (Figure 6.3). Ordering of these transitions has been cross-checked by intensity correlations and also by reverse gating. The two γ-rays 443 keV and 497 keV were found to be in coincidence with the ΔI =1 band but due to lack of sufficient information for constructing the level scheme, these γ-rays were not placed in the level sequence by the earlier workers [8] and it was predicted that, probably, these γ-rays are from the low spin states of ^{204}At and above 10^- isomer. However, we have fitted these two levels decaying from the levels below the ΔI=1 band from the total intensity balance of these transitions (Figure 6.4). Reverse gating on these transitions produces astatine X-rays and the known ^{204}At yrast gamma

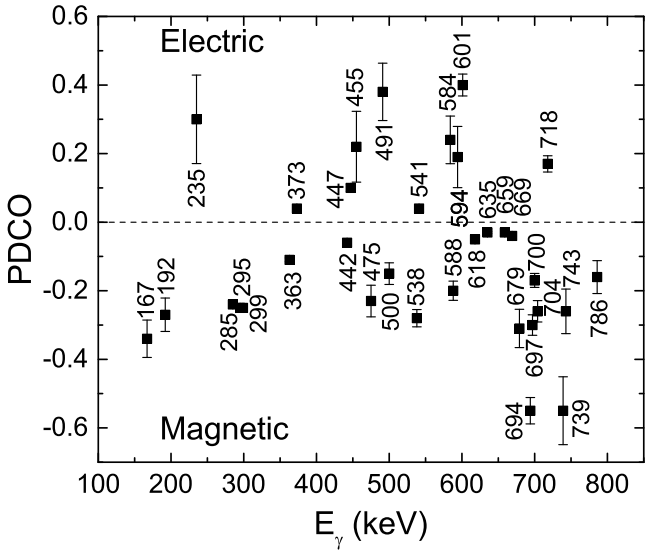

Figure 6.10: PDCO plot of several transitions observed in ^{204}At

rays. The sequence of transitions involving 601, 491, 717, 537 keV γ-rays were previously reported not to have any coincidence relationship with the transitions in the $\Delta I = 1$ band. However, from the present experiment, we have found that γ-rays in the $\Delta I = 1$ band decay into the sequence of transitions involving 718, 491 and 601 keV γ-rays (Figure 6.4 and 6.6). Further investigations into the cross correlation of the transitions reveal the main yrast sequence and new transitions belonging to the $\Delta I = 1$ band. The 601 keV γ-ray was tentatively assigned to be dipole in nature to be consistent with the $E2$ assignment of the neighboring nucleus ^{207}Fr [8]. The 717 and 491 keV γ-rays were assigned quadrupole character from angular distribution measurements [8]. But, from the present DCO ratio measurement by gating on 491 keV $E2$ transition, the 601 keV has been assigned quadrupole character (see Figure 6.8). The linear polarization of the transitions in the $\Delta I = 1$, including cross-over transitions, are shown in Figure 6.10 which establishes electric character of the cross-over transitions and magnetic character of the dipole transitions belonging to the ΔI=1 band. Multipolarities of these transitions obtained by putting gate on 299 keV (see Figure 6.9) and 285 keV transitions in the ΔI=1 sequence confirm dipole character of these transitions and quadrupole character of the cross-over transitions.

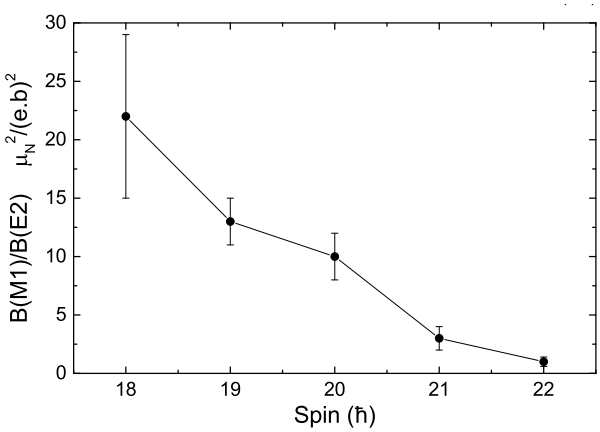

Figure 6.11: The ratio $\frac{B(M1)}{B(E2)}$ as a function of spin of the energy levels in the ΔI=1 band in ^{204}At.

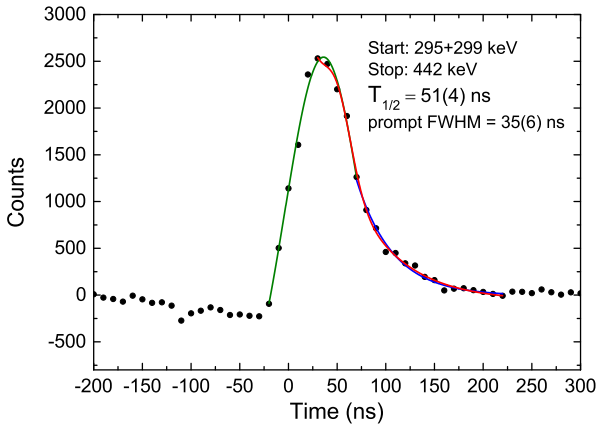

Figure 6.12: Time difference spectra showing the half-life of the isomeric transition in ^{204}At.

A sequence of magnetic dipole transitions with very little deformation creates a rotation-like character where the angular momentum is generated by shears mechanism [215]. General characteristics of the shears band is that the band consists of strong $M1$ transition with very weak cross-over $E2$ transition [215] which produces large values of $\frac{B(M1)}{B(E2)}$ $\geq$20 $(\frac{\mu_N}{e\cdot b})^2$. The value of $\frac{B(M1)}{B(E2)}$ generally decreases with the increase of spin or angular momentum. Similar sequence of shears band was found in lead and bismuth nuclei [215, 232, 233]. In the previous work, no crossover $E2$ transition was observed but by estimating the intensity of the smallest observable peak of the unidentified $E2$ transition, they found large value of $\frac{B(M1)}{B(E2)}$ which promoted them to assign this sequence of levels to be a shears band. The values of $\frac{B(M1)}{B(E2)}$ is comparable to the neighboring Pb or Bi nuclei. We have calculated the ratio of $\frac{B(M1)}{B(E2)}$ using the equation 6.11 and a smooth decreasing trend (Figure 6.11) with the increase of angular momentum or spin is found. This observation supports the previous assignment of the ΔI=1 band to be a shears band. The value of $\frac{B(M1)}{B(E2)}$ ratio at the band head is $\sim$ 22 $\frac{\mu_N^2}{e^2b^2}$ which is comparable with the values found for the shears bands in the lead region [215]. Although these structures are close to the known shears bands in terms of $\frac{B(M1)}{B(E2)}$ ratio, they show somewhat different character. The ^{198,199}Pb [234] nuclei manifest very smooth monotonic increase of gamma ray energy with angular momentum in the magnetic rotational band. These

bands are described as "regular" bands. However, not all bands follow this behavior. In some bands, γ-ray energies stagger as function of the angular momentum. These bands are called irregular shears band. Level repulsion due to the crossings with other bands may give rise to such behavior [215]. It can be noted that similar irregular sequence of low-energy transitions was also suggested to be shears band in ^{205}Rn, which is an isotone of ^{204}At and ^{206}Fr.

A systematic search of isomeric transition has been carried out for ^{204}At by constructing gamma gated E_γ-ΔT matrices which has revealed the presence of new isomer along the linking pathway. The time difference spectrum using 299+295 keV γ-rays (in the ΔI=1 band) as start and 442 keV as stop shows delayed nature of the 442 keV transition in the form of asymmetric tail of a Gaussian distribution. A half-life of 51±4 ns (Figure 6.12) is obtained for 4018 keV level through the exponential fitting of the decay tail of the spectrum. The $i_{13/2}$ intruder neutron hole may be responsible for this isomeric transition.

6.4 Conclusion

The level scheme of ^{204}At, known so far from the Gammasphere experiment [8], has been extended in this thesis work by adding new transitions obtained in our experiment using the Clover array of INGA. Measurement of DCO and PDCO ratios for many transitions enabled us to assign spin-parity of the levels and multipolarities of the transitions. A systematic study for search of the isomeric transition has been made using the tagged γ-γ time difference technique, which has revealed a new isomeric transition of half-life = 51±4 ns. The observation of four weak crossover $E2$ transitions along the proposed ΔI= 1 band, large value of $\frac{B(M1)}{B(E2)}$ ratio at the band head and the smooth decrease of $\frac{B(M1)}{B(E2)}$ ratio with the increase of spin support the existence of the magnetic rotational band in ^{204}At at high spin.

CHAPTER 7

Summary and conclusion

Important roles played by the electromagnetic multipole moments inside the atomic and the nuclear environments, their applications in the studies of the structural aspects of some of the solid materials and nuclear ensembles have been explored in this thesis. The PAC technique which can probe material at atomic length scale, has been used to study the structural properties of some chemical and intermetallic compounds.

Exploiting the electric quadrupole moment of the probe nucleus ^{181}Ta, a comprehensive study of the binary alloys of Zr-Ni and Hf-Ni systems has been performed using this technique. The experimental results of PAC along with the calculated results by density functional theory (DFT) give valuable information on the phase components, phase stability and probe site occupancies in these compounds. It is found that the probe atoms can occupy more than one crystallographic site in a material (viz. Zr_8Ni_{21}/Hf_8Ni_{21}, β-$HfNi_3$). The phase Zr_9Ni_{11} was found to decompose to ZrNi and Zr_7Ni_{10} phases, and Hf_8Ni_{21} decomposed to β-$HfNi_3$ eutectoidally at high temperature. The decompositions of these phases were found to be irreversible. The Hf metal was found to be less soluble in some of the Ni rich Zr-Ni samples viz. Zr_8Ni_{21}, $ZrNi_3$, where the probe atom comes out of the crystallographic Zr sites at high temperature. In the Ni rich Hf samples (viz. Hf_8Ni_{21}, β-$HfNi_3$), the solubility of Hf is found to be less than other Hf-Ni samples (viz. Hf_9Ni_{11},

Hf_7Ni_{10}) as quadrupole interaction due to unreacted Hf was found in these Ni rich Hf-Ni alloys. In the Zr-Ni system, however, no quadrupole interaction due to unreacted Zr was found in any of the Zr-Ni samples. Similar electric field gradients (EFG) were found for isoformulae Zr-Ni and Hf-Ni compounds which supported the isostructurality of these compounds. In all these binary alloys of Zr-Ni and Hf-Ni systems, multiple phases have been found to be produced. Quadrupole frequencies for different component phases were found to decrease with temperature following linear or $T^{3/2}$ temperature dependent relationship in these binary alloys. However, an anomalous temperature dependence of EFG was observed in Hf_9Ni_{11} sample where the quadrupole frequency was found to increase linearly with temperature. The other structural measurements by complementary techniques, viz. X-ray diffraction (XRD) and transmission electron microscopy/selected area electron diffraction (TEM/SAED) techniques have also been performed in Zr-Ni and Hf-Ni binary alloys to determine the phase components in these alloys. The PAC results in these Zr-Ni and Hf-Ni binary alloys have been reconciled with the phase diagram and it is found that production of multiple phases is governed by the presence of congruently melting phases, peritectic reaction, peritectoid reaction, eutectic and eutectoid reactions. Calculations of electric field gradients by density functional theory using WIEN2k simulation package have been carried out and the results are found to be useful to assign the different component phases. Moreover, ab-initio total energy calculations have very successfully predicted the preferred sites of the impurity atoms in the host lattice [viz. Zr(1) and Zr(3) sites in Zr_8Ni_{21}].

The PAC was found to be a powerful technique for determining subtle microstructural changes in a sample. In Rb_2ZrF_6, four different structural modifications have been found and two of these EFGs have been reported for the first time. A displacive phase transition was found to occur spontaneously at room temperature due to the rotation of ZrF_6^{2-} octahedral ionic group about the principal axis in this compound. In another sample of Rb_2ZrF_6, nuclear spin-relaxation has been observed at high temperature due to hopping of fluorine atom in the octahedral cage of ZrF_6^{2-}. However, no such phase transitions

or nuclear spin-relaxation phenomena have been observed in the isostructural Cs_2HfF_6 sample.

From present PAC studies in $ZrF_4{\cdot}3H_2O$ and $HfF_4{\cdot}3H_2O$, both monoclinic and triclinic structures have been found in these trihydrated compounds, which support the isostructurality of isoformulae compounds of Zr and Hf. From previous measurement, both monoclinic and triclinic crystal structures for $ZrF_4{\cdot}3H_2O$ and only monoclinic crystal structure for $HfF_4{\cdot}3H_2O$ were reported. The dehydration processes of these samples have also been studied by temperature dependent PAC measurements.

The effects of nominal Zr impurity ($\sim$6 at%) in Hf metal have been studied from PAC measurements at different temperature. The entropy of formation and binding energy for the probe-impurity pair have been determined following the Arrhenius behavior. The present measured values are found to be comparable with earlier reported values in some other dilute alloys. The Arrhenius behavior is found to be valid in the temperature range 473-773 K. The EFGs for pure Hf and probe-impurity component have been found to decrease linearly with temperature.

From the γ-ray spectroscopic investigation in ^{204}At nucleus, several new γ-ray transitions have been identified for the first time in this thesis. Spin and parity of nuclear energy levels have been assigned by DCO and polarization measurements. A magnetic rotational band is found at high spin states in this nucleus. Several crossover $E2$ transitions have been found along the magnetic rotational band. The $\frac{B(M1)}{B(E2)}$ ratio, which is related to the electric quadrupole moment and magnetic dipole moment of the nucleus, is found to decrease with spin and at the band head. The value of $\frac{B(M1)}{B(E2)}$ ratio is found to be comparable with those for the magnetic rotational bands in lead nuclei, which support the presence of magnetic rotational band in ^{204}At nucleus. An isomeric transition has been found along the linking pathway between the magnetic rotational band and the yrast sequence of transitions.

Bibliography

[1] G. Schatz, A. Weidinger, *Nuclear condensed matter physics: Nuclear methods and applications* (1996).

[2] M. O. Zacate, H. Jaeger, *Defect and Diffusion Forum* **311**, 3 (2011).

[3] R. L. Davidovich, M. A. Pushilin, V. B. Logvinova, A. V. Gerasimenko, *Journal of Structural Chemistry* **54**, 541 (2013).

[4] S. Pellicori, E. Colton, *Thin Solid Films* **209**, 109 (1992).

[5] C. C. Dey, *Journal of Physics and Chemistry of Solids* **78**, 12 (2015).

[6] H. Shen, L. A. Bendersky, K. Young, J. Nei, *Materials* **8**, 4618 (2015).

[7] P. Blaha, K. Schwarz, G. K. H. Madsen, D. Kvasnicka, J. Luitz, *WIEN 2k: An Augmented Plane Wave Plus Local Orbitals Program for Calculating Crystal Properties, Vienna University of Technology, Vienna, Austria*, (2001).

[8] D. J. Hartley, *et al.*, *Physical Review C* **78**, 054319 (2008).

[9] R. Davie, A. Poletti, G. Dracoulis, A. Byrne, C. Fahlander, *Nuclear Physics A* **430**, 454 (1984).

[10] S. Cottenier, Density Functional Theory and the Family of (L)APW-methods: a step-by-step introduction, 2002-2013 (2nd edition), ISBN 978-90-807215-1-7.

[11] T. Kosorukova, V. Ivanchenko, G. Firstov, H. Noël, *Solid State Phenomena (Trans Tech Publlication)* **194**, 14 (2013).

[12] P. Nash, A. Nash, *Bulletin of Alloy Phase Diagrams* **4**, 250 (1983).

[13] H. Morinaga, T. Yamazaki, *In-beam gamma-ray spectroscopy* (1976).

[14] G. L. Catchen, *MRS Bulletin* **20**, 3746 (1995).

[15] T. M. Rearick, G. L. Catchen, J. M. Adams, *Physical Review B* **48**, 224 (1993).

[16] J. Schell, P. Schaaf, D. C. Lupascu, *AIP Advances* **7**, 105017 (2017).

[17] K.-H. Speidel, O. Kenn, F. Nowacki, *Progress in Particle and Nuclear Physics* **49**, 91 (2002).

[18] T. J. Gray, *et al.*, *Physical Review C* **96**, 054332 (2017).

[19] L. Hemmingsen, T. Butz, *Perturbed Angular Correlations of γ-rays (PAC) Spectroscopy* (American Cancer Society, 2011).

[20] R. Dogra, A. Byrne, M. Ridgway, *Journal of Electronic Materials* **38**, 623 (2009).

[21] S. K. Dey, C. C. Dey, S. Saha, *Journal of Physics and Chemistry of Solids* **95**, 98 (2016).

[22] S. K. Dey, C. C. Dey, S. Saha, J. Belošević-Čavor, *Intermetallics* **84**, 112 (2017).

[23] S. K. Dey, C. C. Dey, S. Saha, J. Belošević-Čavor, D. Toprek, *Journal of Alloys and Compounds* **723**, 425 (2017).

[24] G. L. Catchen, T. M. Rearick, *Physical Review B* **52**, 9890 (1995).

[25] C. C. Dey, *et al.*, *Journal of Applied Physics* **109**, 113918 (2011).

[26] J. Schell, *et al.*, *Journal of Applied Physics* **121**, 145302 (2017).

[27] M. B. Barbosa, *et al.*, *physica status solidi (b)* **250**, 801.

[28] A. F. Pasquevich, F. H. M. Cavalcante, J. C. Soares, *Hyperfine Interactions* **179**, 67 (2007).

[29] M. Uhrmacher, *Defect and Diffusion Forum* **311**, 105 (2011).

[30] T. Butz, S. Ryu, S. Jankuhn, S. Das, S. Ghoshal, *Defect and Diffusion Forum* **311**, 137 (2011).

[31] B. N. Ganguly, *et al.*, *Nuclear Instruments and Methods in Physics Research Section B: Beam Interactions with Materials and Atoms* **362**, 103 (2015).

[32] C. Rivaldo-Gómez, G. Cabrera-Pasca, A. Zúñiga, A. Carbonari, J. Souza, *Scientific reports* **5**, 15128 (2015).

[33] P. de la Presa, K. Lieb, M. Uhrmacher, L. Ziegeler, *Zeitschrift für Naturforschung A* **55**, 237 (2000).

[34] J. Schell, *et al.*, *Journal of Applied Physics* **121**, 145302 (2017).

[35] M. Steffens, R. Vianden, A. F. Pasquevich, *Hyperfine Interactions* **237**, 117 (2016).

[36] J. Roth, M. Uhrmacher, R. de la Presa, L. Ziegeler, K. Lieb, *Zeitschrift für Naturforschung A* **55**, 242 (2000).

[37] S. K. Dey, C. C. Dey and S. Saha, *Journal of Physics and Chemistry of Solids* **93**, 145 (2016).

[38] S. K. Dey, C. C. Dey and S. Saha, *Journal of Physics and Chemistry of Solids* **91**, 18 (2016).

[39] T. M. Mendonça, *et al.*, *Phys. Rev. B* **84**, 094524 (2011).

[40] S. Cottenier, *et al.*, *Physical Review B* **63**, 195103 (2001).

[41] M. Forker, *et al.*, *Physical Review B* **87**, 155132 (2013).

[42] A. V. Tsvyashchenko, *et al.*, *Physical Review B* **96**, 245141 (2017).

[43] A. V. Tsvyashchenko, *et al.*, *Physical Review B* **76**, 045112 (2007).

[44] R. L. Rasera, G. L. Catchen, *Ferroelectrics* **150**, 151 (1993).

[45] P. Keßler, K. Lorenz, R. Vianden, *Defect and Diffusion Forum* **311**, 167 (2011).

[46] M. Forker, S. Müller, P. de la Presa, A. F. Pasquevich, *Physical Review B* **68**, 014409 (2003).

[47] A. W. Carbonari, J. Mestnik-Filho, R. N. Saxena, *Defect and Diffusion Forum* **311**, 39 (2011).

[48] S. N. Mishra, *Physical Review B* **77**, 224402 (2008).

[49] S. N. Mishra, S. Bose, P. Vasa, P. Ayyub, *Physical Review B* **71**, 094429 (2005).

[50] S. K. Mohanta, S. N. Mishra, K. K. Iyer, E. V. Sampathkumaran, *Physical Review B* **87**, 125125 (2013).

[51] S. K. Mohanta, S. Sarkar, P. Ayyub, S. N. Mishra, *Physical Review B* **94**, 184431 (2016).

[52] A. A. Tulapurkar, *et al.*, *Physical Review Letter* **85**, 1978 (2000).

[53] V. V. Krishnamurthy, S. N. Mishra, M. R. Press, S. H. Devare, *Physical Review Lett.* **74**, 1661 (1995).

[54] M. Lockwood Harberts, B. Norman, R. Newhouse, G. S. Collins, *Defect and Diffusion Forum* **311**, 159 (2011).

[55] G. S. Collins, X. Jiang, J. P. Bevington, F. Selim, M. O. Zacate, *Phys. Rev. Lett.* **102**, 155901 (2009).

[56] P. Boyer, A. Baudry, *Journal of the Less Common Metals* **129**, 213 (1987).

[57] A. Lerf, T. Butz, *Angewandte Chemie International Edition in English* **26**, 110.

[58] A. Jancso, *et al.*, *Journal of Physics G: Nuclear and Particle Physics* **44**, 064003 (2017).

[59] L. Hemmingsen, K. N. Sas, E. Danielsen, *Chemical Reviews* **104**, 4027 (2004).

[60] S. Chakraborty, *et al.*, *Accounts of Chemical Research* **50**, 2225 (2017).

[61] J. Vibenholt, *et al.*, *Inorganic Chemistry* **51**, 1992 (2012).

[62] A. Jancso, *et al.*, *Journal of Physics G: Nuclear and Particle Physics* **44**, 064003 (2017).

[63] R. L. Rasera, G. L. Catchen, *Ferroelectrics* **150**, 151 (1993).

[64] D. Banerjee, *Study of group IVB metal oxides in bulk and lower dimension using perturbed yy angular correlation technique*, HBNI, (2014).

[65] A. Vasquez, J. Rogers, A. Maciel, *Physics Letters A* **45**, 253 (1973).

[66] A. Vasquez, J. D. Rogers, E. Karlsson, R. Wäppling (Eds.), *Proc. Conf. Uppsala, Uppsala* p. 54 (1974).

[67] J. A. Martínez, *et al.*, *Physical Review B* **35**, 5244 (1987).

[68] F. Ruiz, *et al.*, *International Journal of Hydrogen Energy* **33**, 3576 (2008). 2nd National and 1st Latin American Congress, Hydrogen and Sustainable Energy Sources.

[69] J. Nei, K. Young, S. Salley, K. Ng, *Journal of Alloys and Compounds* **516**, 144 (2012).

[70] J. Nei, *et al.*, *International Journal of Hydrogen Energy* **37**, 16042 (2012). Advances in Hydrogen Production (Selected papers from ICH2P-2011).

[71] K.-h. Young, J. Nei, *Materials* **6**, 4574 (2013).

[72] K. Young, T. Ouchi, M. A. Fetcenko, W. Mays, B. Reichman, *International Journal of Hydrogen Energy* **34**, 8695 (2009).

[73] F. Ruiz, E. Castro, H. Peretti, A. Visintin, *International Journal of Hydrogen Energy* **35**, 9879 (2010).

[74] K. Young, J. Nei, T. Ouchi, M. Fetcenko, *Journal of Alloys and Compounds* **509**, 2277 (2011).

[75] J. Joubert, M. Latroche, A. Percheron-Guégan, *Journal of Alloys and Compounds* **231**, 494 (1995).

[76] J. K. Stalick, L. A. Bendersky, R. M. Waterstrat, *Journal of Physics: Condensed Matter* **20**, 285209 (2008).

[77] K. Siegbahn, *Alpha-, Beta- and Gamma-Ray Spectroscopy* (Elsevier Science, 2012).

[78] J. M. Blatt, V. F. Weisskopf, *Theoretical nuclear physics* (Courier Corporation, 1991).

[79] J. Christiansen, *Hyperfine interactions of radioactive nuclei*, vol. 31 (Springer Science & Business Media, 2012).

[80] H. Rinneberg, *Atomic Energy Review* **17**, 477 (1979).

[81] E. Karlsson, *Solid state phenomena: as seen by muons, protons, and excited nuclei* (1995).

[82] R. M. Steffen, *Angular Correlations in Nuclear Disintegration*, Springer Netherlands, (1971).

[83] T. Butz, *Hyperfine Interactions* **52**, 189 (1989).

[84] A. Tacu, *Stability of polymersomes containing* ^{111}In *using pertubed angular correlation spectroscopy*, (2013).

[85] R. Béraud, I. Berkes, J. Daniére, G. Marest, R. Rougny, *Nuclear Instruments and Methods* **69**, 41 (1969).

[86] A. Abragam, R. V. Pound, *Physical Review* **92**, 943 (1953).

[87] A. G. Marshall, C. F. Meares, *The Journal of Chemical Physics* **56**, 1226 (1972).

[88] G. L. Catchen, T. M. Rearick, *Physical Review B* **52**, 9890 (1995).

[89] W. R. Leo, *Techniques for nuclear and particle physics experiments: a how-to approach* (Springer Science & Business Media, 2012).

[90] G. F. Knoll, *Radiation detection and measurement* (John Wiley & Sons, 2010).

[91] A. R. Arends, *et al.*, *Hyperfine Interactions* **8**, 191 (1980).

[92] C. C. Dey, *Pramana* **70**, 835 (2008).

[93] T. Butz, *et al.*, *Physica Scripta* **54**, 234 (1996).

[94] D. C. Torumba, *Density functional theory studies in nuclear condensed matter physics: hyperfine interactions at lanthanide impurities in iron and the temperature dependence of electric-field gradients in metals*, (2006).

[95] J. P. Perdew, K. Burke, M. Ernzerhof, *Physical Review Letter* **77**, 3865 (1996).

[96] N. W. Ashcroft, N. D. Mermin, *Solid State Physics* (2005).

[97] P. Blaha, K. Schwarz, P. Herzig, *Physical Review Letter* **54**, 1192 (1985).

[98] K. Koch, S. Cottenier, *Analysis of an Electric-Field Gradient (EFG): the EFG-switch in LAPW2* (2011).

[99] R. Vianden, *Hyperfine Interactions* **35**, 1077 (1987).

[100] R. L. Rasera, *et al.*, *Journal of Physics F: Metal Physics* **8**, 1579 (1978).

[101] C. C. Dey, *Solid State Communications* **179**, 43 (2014).

[102] T. Butz, S. K. Das, C. C. Dey, S. Ghoshal, *Zeitschrift für Naturforschung A* **68**, 610 (2013).

[103] M. Moszyński, *et al.*, *Nuclear Instruments and Methods in Physics Research Section A: Accelerators, Spectrometers, Detectors and Associated Equipment* **567**, 31 (2006). Proceedings of the 4th International Conference on New Developments in Photodetection.

[104] S. K. Dey, C. C. Dey and S. Saha, *Proceedings of the DAE-BRNS Symp. on Nucl. Phys.* **60**, 992 (2015).

[105] A. Hrynkiewicz, K. Królas, *Physical Review B* **28**, 1864 (1983).

[106] U. Wrede, T. Schaefer, R. Vianden, *Zeitschrift für Physik B Condensed Matter* **64**, 461 (1986).

[107] W. Witthuhn, W. Engel, *Electric Quadrupole Interaction in Noncubic Metals* (Springer Berlin Heidelberg, Berlin, Heidelberg, 1983), pp. 205–289.

[108] A. Kulińska, *Perturbed Angular Correlation method in materials science* (Institute of Nuclear Physics Polish Academy of Sciences, 2013).

[109] A. Lerf, T. Butz, *Hyperfine interactions* **36**, 275 (1987).

[110] D. Hall, C. Rickard, T. Waters, *Journal of Inorganic and Nuclear Chemistry* **33**, 2395 (1971).

[111] F. Gabela, B. Kojić-Prodić, M. Šljukić, Ž. Ružić-Toroš, *Acta Crystallographica Section B* **33**, 3733 (1977).

[112] C. Rickard, T. Waters, *Journal of Inorganic and Nuclear Chemistry* **26**, 925 (1964).

[113] J. A. Martínez, M. C. Caracoche, A. M. Rodríguez, P. C. Rivas and A. R. López García, *Chemical Physics Letters* **102**, 277 (1983).

[114] P. C. Rivas, *et al.*, *Hyperfine Interactions* **39**, 181 (1988).

[115] C. C. Dey, *Chemical Physics Letters* **612**, 8 (2014).

[116] T. Butz, S. K. Das, Y. Manzhur, *Zeitschrift für Naturforschung A* **64**, 103 (2009).

[117] W. G. Thies, H. Appel, R. Heidinger, G. M. Then, *Hyperfine Interactions* **30**, 153 (1986).

[118] R. L. Armstrong, *Journal of Magnetic Resonance (1969)* **20**, 214 (1975).

[119] A. Abragam, R. Pound, *Physical Review* **92**, 943 (1953).

[120] C. Tiwary, V. V. Gunjal, D. Banerjee, K. Chattopadhyay, *MATEC Web of Conferences* (EDP Sciences, 2014), vol. 14, p. 01005.

[121] Y. Yokoyama, K. Fujita, A. R. Yavari, A. Inoue, *Philosophical Magazine Letters* **89**, 322 (2009).

[122] S. Pang, T. Zhang, K. Asami, A. Inoue, *Materials Transactions* **43**, 1771 (2002).

[123] D. Zander, U. Köster, *Materials Science and Engineering: A* **375**, 53 (2004).

[124] M. Carl, J. D. Smith, B. Van Doren, M. L. Young, *Metals* **7**, 511 (2017).

[125] J. Zhang, R. Singer, *Metallurgical and materials Transactions A* **35**, 1337 (2004).

[126] V. Ivanchenko, T. Kosorukova, M. Samohin, S. Samohin, Yu. Butenko, *Patent of Ukraine on useful model* p. 26254 (2007).

[127] S. Alzahrani, M. Khan, *AIP Advances* **7**, 055706 (2017).

[128] V. Provenzano, *et al.*, *IEEE Transactions on Magnetics* **46**, 502 (2010).

[129] R. B. Wright, J. G. Jolley, M. S. Owens, D. L. Cocke, *Journal of Vacuum Science & Technology A: Vacuum, Surfaces, and Films* **5**, 586 (1987).

[130] X.-Y. Song, X.-B. Zhang, Y.-Q. Lei, Z. Zhang, Q.-D. Wang, *International Journal of Hydrogen Energy* **24**, 455 (1999).

[131] K. Young, *et al.*, *Journal of Alloys and Compounds* **480**, 521 (2009).

[132] A. Matsuyama, H. Mizutani, T. Kozuka, H. Inoue, *Journal of Alloys and Compounds* **714**, 467 (2017).

[133] P. Jain, C. Gosselin, N. Skryabina, D. Fruchart, J. Huot, *Journal of Alloys and Compounds* **636**, 375 (2015).

[134] A. Kamble, P. Sharma, J. Huot, *International Journal of Hydrogen Energy* **43**, 7424 (2018).

[135] A. Baudry, *et al.*, *Journal of Physics: Condensed Matter* **4**, 5025 (1992).

[136] J. A. Davidson, *Titanium molybdenum hafnium alloys for medical implants and devices*, US Patent 5, 954, 724, (1999).

[137] M. Kirkpatrick, W. Larsen, *Transactions of American Society for Metals* **54** (1961).

[138] P. Nash, C. S. Jayanth, *Bulletin of Alloy Phase Diagrams* **5**, 144 (1984).

[139] G. Ghosh, *Journal of Materials Research* **9**, 598616 (1994).

[140] L. Bsenko, *Journal of the Less Common Metals* **63**, 171 (1979).

[141] X. Tao, *et al.*, *Journal of Alloys and Compounds* **752**, 412 (2018).

[142] C. Becle, B. Bourniquel, G. Develey, M. Saillard, *Journal of the Less Common Metals* **66**, 59 (1979).

[143] E. Smith, R. W. Guard, *The Journal of The Minerals, Metals & Materials Society* **9**, 1189 (1957).

[144] D. Kramer, *Transactions of the Metallurgical Society of AIME* **251**, 256 (1959).

[145] J. van Vucht, *Journal of the Less Common Metals* **11**, 308 (1966).

[146] G. H. Jóhannesson, *et al.*, *Physical Review Letter* **88**, 255506 (2002).

[147] K. P. Gupta, *Journal of Phase Equilibria* **22**, 73 (2001).

[148] Z. Kejun, J. Zhanpeng, *Journal of Less-Common Metals* **166**, 21 (1990).

[149] J. M. Joubert, R. cerný, K. Yvon, *Zeitschrift für Kristallographie - New Crystal Structures* **213**, 227 (1998).

[150] L. Bsenko, *Acta Crystallographica Section B* **34**, 3204 (1978).

[151] L. Bsenko, *Acta Crystallographica Section B* **34**, 3201 (1978).

[152] J. Glimois, C. Becle, G. Develey, J. Moreau, *Journal of the Less Common Metals* **64**, 87 (1979).

[153] S. K. Shadangi, S. C. Panda, S. Bahn, *Acta Crystallographica Section B* **38**, 2092 (1982).

[154] X. Song, Z. Zhang, X. Zhang, Y. Lei, Q. Wang, *Journal of Materials Research* **14**, 12791285 (1999).

[155] S. Panda, S. Bhan, *Z. Metallk.* **64**, 793 (1973).

[156] S. Panda, S. Bhan, *Journal of the Less Common Metals* **34**, 344 (1974).

[157] J. Liu, L. Zhu, X. Huang, G. Cai, Z. Jin, *Computer Coupling of Phase Diagrams and Thermochemistry* **58**, 160 (2017).

[158] M. Kirkpatrick, J. Smith, W. Larsen, *Acta Crystallographica* **15**, 894 (1962).

[159] J.-M. Joubert, R. Cerný, K. Yvon, M. Latroche, A. Percheron-Guégan, *Acta Crystallographica Section C: Crystal Structure Communications* **53**, 1536 (1997).

[160] P. Silva, H. Saitovitch, J. Cavalcante, M. Forker, *Journal of Magnetism and Magnetic Materials* **322**, 1841 (2010).

[161] M. Marszalek, H. Saitovitch, P. Silva, *Zeitschrift Naturforschung Teil A* **55**, 49 (2000).

[162] B. Wodniecka, M. Marszatek, P. Wodniecki, A. Z. Hrynkiewicz, *Hyperfine Interactions* **80**, 1039 (1993).

[163] A. N. Poynor, S. E. Cumblidge, R. L. Rasera, G. L. Catchen, A. T. Motta, *Hyperfine Interactions* **136**, 549 (2001).

[164] A. Umićević, *et al.*, *Journal of Alloys and Compounds* **475**, 38 (2009).

[165] B. Cekić, *et al.*, *Journal of Alloys and Compounds* **480**, 40 (2009). Proceedings of the 16th International Conference on Solid Compounds of Transition Elements (SCTE 2008).

[166] C. C. Dey, S. Srivastava, *Physica B: Condensed Matter* **427**, 126 (2013).

[167] C. C. Dey, R. Das, S. Srivastava, *Journal of Physics and Chemistry of Solids* **82**, 10 (2015).

[168] A. Baudry, P. Boyer, M. A. Chikdene, *Journal of Physics: Condensed Matter* **2**, 8075 (1990).

[169] A. Chikdene, A. Baudry, P. Boyer, *Journal of Physics F: Metal Physics* **18**, L187 (1988).

[170] A. Baudry, P. Boyer, A. Chikdene, *Hyperfine Interactions* **60**, 727 (1990).

[171] H. Drulis, W. Iwasieczko, V. Zaremba, *Journal of Magnetism and Magnetic Materials* **256**, 139 (2003).

[172] A. Amamou, *Solid State Communications* **37**, 7 (1981).

[173] C. C. Dey, *Journal of Magnetism and Magnetic Materials* **342**, 87 (2013).

[174] L. A. Errico, *et al.*, *Journal of Physics: Condensed Matter* **22**, 215501 (2010).

[175] P. Wodniecki, *et al.*, *Europhysics Letters* **77**, 43001 (2007).

[176] J. Gil, *et al.*, *Solid State Phenomena (Trans Tech Publ.)* **170**, 293, (2011).

[177] S. K. Dey, C. C. Dey, S. Saha, G. Bhattacharjee, D. Banerjee, D. Toprek, *arXiv:1809.08114* .

[178] P. E. Blöchl, O. Jepsen, O. K. Andersen, *Physical Review B* **49**, 16223 (1994).

[179] A. Kokalj, *Journal of Molecular Graphics and Modelling* **17**, 176 (1999).

[180] T. Butz, A. Lerf, *Physics Letters A* **97**, 217 (1983).

[181] P. Wodniecki, B. Wodniecka, A. Kuliska, M. Uhrmacher, K. Lieb, *Journal of Alloys and Compounds* **385**, 53 (2004).

[182] J. Belošević-Čavor, V. Koteski, J. Radaković, *Solid State Communications* **152**, 1072 (2012).

[183] J. Rodríguez-Carvajal, *Physica B: Condensed Matter* **192**, 55 (1993).

[184] F. R. Eshelman, J. F. Smith, *Acta Crystallographica Section B* **28**, 1594 (1972).

[185] S. K. Dey, C. C. Dey, S. Saha, J. Belošević-Čavor, D. Toprek, *arXiv:1703.10035v1*.

[186] I. Bulyk, Y. Basaraba, A. Trostianchyn, *Journal of Alloys and Compounds* **376**, 95 (2004).

[187] J. Christiansen, *et al.*, *Zeitschrift für Physik B Condensed Matter* **24**, 177 (1976).

[188] J. P. Dattagupta, K. Schubert, *Z. Met.* **64**, 789 (1973).

[189] F. D. Murnaghan, *Proceedings of the National Academy of Sciences* **30**, 244 (1944).

[190] A. Jain, *et al.*, *APL Materials* **1**, 011002 (2013).

[191] F. Boer, R. Boom, W. Mattens, A. Miedema, A. Niessen, Cohesion in metals: transition metal alloys, cohesion and structure (1989).

[192] O. Levy, G. L. Hart, S. Curtarolo, *Acta Materialia* **58**, 2887 (2010).

[193] R. G. Hennig, A. E. Carlsson, K. F. Kelton, C. L. Henley, *Physical Review B* **71**, 144103 (2005).

[194] J.-M. Joubert, R. Cerný, K. Yvon, M. Latroche, A. Percheron-Guégan, *Acta Crystallographica Section C* **53**, 1536 (1997).

[195] S. K. Dey, *et al.*, *Journal of Solid State Chemistry* **269**, 476 (2019).

[196] M. E. Kirkpatrick, D. M. Bailey, J. F. Smith, *Acta Crystallographica* **15**, 252 (1962).

[197] I. Yaar, *et al.*, *Hyperfine Interactions* **159**, 351 (2004).

[198] V. N. Svechnikov, A. K. Shurin and G. P. Dmitriyeva, *Russ. Metall. Fuels* **6**, 95 (1967).

[199] K. Zeng, Z. Jin, *Journal of the Less Common Metals* **166**, 21 (1990).

[200] P. Wodniecki, B. Wodniecka, A. Kuliska, M. Uhrmacher, K. Lieb, *Journal of Alloys and Compounds* **365**, 52 (2004).

[201] C. Dai, P. Saidi, Z. Yao, M. R. Daymond, *Acta Materialia* **140**, 56 (2017).

[202] B. Wodniecka, *et al.*, *Journal of Alloys and Compounds* **219**, 132 (1995). Eleventh international conference on solid compounds of transition elements.

[203] P. Wodniecki, B. Wodniecka, A. Kuliska, M. Uhrmacher, K. Lieb, *Journal of Alloys and Compounds* **312**, 17 (2000).

[204] P. Wodniecki, B. Wodniecka, A. Kulińska, A. Hrynkiewicz, *Zeitschrift für Naturforschung A* **53**, 355 (1998).

[205] P. Wodniecki, A. Kulińska, B. Wodniecka, A. Hrynkiewicz, *Zeitschrift für Naturforschung A* **53**, 349 (1998).

[206] P. Wodniecki, B. Wodniecka, M. Marszałek, A. Hrynkiewicz, *Zeitschrift für Naturforschung A* **51**, 437 (1996).

[207] H. Petrilli, M. Marszalek, H. Saitovitch, *Zeitschrift für Naturforschung A* **51**, 537 (1996).

[208] J. P. Perdew, K. Burke, M. Ernzerhof, *Physical Review Letter* **78**, 1396 (1997).

[209] Y. Zhang, W. Yang, *Physical Review Letter* **80**, 890 (1998).

[210] K. S. Krane, D. Halliday, *Introductory nuclear physics*, (Wiley New York, 1988).

[211] P. Regan, *Post Graduate Nuclear Experimental Techniques (4NET) Course Notes*, University of Surrey (2003).

[212] F. Dnau, *Nuclear Physics A* **471**, 469 (1987).

[213] M. Pfützner, *et al.*, *Physical Review C* **65**, 064604 (2002).

[214] K. A. Gladnishki, *et al.*, *Physical Review C* **69**, 024617 (2004).

[215] R. M. Clark, A. O. Macchiavelli, *Annual Review of Nuclear and Particle Science* **50**, 1 (2000).

[216] R. V. Janssens, T. L. Khoo, *Annual Review of Nuclear and Particle Science* **41**, 321 (1991).

[217] K. Heyde, J. L. Wood, *Reviews of Modern Physics* **83**, 1467 (2011).

[218] X. Feng, *et al.*, *The European Physical Journal A - Hadrons and Nuclei* **6**, 235 (1999).

[219] S. Frauendorf, *Nuclear Physics A* **557**, 259 (1993).

[220] A. Gavron, *Physical Review C* **21**, 230 (1980).

[221] R. Palit, *Nuclear Instruments and Methods in Physics Research Section A: Accelerators, Spectrometers, Detectors and Associated Equipment* **680**, 90 (2012).

[222] D. Kanjilal, *Spectroscopy of Trans-Lead Nuclei*, Jadavpur University (2013).

[223] R. K. Bhowmik, S. Muralithar, R. P. Singh, *DAE-BRNS symposium on nuclear physics: contributed papers, V. 44B* (2001).

[224] D. Radford, *Nuclear Instruments and Methods in Physics Research Section A: Accelerators, Spectrometers, Detectors and Associated Equipment* **361**, 297 (1995).

[225] M. Schmorak, *Nuclear Data Sheets* **72**, 409 (1994).

[226] A. Krmer-Flecken, *et al.*, *Nuclear Instruments and Methods in Physics Research Section A: Accelerators, Spectrometers, Detectors and Associated Equipment* **275**, 333 (1989).

[227] R. K. Bhowmik, ed. S. Bhattacharya, S. Banerjee, *Nuclear dynamics at low and medium energies and Nuclear structure*, Narosa.

[228] K. Krane, R. Steffen, R. Wheeler, *Atomic Data and Nuclear Data Tables* **11**, 351 (1973).

[229] P. Jones, *et al.*, *Nuclear Instruments and Methods in Physics Research Section A: Accelerators, Spectrometers, Detectors and Associated Equipment* **362**, 556 (1995).

[230] C. Droste, *et al.*, *Nuclear Instruments and Methods in Physics Research Section A: Accelerators, Spectrometers, Detectors and Associated Equipment* **378**, 518 (1996).

[231] K. Starosta, *et al.*, *Nuclear Instruments and Methods in Physics Research Section A: Accelerators, Spectrometers, Detectors and Associated Equipment* **423**, 16 (1999).

[232] N. Amita, A. K. Jain, B. Singh, *Atomic Data and Nuclear Data Tables* **74**, 283 (2000).

[233] A. O. Macchiavelli, *et al.*, *Physical Review C* **58**, R621 (1998).

[234] L. F. Yu, P. W. Zhao, S. Q. Zhang, P. Ring, J. Meng, *Physical Review C* **85**, 024318 (2012).